A Process-Based Model for Beach Profile Evolution

A Dissertation
Presented to
The Academic Faculty

by

Hüseyin Demir

In Partial Fulfillment
of the Requirements for the Degree
Doctor of Philosophy

School of Civil and Environmental Engineering
Georgia Institute of Technology
December 2007

A Process-Based Model for Beach Profile Evolution

Approved by:

Dr. Paul A. Work, Advisor
School of Civil and Environmental Engineering
Georgia Institute of Technology

Dr. Terry W. Sturm
School of Civil and Environmental Engineering
Georgia Institute of Technology

Dr. Kevin A. Haas
School of Civil and Environmental Engineering
Georgia Institute of Technology

Dr. Clark R. Alexander Jr.
Skidaway Institute of Oceanography

Dr. Hermann M. Fritz
School of Civil and Environmental Engineering
Georgia Institute of Technology

Date Approved: June 26,2007

ACKNOWLEDGEMENTS

I would like to thank my advisor Dr. Paul Work for his valuable guidance throughout my study and his positive outlook that gave me motivation after all our meetings.

I would like to thank Dr. Kevin Haas for always having the time for helping me in understanding and debugging the numerical models. I would like to express my appreciations to Dr. Clark Alexander, Dr. Hermann Fritz, and Dr. Terry Sturm for serving on my thesis committee and for their valuable comments.

I am thankful to Dr. George Voulgaris from the University of South Carolina and his team for making the field measurements possible. I would like to thank my friends and colleagues Brian, Lindsay, Jeseon and Servet and for their hard work during the experiments and making them enjoyable experiences. I would also like to thank my roommates Kemal and Zafer for their friendship and support. I am thankful to Dr. Ayse Erdolen for bringing a piece of home to Savannah.

I would like to thank my mom, dad and brother for their love and unconditional support. I would like to thank Meryem for her endless love and for giving me the reason and the power to carry on whenever I felt down.

I would like to thank my Iriver and all the podcasts for making the fifty thousand miles I traveled between Savannah and Gainesville almost pleasant.

This study was funded by South Carolina Sea Grant Consortium's South Carolina Coastal Erosion Study and USGS Woods Hole Science Center for Coastal and Marine Geology.

TABLE OF CONTENTS

LIST OF TABLES

LIST OF FIGURES

LIST OF SYMBOLS AND ABBREVIATIONS

$V_{b,\alpha}$	bottom mean current above the wave boundary layer (m/s)
$u_{0,\alpha}(t)$	bottom orbital velocity above the wave boundary layer (m/s)
$\tau_{\alpha}^{B}(t)$	bottom shear stress (N/m^2)
∇	horizontal gradient operator (m^{-1})
γ_s	specific weight of sediment ($kg\ m^{-2}s^{-2}$)
γ	specific weight of water ($kg\ m^{-2}s^{-2}$)
$u_{\alpha}^{'}(t)$	turbulent component of velocity in (m/s)
τ_{α}^{S}	wind shear stress (N/m^2)
$A(x,y)$	complex wave amplitude in REF/DIF
a_N	Nielsen's bottom roughness coefficient
$c(z,t)$	volumetric sediment concentration (m^3/m^3)
c_0	bed concentration (1-p)
C_D	drag coefficient
C_G	group velocity (m/s)
c_m	maximum reference concentration (m^3/m^3)
C_p	wave phase velocity (m/s)
$c_r(t)$	reference concentration (m^3/m^3)
D	wave energy dissipation due to wave breaking, (kg/s^3)
d	sediment diameter (m)
d_{50}	median sediment diameter (m)
$d_c(t)$	erosion depth (m)

$f_{2.5}$	grain roughness friction factor
f_{cw}	bottom friction factor
f_w	wave friction factor
g	gravitational acceleration (m/s^2)
h	local water depth (m)
H	wave height (m)
H_b	breaking wave height (m)
H_{mo}	Spectrum-based wave height (m)
h_o	still water depth (m)
H_{rms}	root-mean-square (rms) wave height (m)
H_s	significant wave height (m)
k	turbulent kinetic energy (m^2/s^2)
k_n	wave number (m^{-1})
l	turbulent length scale (m)
L	wavelength (m)
m	parameter controlling the shape of the velocity profile inside the sheet flow layer
$M_{sus}(t)$	total volume of suspended sediment (m^3/m^2)
n	parameter controlling the shape of the concentration profile inside the sheet flow layer
n_{BL}	empirical constant for wave boundary layer thickness taken as 2
P	pressure (N/m)
p	bed porosity
$pf(t)$	sediment pick-up rate (m/s)
q_α	volumetric sediment transport rate in α direction (m^2/s)
q_{slp}	slope-related sediment transport rate (m^2/s)

R_*	Grain size Reynolds number
Q_α	total volume flux of sediment (m^2/s)
S	bottom orbital velocity skewness
s	specific gravity (γ_s / γ)
$S_{\alpha\beta}$	radiation stress, mean momentum flux due to waves (N/m)
T	wave period (s)
T_m	mean wave period (s)
T_p	peak wave period (s)
tv	time variation of eddy viscosity
$U(t)$	wave orbital velocity just outside the wave boundary layer (m/s)
$u(z,t)$	orbital wave boundary layer velocity in wave direction (m/s)
$U_*(t)$	shear velocity (m/s)
$U_{*c}(t)$	current shear velocity (m/s)
U_{*wcm}	maximum combined shear velocity (m/s)
U_0	bottom orbital wave velocity amplitude (m/s)
U_c	bottom orbital velocity under the crest (m/s)
$u_r(t)$	velocity at the reference level
U_{rms}	Root-mean-square bottom orbital velocity (m/s)
$u_s(z,t)$	streaming velocity (m/s)
U_t	bottom orbital velocity under the trough (m/s)
$U_T(t)$	magnitude of the combined wave-current velocity just outside the wave boundary layer (m/s)
$u_{T\alpha}(z,t)$	instantaneous total velocity (m/s)
$u_\alpha(z,t)$	wave component of velocity (m/s)

$V_\alpha(z,t)$	mean component of velocity (m/s)
$w(z,t)$	orbital wave boundary layer velocity in vertical direction (m/s)
w_f	sediment fall velocity (m/s)
W_α	wind velocity at the 10 meter elevation (m/s)
z_a	theoretical bed level for current (m)
α_{CN}	coefficient in Crank-Nicholson scheme defining weight of the n+1th time step
α_{ML}	ratio of the mixing length *l*, to water depth
β	ratio of sediment diffusivity to eddy viscosity
$\delta(t)$	wave boundary layer thickness (m)
$\delta_s(t)$	sheet flow layer thickness (m/s)
ε	turbulent dissipation rate (m^2/s^3)
σ	wave angular velocity (1/s)
σ_r	wave roller angle (deg)
$\varepsilon_s(z,t)$	the sediment diffusion coefficient (m^2/s)
$\zeta(t)$	water surface elevation abo*ve still water level* (m)
η	ripple height (m)
$\theta(t)$	Shields parameter
θ_c	critical Shields parameter
θ_r	modified effective Shields parameter
θ_{sf}	skin friction Shields parameter
κ	von Karman's constant taken as 0.4
λ	ripple length (m)
ν	eddy viscosity (m^2/s)
$\nu_t(z,t)$	turbulent eddy viscosity (m^2/s)
ν_{tc}	current eddy viscosity (m^2/s)

ρ	density of water (kg m^{-3})
ρ_a	air density (kg/m^3)
τ	bed shear stress (N/m^2)
τ_{str}	streaming shear stress (N/m^2)
ω	wave angular frequency (rad s^{-1})

SUMMARY

Beach profile models predict the changes in bathymetry along a line perpendicular to the shoreline. These models are used to forecast bathymetric changes in response to storms, sea level rise or human activities such as dredging and beach nourishment. Process-based models achieve this by simulating the physical processes that drive the sediment transport as opposed to behavior models which simulate observed profile changes without resolving the underlying processes. Some of these processes are wave shoaling and breaking, boundary layer streaming, and offshore-directed undertow currents. These hydrodynamic processes control the sediment processes such as sediment pick-up from the bottom, diffusion of the sediment across the water column and its advection with waves and currents.

For this study, newly developed sediment transport and boundary layer models were coupled with existing models of wave transformation, nearshore circulation and bathymetry update, to predict beach profile changes. The models covered the region from the dry land to a depth of 6-8 meters, spanning up to 500 meters in the cross-shore direction. The modeling system was applied at storm time scales, extending from a couple of hours to several days. Two field experiments were conducted at Myrtle Beach, SC, involving the collection of wave, current and bathymetric data as a part of this study. The results were used to calibrate and test the numerical models along with data from various laboratory studies from the literature.

The sediment transport model computes the variation of sediment concentrations over a wave period and over the water column, solving the advection-diffusion equation using the Crank-Nicholson finite-difference numerical scheme. Using a new approach, erosion depth thickness and sediment concentrations within the bed were also predicted. The model could predict sediment transport rates for a range of conditions, within a

factor of two. It successfully computed the sediment concentration profile over the water column and within the bed and its variation throughout a wave period. Erosion depth and sheet flow layer thickness were also predicted reasonably well.

Wave heights across the profile were predicted within ten percent when the empirical wave breaking parameter was tuned appropriately. Mean cross-shore velocities contain more uncertainty, even after tuning. The importance of capturing the location of the maximum, near-bottom, cross-shore velocity when predicting bar behavior was shown. Bar formation, erosion, accretion, onshore and offshore bar movement were all computed with the model successfully.

1. INTRODUCTION

The need to understand and model sediment transport along the coasts of the world is increasing as the navigational, economic, touristic and recreational activities intensify. Sedimentation and erosion around structures, backfill of dredged channels, the response of the shore to storms and the effects of sea level rise are some of the reasons or processes that make the research in this area worthwhile. Predictive models have engineering applications such as comparing effects of various proposed structures or describing the effects of a planned offshore dredging project.

The area of interest for this study is the nearshore region. This region extends from the land-water interface to a vaguely defined depth which is taken as roughly 10 meters for this study. Hydrodynamics and sediment transport in this region are complex, three-dimensional processes, like most other physical phenomena in nature. The first models for beach profile evolution were behavior-oriented models lumping various processes together without resolving them separately to simulate the observed behavior. Process-based models simulate the underlying physical processes such as solving for the details of hydrodynamics to derive the sediment transport (De Vriend et al. 1993a). While still far from a full solution of the governing equations at the field scale, our understanding and modeling capabilities of hydrodynamics are better than for sediment transport. This is firstly because sediment transport depends on hydrodynamics. Also measuring and quantifying sediment transport is much harder and the available lab and field data are limited.

As the waves approach the shore their heights increase (after an initial small decrease) until they begin to break. The flux of momentum due to waves, called the radiation stress, also changes with the wave heights. The change in the cross-shore component of the radiation stress creates a set-down of the mean water surface prior to

breaking, and forces a set-up or increase in the mean water level after that. The longshore component of the radiation stress drives the longshore currents, which dominate over tidal currents in and near the surf zone, even under moderate wave conditions. The crests of the waves become higher than the troughs are deep as the waves approach shore. This leads to a skewness in the water level time series that also affects wave orbital velocities and results in higher maximum onshore velocities than offshore. The front face of a breaking wave, in which the water is tumbling down, is the roller. This very active zone may inject significant turbulence into the water column.

There is a net flux of water in the wave propagation direction, concentrated between the trough and crest of the wave. This flux is balanced by offshore-flowing currents at the bottom of the water column, called undertow, and/or rip currents. Even in the presence of undertow, there is a thin layer of onshore flow due to waves, limited to the boundary layer, called steady streaming. These are some of the important flows or processes that are observed or take place in the nearshore region and force the sediment transport (Fredsoe and Deigaard 1992).

The most successful methodology applied to date for modeling beach profile behavior has involved the use of models that are simple and take into account only the most relevant process or processes (De Vriend et al. 1993b). Of course the definition of "most relevant" is constantly changing with the science. Coastal area models of two-dimensional sediment transport at estuaries or around structures generally do not include detailed hydrodynamics to solve for coastal profile evolution. Longshore and cross-shore sediment transport are usually modeled separately using the time scale difference between them. Longshore sediment transport is generally slower and modeled at monthly or longer periods; cross-shore sediment transport is faster and can create significant bathymetric changes in hours to days. Longshore averaging of profiles is routinely employed when modeling cross-shore sediment transport to exclude the effects of longshore variations and complex three dimensional circulations. Computational

limitations are also an important factor. More advanced hydrodynamic models that can resolve the short wave phases can at the present time be applied only one-dimensionally and/or for shorter periods of time.

In this study, existing models for wave transformation and hydrodynamics are coupled with a new sediment transport and boundary layer model. Each sub-model is compared to measured data. Process-based profile modeling is still in its infancy and generally these kinds of models are not used to resolve the effects of longshore variations. They are applied for longshore uniform cases and/or longshore averaging is applied to remove effects of longshore variation. On open beaches the bathymetric changes due to longshore sediment transport occur over much longer time scales than cross-shore sediment transport. Even though the model system is capable of modeling sediment transport in both longshore and cross-shore directions, only the cross-shore sediment transport and profile evolution is the subject of this study. The model is applied at a storm time scale, which extends from a few hours to a few days. The quasi-3D, short wave-averaged hydrodynamics model can simulate most of the processes important for cross-shore sediment transport directly. Processes or features not captured by the basic equations, such as wave skewness, are included by empirical equations. The sediment transport model solves for the concentration profile from within the bed up to the water surface and its variation within a wave period. The model solves the advection-diffusion equation in 1D vertical and takes into account phase lag effects due to sediment suspension and settling.

The second chapter of this thesis includes a literature review, providing background material on relevant physical processes and previous modeling efforts. The third chapter describes the field data collected for this study during two different field experiments in 2003 and 2005 at Myrtle Beach, South Carolina. Wave and current measurements across a profile, bathymetric measurements, sediment sampling and video image collection were conducted in these field campaigns. The collected data were used

for hydrodynamic model comparisons. The details of the various models used and developed and their interaction with each other are explained in the fourth chapter.

Model testing and calibration results are divided into two chapters. Chapter Five covers only the wave boundary layer and the sediment transport models which were developed for this study. The data sets used for validation, which were taken from available literature, include experiments from oscillatory flow tunnels and wave tunnels, including monochromatic waves, random waves and waves with currents.

The whole model system, including the hydrodynamic model, is calibrated and tested with three different laboratory experiments from the literature in Chapter Six. The data include a case of bar formation, an erosional case with offshore bar movement and an accretional case with onshore bar movement. Application of the model to the Myrtle Beach field case is also described in this chapter. Hydrodynamic model results are compared with measurements which were updated every 30 minutes for a three-day simulation. The last chapter is the conclusions chapter, which summarizes the findings of the study, comments on its limitations and suggests areas for improvement and further study.

2. LITERATURE REVIEW

2.1. Introduction

Bathymetric changes in the nearshore are a result of many processes such as undertow, wave breaking and wave skewness. Most of these processes interact with each other creating a complex system. This literature review focuses more on sediment transport processes rather than hydrodynamics. Details of hydrodynamic processes are discussed as they relate to the sediment transport. Even though both are equally important in morphology modeling, this choice was made since most of the model development effort in this work has been devoted to sediment transport. Section 2.2 gives a brief introduction to the hydrodynamic processes in the nearshore.

The area of interest of this study is the nearshore region which might roughly be defined as the region extending from the shore to a depth of 10 m. Most of the processes discussed here are on the short wave scale (4-20 sec.). These waves dominate the beach profile change at the storm time scale (hours to days). They may also be enough to explain the beach profile behavior on a longer period extending to weeks.

2.2. Hydrodynamics

Waves created by winds propagate without being affected by the bottom in deep water. The orbital velocities, which decay with depth, are not felt at the bottom. As the waves approach shallow water, the waves slow down and wavelengths (L) decrease following the dispersion relationship.

$$\omega^2 = gk \tanh(k_n h) \tag{2.1}$$

where ω is the angular frequency of the wave ($\omega=2\pi/T$), g is the gravitational acceleration, k_n is the wave number ($k_n=2\pi/L$) and T is the wave period. The waves shoal and their wave height increases. The crest of the wave becomes higher than the trough's depth. Similarly, wave orbital velocities, which are sinusoidal in deep water, become skewed in shallower water, with forward velocities becoming larger than the backwards velocities (Figure 2.1). The mean velocity is still zero for skewed orbital velocities, but higher order moments of the velocity become non-zero which can create a net sediment transport even without a mean flow.

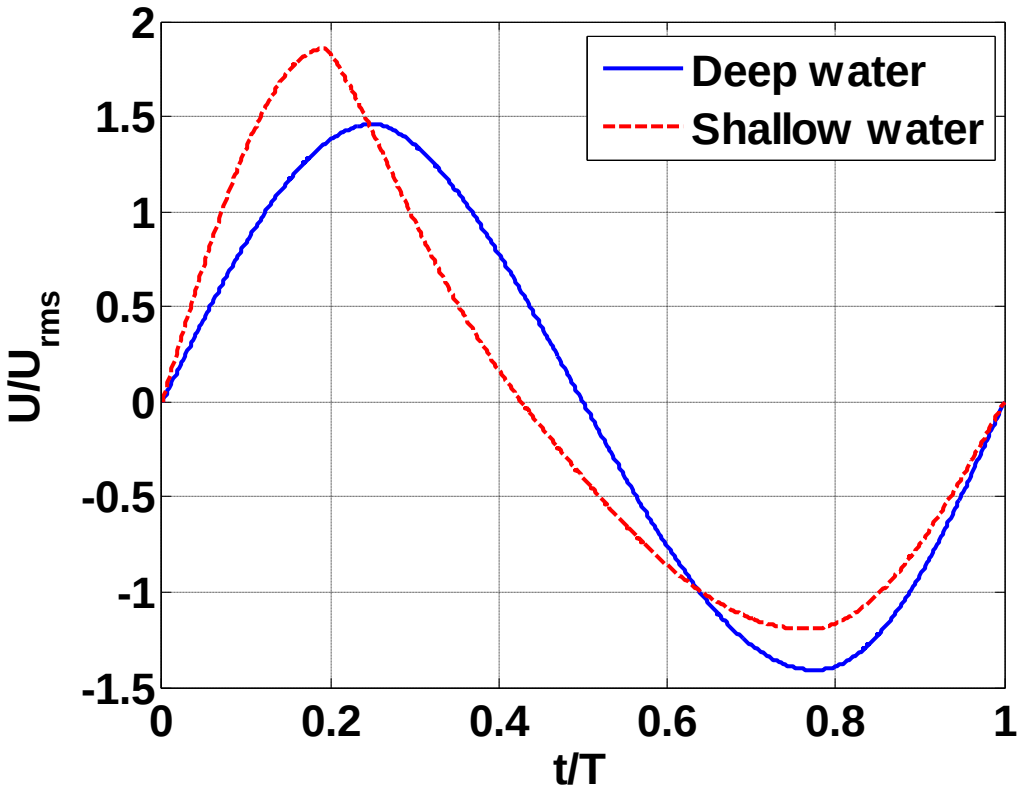

Figure 2.1. Sketch of wave orbital velocities normalized by U_{rms} in deep water and shallow water.

Waves move in wave groups. The wave groups have celerity different than the celerity of individual waves. The group speed is equal to half the celerity of individual waves in deep water and in shallow water they are the same (e.g. Dean and Dalrymple 1991). Long waves which are related with the wave group are called bound-long waves.

If the waves are approaching the shore with an angle they turn towards shore normal as a result of refraction. There is no net mass flux below the trough level. However above the trough a net mass of water is carried by waves in the wave propagation direction. Waves which are increasing in height and decreasing in length begin to break close to the shore losing most of their energy. As the waves become unstable air is entrained into the wave creating a roller which slides downwards from the crest of the wave (Fredsoe and Deigaard 1992). These rollers create additional mass flux in the wave propagation direction (Figure 2.2). Another source of net flow in wave direction is the mass drift or Stokes drift which occurs in irrotational flow. To compensate for the onshore-directed flow created by the waves, rollers and mass drift, an offshore directed current forms close to the bottom called the undertow (Figure 2.2). There might also be strong local jets of offshore flow in the breaking region, called rip currents.

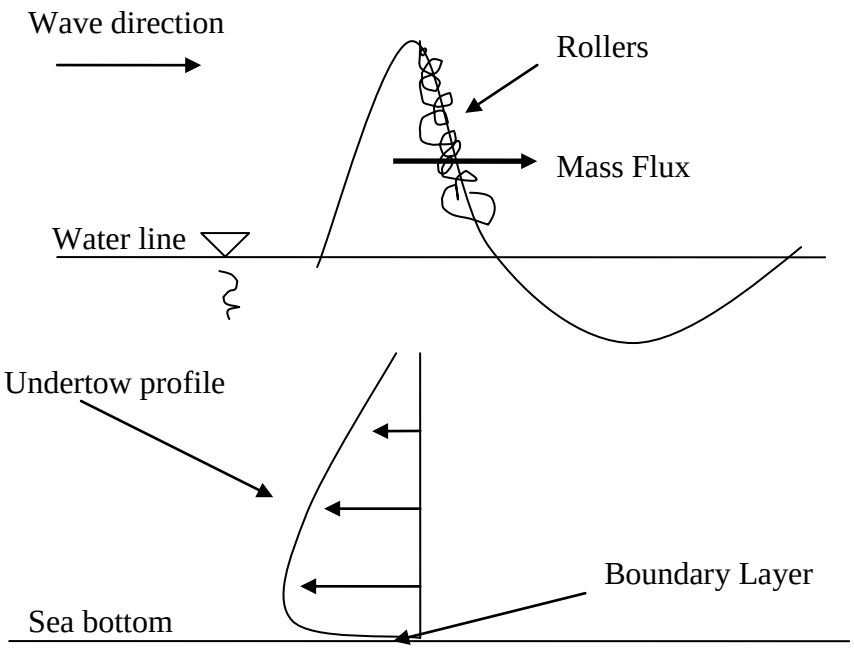

Figure 2.2. Sketch of a wave (propagating to the right) in the surf zone showing rollers and the undertow profile.

At the bed the horizontal velocity is zero. The velocities are reduced from their irrotational flow values just above the bed. Viscous forces become significant here where vertical velocity gradients are strong. This region between the bed and where the flow is irrotational is called the wave boundary layer (Figure 2.2).

Tidal currents are also present in the nearshore. On an open coast they are in the longshore direction. Their magnitudes are generally much less than wave generated longshore currents(Van Rijn et al. 2003). Winds also create longshore currents and wind set-up in the nearshore region (Schoonees and Theron 1995). Tidal currents are more important around estuaries (Sutherland et al. 2004) and in the offshore region (Grant and Madsen 1986). The major effect of tides in the nearshore region is the change in water levels and hence the location of the shoreline.

2.3. Oscillatory Boundary Layer

The sediment transport formulas discussed in Section 2.6 make use of a representative velocity; usually the velocity just outside the boundary layer. Depth-resolving models, on the other hand, need the whole velocity profile. Predicting the velocity in the wave boundary layer becomes critical since the major part of the sediment transport takes part within the wave boundary layer (e.g. Davies and Li 1997). The details of the boundary layer modeling will be discussed within the modeling section. Processes of the oscillatory boundary layer and concepts used in its modeling are introduced here.

2.3.1. Eddy Viscosity

Eddy viscosity is widely used to model the effects of turbulence. This is a tool to model the highly complex and still not very well-understood turbulent stresses in the boundary layer flow. There are various methods for solving for eddy viscosity, from simple expressions to complex models. The simplest solutions use time-invariant, pre-specified expressions, giving eddy viscosity as a function of elevation above the bottom.

Constant, linear and parabolic shapes, or some combination of these have all been used. These are also called zero-equation solutions and are based on Prandtl's mixing length approach (e.g. Kundu and Cohen 2002) . This theory assumes that eddy viscosity can be expressed as a product of a length scale, mixing length *l* and a velocity scale, taken as the square root of the turbulent kinetic energy, *k*.

$$\begin{aligned} \nu_t &= l\sqrt{k} \\ k &= \frac{1}{2}(\overline{u'^2} + \overline{v'^2} + \overline{w'^2}) \end{aligned} \tag{2.2}$$

Here the prime denotes turbulent velocities and the overbar denotes turbulent averaging. Commonly used expressions for the above scales for steady flows are

$$\begin{aligned} l &\propto \kappa z \\ \sqrt{k} &\propto u_* \end{aligned} \tag{2.3}$$

where u_* is the shear velocity, κ is the von Karman's constant and *z* is the distance from bottom. . Using these expressions gives a linear eddy viscosity shape

$$\nu_t = \kappa u_* z \tag{2.4}$$

Different shapes for the eddy viscosity profiles are also used. Another popular approach is to define turbulent kinetic energy in terms of velocity gradients (e.g. Ribberink and Al-Salem 1995).

$$\nu_t = \kappa^2 z^2 \left|\frac{\partial u}{\partial z}\right| \tag{2.5}$$

One-equation models are also based on the mixing length approach, but they solve the transport equation for turbulent kinetic energy to find *k*, using time-varying flow parameters (e.g. Rakha et al. 1997).

$$\frac{\partial k}{\partial t} = \frac{\partial}{\partial z}\left(\nu_t \frac{\partial k}{\partial z}\right) + \nu_t \left(\frac{\partial u}{\partial z}\right)^2 - c_2 \frac{k^{\frac{3}{2}}}{l} \qquad \textbf{(2.6)}$$
$$l = \kappa \sqrt[4]{c_2}\, z$$

Here c_2 is a constant derived from experimental data. In a *k*-ε two-equation model, the length scale *l* varies temporally and spatially as a function of the turbulent dissipation rate ε. The new unknown, ε, is solved by the introduction of a new equation: transport of turbulent dissipation rate.

In sediment transport studies all of these and many other kinds of turbulence closure schemes have been used. One-equation models were used by Bakker (1974a), Davies (1995), and Deigaard et al. (1986). Fredsoe et al. (1985) used a parabolic eddy viscosity distribution that varied within a growing boundary layer (Fredsoe 1984), resetting to zero with each flow reversal. Lee and Hanes (1996) used a three-layered, time-invariant eddy viscosity based on Wikramanayeke (1993). Grasmeijer and Kleinhans (2004) used a linear eddy viscosity profile.

Puleo et al. (2004) compared six one-dimensional, wave bottom boundary layer models with different turbulence closure schemes with lab data for smooth and rough bottoms. Linear and parabolic eddy viscosity models performed as well as the *k*, *k*-ε, and *k*-ω closure models when predicting the velocities. Shear stress was predicted the best by the *k*-ω scheme, compared to the data for smooth flow. All models except the laminar model overpredicted the shear stresses.

Malarkey et al. (2003) compared the results of a k-ε model with the data for flow over 0.21 mm sand in an oscillating water tunnel (Dohmen-Janssen et al. 2001) and found that it performed better than a k-model in predicting the time-averaged velocity profile.

Davies (1995) used a one-equation turbulent closure model based on mixing length theory to solve for eddy viscosity. The results were in qualitative agreement with previous studies that used constant eddy viscosity.

Trowbridge and Madsen (1984a) developed a time-varying eddy viscosity model for predicting boundary layer velocities. They could predict the velocities accurately, but the results were similar to time-invariant models. Vertical variation of the eddy viscosity was more important. However time-varying effects are more pronounced on shear stress components. They suggested finding velocities by a time-invariant model and using a time-varying eddy viscosity to predict shear stresses for a simple and efficient calculation.

Sajjadi and Waywell (1997) concluded that both k and k-ε models gave serious errors when compared to data and suggested that differential second-moment (DSM) closure should be used.

Black and Vincent (2001) used an eddy viscosity constant in time and space and made predictions of concentration profiles close to the bed that were better than the usual predictions in the literature using complex turbulence closure schemes. Davies et al. (1997) could find no evidence supporting the use of the more sophisticated closure schemes rather than simpler approaches.

Time-invariant models perform as well as the more complex models in terms of predicting velocities, but their performance decreases for predicting shear stresses. However as seen above, there is not a consensus on the performance of the various turbulence closure schemes, especially in terms of sediment transport.

The problem becomes more complex in the case of a mobile bed, because high concentrations of sediment damp the turbulence close to the bed. Hagatun and Eidsvik

(1986) were the first to include the effects of turbulence damping in an oscillatory flow sediment transport model. Others have since included these effects (e.g. Holmedal et al. 2003; Li and Davies 2001). However these constitute a minority of the works in the literature. Stratification effects that were used previously (Holmedal et al. 2003) were later excluded, arguing the models still perform well without them (Holmedal et al. (2004).

2.3.2. Steady Streaming

Steady streaming is specific to the wave boundary layer and has many names in the literature including boundary layer drift (Nielsen 1992), induced streaming , Eulerian streaming (Svendsen 2006), wave-induced mass transport (Trowbridge and Madsen 1984b), Eulerian drift (Davies and Villaret 1999). Steady streaming is a net velocity in the direction of wave propagation created due to the interaction of the horizontal and vertical velocity inside the wave boundary layer. The wave propagation direction is defined as the positive direction. In case of oscillatory wave tunnels the positive direction is defined as the positive skewness direction. Even though it is small compared to the orbital velocity it can have a significant impact on sediment transport since it is creating a net flux.

Longuet-Higgins (1953) was the first to theoretically predict steady streaming for the case of constant eddy viscosity. Trowbridge and Madsen (1984b) showed that it would be smaller for turbulent boundary layers and could even reverse direction at the top of the boundary layer for long waves in a theoretical study. Davies and Villaret (1999) could reproduce measured streaming profiles that were in the wave propagation direction close to the bottom and then changing direction at the top of the boundary layer for skewed waves.

Ribberink and Al-Salem (1994) measured net negative velocities close to the bottom in their measurements in an oscillatory water tunnel using skewed velocity time

series. This “skewness related streaming” is different from the wave boundary layer streaming since it is not related to vertical velocities. It is caused by the difference in turbulent energy in the two half cycles of the wave period. This phenomenon can be reproduced by a boundary layer model with time-varying eddy viscosity.

Deigaard et al (1999) included the effects of boundary layer streaming, mass drift (Stokes drift), and bound long waves in a standard boundary layer model with a one-equation turbulence closure scheme. They used a first-order Stokes wave which would otherwise result in zero net sediment transport without the above processes. Streaming was found to have the strongest effect, followed by mass drift, which are both in the wave direction. The bound long waves create offshore sediment transport, which under some conditions might create a net negative transport.

In a numerical model (Henderson et al. 2004) inclusion of nonlinear advective terms responsible for boundary layer streaming and the Stokes drift were necessary to predict onshore bar movements measured at Duck, NC .

2.4. Beach Profile Behavior

Seasonal profile changes are observed in most beaches. Winter profiles are often steep, usually accompanied by a bar formed by rapid erosion during storm events (Figure 2.3). Summer profiles are formed by long-term slow accretion of the beach under mild wave conditions (Dean et al. 2002). The bar might disappear seasonally or might be a persistent feature. Existing bars move offshore during storms and move onshore during the following recovery periods.

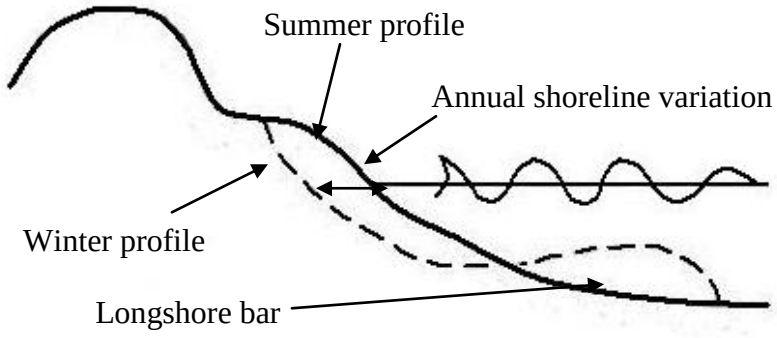

Figure 2.3. Seasonal profile changes modified from Dean et al. (2002).

Annual shoreline variations (horizontal movement of the waterline) may be around 5-40 meters, and bar movements up to 150 meters may occur (Dean and Dalrymple 2002). Most shorelines are characterized by the existence of single or multiple longshore bars. They might be interrupted by rip channels or other 3D structures which change temporally and spatially. Longshore bars are generally created close to shore, they migrate offshore and decay around the time a new bar is generated (Shand et al. 1999). This cycle may take from one year (Kuriyama 2002) to 20 years (Ruessink and Kroon 1994) depending on longshore currents, nearshore slope (Shand et al. 1999) or existence of multiple bars (Ruessink and Terwindt 2000). One mechanism explaining the offshore bar movement is sediment transport being offshore directed on bar crests and onshore on troughs.

Even though this cyclic behavior is common, it is not universal. Aerial photograph observations along Prince Edward Island, Canada spanning up to 50 years showed three to four bar systems that were fairly stable (Boczar-Karakiewicz et al. 1995). The bar closest to the shore was the most active, sometimes merging with the beach.

The generation of bars has intrigued scientists and many theories have been proposed, especially over the last three decades. There are a lot of mechanisms that have been proposed and there is no clear consensus on which ones dominate in which

conditions. The first approach was to find a parameterization to predict if a bar would form or not. Steep waves have long been known to erode beaches and create bars. Dean (1973) argued that sediment will move offshore if sediments suspended under the crest of the wave do not settle before the oscillatory velocity changes direction moving the sediments offshore. He assumed that the sediment is suspended to a height proportional to the breaking wave height and came up with the following condition for offshore sediment movement and bar formation

$$\frac{H_b}{w_f T} > 0.85 \qquad \textbf{(2.7)}$$

where H_b is the breaking wave height and w_f is the sediment fall velocity. The left hand side of the equation has since been referred to as the Dean Number (Dean and Dalrymple 2002). The empirical constant was determined by looking at wave tank tests. Later the constant was modified by researchers by looking at other data sets. Kraus and Larson (1988) modified the constant to 2.75. Wright and Short (1984) introduced an intermediate region using two constants, 1.0 and 6.0.

Convergence of sediment transport around wave breaking is a well accepted mechanism that can explain longshore bar formation (Dally and Dean 1984; Stive and Battjes 1985). Waves increase in skewness as they approach breaking, typically creating an onshore sediment transport. Undertow becomes stronger around and shoreward of breaking generating offshore sediment transport. These two converge around wave breaking creating a bar. Accounting for an increase in sediment suspension due to wave breaking, turbulence was also shown to be important in bar formation (Black et al. 1995; Dally and Dean 1984). Field observations supporting this mechanism were made by Thornton et al. (1996) and Aagaard et al. (1998), among others.

Davies and Villaret (1999) showed that the sediment transport can be in the wave propagation direction close to the bottom due to waves and it can be in the offshore direction on the upper part of the boundary layer due to undertow. Dulou et al.(2002) showed the importance of this in predicting bar formation and the requirement for the detailed modeling of the boundary layer.

Roelvink and Stive (1989) give a summary of the various mechanisms proposed for bar formation that do not depend on the surf zone processes discussed above. Reflecting free long waves, leaky long waves, edge waves, resonant reflection of wave groups, and nonlinear interaction of wave harmonics are some of the mechanisms proposed, focusing on the wave field. Bars form at the anti-nodes of standing or partially standing long waves (e.g. Holman and Sallenger 1993). Bars were formed by reflected long waves and the coupling between waves in lab studies and they were stable in some of the cases (Dulou et al. 2000; e.g. O'Hare and Davies 1990). The mechanisms discussed are not alternatives to each other, but may be effective in different cases or might act simultaneously (Aagaard 1988).

2.5. Transport Modes

Sediment transport, whether in river or coastal environments, is commonly split into two modes (e.g. Sleath 1984). Sediment transported in the water column without continuous contact with the bed is referred to as suspended sediment. Transport of sediment particles by rolling, sliding and saltation while in at least occasional contact with the bed is called the bedload transport. Sheet flow is a kind of bedload where the sediments are transported in a layer 10-60 grain diameters thick under strong shear stresses. One of the many expressions (Camenen and Larson 2005) for inception of sheet flow is from Komar and Miller (1975)

$$\theta R_*^{\frac{1}{3}} > 4.4$$
$$\theta = \frac{\tau}{(\gamma_s - \gamma) d_{50}} \qquad \textbf{(2.8)}$$
$$R_* = \frac{U_0 d_{50}}{\nu}$$

where θ is the non-dimensional shear stress or the Shields parameter, R_* is the grain size Reynolds number, τ is the bed shear stress, d_{50} is the median sediment diameter, γ_s and γ are the specific weights for the sediment and water respectively.

There are also other modes of transport classifications used by some researchers. Wash load is the transportation of very fine sediments that are not represented in the bed, which is usually ignored (Fredsoe and Deigaard 1992) since it is not deposited with the coarser fraction in many cases.

The swash zone can be loosely defined as the part of the beach which is under water during only part of the wave period due to wave run-up and run-down. The sediment carried in this zone is sometimes categorized as the swash load (Dean and Dalrymple 2002). Swash zone processes are complex and our understanding of it is not very good. Processes that are not relevant in the surf zone, like infiltration and exfiltration of water into the sand, flow separation near beach steps, etc., become significant. The effects of bed slope, infra-gravity waves, inertial forces on sediment particles and bore-generated turbulence becomes more pronounced. A good review of hydrodynamic and sediment transport processes and modeling approaches has been made by Elfrink and Baldock (2002). In a more recent study Clarke et al. (2004) modeled the flow of water in and out of the bed and showed the importance of permeability in swash zone hydrodynamics. The swash zone is not handled differently than the surf-zone in this study or in any of the studies discussed here and the errors are expected to be higher in this zone.

2.6. Sediment Transport Formulations

Research on sediment transport in the surfzone, especially in earlier days, benefited greatly from research done on riverine sediment transport, which has been worked on for a long time and is physically simpler because of the uni-directional nature of the flow, typically assumed to be without wind waves. The models modified from steady state applications are generally “quasi-steady” since the sediment transport is related to the instantaneous velocity and does not take into account history effects from previous phases or previous wave cycles. In comparison the sediment transport models discussed in the next section that solve for the distribution of sediment over the water column are unsteady. Sediment suspended in previous time steps is still in suspension and the history of the flow does affect the current sediment transport rate. In most of these models shear stress is related to the instantaneous velocity. Some researchers (e.g. Malarkey et al. 2003) have also used the term “quasi-steady” to refer to this aspect of this second type of models.

The "Energetics" approach is one of the most widely used sediment transport models for cross-shore sediment transport modeling. It is based on the work of Bagnold (1956) on river flows where he proposed that the sediment transport is proportional to the rate of dissipation of flow energy in a stream. The proportionality constant is named the efficiency factor. The dissipation rate of the stream is defined as the product of the shear stress at the river bottom, which puts the sediment in movement, making it available for transport, and the free stream velocity, which transports the sediment. Bagnold (1966) included different efficiency factors for bedload and suspended sediment transport and incorporated the effects of slope and grain fall speed into the formulation.

Relating the sediment transport to the shear stress is another approach used in coastal sediment transport modeling (Madsen and Grant 1976). A non-dimensional shear stress or Shields parameter θ is generally used for this method. Both of these approaches relate the sediment transport to some power of the instantaneous velocity at the bed.

Bowen (1980) and Bailard (1981) developed models for coastal environments based on the work of Bagnold (1966), adding the effect of oscillatory flows which could be applied both in the longshore and cross-shore directions. Nairn and Southgate (1993) give a summary of the limitations of the energetics approach: it does not take the critical shear stress into account and predicts sediment transport for any finite velocity, so it is not valid for cases where there is very little or no sediment transport. The formulation was derived for a flat bed and does not apply to rippled beds. Another assumption is the instantaneous suspension of sediments (quasi-steady), so phase lags between velocities and sediment concentrations are ignored. Roelvink and Stive (1989) removed one of the limitations by including wave breaking turbulence.

Watanabe et al. (1986) proposed a total load formula under the combined action of currents and waves. The formula is based on the power model concept where the volume of sediments set in motion is assumed proportional to the excess shear stress and the sediment is transported by the mean and oscillatory flow. The difference of this model from the energetics approach is the inclusion of the critical shear stress. When this model is applied in the cross-shore direction, the direction of sediment transport is found by an empirical transport direction function. Wave breaking turbulence was included by Ohnaka and Watanabe (1990).

Aagaard et al. (2002) measured suspended sediment fluxes on a gently sloping beach on the Danish North Coast during a time when nearshore bar migration was observed. Using these measurements, sediment flux magnitudes and directions were parameterized using the Shields parameter, relative water depth, wave orbital velocity, wave height and bed slope. 57.9% of the variance in sediment flux could be explained by this parameterization.

Ribberink and Al-Salem (1994) compared the quasi-steady sediment transport formulas of Madsen and Grant (1976), Bailard (1981) and Sawamoto and Yamashita (1986) against lab data from an oscillating water tunnel. The Madsen and Grant (1976)

approach over-predicted the net transport rates by a factor of 2-10. The Bailard (1981) formula gave the best prediction (within a factor of two of the measurements). This quasi-steady formula could perform well, because the sediment transport was confined to a thin layer of a couple of centimeters close to the bed and the non-steady affects were not very important. As the ripple size increases, vortex shedding from ripples increases and unsteady effects become more important. For a given orbital velocity sediment transport rate increased with wave period. This could not be predicted by any of the above models since this is an unsteady effect. In a continuation work (Ribberink and Al-Salem 1995) employed a 1D vertical boundary layer flow and diffusion model which could predict this phenomenon. Suspended sediment transport away from the bed was not predicted well in terms of phase or magnitude, but the overall magnitude of the sediment transport was satisfactory since most of the sediment transport took place close to the bed where the model was more successful.

Ribberink (1998), backed up by experimental evidence, argued that bedload transport can be modeled in a quasi-steady way since phase lags between orbital velocities and concentrations in the sheet flow region are negligible. Using lab data from steady, oscillatory and combined flows with symmetrical and asymmetrical waves, a bedload formula was created. A classical form of sediment transport proposed by Meyer-Peter and Muller (1948) where non-dimensional bedload is proportional to a power of excess shear stress was used. Fully developed ripples, non-collinear waves and the effects of wave breaking-induced turbulence were not included during the development.

A large class of more advanced models include computations of the distribution of suspended sediment in the water column. This, combined with a computed velocity profile, is used to describe the sediment transport. These depth-resolving sediment transport models are explained in the next section.

2.7. Concentration Profile Measurements and Models

Sediments go into suspension due to presence of waves and currents. Once suspended the sediments can diffuse upwards because of random turbulence or can be convected upwards with turbulent eddies. At the same time gravity is pulling the sediments back to the bed, controlled by the fall velocity of the sediment. Reference concentration formulations or pick-up functions are generally used to model the amount of sediment that goes into suspension. These formulations are proportional to shear stress and cannot predict the concentrations peaks around flow reversal when shear stress goes to zero. Applications of diffusion and convection type models to flows over flat and rippled beds and comparison of results to measurements are discussed in this section.

2.7.1. Diffusion Models

One method to predict the sediment concentration profile under waves is to model the movement of sediment particles as a diffusion process. Diffusion models, coupled with boundary layer models, can take into account the phase lag between the bottom shear stress and velocity and include the delayed response of the sediment. This approach has been used to find sediment concentrations in steady, turbulent, open channel flows for decades. Rouse (1937) solved the diffusion equation by applying a parabolic turbulent sediment diffusion coefficient, proportional to the eddy viscosity, giving the now famous Rouse profile. However application to oscillatory flow occurred much later.

Bakker (1974b) was the first to solve for velocities and sediment concentrations under oscillatory flow inside and outside the wave boundary layer. He used a time-varying eddy viscosity formula based on mixing length theory. The basic idea of a diffusion model which involves solving for the suspended sediment concentration in a 1D vertical grid did not change much since then (e.g. Davies and Thorne 2005; Deigaard et al. 1987). However various bottom boundary conditions and turbulence closure models

have been used. The effects of higher order terms in the advection-diffusion equation have been investigated.

2.7.2. Bottom Boundary Condition for Diffusion Models

There are two approaches for defining the bottom boundary condition for the sediment diffusion problem. A Dirichlet-type boundary condition defines the value of the concentration at the bottom and is referred to as the reference concentration. The Neumann-type boundary condition specifies the flux of sediment at the bottom and is called the pick-up function.

Reference concentration formulas are generally based on formulas developed for steady flow. One popular formula is by Engelund and Fredsoe (1976) which is based on the ideas of Bagnold (1956). The volumetric reference concentration is a function of the time varying non-dimensional Shields parameter θ.

$$\theta = \frac{\tau}{\rho(s-1)gd_{50}} \tag{2.9}$$

where τ is the shear stress, ρ is the water density, s is the relative grain density and d_{50} is the median grain diameter. The formula was modified by Fredsoe et al. (1985) slightly to give

$$c_r = \frac{0.65}{(1+1/\lambda)^3}$$

$$\lambda = \begin{cases} \left(\dfrac{|\theta| - \theta_c - \dfrac{\pi p_*}{6}}{0.027|\theta| s} \right)^{\frac{1}{2}} & \text{for} \quad |\theta| > \theta_c + \dfrac{\pi p_*}{6} \\ 0 & \text{for} \quad |\theta| < \theta_c + \dfrac{\pi p_*}{6} \end{cases} \qquad \textbf{(2.10)}$$

$$p_* = \left[1 + \left(\frac{\pi/6}{|\theta| - \theta_c} \right)^4 \right]^{-\frac{1}{4}}$$

The volumetric reference concentration c_r is defined at $z=2d_{50}$. θ_c is the critical Shields parameter, λ is linear concentration and p_* is the probability of transport of particles in a single layer.

The formula was further modified by Zyserman and Fredsoe (1994) after comparing with laboratory data.

$$c_r = \frac{0.331(\theta - \theta_c)^{1.75}}{1 + \dfrac{0.331}{c_m}(\theta - \theta_c)^{1.75}} \qquad \textbf{(2.11)}$$

The maximum concentration c_m is equal to 0.46. This equation was derived using data from sands ranging in diameter from 0.19 mm to 0. 54 mm. The maximum Shields parameter was around 2 in the data sets used.

Nielsen (1986) suggested a formula using a modified effective shear stress θ_r which is based on grain roughness or skin friction Shields parameter θ_{sf}

$$\theta_{sf} = \frac{0.5 f_{2.5} u_w^{\ 2}}{(s-1) g d_{50}}] \tag{2.12}$$

u_w is the bottom wave orbital velocity amplitude, $f_{2.5}$ is the grain roughness friction factor based on $2.5d_{50}$. The formula is given as

$$c_r = 0.005\theta_r^3$$
$$\theta_r = \theta_{sf} \frac{1}{(1-\pi\eta/\lambda)^2} \tag{2.13}$$

The correction to the skin friction takes into account the contraction of streamlines around ripples where η is the ripple height and λ is the ripple length.

Lee et al (2004) used field data collected under a wide range of conditions at depths of 13-20 meters to investigate reference concentrations. They made a regression analysis and came up with the formula

$$c_r = A[\theta_{sf} \frac{u^*_{sf}}{w_f}]^B \tag{2.14}$$

u^*_{sf} is the corresponding shear velocity for skin friction Shields parameter θ_{sf}, and w_f is the fall velocity. A and B are the constants found from the regression analysis as 2.58 and 1.45 g/l, respectively. Note that the resulting equation is to the 4.35 power of the velocity rather than the more commonly used third power. The inclusion of the settling velocity takes into account that only a fraction of the mobilized sand goes into suspension. Another difference of this formula from others is that it is applied at 1 cm above the bed. This formula was developed using field data rather than lab data which makes it different from all other models and has an advantage for field applications. However the fact that it

is applied at 1 cm creates a problem for sediment transport applications since significant sediment transport can take place below 1 cm.

Thorne et al. (2002) measured reference concentrations under regular and irregular waves in a large-scale flume using Acoustic Backscatter sensors (ABS). Nielsen's (1986) formula overpredicted the concentrations and a coefficient of 0.0022 fit the data better than value of 0.005 used in Equation 2.13. However the cubic relationship between concentration and the modified Shields parameter was supported by the data.

Figure 2.4 shows the reference concentrations predicted by the models discussed above. The model of Smith and McLean (1977), which is similar to Zyserman and Fredsoe (1994) equation (Equation 2.11) in form, is also included. Lee et al. (2004) used a reference height of 1 cm, differing from all the others and hence their model gives a consistently lower concentration than the others. Even though the figure does not allow a direct comparison of all the various methods, it does give an idea about the wide variability even in widely used formulations. The large differences arise from the fact that neither shear stress nor reference concentration are measured directly, but predicted from measurements using other models and extrapolations.

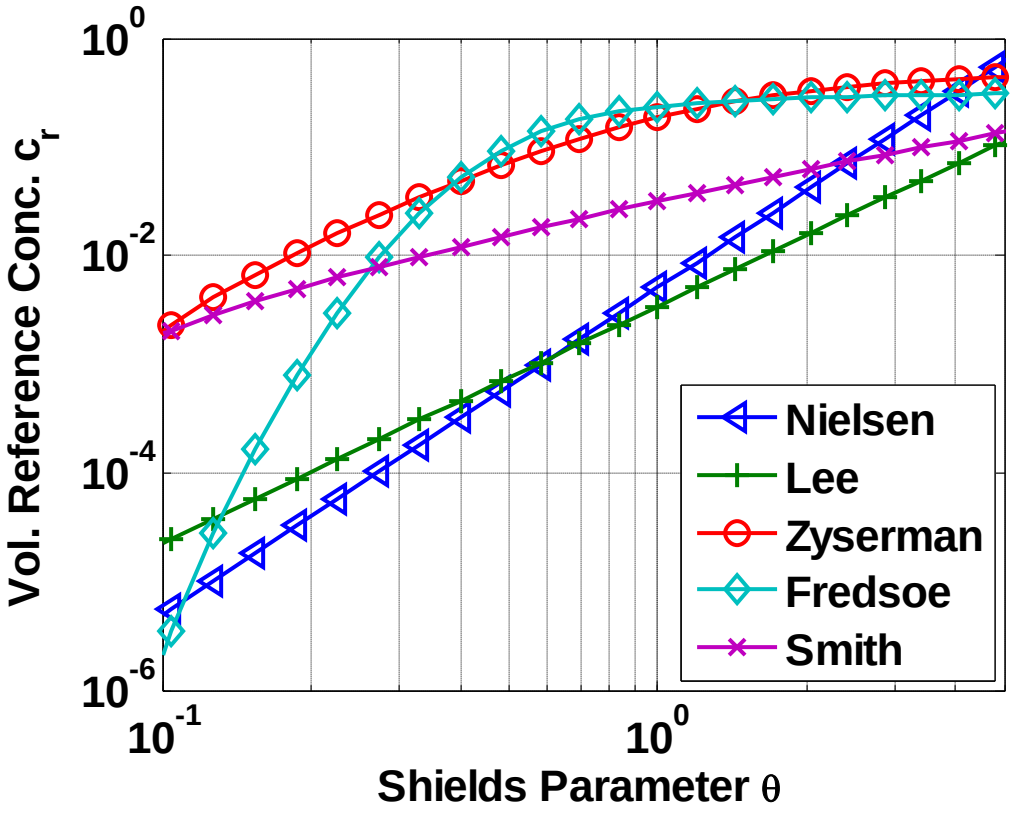

Figure 2.4. Reference concentration predicted by different formulas. Note that the Zyserman and Fredsoe formulas are a function of total Shields parameter while the rest are a function of skin friction Shields parameter.

An inspection of the data used for developing the Zyserman reference concentration shows that it performs better than the Fredsoe concentration for lower values of the Shields parameter, and their performance is equally good for the mid-range of Shields stress values. There is insufficient data for conclusive comparisons at the higher concentrations. Recent, detailed, time-varying concentration measurements are available for oscillatory flows (Dohmen-Janssen et al. 2001; McLean et al. 2001; Ribberink and Al-Salem 1994; Ribberink and Al-Salem 1995). In these data sets reference concentration at high Shields parameters were observed not to exceed 0.3. This result is closer to the predictions made by the Zyserman expression.

Pick-up functions

Pick-up functions give the rate at which sediment is picked up from the bottom and define the gradient of the concentration rather than the concentration itself. The pick-up function *pf(t)* is related to the concentration gradient with

$$pf(t) = -\varepsilon_S \frac{\partial c}{\partial z} \tag{2.15}$$

where c is the volumetric sediment concentration and ε_s is the sediment diffusion coefficient. The reference concentration approach assumes that the concentration at the bottom is in equilibrium with the shear stress. In unsteady flows the validity of this assumption is questionable, for example you can have a finite concentration due to settling from above even when the shear stress is zero (Nielsen 1992). The pick-up function differentiates between grains that are settling and being entrained and allows for finite sediment concentration when the shear stress is zero.

Using a carefully designed experimental set-up Van Rijn (1984) measured the pick up rate in an open channel flow by means of a sediment lift feeding sediment to the bottom at a rate equal to sediment pick-up from the bottom. Using the data and comparing it with previous models for sediment pick-up he developed a new sediment pick-up function. Later he applied (Van Rijn 1986) this function to predict sediment transport under steady currents. The sediment pickup function was assumed equal to the sediment flux at an elevation two times the grain diameter. His results were comparable to the Meyer-Peter-Muller formula.

However there are very few pick-up functions proposed in the literature compared to reference concentration formulations. Even though the pick-up function method is theoretically more realistic the lack of data for pick-up rates limits its application. If the change in bed elevation during one wave period is assumed zero the pickup of sediment

from the bed and the settling are in equilibrium and the pick-up function can be written as a function of a reference concentration (e.g. Nielsen 1992).

$$pf(t) = w_f c_r \quad \textbf{(2.16)}$$

This enables widely available reference concentrations to be cast in terms of pick-up functions and direct comparison of the two approaches.

Nielsen et al (2002) investigated vertical fluxes of sediment transport and concluded that a diffusion model with a reference concentration cannot correctly model the sediment entrainment process. A pick-up function modified from his earlier work (Nielsen 1992) could predict the upward flux during flow acceleration.

Davies and Li (1997) compared a reference concentration formula (Engelund and Fredsoe 1976), a pickup formula based on this reference concentration formula (using Equation 2.16), and an original pick-up formula (Van Rijn 1984). Van Rijn's formula under-estimated the sediment transport. The other two methods did equally well. No significant change in sediment transport rate was observed when the pick-up function was used compared to the reference concentration.

2.7.3. Convective Models

The diffusion process discussed above assumes that the movement of sand particles occurs at small, random length scales, creating a sediment flux proportional to the sediment concentration gradient. However not all sand is moved in disorganized random walk style. Bursts of sediment can be moved up high into the water column with a strong velocity such as is the case with bursts over vortex ripples. Nielsen (1992) added a convection mechanism for upward sediment flux giving a combined diffusion – convection model. The sand is convected upwards with a convection velocity until it reaches an entrainment height given by an entrainment probability function and begins to

settle down with the fall velocity. The convection velocity and the entrainment probability function are generally empirical.

A diffusion model with a time-invariant eddy viscosity (Wikramanayeke 1993), a convection model, and a combined convection-diffusion model (Nielsen 1992) were compared by Lee and Hanes (1996). The diffusion model worked better under high wave conditions, whereas the convection model was more accurate under low wave conditions, and the combined model was best overall. Accounting for multiple sediment sizes decreased concentration gradients, and improved results for energetic conditions when used with the combined model.

A scaling parameter which predicts the cases where vortex shedding is important was introduced by Lee et al. (2002). It could predict where the diffusion model breaks down successfully. However including advection within the model did not improve the model results. Increasing the wave boundary thickness arbitrarily to 50 cm gave the best results.

Thorne et al. (2002) used a diffusion type model. However they could simulate convective effects by modifying the eddy viscosity profile.

Even though convective effects may also be important in some cases, using a convective or combined diffusion-convection model under field conditions did not always improve results. The effects of convection predicted by the models were mostly on the concentration profile shapes rather than the net sediment transport rates.

2.7.4. Rippled Beds

When the shear stress is sufficient to move sediments, the bed becomes unstable and various bed forms appear. Most common of those forms are ripples. These are small sand waves that are less than 60 cm in length and 6 cm in height (Fredsoe and Deigaard 1992). Starting from an initial disturbance, ripples begin to form and grow and spread over the bed. When the shear stress is high enough and the ripple heights increase, flow

separation occurs in the lee of the ripples. As the pressure gradient changes direction a vortex is shed from this separation zone and enters the water column above. These fully formed ripples are called vortex ripples (Figure 2.5). Zedler and Street (2006) showed the highly nonlinear structure of the vortex structure over long-wave ripples for oscillatory flow using a large eddy simulation. The sediments were swept into the lee vortex and ejected into the water column.

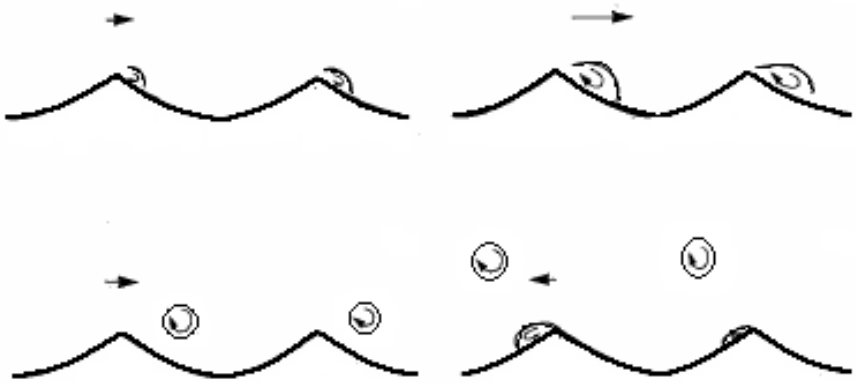

Figure 2.5. Formation of vortices over a vortex ripple. The straight arrow shows the orbital velocity. The circles are separation bubbles formed behind the ripple. Reproduced from Fredsoe and Deigaard (1992).

As the shear stress increases the bedforms disappear and the bed becomes flat. On the other hand if the flow is so weak that no sediment transport occurs the bed is covered with relic bed forms which are left over from previous events.

Bed forms complicate the definitions of parameters such as reference level and bed roughness used in diffusion-type modeling. Non-diffusive processes such as vortex shedding also become significant. The diffusion-type model's applicability can be extended to cases with bedforms in a bedform-averaged sense.

Grasmeijer and Kleinhans (2004) predicted the suspended sediment transport for a rippled bed near the coast of Egmond aan Zee using a 1DV diffusion model. They developed a ripple predictor which performed better than the predictors in the literature, for a set of data from various field and lab measurements. The ripple dimensions affected the model by affecting the shear stress due to Nielsen's modified shear stress formula

(Nielsen 1986). Three different reference concentration formulas were compared (Lee et al. 2004; Nielsen 1986; Zyserman and Fredsoe 1994) and the Lee et al. model gave the best results. A linear time-invariant eddy viscosity was used.

A practical sand transport model (Bijker 1968) and a research model based on Davies and Li (1997) were applied at three different sites by Davies and Villaret (2002). Rippled beds were modeled differently than flat beds, with the inclusion of a modified eddy viscosity profile. The Engelund and Fredsoe (1976) reference concentration was applied for flat beds. A pick-up function scaled with Nielsen's method (1992) was used for rippled beds. Both models predict sediment concentrations under non-breaking wave conditions within a factor of ± 5. Prediction of the ripple dimensions used in prediction the bed roughness was seen as the greatest reason for this variability other than the variability in measurements themselves.

Sleath and Wallbridge (2002) extended a previous study (Zala Flores and Sleath 1998) to cover rippled beds. They observed that velocity profiles within the mobile layer were approximately linear, when measured from the stationary bed. When the horizontal pressure gradient close to the bed was low compared to the shear stress a quasi-steady treatment of the flow in the mobile bed layer was acceptable.

Davies and Villaret (1999) used an eddy viscosity model that does not change with elevation, but varies with time to model sediment to model the convection and diffusion process over rippled and very rough beds.

A two-layer, time-varying eddy viscosity model was proposed by (Davies and Thorne 2005). The pick-up function with the maximum entrainment during flow reversal was used. This model has been compared with detailed measurements and could predict the time-varying and mean concentrations. However, sediment diffusivity was tuned to four times the eddy viscosity to force the model results to match the measurements.

The entrainment of sediments above a rippled bed in oscillatory flow is a phenomenon that is not well understood. There are various models proposed with varying

degrees of success. All of them try to incorporate the convective nature of the process in various ways. These models have been tested in limited conditions and most of them require parameters that need to be derived from measured data.

2.7.5. Sheet Flow

As the velocity increases, washing away the bed forms, the bed becomes flat and sediment begins to move in very high concentrations in a thin layer a few mm thick. This type of flow, called sheet flow, is important since it can move a significant amount of sediment. The sheet flow layer is defined as the portion of the flow where inter-granular forces are important and the top of the sheet flow region is generally defined as the point where concentration reaches 0.08 m^3/m^3 (Bagnold 1956).

Sumer et al. (1996) studied sheet flow for steady flows in a flume with a rigid lid. The velocity inside the sheet flow layer fit a power law representation. The concentration profile was linear within the bottom half of the flow and it was logarithmic for the top half.

Most of the lab studies investigating sheet flow were done in oscillatory wave tunnels (OWT). In this setup there is no free surface, no vertical velocities and no horizontal variation in velocity, unlike the situation under waves.

Ribberink and Al-Salem (1994) observed that the suspended sediment concentration profile above the sheet flow region could be modeled using a linearly increasing eddy viscosity, while the profile over rippled beds was better described using a constant eddy viscosity; highlighting the different physics involved. Ribberink and Al-Salem (1995) were one of the first to make detailed concentration measurements inside the oscillatory sheet flow layer at full scale. The sheet flow had two different layers; the bottom layer was the pickup layer where concentrations decreased with increasing stress and the top layer was the diffusion layer where the concentrations correlated with the shear stress.

Most of the sediment transport takes place in the sheet flow layer. Quantifying it is important in predicting sediment transport rates. Sumer et al. (1996) found the thickness of the sheet flow layer to increase linearly with the Shields parameter, in agreement with previous research (Sawamoto and Yamashita 1986; Wilson 1989). Dohmen-Janssen et al. (2001) measured sheet flow layer thickness and the erosion depth, which is the thickness of the layer below the initial bed level that is mobilized. Contrary to previous expressions (Zala Flores and Sleath 1998) they found that the erosion depth and sheet flow layer thickness increases with decreasing sand size. O'Donoghue and Wright (2004) found similar trends with their OWT experiments.

Ribberink and Al-Salem (1995) observed that concentrations in the sheet flow layer were in phase with velocities unlike the suspension layer which had lags. Zala Flores and Sleath (1998) investigated the mobile layer in oscillatory sheet flow in the laboratory using sand (0.41 mm), PVC (4.3 mm), and acrylic pellets (0.7 mm). The authors found that inertia and acceleration effects which cause the quasi-steady assumption to break down were not significant enough to affect the integrated quantities such as sheet flow layer thickness and sediment transport rate.

Dohmen-Janssen et al. (2002) found that unsteadiness became important for small grain sizes and small wave periods, decreasing the net sediment transport. When the settling time of sand is large compared to the wave period the sediment that was suspended under the wave crest stays suspended and is transported in the opposite direction under the trough (or vice versa) introducing phase lag effects which result in a decrease in sediment transport. They developed a parameter P:

$$P = \frac{\omega \delta_s}{w_f} \qquad \textbf{(2.17)}$$

where δ_s is the sheet flow layer thickness, w_f is the settling velocity, and ω is the angular frequency of the wave motion. For P<0.5 the phase lag effects can be neglected. For sand sizes bigger than 0.21 mm the unsteady effects became important only for extreme cases that are not common in the field like bottom orbital velocities bigger than 2.5 m/s.

O'Donoghue and Wright (2004) and Hassan and Ribberink (2005) found significant phase lags for fine sand (d_{50}=0.13 mm). In some cases with skewed waves and without a mean current, net offshore sediment transport was observed. Camenen and Larson (2005) came up with a new formula for the critical wave orbital velocity for the inception of sheet flow after investigating lab data and available formulas. They also came up with a correction formula for sheet flow magnitude for the effects of phase lag. Their formula could predict negative transport as observed in some experiments, unlike the (Dohmen-Janssen et al. 2002) formula, which gives only positive correction factors.

Choosing the correct roughness height is important for predicting the shear stress. Bed roughness height is normally on the order of grain diameter. Dohmen-Janssen et al. (2001) estimated bed roughness by looking at velocity profiles and saw that roughness increased for fine sediments. Sheet flow layer thickness was found to be a better representation of the roughness height due to mobile bed effects. This improved their velocity predictions, but caused over-prediction of concentrations which was compensated by decreasing the diffusion coefficient. McLean et al. (2001) also found that using sheet flow layer thickness improved results. O'Donoghue and Wright (2004) on the other hand, found $2.5d_{50}$ to be a better representation of roughness height.

The only full-scale lab experiments for sheet flow dynamics under waves were conducted at the Large Wave Flume in Hannover, Germany (Dohmen-Janssen and Hanes 2002). Monochromatic waves similar to cnoidal waves in shape were used. The tests were designed to be compared to a OWT study for cases without mean currents (Ribberink and Al-Salem 1994). Net transport rate calculated from bathymetric changes showed a linear relationship with the third power of velocity moment for both cases.

However the transport under the waves was 2.5 times more than the OWT due to the differences in these methods. Boundary layer streaming is present only under waves and can explain most of the difference in the sediment transport rates. The thickness of the sheet flow layer was found to agree well with the expression by Sumer et al. (1996) for steady flow both for waves and the OWT. The concentrations within the boundary layer were generally in phase with the free stream velocity. Very small concentration gradients in the suspended sediment high in the water column were thought to be caused by the presence of fine sediments and background turbulence. The concentrations in the suspension layer showed significant lag, the peak being under the trough, above the 18 mm elevation. The suspended sediment under waves was significantly larger than in the OWT cases, but still constituted a small fraction of the total load.

The same authors repeated the experiments with random waves (Dohmen-Janssen and Hanes 2005). The thickness of the sheet flow layer was only a function of the wave above it and was not affected by the wave group and followed the expression by Sumer et al. (1996). The sediment transport relationship did not change either. These show the instantaneous behavior of the sheet flow layer. Suspended sediment concentrations were affected by the wave group properties. The grain velocities inside the sheet flow layer were close to the fluid velocities expected above a stationary bed. Closer to the bed the velocities decreased from these values due to grain-grain interactions and inertia.

The difference between the results of the OWT tests discussed above (Ribberink and Al-Salem 1994) and the wave flume (Dohmen-Janssen and Hanes 2002) experiments, which is not explained by a simple velocity moment relation, was explained by Nielsen and Callaghan (2003). Their empirical method introduced a phase lag to the shear stress to account for the asymmetric accelerations under the wave and an additional term for boundary layer streaming.

Malarkey et al. (2003) developed a model for sheet flow with an empirical quadratic concentration profile for sediment concentration and a linear concentration for

velocity. The concentration started with the bed value equal to 0.52 up to 0.08 which is defined as the top of the sheet flow layer. The velocity matched the boundary layer solution at the top and was zero at the bottom. The sheet flow layer thickness was defined as

$$\frac{\delta}{d_{50}} = 6\theta + 10 \qquad \textbf{(2.18)}$$

The reference concentration becomes a constant at a value of 0.08, but is defined at a changing location. The constant term in the sheet flow layer thickness allows non-zero concentrations at flow reversal. A fit to lab (Dohmen-Janssen et al. 2001) data gave β parameters (ratio of sediment diffusivity to eddy viscosity) of 0.5, 1 and 3 for fine, medium, and coarse sand respectively.

Thorne et al. (2002) measured sediment concentrations at Deltaflume in the transitional regime where ripples were beginning to wash out. Nielsen's (1986) reference concentration formula, which was developed for both plane and rippled beds, was used. The formula's dependence on modified Shield's parameter was satisfactory, but the best-fit constant coefficient was 2.3 times the suggested value. The difference between the grain diameters in the bed and suspension was given as a possible explanation.

Since the sediment concentrations are so high in the sheet flow layer, the flow itself is also affected and the assumption that sediment moves with the flow begins to break down. Models which treat the sheet flow layer as a two-phase flow are being developed and used increasingly (e.g. Dong and Zhang 2002; Hsu et al. 2003; Hsu and Ou 1994; Jenkins and Hanes 1998). Even though the complexities of these models prevent them from being used at morphodynamic models for the time being, they can give insight into the physical processes. One such model was used by (Hsu and Hanes 2004) to investigate the effects of wave shape on sediment transport using a grain

diameter of 1.1 mm. Under a saw-tooth wave, sediment concentrations were in phase with the free-stream acceleration rather than the velocity, due to the horizontal pressure gradients. However under a second-order Stokes wave the concentration time series followed the free stream velocity partly due to the fact that velocity and acceleration peaks were close to one another in time due to the nonlinearity of the wave. A visible amount of sediment was in motion during the flow reversal. The authors conclude that the sediment transport may be parameterized by the Meyer-Peter and Muller formula (e.g. Sturm 2001), but the shear stress cannot be defined only in terms of the free-stream velocity by looking at the results from the saw-tooth wave.

2.7.6. Concentration Peaks around Flow Reversal

Concentrations peak under the crest and trough of the waves as shear stresses reach their maximum values. Additional secondary concentration peaks occurring near the flow reversal in wave motion have been observed by many researchers in detailed laboratory measurements (Davies and Li 1997; Ribberink and Al-Salem 1995; Staub et al. 1996) . One example where this peak (t=5.5 s) clearly stands out is given in Figure 2.6. This peak, which is smaller than the main peak close to the bed, does not decay as fast as the main peak and becomes dominant up in the water column. This secondary peak cannot be correctly modeled by standard diffusion or convection-type models. Reference concentrations that are a function of shear stress cannot predict this peak either, since the shear stress is close to minimum around flow reversal.

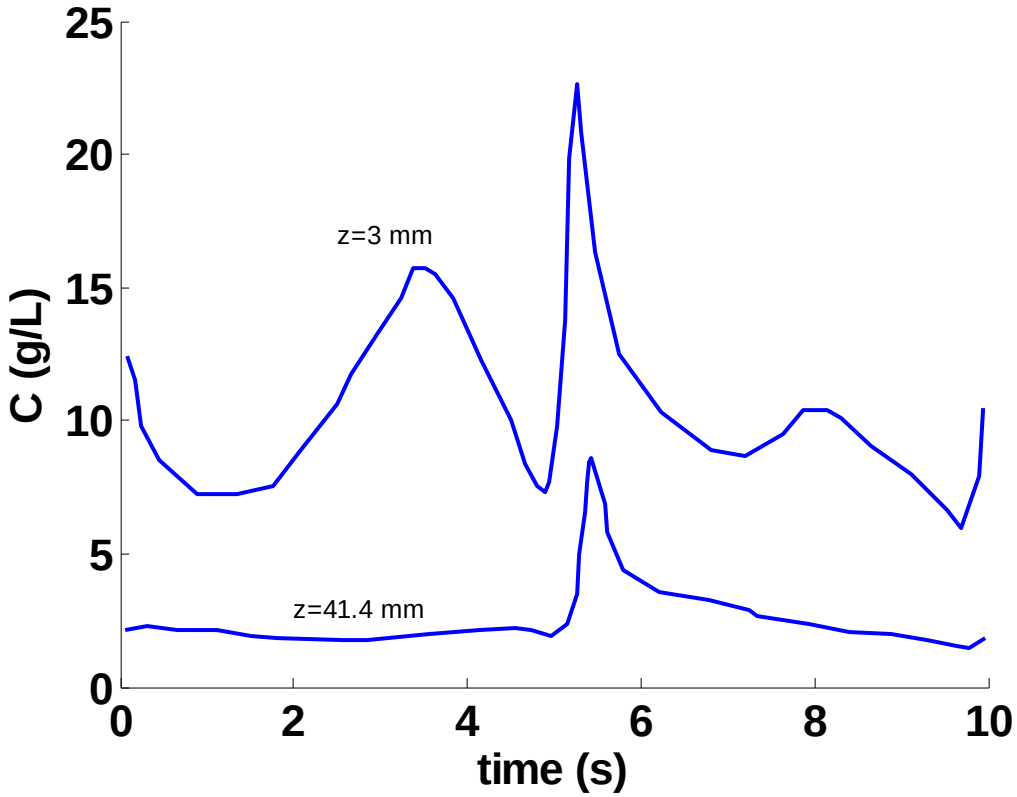

Figure 2.6. Measured concentrations as a function of time in the wave boundary layer under a wave at z=3 and 41.4 mm. The secondary peak around flow reversal can clearly be seen (from Davies and Li 1997 figure 12).

Secondary peaks in the near-bed concentration time series occur as a flow separation bubble behind a vortex ripple breaks and shed into the water column. However this may also be observed in sheet flow conditions. This secondary peak has been argued to be due to shear instabilities (Foster and Holman 1994).

Black (1994) tried to reproduce the secondary peak using a Lagrangian advection-diffusion model. He introduced additional entrainment during flow reversal and modified the reference concentration formulation used in the pickup function was used as the bottom boundary condition. However his method was developed using a small data set and needs further development to have prediction capabilities for other cases.

In an analytical model Davies and Villaret (1999) found eddy viscosity parameters from data, giving an eddy viscosity with peaks around flow reversal. This

model, which uses strongly time varying eddy viscosity, could reproduce the behavior of the convective peaks around flow reversal above rippled beds.

The effect of the convective peaks on the time-averaged concentrations at flow reversal were estimated as less than 10% for sheet flows (Dohmen-Janssen et al. 2001). This phenomenon cannot be modeled by the vast majority of the models used in literature, but this did not introduce significant errors to sediment transport rate predictions.

2.8. Representative Wave

Ocean waves are random in nature with some known statistical parameters. If direct measurements of waves and currents are made, the whole measured time series can be used as forcing in the models (e.g. Hoefel and Elgar 2003). However in general whole time series are not measured due to high power and storage requirements. Instead bursts of data to predict the statistical parameters that are assumed to be constant until the next burst are measured.

Spectral wave transformation models (e.g. REF/DIF S (Kirby and Dalrymple 1983)) that can model the random nature of the waves are widely used. A synthetic time series of wave orbital velocities can be created using modeled wave spectra. There are also time-resolving wave models that can model velocity time series. However even when velocity time series are available by some method, using the series in a sediment transport model is computationally expensive. Instead, a representative wave and a corresponding orbital velocity are generally used in sediment transport modeling. Choosing the right set of statistical parameters to use for the representative wave is important and has to be determined differently for different modeling approaches. This is not always a straightforward task since all sediment transport formulations are non-linearly dependant on the velocity.

Holmedal et al. (2004) used representative velocity that has the same rms bottom orbital velocity as a random wave and predicted the sediment transport within 30% of the values calculated directly from random time series over a range of wave current parameters.

Dibajnia et al. (2001) found significant (mean of the largest one-third) wave periods and orbital velocities to be the best parameters for the representative wave. They used a semi-empirical transport model which uses various velocity parameters rather than a velocity time series. The model that employed representative waves could predict the sediment transport, but model coefficients had to be modified from the standard case. For large waves with currents, two different representative waves were required since the use of only one wave defined by significant wave height led to an underestimation sediment transport.

In the model study by Deigaard et al. (1999), group waves created 33% more sediment transport than regular waves with the same rms wave height. However the waves were not modeled as skewed and there was no mean current simulated. In the presence of these real-world contributions with skewed waves and mean currents the difference is expected to be less.

Dohmen-Janssen and Hanes (2005) measured sediment transport in a wave flume with prototype scale waves and without mean currents. The sequence of waves within the group did not change the sediment transport rate. The sediment transport rates that were observed with regular monochromatic waves did not change due to the presence of the wave groups.

The use of representative waves is common in sediment transport modeling. The errors included due to this approach are generally small compared to the natural scatter in the measured data.

2.9. Grain Size Distribution

The sand in the nearshore consists of a range of grain diameters. In most models it is represented by one grain size, usually the median grain size, d_{50}. Using multiple grain sizes instead of only the median grain diameter is a more realistic way to model sediment concentrations. Fredsoe et al. (1985) represented the sediment by three different grain diameters. The effect was to increase the suspension away from the bed in very small amounts. Lee et al. (2002) included multiple grain sizes and the model predictions away from the bed under storm conditions improved. Davies et al. (2002) compared model results with measured sediment transport rates. Using multiple sand sizes improved results significantly only in one of the four cases.

Median grain diameters typically show variability across the beach profile. Kaczmarek et al. (2004) also showed that grain size distributions can change temporally too in a few hours under storm conditions.

Not all of the grain diameters represented in the bed go into suspension under any given wave. As a result the mean sediment diameter in the bed and in the suspension layer may be different. Davies and Thorne (2005) have taken this into account and used a mean grain diameter smaller than the bed value to model suspended sediments.

2.10. Profile Evolution Models

Profile evolution models were grouped into four categories by Roelvink and Broker (1993).These are: descriptive, equilibrium profile, behavior-oriented and process-based models. The simplest are the descriptive models where beaches and beach states are classified in terms of their shape and behavior. Equilibrium profile models proscribe the final shape of a beach profile (Bruun 1962; Dean 1977) . This idea has been extensively used with beach nourishment modeling.

Empirical profile evolution models, also called behavior-oriented models, describe the evolution of the profile as observed in nature mathematically, but the

underlying processes may not be related to the physics. This type of models mimics the observed behavior of physical systems with the help of simple mathematical models (De Vriend et al. 1993a). The mathematical model may not have any relationship to the real physics of the process. These types of models are simple and computationally efficient. However they are limited in application to the time frames and scales of the observations. The Kriebel (1982) model is an example of this type where the sediment transport rate is proportional to the deviation from a prescribed equilibrium profile. The response of a profile to beach nourishment can be modeled by this approach, but the storm erosion or the behavior of bars cannot be modeled. Masselink (2004) modeled the formation and evolution of an inter-tidal bar system using a behavior-oriented model based on the shape function of Russell and Huntley (1999). In this model sediment transport is given a prescribed shape across the profile whose magnitude is found by applying a sediment transport formulation. Various modifications are made to the model such as setting sediment transport to zero when a critical bed slope is reached, giving an insight to the development of a behavior-oriented model.

The fourth and the most sophisticated group of models are process-based models, which describe profile changes by simulating the underlying physics. These models generally consist of a wave transformation module, current field module, sediment transport module and a bathymetric change module. The levels of interaction between the modules define the complexity and limitations of the resulting model (De Vriend et al. 1993b). The models in which the bed change does not affect the hydrodynamics are called initial sedimentation/erosion models. Only the initial response of the bed can be modeled with this approach. Medium-term morphodynamic models couple the hydrodynamics and the bed change, making it possible to model the dynamic behavior of the system. Coupling of the waves and currents might also be necessary in some cases like strong rip currents. Various process-based models with different levels of coupling and complexity are discussed below.

Nairn and Southgate (1993) developed a morphodynamic model for profile modeling that later became the COSMOS model. The energetics approach was used with some improvements. Instead of using a single value for the mean current, the current profile was multiplied by the concentration profile to find the sediment transport due to mean flow. An improved friction factor for sheet flow conditions was used. Sediment transport predictions at prototype scale agreed well with measurements for three different offshore transport cases and one onshore transport case. The performance of the model deteriorated for a small-scale lab test with onshore sediment transport, since ripple effects became significant where the energetics approach is not valid. The onshore migration of a bar during the end of a storm was predicted successfully. The success of the model was attributed to the still large wave periods and currents making phase-dependent transport negligible. The formation of a multi-bar system could be modeled only after including long wave effects, showing their importance in such cases.

Thornton et al. (1996) investigated bar generation on a natural beach. Direct hydrodynamic measurements were used instead of a model. The Bailard (1981) sediment transport formula was employed. The sediments mobilized by strong longshore currents were moved offshore by the undertow. Skewed short wave orbital velocities generated onshore transport. Longshore bars formed where these two opposing forces converged. Gallagher et al. (1998) used the same approach with a bigger and more detailed data set with similar results. Both models could simulate the offshore migration of bars during storm conditions, but could not predict their onshore migration at moderate wave conditions. The instantaneous response of the sediment transport formulation to hydrodynamics without any phase lag was suggested as the main reason for the failure to predict onshore bar movement.

Hoefel and Elgar (2003) included the effect of acceleration skewness to the energetics approach. Acceleration skewness, which is measured more easily, is used as a proxy for pressure gradients created under skewed waves which may create onshore

sediment transport. With this new approach onshore bar migration under moderate waves which could not be modeled by the energetics only models (Gallagher et al. 1998; Thornton et al. 1996) could be predicted.

Nonlinear dispersive shallow water theory was used by (Boczar-Karakiewicz et al. (1995) for a model describing bar generation, not including wave breaking and long waves. This model focuses on the wave field rather than surf zone hydrodynamics, but could predict the different spacing of longshore bars at different locations. Wave periods and bottom slope were the main parameters controlling the bar formation. The model did not make any predictions for bar transformation.

Van Rijn et al. (2003) compared five process-based morphodynamic models for their ability to predict profile changes at storm and seasonal scales. These models, developed at different European institutions, are UNIBEST-TC (Bosboom et al. 1997) COSMOS (Nairn and Southgate 1993) , CROSMOR2000 (Van Rijn 2000), BEACH 1/3D (O' Connor et al. 1998) and CIIRC (Sierra et al. 1997). Most of those models have been in constant development for more than a decade. Roelvink and Broker (1993) compare earlier versions of some of these models.

All of the hydrodynamic models were depth- and phase-averaged and included rollers in their wave forcing. Even though the models were linear, asymmetry of near-bed velocities was included using higher-order models (Stream function model, UNIBEST) or empirical results (COSMOS, CROSMOR, Isobe and Horikawa 1982). The models that did not include the wave asymmetry explicitly in the hydrodynamics (BEACH, CIIRC) used the Watanabe et al. (1980) sediment transport model, which includes asymmetry empirically by the transport direction indicator. Low-frequency wave effects were included only in the CROSMOR model. Only UNIBEST included lateral mixing of longshore currents. Making the breaking coefficient a function of the local bottom slope and wave steepness improved the accuracy of the results. All of the models could predict storm scale profile changes when the hydrodynamics models were tuned up properly.

Only UNIBEST and CROSMOR could be applied at the seasonal time scale without blowing up. Both of these models used the Ribberink (1998) bedload and Van Rijn (1993) suspended sediment formulas. Additionally, only these two models included Longuet-Higgins (1953) near bed streaming. All the models could predict offshore bar migration, but were not successful at predicting shoreline changes. The paper also claims that they can predict onshore bar migration. However the observed onshore bar migration was very small and the results produced by the models might be flattening of the bar rather than onshore movement.

The model proposed by Dibajnia et al. (2001), which used a sediment transport model similar to Watanabe et al. (1980), could reproduce erosional and accretional beach profiles under different wave conditions. However only initial sediment transport rates were investigated and beach morphology was not modeled.

Wave-resolving hydrodynamic models looks promising for the future, with their ability to solve for skewness and phase lags directly, but their immense demand on computing resources limits their usability to research applications at the present time. Even running a one-dimensional vertical model that solves for hydrodynamics at just 14 points along a profile takes about 30% of the real time simulated (Henderson et al. 2004).

Henderson et al. (2004) simulated profile evolution using a 1D (vertical profile) wave-resolving eddy-diffusive boundary layer model. The model could predict one of the two onshore bar movements and one offshore bar movement events at Duck, North Carolina during the Duck94 field experiment. However even though it is a much more complex and computationally expensive model than Hoefel and Elgar (2003) its performance was not better. It was found that Stokes drift was important in predicting onshore bar movement. Free stream and near-bed velocities had a phase difference of 25 degrees and correlation of concentrations with near-bed velocities was much higher. The model did not take into account bedload transport, breaking wave turbulence, spatial variations in bottom roughness and bed slope effects.

Kobayashi and Johnson (2001) assumed that suspended sediment transport is the only form of transport in their model, which included advection and storage of sediment along with suspension and settling in a depth-integrated sense. This is an initial response model and does not describe the effect of changing bathymetry on the hydrodynamics. It could successfully predict erosional, accretional and neutral profile changes from a large flume. It was found that the net sediment transport is a result of the small difference between onshore transport by oscillatory currents and sediment suspension and offshore transport of mean suspension due to mean currents.

Wave-averaged models were used in most applications to solve for hydrodynamics. The energetics approach with various modifications is the most widely used sediment transport formula. Its basic limitation, a quasi-steady assumption, is not present in models that solve the vertical advection-diffusion equation with an intra-wave approach. A more fundamental way to include unsteady effects is using wave-resolving models. However these models are very time consuming and a clear advantage in predictive capabilities has not been shown yet. Overall most models could predict erosional profiles at storm scales, but the prediction of long-term recovery of profiles and onshore bar movement was not as successful. The effects of long waves have been shown to be important in correct modeling of bar morphology in some cases. The effects of acceleration skewness have recently been shown to be significant and needs more attention.

3. FIELD DATA COLLECTION AND ANALYSIS

The field data used for this study were collected as a part of the South Carolina Coastal Erosion Study (SCCES). The goal of this project is to identify physical processes related to the coastal erosion around northern South Carolina. This thesis is a part of this bigger project and a subset of the data focusing on the nearshore region was used for it. This data were utilized in calibrating and testing hydrodynamic and morphodynamic models. Figure 3.1 is a map of the SCCES study area showing the locations of field experiments and measurement stations. Waves, currents, water levels and water temperatures were measured at these stations

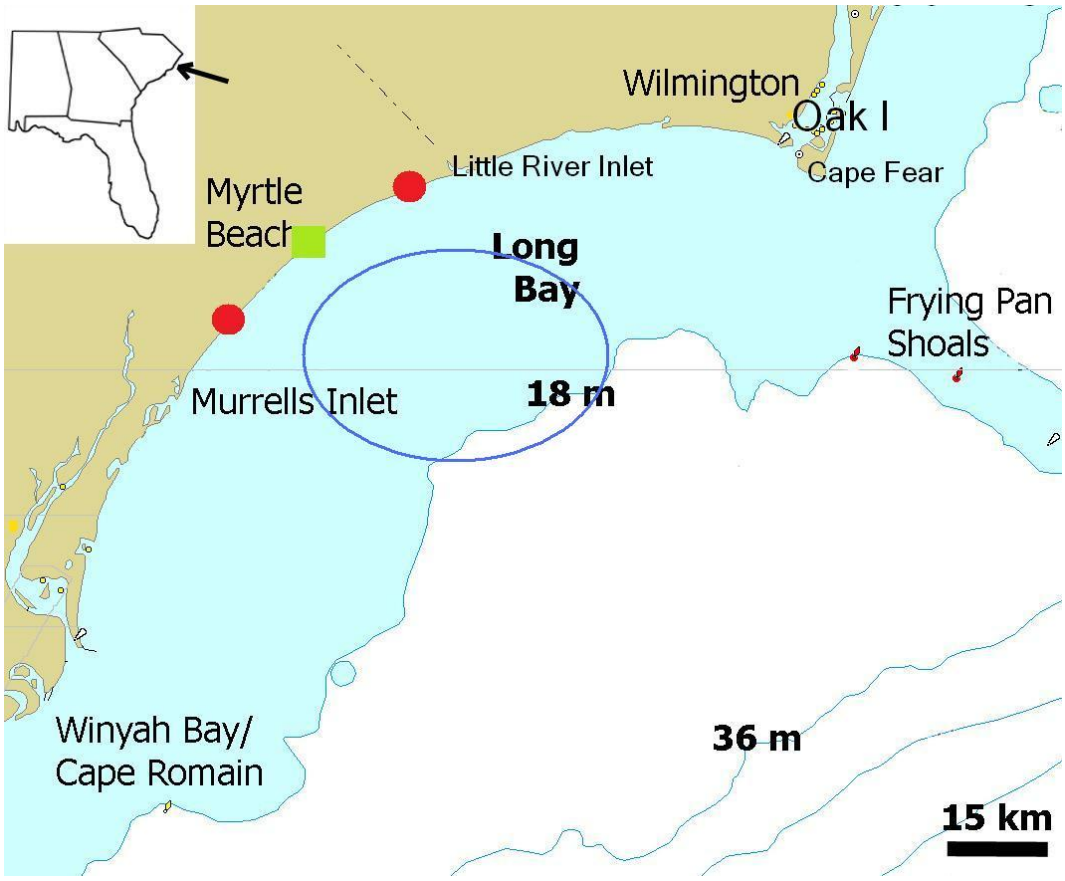

Figure 3.1. Map showing locations of field data collection efforts. Red circles: 2005 N. Myrtle Beach and Myrtle Beach nearshore experiment. Green square: 2003 nearshore experiment, Blue ellipse: 2003 offshore data collection area.

Six months of offshore wave and current data were collected between October 2003 and April 2004. Offshore data collection was focused around a large shoal in Long Bay. Surf zone data were collected in two separate field experiments in December 2003 and December 2005 shoreward of the shoal. Coordinated Universal Time (UTC) was used throughout the experiment. All dates and times given are also in UTC unless stated otherwise.

3.1. 2003 Nearshore Data

Nearshore hydrodynamic (Obley et al. 2004) and bathymetric (Haas et al. 2004) data were collected at Myrtle Beach, SC between Dec. 10 and Dec. 15, 2003. During this period, hydrodynamic measurements were also taking place offshore. The goal of the nearshore experiment was to have simultaneous measurements at the nearshore that could be used together with the offshore measurements to model large scale hydrodynamics and observe the possible effects of offshore processes on the nearshore. Four instruments placed on a profile measured waves and currents. Bathymetric data were collected daily along the instrument profile and the surrounding area. Continuous digital video imagery of the surf zone was also captured during the experiment. Sediment samples were also taken. This data set was not used for hydrodynamic modeling since the most offshore instrument used was about 2.5 meters deep and bathymetric data collected were also limited to the same depth. This data set does not cover desired range and the measurements for the modeling. Collected velocity data were used to investigate the wave skewness and wave orbital velocities. The data set is explained briefly.

Bathymetric data were collected with two Ashtech Z-12 GPS (Global Positioning System) receivers in DGPS (Differential Global Positioning System) mode and a Sokkia SET610 Total Station. Bathymetric data were also collected by Coastal Carolina University in the same area on May 11, 2004. The spatial extent of this data set is shown in Figure 3.2 compared to the 2003 experiment total station and GPS data. A local

coordinate system is used in all the figures for the 2003 nearshore experiment. The UTM coordinate system was converted to the local coordinate system by subtracting 3738300 m from the Northing coordinates and 705500 m from the Easting coordinates and rotating 218.6 degrees counter-clockwise. In the resulting coordinate system x-axis is shore parallel SW being the positive direction and y-axis is shore normal going offshore positive. Vertical elevations are given in NAVD88.

There are four profiles that correspond to the measurement area. One of the profiles is shown in Figure 3.3. The slope is relatively steep nearshore (0.03) until 300 meters distance when it decreases sharply to 0.004.

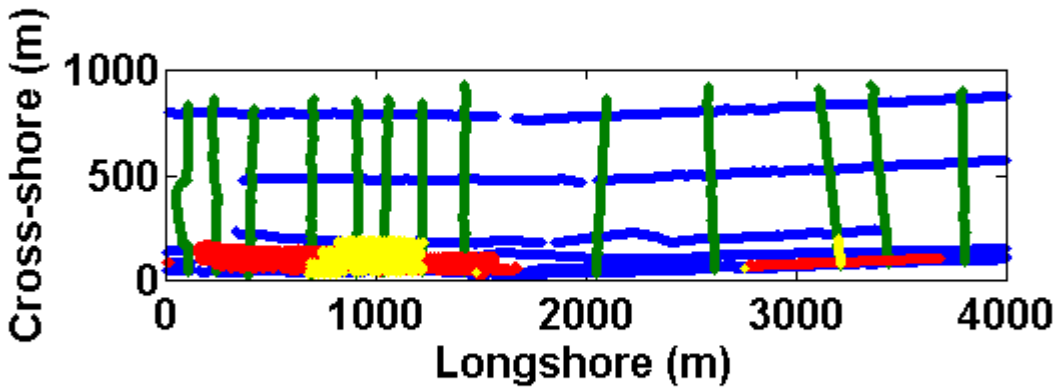

Figure 3.2. Locations surveyed on May 11, 2004 (blue), and surveyed by GPS (red) and total station (yellow) during the 2003 nearshore experiment.

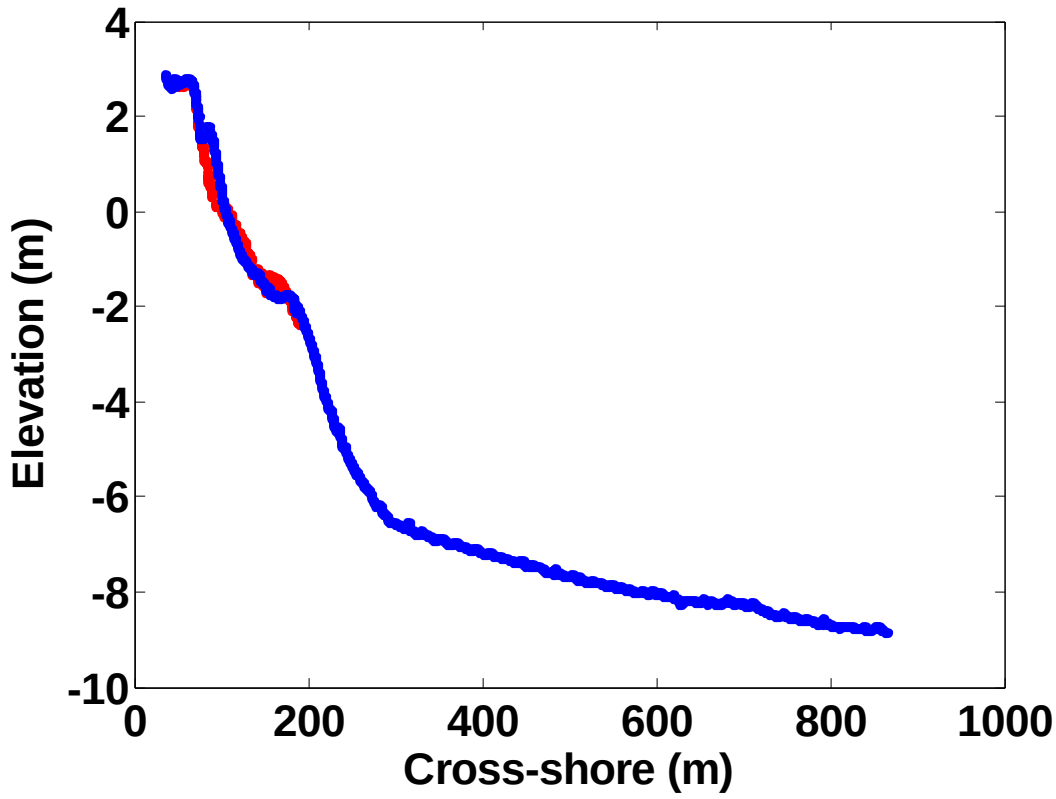

Figure 3.3. Bathymetric profile measured by Coastal Carolina University between longshore location 1020-1070 m (blue) and data collected by TS (red) during the 2003 nearshore experiment. Vertical datum NAVD88.

The total station was used to take profile and general bathymetric measurements in the surf zone reaching to water depths up to 1.5 meters during low tide where the GPS could not be taken. The measurements covered an area extending 500 meters in the longshore and 200 meters in the cross-shore. It was also used to measure control points for the video survey. GPS was employed to measure topography densely covering a larger area.

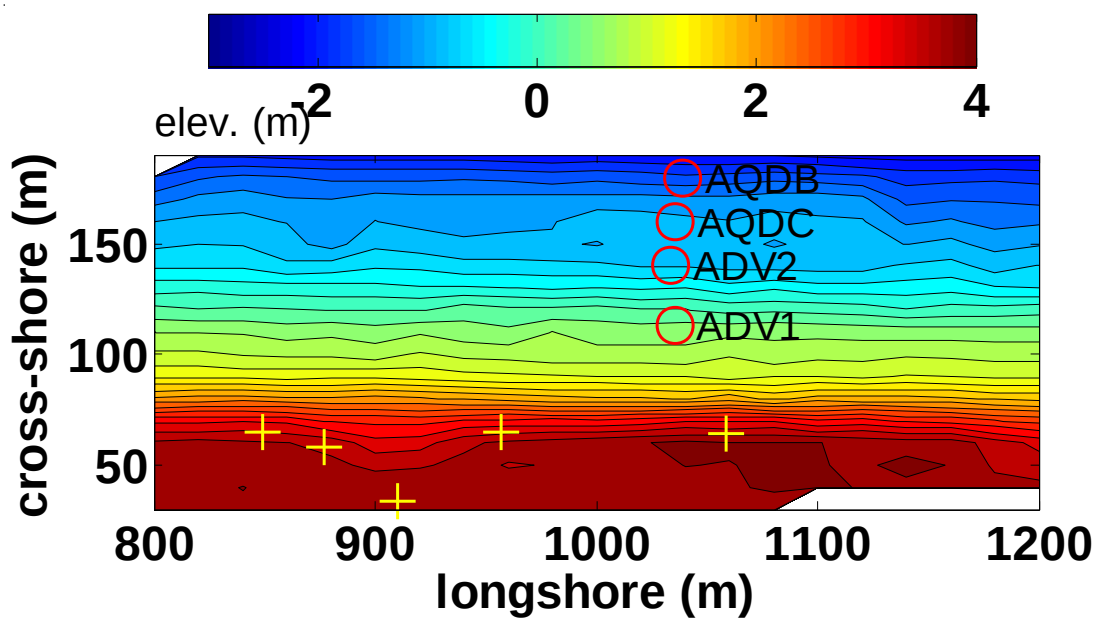

Figure 3.4. Bathymetric grid created using total station measurements from 2003 field experiment. Pluses show control points on the dry beach. Circles show gage locations on December 12. Axes not to same scale.

Hydrodynamic measurements were made with two Nortek Aquadopp upward-looking current profilers and two Sontek Triton downward-looking acoustic Doppler velocimeters (ADV) for six days. The ADVs measured three velocity components at a point approximately 20 centimeters above the seafloor. The profilers measured the velocity profile in 40 cm bins beginning 40 cm above the bed. All the instruments also measured pressure, temperature, heading, pitch, and roll. The instruments were placed in the surf zone along a profile manually during low tide (Figure 3.4). The deepest instrument was at 1.5 meters mean depth at low tide. Tide range was around 1.5 meters.

The instruments were recovered for downloading data and battery replacement every one or two days. The instrument locations changed less than a meter (horizontally) between deployments after the first day. The ADVs collected continuous data at 2 Hz and the profilers at 1 Hz. The offshore Aquadopp's (AQDB) velocity sensors stopped working after 10 minutes of the first deployment, providing only pressure data for the rest of the experiment.

The instrument profile (Figure 3.5) was surveyed daily during the 2003 Myrtle Beach nearshore experiment. The profile measurements are shown in Figure 3.6. Erosion above *z*=0 (NAVD88) and accretion below this elevation was observed. Most of the bathymetric change is assumed to have occurred on December 14 when the wave heights increased two fold (Figure 3.7). This is supported by the fact that almost no change was observed on December 12. Local bathymetric change was at most 15 cm. The measurement accuracy is within a couple of cm on dry land (z>-0.5 m), but errors in submerged portions of the profile are greater due to wave action.

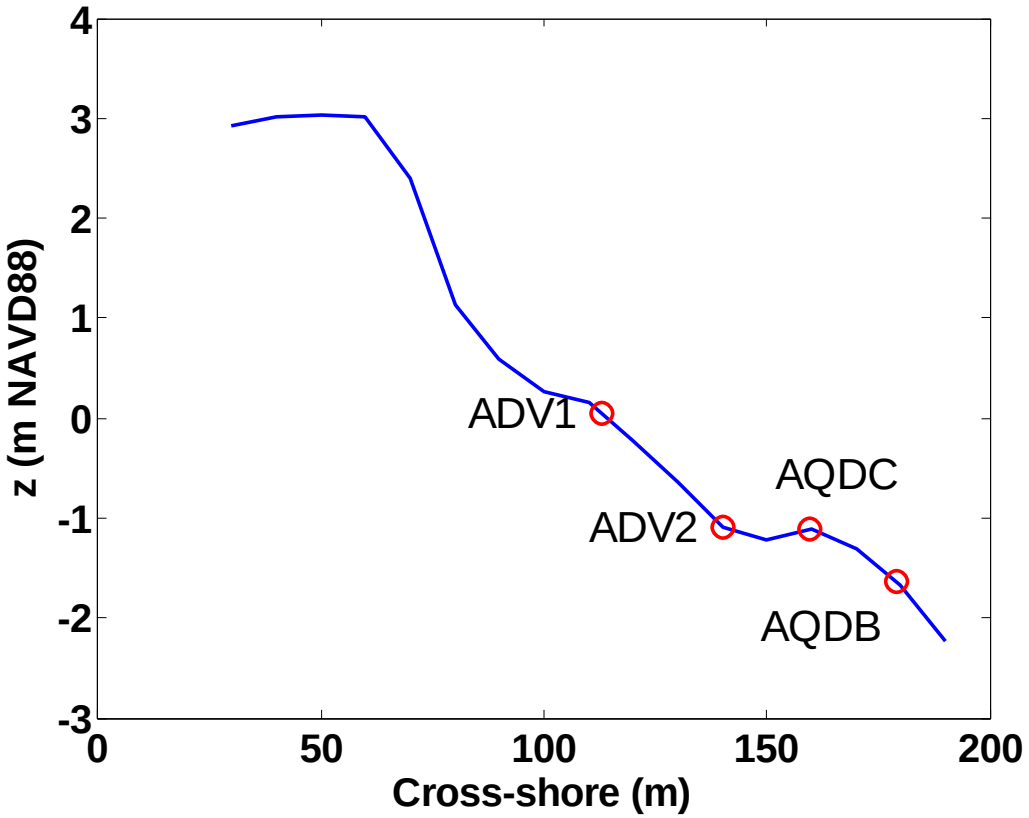

Figure 3.5. Locations of instruments along the profile.

On December 14, the two inner instruments tipped over and did not provide good data. There were only two instruments working when the bathymetric changes occurred,

but the offshore instrument reported only non-directional wave height data and no current data.

Modeling bathymetric changes for this period was considered. The most offshore instrument is a cross-shore coordinate 185 meters at 2 meters depth (NAVD88) within the surf zone. In order to model the surf zone the offshore boundary should be outside the surf zone. One method to get wave conditions at the offshore boundary of the model domain is to un-shoal and un-refract the waves from the inner instrument locations to the desired depth using linear wave theory. However there is no straightforward way to un-break the waves to calculate the offshore wave height correctly. Water depth at the offshore instrument varied between 2.8 and 1.6 meters. For the energetic conditions on December 15, the wave height to water depth ratio becomes as large as 0.6, showing that the wave heights are depth limited. Variation of wave height (Figure 3.7) closely following water depths is also an indication of this. If the wave heights are depth limited, wave energy is lost before reaching the most offshore instrument and the wave heights at the offshore boundary can not be predicted by un-shoaling.

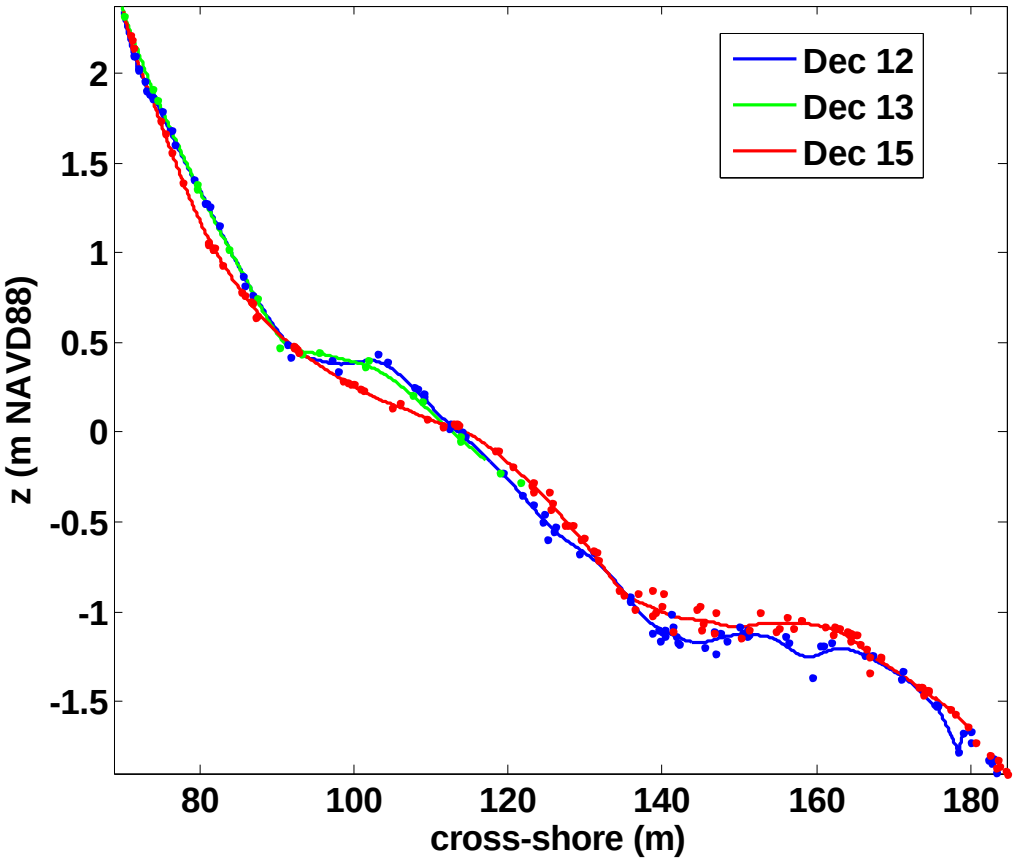

Figure 3.6. Measured profiles along the instrument transect during 2003 Myrtle Beach Nearshore Experiment. Legend shows the days of the measurements during December 2003. Dots show actual measurements and the continuous curves are spline fits to these measurements.

For the 2003 experiment, there is one instrument for velocity calibration and two instruments for wave height calibration which is not sufficient. The swash zone processes are not included in the model so only the change between 145 and 165 meters can be expected to be captured by the model. Many assumptions are needed to model bathymetric changes for the discussed data set and there is not enough data for calibration. The surveyed portion of the beach is small compared to the swash zone. The amount of change is 15 cm which is not significant compared to the 10 cm certainty in bathymetric measurements. Due to the above reasons bathymetric modeling was not performed for this data set.

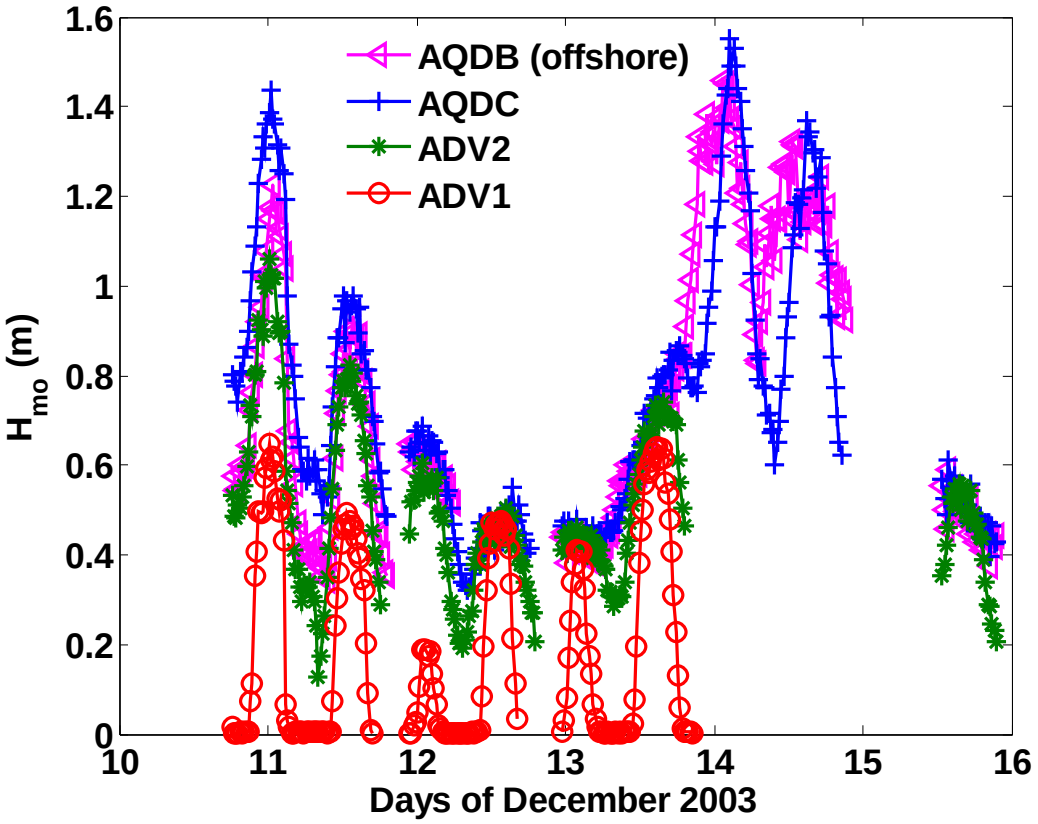

Figure 3.7. Wave heights measured during 2003 Nearshore Experiment before filtering.

Data from all sensors were split into 20-minute bursts. The mid-time of all bursts were 0, 20 or 40 minutes past the hour. Data were initially filtered for bad data points such as spikes. Later it was filtered further for qualitative analysis. If the top of the measurement volume for an instrument (bottom bin for Aquadopps) became dry for any part of the burst that burst was discarded. A lot of bubbles may form close to the surface especially in the surf zone. These bubbles also degrade the quality of the data. Additionally, if the distance between the wave trough and the top of the measurement volume was less than 50% of the wave height (H_{mo}), that data were discarded. The number of bursts available before and after the final filtering can be seen in Table 3.1.

Table 3.1. Total number of bursts for each instrument and the number used for analysis

Inst Name	Bursts after initial filtering	Bursts used in skewness analysis
AQDB	266 (only pressure data)	0
AQDC	301	220
ADV2	225	188
ADV1	188	38
Total	**980**	**446**

At the end a total of 446 out of 980 bursts were used for further skewness analysis. It can be seen that more of the bursts from the instruments in shallower water were discarded since the measurement volume was out of the water for longer periods.

Seven sand samples were collected across the profile on which the instruments were placed by hand. The samples were analyzed by sieve analysis. The median diameter decreased from 0.40 mm on the beach to 0.20 mm at the two meters depth (NAVD88). The mean diameter showed a similar trend (Figure 3.8). The sampling was done just once along one profile, so longshore and temporal variability are not known.

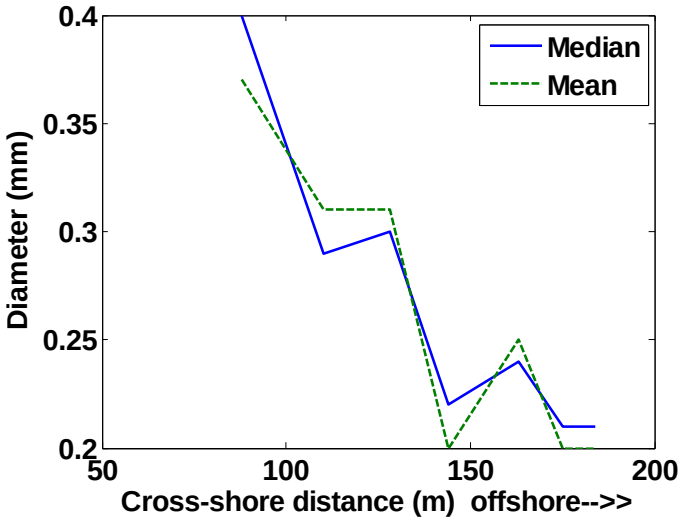

Figure 3.8. Mean and median sand grain diameters collected across the instrument profile.

2003 experiment supplied us with detailed velocity measurements and bathymetric data that were used in examining orbital velocity skewness and the

parameters affecting it. The group also gained valuable experience in surveying by GPS and total station, surveying the surf zone by video and programming and deploying wave and current gages.

3.2. 2005 Nearshore Experiment

A second nearshore field survey was conducted at Myrtle Beach during December 10-18, 2005 (Work and Wiederhold 2006) by two teams from Georgia Tech Savannah (GTS) and the University of South Carolina. Simultaneous measurements were taken at two sites approximately 10 km apart (Figure 3.1). The objective of the study was to investigate both temporal and longshore variability of hydrodynamic conditions by comparing the results from the two sites over a brief period. The experimental methodology was similar to the 2003 experiment, but more extensive. Hydrodynamic and bathymetric measurements were taken at both sites along with sediment samples. Video images of the surf zone were also recorded to investigate waves, longshore currents and methods of quantifying them from the images (Haas and Cambazoglu 2006; Yoo et al. 2005) The instruments used and the data collected at the two sites were very similar. This thesis focuses on the data collected at the North Myrtle Beach site by the GTS team.

3.2.1. Beach Morphology Measurements

The beach morphology was measured using a Sokkia SET610 Total Station, prisms placed on rods, a DGPS system consisting of two Ashtech Z12 GPS receivers (one rover, one base) and a fathometer. For land measurements, the GPS rover was placed on an all-terrain vehicle (ATV) (Figure 3.9) or a backpack. For bathymetric measurements, the GPS rover was placed on an inflatable Zodiac boat, along with the fathometer. The goals of the morphology survey were:

- Collect information to define a bathymetric grid for hydrodynamic and morphological models.

- Identify the positions of the instruments and sand sampling locations.
- Measure reference points on the dry beach to rectify the video images

Figure 3.9. A Honda ATV equipped with a GPS receiver was used for surveying the dry beach at or near low tide.

First, three control points on the beach were defined using the total station, referencing each to two available South Carolina Coastal Council benchmarks (5735, 5730A). Daily profile measurements were taken with the total station, along the profile defined by the instruments and along two parallel profiles 50 m to either side of the instrumented profile. The profiles extended from the top of the high tide level down to -2.5 m (NAVD88). This lower limit is at a depth of 1.5 m near low tide, near the limit where a walking/swimming rodman can reach while he is still able to keep the rod still. The total station was also used to survey reference points to be used in the rectification of video images. This was repeated daily to account for possible changes in the camera location.

For GPS measurements the base station was set on one of the control points, the rover was set on an ATV, a backpack carried by a person, or the boat. The base station

sent radio corrections to the rover at 1 Hz. This is called the real time kinematic (RTK) mode. The receiver was carried by a person to take measurements along the shoreline and in knee deep water during low tide. The ATV was used to take measurements on the dry beach from the low tide level to, or above, the high tide level. Using the ATV, large portions of the beach could be surveyed quickly. About three km of beach was surveyed using the ATV.

An inflatable Zodiac boat was used for the bathymetric surveys. The GPS antenna was connected to the transom of the boat just above the transducer of the fathometer. The fathometer and the GPS collected data simultaneously. Both instruments were connected to a laptop equipped with Hypack surveying software. Figure 3.10 shows the setup. The laptop, the GPS receiver, the fathometer and their batteries were all enclosed in the white box seen in Figure 3.10. The GPS antenna and the yellow rod carrying the fathometer transducer can also be seen.

Figure 3.10. A laptop with Hypack surveying software connected to a GPS receiver and a fathometer (all in white box) was used to measure bathymetry. The GPS antenna (round white disk) and the

fathometer transducer (at the end of the yellow rod (not seen)) are mounted to the transom of the boat.

A local coordinate system was created where the x-axis is parallel to the shoreline. A 210 degrees counter-clockwise rotation was made from the East to the new x direction (Figure 3.11). The positive y direction points offshore. The origin was shifted to coincide with control point 1 (CP1). All the plots are in this coordinate system.

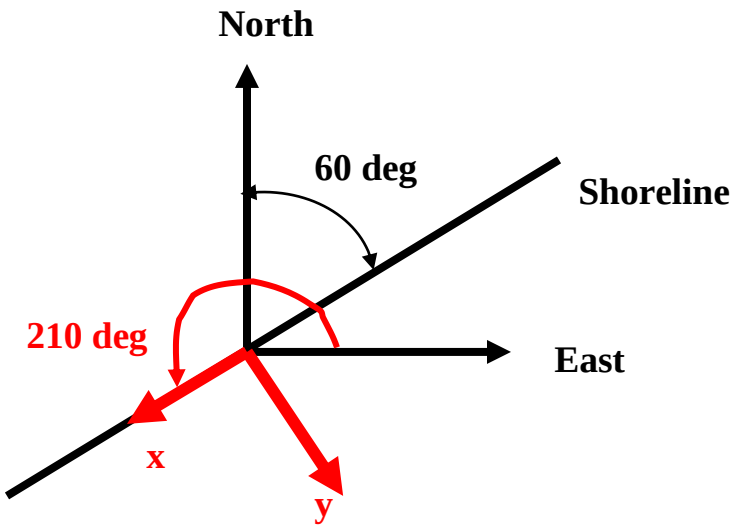

Figure 3.11. A new coordinate system was created aligned with the shoreline rotating 210 degrees ccw from East to the new x coordinate. The origin is located at CP1 (3742526N, 711842E UTM).

The locations of the points surveyed on the beach are shown in Figure 3.12. The shoreline orientation was defined according to the portion of the beach around the instrument locations. The ATV surveys which cover three km of beach are not straight because the shoreline orientation is changing.

Bathymetric surveys cannot be taken inside the surf zone with the boat because breaking waves rock the boat too much to allow good measurements. The boat surveys were done close to high tide so that the boat could come as close to the shore as possible. The backpack surveys were done during low tide, so there was no gap between the two surveys. Figure 3.13 shows all the data used to create a bathymetric map for the North Myrtle Beach site. This area extends about one km in the longshore direction and 600 m

in the cross-shore direction. The gridding/mapping tool “Surfer” was used to interpolate the data using the krigging method to create the bathymetric map in Figure 3.14. The bathymetry is generally longshore uniform. There are some non-uniformities around y=150 where the longshore bar is. The mean slope is about 1.7%, decreasing in the offshore direction.

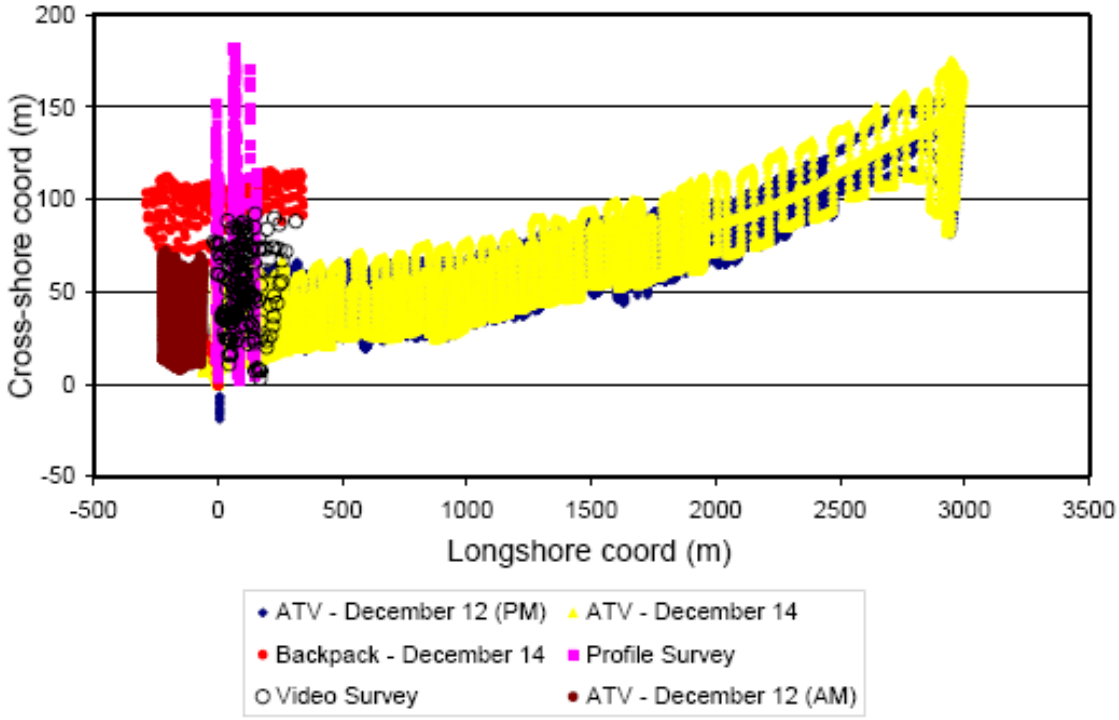

Figure 3.12. Points surveyed on the beach using total station and GPS with backpack and ATV. Note that scales are different in x and y directions.

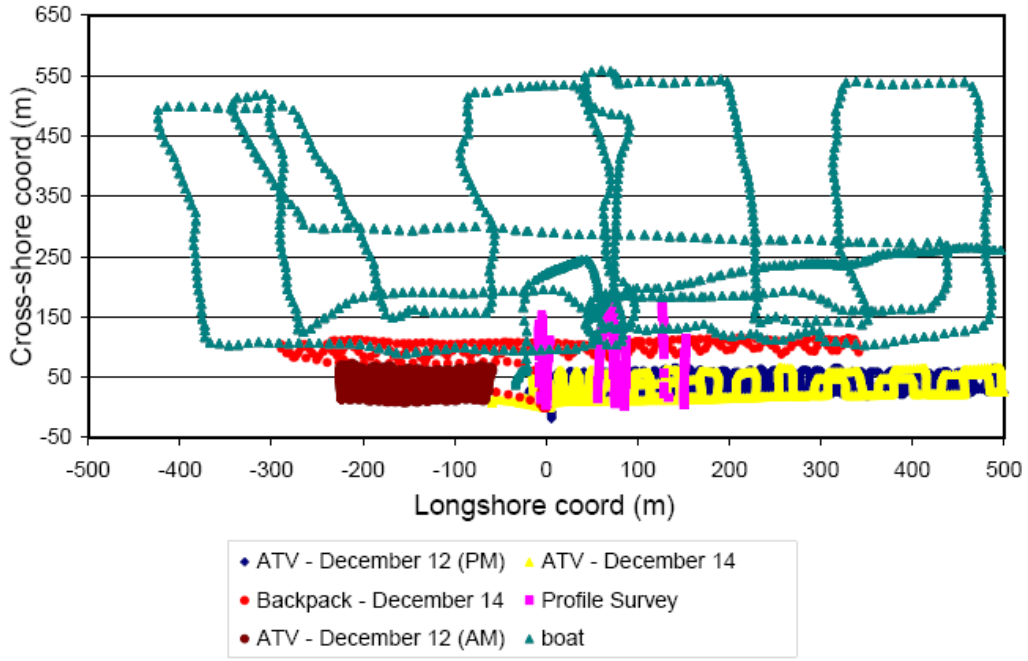

Figure 3.13. Land and sea survey points around the instrument profile at x = 90 m.

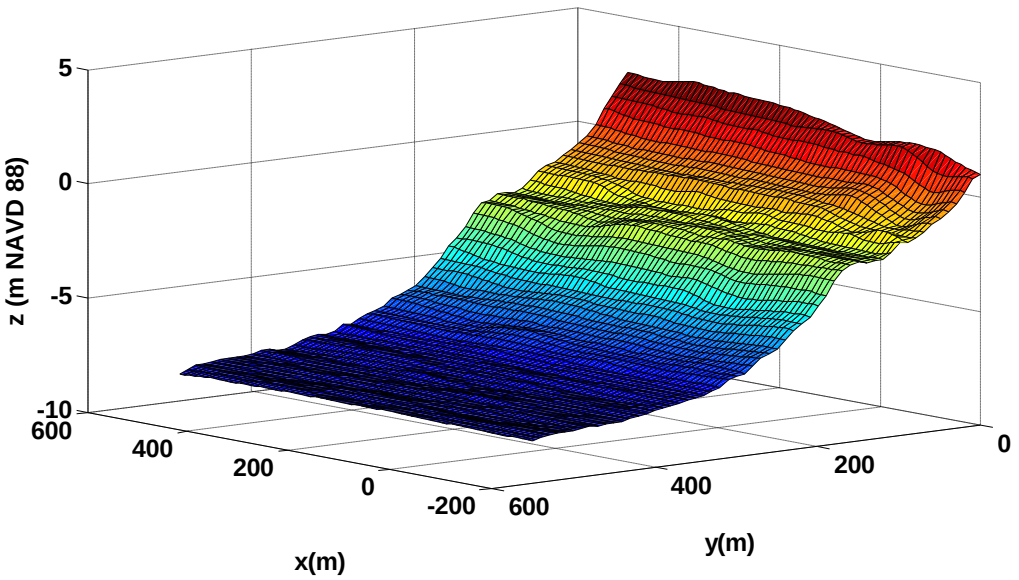

Figure 3.14. Bathymetric map created using data from Total Station, boat, backpack and ATV measurements.

3.2.2. Hydrodynamic Measurements

Hydrodynamic data were collected with four instruments placed along a profile (Figure 3.15). The instruments used were one RDI Workhorse ADCP, two Nortek Aquadopp Profilers and a Sontek Triton ADV. The parameters of the sampling scheme and the properties of the instruments are given in Table 3.2. The goal was to measure wave heights, wave orbital velocities and currents in and around the surf zone and the change in their values across the surf zone. This information helps us in understanding the hydrodynamic processes and is used in calibration and verification of numerical models of wave transformation and hydrodynamics.

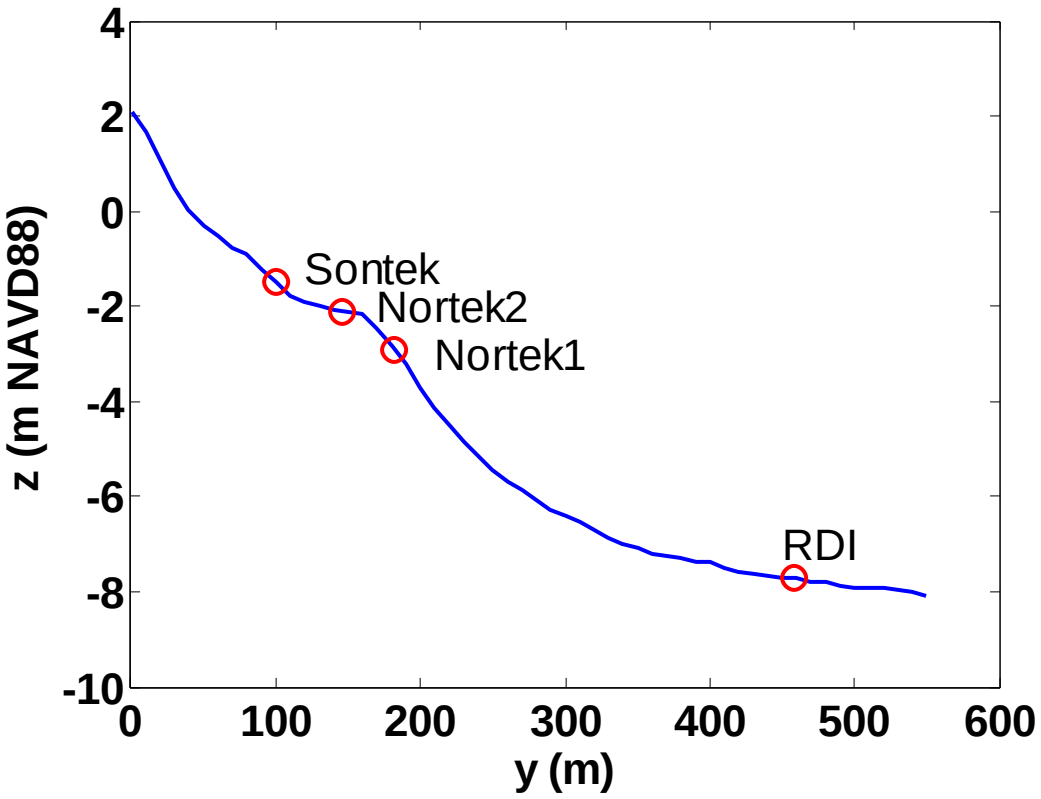

Figure 3.15. Locations of instruments used for wave and current measurements.

All instruments used are acoustic instruments which calculate the velocity along three (Nortek, Sontek) or four (RDI) beam directions by measuring the Doppler shift in reflected sound. They also all have pressure, temperature, pitch and roll sensors and a

compass. Wave height is calculated based on pressure or velocity measurements. Wave direction is interpreted from velocities. The temperature is used to calculate speed of sound, which is required to find velocities.

Table 3.2. Programming parameters and deployment characteristics for all in situ sensors. Burst interval is elapsed time between the beginning of one burst and the next; burst duration is the amount of time the instrument is turned on to collect a single burst. Nortek instruments skipped the first 18 minutes at the top and bottom of the hour when recording mean velocity, while collecting wave burst data.

Parameter	Triton ADV	Aquadopp (usgs0101)	Aquadopp (gts0101)	RDI ADCP
Acoustic Frequency	10 MHz	2 MHz	2 MHz	1.2 MHz
Sampling Rate	2 Hz	2 Hz	2 Hz	2 Hz
Burst interval for wave time series	1800 sec	1800 sec	1800 sec	1800 sec
Wave burst duration	1024 sec	1024 sec	1024 sec	1024 sec
Burst interval for mean velocity	1800 sec	60 sec	60 sec	300 sec
Avg. Interval for mean velocity	30 sec	30 sec	30 sec	60 sec
Coordinates (UTM Zone 17, m)	E 711829.77 N3742402.62	E 711858.840 N 3742367.619	E 711882.483 N 3742339.322	E712008.24 N3742093.24
Blanking distance	N/A	0.10 m	0.10 m	1 m
Bin Size	N/A	0.25 m (0.50 m for wave bursts)	0.25 m (0.50 m for wave bursts)	0.50 m
Number of Bins	N/A	12	12	20
Mean depth for deployment period (raw press + altitude)	1.25 m	3.39 m	3.92 m	7.24 m
Altitude above seafloor	0.23 m (mean)	0.25 m	0.25 m	0.20 m
First Good Burst	12/12/2005 16:02	12/11/2005 15:56	12/11/2005 17:21	12/13/2005 18:00
Last Good Burst	12/17/2005 18:57	12/17/2005 14:28	12/17/2005 19:30	12/16/2005 21:30

The RDI ADCP can be seen placed in its frame before deployment in Figure 3.16. The instrument itself is in the foreground of the picture, with the battery pack behind. The four upward-looking transducers can be seen. The resulting acoustic beams can measure

the velocity at various bins over the water profile. This instrument was placed at the most offshore location, at a depth of around -7.5 m (NAVD88). The instrument was towed through the surf zone to its deployment location with the Zodiac boat. The floats seen in the photograph gave it the required buoyancy.

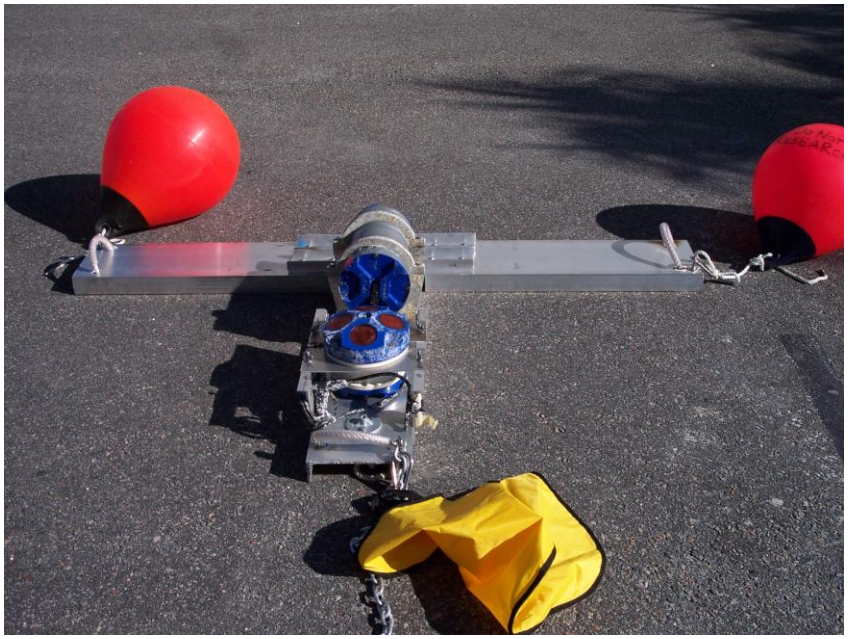

Figure 3.16. RDI ADCP placed on its frame before deployment. Floats used to tow it to its location.

Two Nortek Aquadopp Profilers were placed near the -3 m (Nortek1) and -2 m (Nortek2) depth contours (datum NAVD88). Four people carried the instruments to their locations and placed them on the sea bottom during low tide. These instruments had a smaller frame for easy carrying (Figure 3.17). Three upward-looking transducers are seen in the photo. They can measure the profile of water velocity above them. The transducers were covered with a pepper and Vaseline mixture to protect them from fouling. Lead weights seen in the photo were added to increase stability.

Figure 3.17. One of the two Nortek Aquadopp instruments deployed at the North Myrtle Beach site.

The Sontek Triton ADV was placed closest to the shore. A pipe was jetted into the sand. The rest of the frame was bolted (Figure 3.18) and the instrument was secured to the frame. This instrument is different than the other three, because it takes measurements within just one small sampling volume rather than large bins and thus does not report measured velocity profiles. The measurement volume is just below the arms seen in Figure 3.18 on the right.

Figure 3.18. Left: The Sontek Frame before the instrument placed. Right: The downward looking arms of the Sontek Triton (in a different frame from a previous field work).

The measurement volume for the Sontek ADV was 23 cm above the sea floor. The center of the first bin was 60 cm above the sea floor for the Nortek instruments. The corresponding distance was 1.45 meters for the RDI instrument. All the instruments measured bursts of data for 1024 seconds every 30 minutes (Table 3.2). This data were used to calculate wave statistics and spectra. The Iterated maximum likelihood method was used for spectral analysis. RDI data were processed with vendor-provided software (Wavesmon). Data files from the other instruments were processed with DIWASP software (Johnson 2002). Iterated maximum likelihood method (IMLM) was used for calculating the directional wave spectra for all instruments to be consistent with Wavesmon methodology. Wave height, H_{mo} was calculated from the directional spectra using the definition:

$$H_{mo} = 4\sqrt{\int_{f_{\min}}^{f_{\max}} \int_{0}^{2\pi} E(f,\theta)} \qquad \textbf{(3.1)}$$

where $E(f,\theta)$ is the spectral energy density (m^2/(Hz-deg)) , f is the wave frequency and θ is direction. Energy between 0.05(fmin) and 0.35(fmax) hertz is included in the calculation since there is too much noise outside this range. Mean wave period T_m is defined as the inverse of the mean frequency f_m.

$$f_m = \frac{\int_{f_{min}}^{f_{max}} f \int_0^{2\pi} E(f,\theta)}{\int_{f_{min}}^{f_{max}} \int_0^{2\pi} E(f,\theta)} \quad \textbf{(3.2)}$$

Figure 3.19 shows time series of the wave heights. Wave heights increase from the offshore instrument (RDI) to Nortek1 as a result of shoaling. They stay the same or decrease at Nortek2, depending on the location of wave breaking. Most of the time the waves break before they reach the inner instrument (Sontek) so it has generally the smallest wave height. The maximum offshore wave height is 1.3 meters, which occurs around day 16 (December 16, 2005). The gaps in the Sontek data set reflect the times when it is out of the water during low tide.

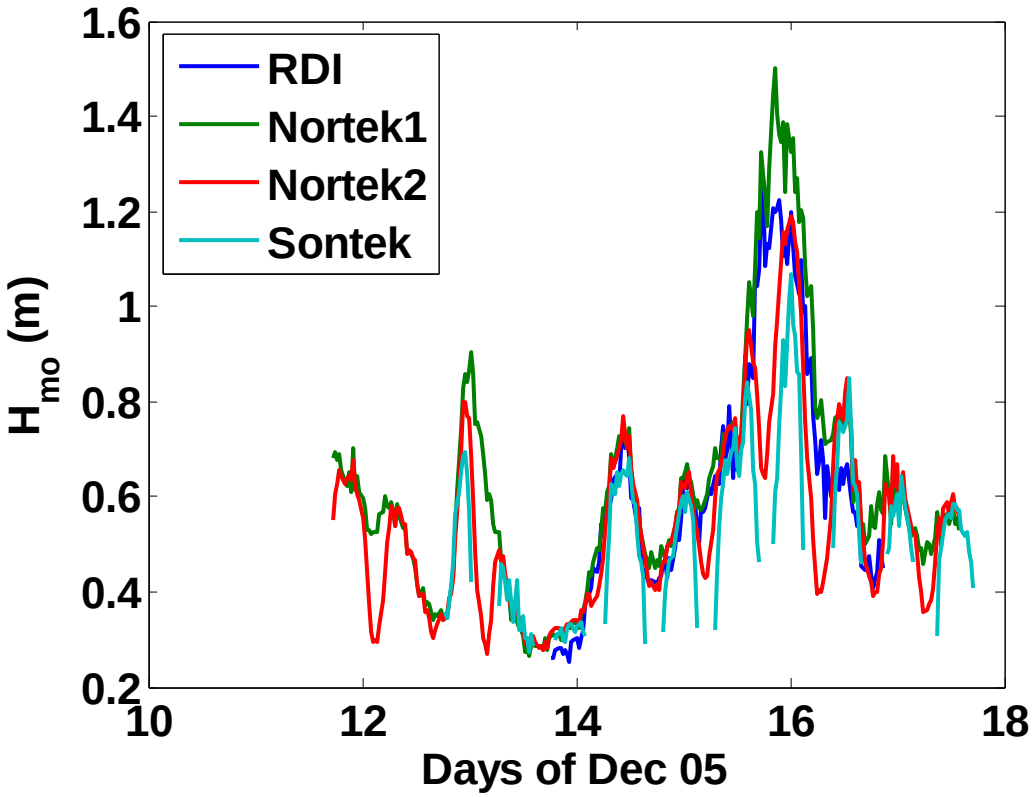

Figure 3.19. Wave heights measured at North Myrtle Beach site. The label shows the instruments from the most offshore (RDI) to the most inshore (Sontek).

The mean wave period fluctuated between 4 and 8 seconds (Figure 3.20). The periods are very close at all instruments when they are less than six seconds. For larger periods, the wave periods decrease at the inner instruments as waves with longer periods break earlier than the smaller ones. Nonlinear wave interactions also contribute to the decrease in wave period.

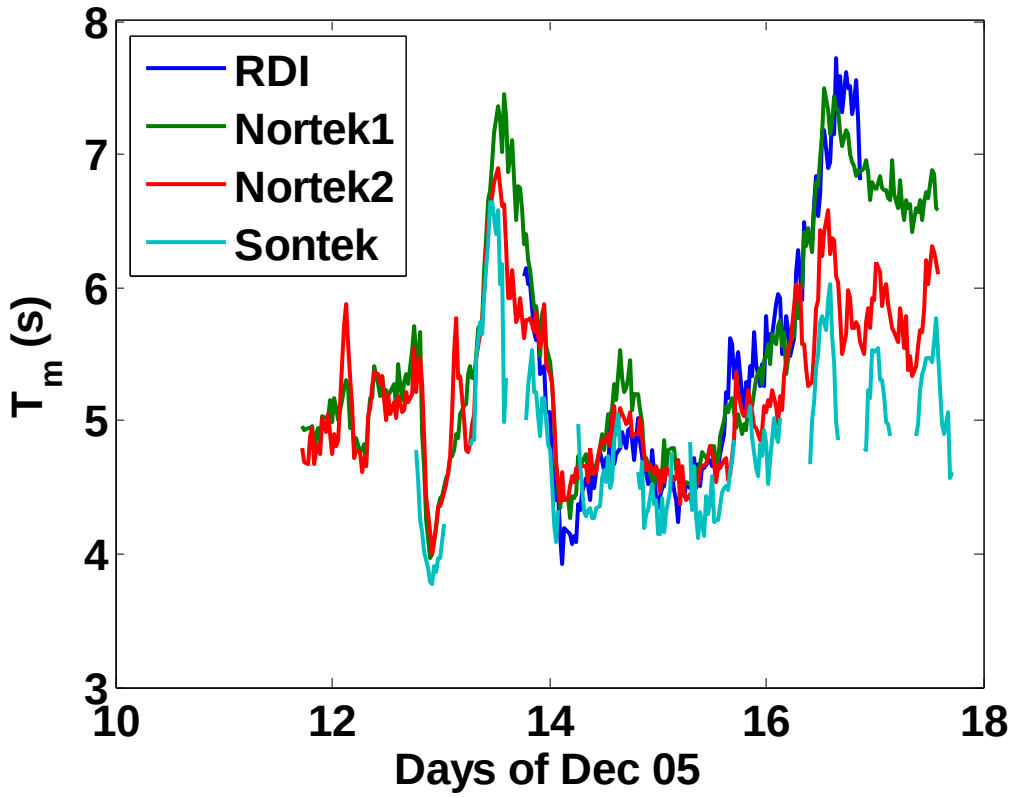

Figure 3.20. Mean wave periods measured at North Myrtle Beach site. The label shows the instruments from the most offshore (RDI) to the most inshore (Sontek).

Mean wave direction was computed from directional spectra for all instruments. Inspection of the results showed that there was a problem with the wave angles at both of the Nortek instruments. By comparing computed wave angles with images from the captured video this was verified. An example image is shown in Figure 3.21. The image is rectified so the directions correspond to real world coordinates. The waves are coming from the east and refracting as they approach the shore. The problem was fixed by increasing the wave angles 13 and 23 degrees for Nortek1 and Nortek2 respectively. These numbers were chosen such that when the waves at the offshore instrument are shore normal the waves at the Nortek instruments are shore normal too. The simple shift in angle suggests that the problem is a compass error caused by faulty compass calibration or the compass being affected by chains and anchors. The corrected wave angles are shown in Figure 3.22. The waves are initially coming from south. They turn

towards east around December 14 and turn southward again on December 16. Waves refract and wave angles decrease as the waves approach shore. The most inner instrument (Sontek) does not follow this trend and is generally higher. This might be caused by reflection from the shore and or might be influenced by the greater noise in the data from this sensor, due to its location in or near the swash zone.

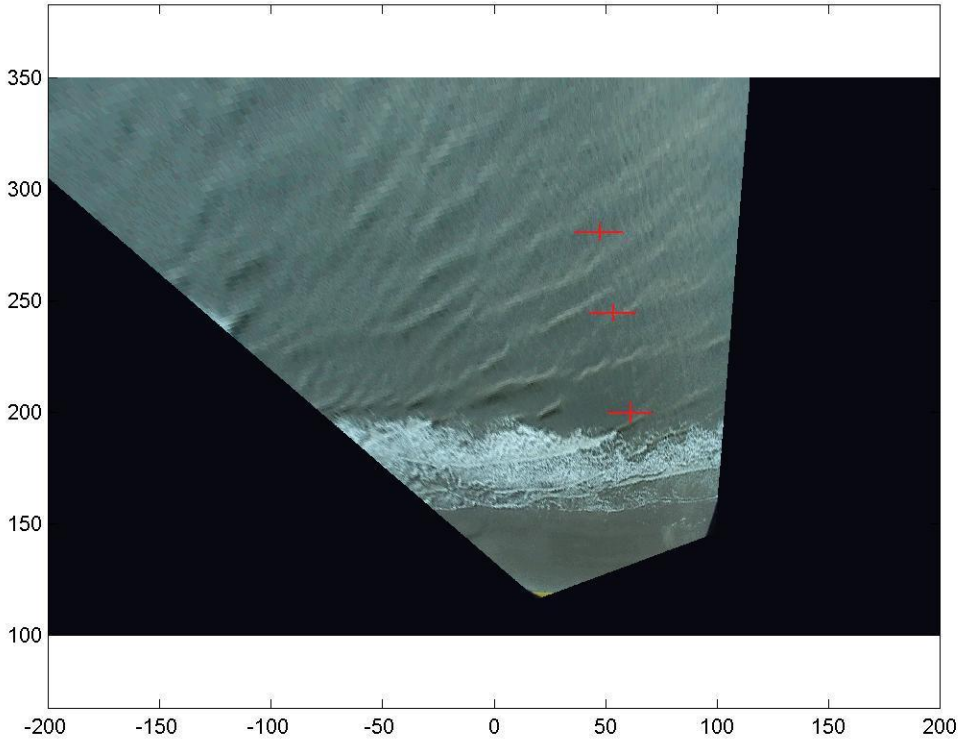

Figure 3.21. Rectified image of the surfzone. The numbers on the axes correspond to local coordinate system. The red crosses show the locations of the inner 3 instruments (December 14 14:58 UTC).

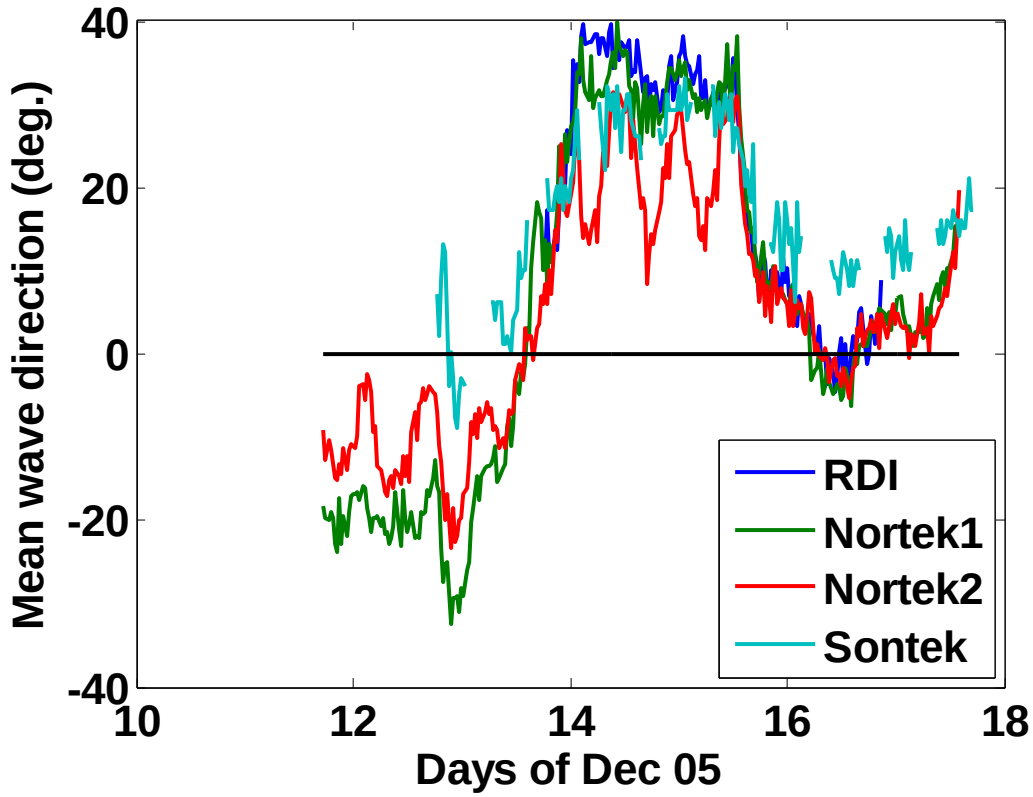

Figure 3.22. Mean wave direction measured at North Myrtle Beach site. Zero shows normal incidence. Positive angles show waves coming from northeast of shore normal. The label shows the instruments from the most offshore (RDI) to the most inshore (Sontek).

Figure 3.23 shows time-averaged cross-shore currents measured at the bottom bin for each instrument. The mean flow is dominated by the undertow and it is offshore directed. The flow is strongest at the inner instruments and decreases to almost zero at the offshore instrument. Longshore currents are given in Figure 3.24. The flow is strongest at Nortek2. The longshore current loses its strength offshore (Nortek1) and inshore (Sontek) of this location. The RDI instrument is sufficiently far offshore that its measured mean velocities are controlled more by tides than waves and its signal is very different than the others.

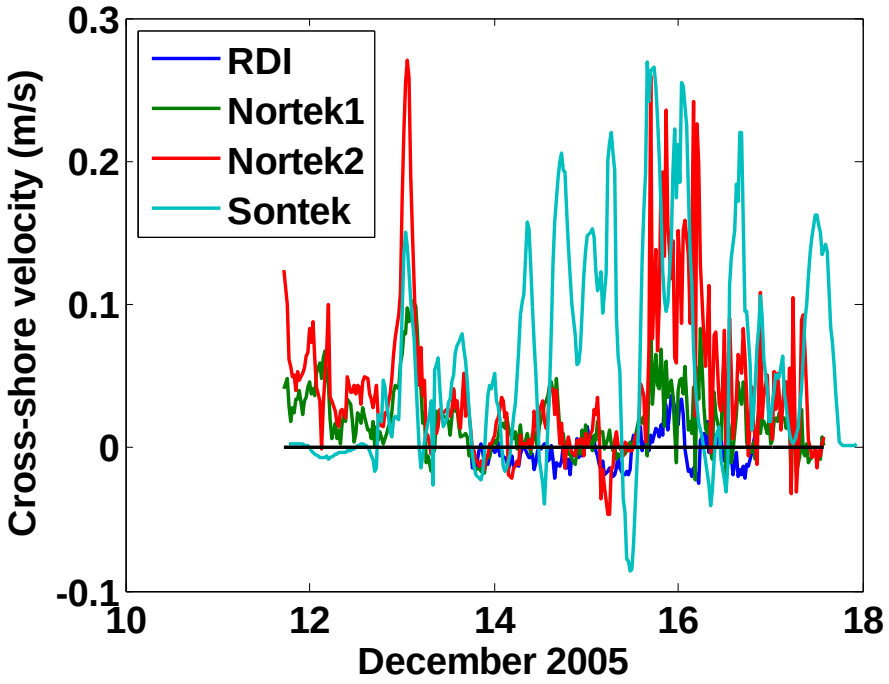

Figure 3.23. Cross-shore velocity measured at the bottom bin of the instruments at North Myrtle Beach site. Positive values show offshore flow. The label shows the instruments from the most offshore (RDI) to the most inshore (Sontek).

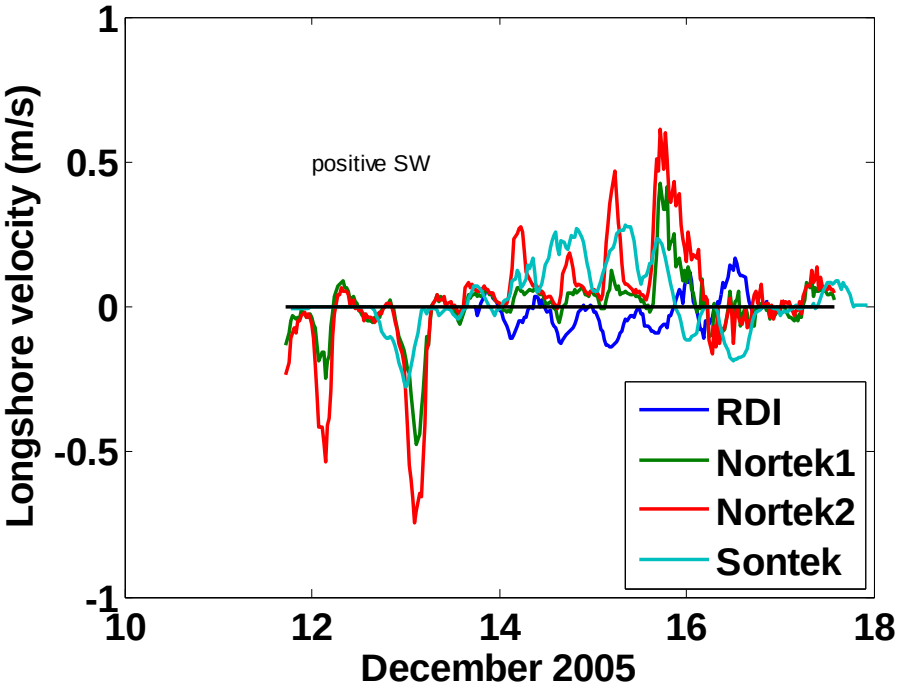

Figure 3.24. Long-shore velocity measured at the bottom bin of the instruments at North Myrtle Beach site. Positive values show flow towards southwest.

Bathymetric and hydrodynamic data were collected and video images of the surf zone were captured during this 8 day field experiment. A lot of variation was observed in this period of time. Wave heights in the range 0.3-1.5 meters, mean wave periods between 4-8 meters were observed. Wave angles spanned a 70 degree range and longshore currents exceeding 0.5 meters in both directions were measured. Bathymetric measurements lead to the creation of a map of an area 800 meters in the longshore direction and 500 meters in the cross-shore direction extending to 8 meters depth. A small longshore bar was observed. There was not much longshore variability of the bathymetry. Significant bathymetric changes were not observed during the measurement period.

4. MORPHODYNAMIC MODELING

Predicting the morphological changes in the nearshore requires much information about the forces and the environment such as waves, currents and the bathymetry. Required information can seldom be directly measured completely so numerical models are employed for predicting the forces as well as the sediment transport and bathymetric changes. Different models are required for different processes such as wave transformation, formation of currents, and sediment transport. The complexity of the system is influenced both by the individual processes and the interactions between them. The spatial and temporal scales of interest and the availability of the resources dictate the amount of complexity of the system of models that will be used. A system of models was set up to predict hydrodynamics and morphological changes along a beach profile up to a depth of 8 m for periods extending to three days. The various numerical models employed and developed for this study are explained in this chapter. The validation of those models will be discussed in the next two chapters.

Waves and currents create the forces that dominate the morphologic change in the nearshore and they need to be predicted within the whole domain of interest. The numerical modeling for this study is done using part of the Nearshore Community Model (NearCom) (Kirby 2006) .This is actually a platform which combines models of nearshore waves, circulation, sediment transport and morphology evolution. This platform was chosen because it provides various options for each model; it is freely available, open source and can be modified as required. A new sediment transport model and a boundary layer model were developed for this study and it was coupled with existing models of wave, circulation and morphology update. Existing models were also modified for correction of bugs and improved performance as necessary.

The master program in NearCom handles data input, output and communication between models. There are various choices for each model. The models chosen from available options and new models developed are introduced below. Figure 4.1 is a flowchart of the data input/output and data exchange between models. There are complex interactions and feedback mechanisms between processes in each model, creating highly nonlinear morphological behavior.

The basic input to the system is the initial bathymetry and wave conditions at the offshore boundary of the computational grid. The wave model used is REF/DIF S (Kirby et al. 2004), which calculates the wave field throughout the domain. This is a spectral, depth-averaged, two dimensional finite-difference model. Wave orbital velocities, wave-induced forcing that drives the currents, and wave energy dissipation which affects currents and sediment suspension are also computed in this model. The model is based on linear mild slope equation with some non-linear corrections. The wind stress is not included.

The circulation model SHORECIRC (Svendsen et al. 2002) is also a finite-difference model. It is unsteady and can model the time variation of currents. Its basic equations are depth-averaged, but it can give vertical variations of the currents. SHORECIRC uses the bathymetry and the wave-averaged forcing from the wave model as input. Turbulence created by breaking waves is also taken into account. Vertical velocity profiles in the longshore and cross-shore directions are the main output of this model. However SHORECIRC does not resolve the velocity field inside the wave boundary layer.

A wave boundary layer model was developed that uses the mean flow and orbital velocities at the top of the wave boundary layer as forcing to compute the velocity field within this layer. The boundary layer equations are solved in a one-dimensional vertical grid using finite differences. Variations in velocity profile and shear stress inside the boundary layer throughout the wave period are calculated by this model.

The newly developed sediment transport model determines the sediment concentration profile over the water column by solving a diffusion equation in a one-dimensional vertical grid, also using finite differences. It is a wave-resolving model; calculating the sediment concentration throughout a wave period. This model uses shear stress, the velocity profile (including terms calculated by the various models) and the wave breaking turbulence as input and it outputs the depth integrated sediment transport rate. The sediment transport model calculates the concentration profile over the water column and its change during a wave period. However the goal is to find the depth and wave-averaged sediment transport rate to calculate the resulting bathymetric changes.

Bathymetry is updated by the morphology model, which solves the mass conservation equation for the sediment. The new bathymetry is used as input for a new cycle of modeling.

The model domain extends from the offshore boundary at approximately 10 meters depth, onto dry land, past the high tide level by a couple of meters in elevation. The same rectangular grid is used for all models (There is also a 1D vertical grid at every node of this rectangular grid used for the sediment transport model). Grid spacing is uniform in the longshore and cross-shore directions, but these grid spacings maybe different from one another. Grid spacings one to five meters were used. These are the general characteristics of the model domain. It was modified according to the requirements of different runs.

To increase the efficiency of the model, not all models are updated at all time steps. The update of the morphology is computationally the least costly, and bathymetry is updated using the same transport rates until a “significant” change occurs in the bathymetry such that waves and circulation are altered. Deciding on the “significant” bathymetry change is a part of the optimization of the numerical model. Of course wave forcing is updated when there is a change in offshore conditions regardless of amount of bathymetric change. The details of each model are explained in the following sections.

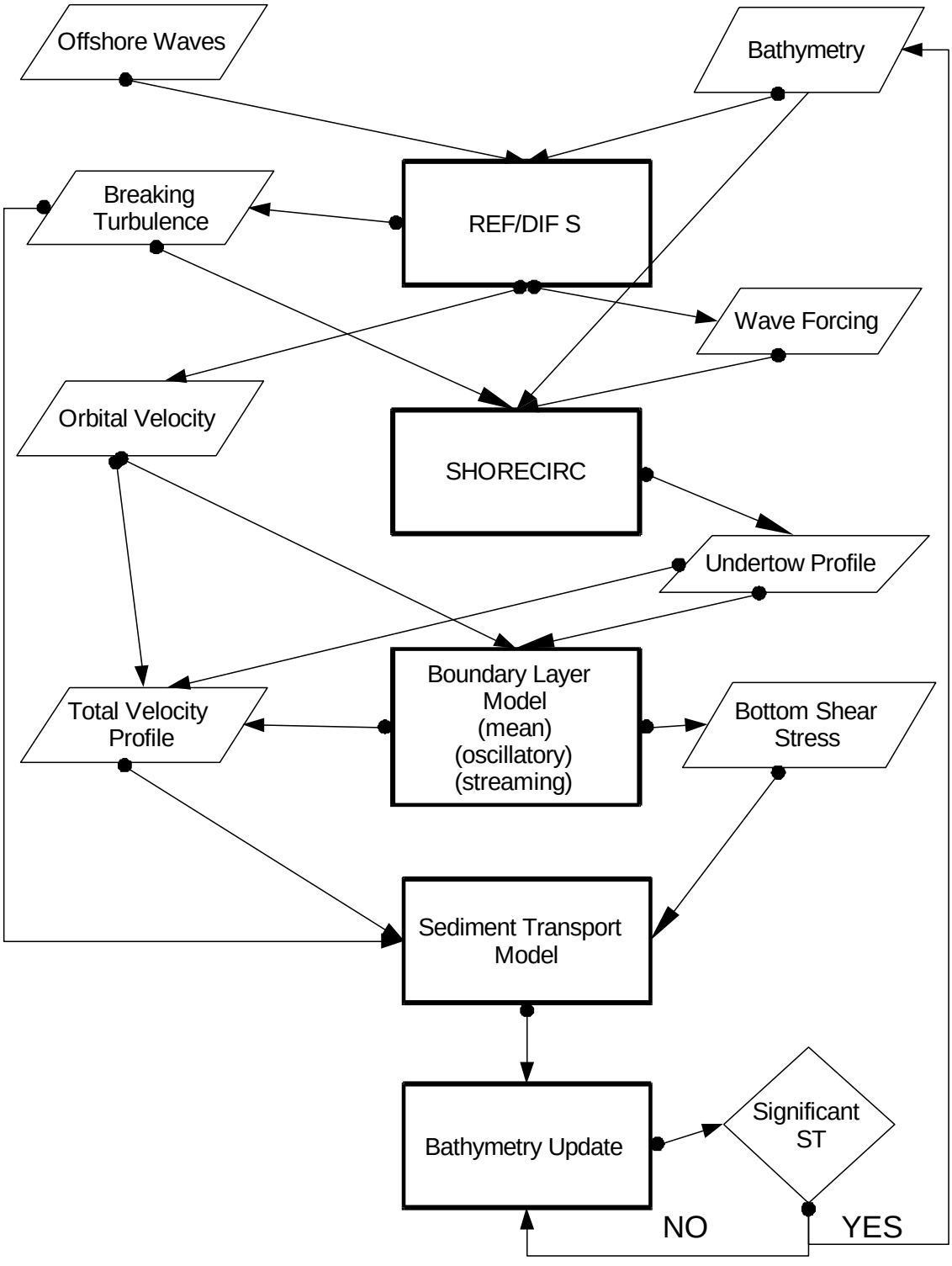

Figure 4.1. Flowchart of the modeling approach used in this study. Dark rectangles show models. Parallelograms show input and output data and diamonds show decisions

4.1. Wave Model Ref/Dif S

REF/DIF S is a weakly nonlinear, combined refraction and diffraction wave transformation model (Kirby and Dalrymple 1983). It is a well-established model that has been tested extensively and used by many researchers and engineers (Kirby 2001). It can simulate shoaling, refraction, diffraction, energy dissipation and depth-induced breaking, by solving the mild slope equation introduced by Berkhoff (1972).

$$\nabla C_p C_g \nabla A + \sigma^2 \frac{C_G}{C_p} A = 0 \qquad \textbf{(4.1)}$$

where *A(x,y)* is the complex wave amplitude, including both amplitude and phase information, ∇ is the horizontal gradient operator, C_p is the wave celerity, C_G is the group velocity and σ is the wave angular velocity. The mild slope equation makes use of linear wave theory, integrated in the vertical direction over the entire water column. Even though the mild slope assumption was invoked, the model was shown to be good up to slopes of 1:3 (V:H). The (weak) nonlinearity of the model comes from the use of a nonlinear dispersion equation, written to permit the inclusion of mean currents. The elliptical mild slope equation is solved with a parabolic approximation. A finite-difference numerical method with an iterative Crank-Nicolson scheme is used. Bottom friction is included for turbulent bottom boundary layers and porous sand. A spectral version of the model, REF/DIF S, was used in this study. This version can simulate random waves by superposing many waves with different frequencies and directions. Since waves in nature are always random, this gives a more realistic result compared to monochromatic waves. For example wave breaking occurs smoothly over a distance in the spectral model, whereas the monochromatic wave breaks abruptly at one point. However interactions between various frequency components are not modeled.

Offshore wave conditions are specified at the seaward boundary of the grid. Transmitting boundary conditions are used at the sides. This model was chosen because it can model wave refraction and diffraction in the surf zone for random waves and it is efficient enough to be applicable at scales of kilometers and can be run for periods spanning days. It does not simulate wave reflection. It was also one of the models that was integrated with SHORECIRC within NearCom.

Onshore volume flux due to waves is an important property of the wave model that controls the mean undertow. The volume flux has two main parts; one due to the wave itself Q_w and one due to the rollers Q_r. The wave volume flux Q_w is represented as

$$Q_w = \frac{gH^2}{c} B_0 \qquad \textbf{(4.2)}$$

where B_0 is the wave shape factor defined as $B_0 = \overline{\left(\frac{\eta}{H}\right)^2}$. The value of B_0 is equal to 0.125 for sinusoidal waves and it is equal to 0.083 for saw-tooth shape waves. These show the two limits of the parameter at the offshore and well within the surfzone respectively. The value of B_0 was taken as 0.083 for this study. Theoretically this would cause an overestimation in wave flux outside the surfzone. However this was not observed as will be shown in Chapter 6.

For the roller contribution Lippmann et al. (1996)'s expression is used

$$Q_r = \frac{B^3 < H_b >^3}{4hT \tan(\sigma_r)} \qquad \textbf{(4.3)}$$

where B is a free parameter also used in the wave breaking model (Thornton and Guza 1983), $<H_b>$ is the breaking wave height integrated over the random wave probability

distribution and is a function of local wave height, σ_r is the wave angle the roller makes with the horizontal. This angle is not easily measured and is used as a free parameter for fitting data to the model.

A simpler expression for the roller contribution is given by Svendsen (2006). It is cited here for easy comparison of the two contributions

$$Q_r = \frac{gH^2}{c} 0.06 \frac{h}{H} \quad \textbf{(4.4)}$$

For breaking waves the ratio of H/h is called the breaking wave coefficient γ. Its value is in the range 0.3 to 0.6 for random waves. Using Equations 4.2 and 4.4 and assuming γ=0.55 and B_0=0.083. The ratio Q_w/Q_r is equal to 0.76. Outside the surfzone there are no rollers, inside the surf zone the volume flux due to rollers exceed the wave contribution.

4.2. Circulation Model SHORECIRC

SHORECIRC is a circulation model that solves for wave-generated currents in the nearshore. The model is based on depth-integrated, short-wave averaged equations. Velocity profiles are solved locally and analytically in terms of depth-integrated quantities, making the model quasi-3D.

The theory behind the model is explained by Svendsen and Putrevu (1994) and Putrevu and Svendsen (1999) . The first version of the model was introduced by Van Dongeren et al. (1994). The current version of the model that is available publicly can be found on the NEARCOM website (Kirby 2006).

The model has been tested in various settings and applications including lab experiments, field experiments, surf beats (Van Dongeren et al. 1995), longshore currents (Haas and Hanes 2004), infra-gravity waves (Van Dongeren et al. 1996), shear waves, rip currents (Haas et al. 2003) and flow around submerged breakwaters (Drei et al. 2000) . It

has been applied to both simple and complex geometries (Drei et al. 2000) .The model has been applied in laboratory scales and field scales up to hundreds of meters successfully. The model was also used as a driver in longshore (Haas and Hanes 2004) and cross shore (Qin and Svendsen 2003) sediment transport models. Applications of the model have been generally limited to hours to days, but this is not a theoretical limitation and can be extended as required, limited primarily by computing resources. The model was developed for the nearshore region extending roughly to 10 meters depth. This is not an important limitation for the purposes of this study since most of the significant sediment transport of interest takes place landward of this boundary.

4.2.1. Governing Equations

The conservation of mass and the momentum equations within SHORECIRC are set up in terms of volume fluxes and velocities. The instantaneous total velocity, $u_{T\alpha}$ is divided into three parts: turbulent $u_{\alpha}^{'}$, wave, u_{α}, and mean current V_{α}

$$u_{T\alpha} = u_{\alpha}^{'} + u_{\alpha} + V_{\alpha} \tag{4.5}$$

The mean current component is further divided into depth-uniform $V_{m\alpha}$, and depth-varying $V_{d\alpha}$ components:

$$V_{\alpha} = V_{m\alpha} + V_{d\alpha} \tag{4.6}$$

Total volume flux Q_{α} is defined as:

$$Q_{\alpha} = \overline{\int_{-h_o}^{\zeta} u_{T\alpha} dz} \tag{4.7}$$

where h_o is the still water depth and ζ is the water surface elevation above h_o. The local water depth h is defined as $h=h_o+\overline{\zeta}$, the overbar denoting time averaging.

`

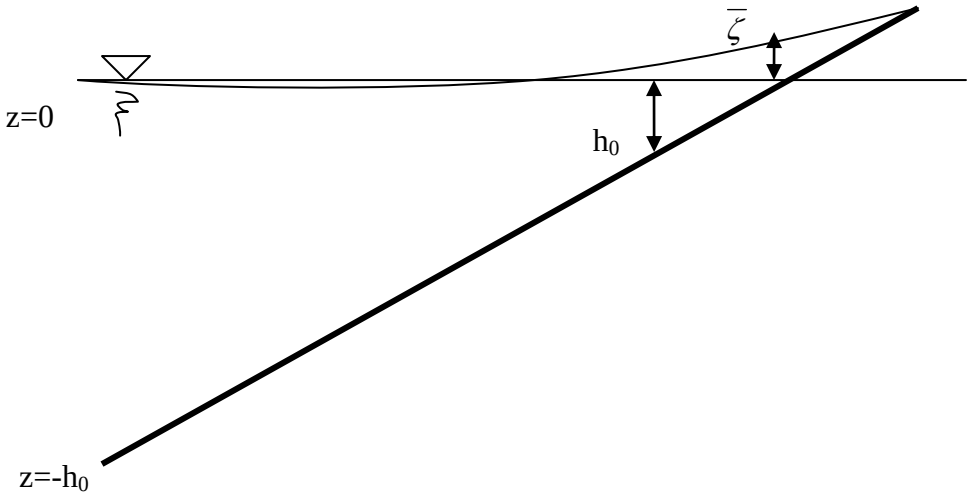

Figure 4.2. Sketch showing still water level h_0 and wave set-up.

Using these definitions, the depth-integrated, time-averaged momentum and mass conservation equations, in tensor notation, become

$$\frac{\partial Q_\beta}{\partial t}+\frac{\partial}{\partial x_\alpha}\left(\frac{Q_\alpha Q_\beta}{h}\right)+\frac{\partial}{\partial x_\alpha}\int_{-h_o}^{\overline{\zeta}} V_{d\alpha}V_{d\beta}dz+\frac{\partial}{\partial x_\alpha}\overline{\int_{\zeta_t}^{\zeta}\left(u_\alpha V_{d\beta}+u_\beta V_{d\alpha}\right)dz}+$$
$$g\left(h_0+\overline{\zeta}\right)\frac{\partial\overline{\zeta}}{\partial x_\beta}-\frac{\tau_\beta^S}{\rho}+\frac{\tau_\beta^B}{\rho}+\frac{1}{\rho}\frac{\partial}{\partial x_\alpha}\left(S_{\alpha\beta}-\overline{\int_{-h_o}^{\zeta}\tau_{\alpha\beta}dz}\right)=0 \qquad \textbf{(4.8)}$$

$$\frac{\partial\overline{\zeta}}{\partial t}+\frac{\partial Q_\alpha}{\partial x_\alpha}=0 \qquad \textbf{(4.9)}$$

Radiation stress $S_{\alpha\beta}$ is defined as

$$S_{\alpha\beta} = \overline{\int_{-h_o}^{\zeta} \left(p\delta_{\alpha\beta} + \rho u_\alpha u_\beta\right) dz} - \delta_{\alpha\beta}\frac{1}{2}\rho g h^2 - \rho\frac{Q_{w\alpha}Q_{w\beta}}{h} \quad \textbf{(4.10)}$$

The bottom boundary layer is represented by a shear stress in the model. Bottom shear stress is calculated as the time average of instantaneous shear stress, which is given by

$$\tau_\alpha^B(t) = \frac{1}{2}\rho f_{cw}(u_{0,\alpha}(t) + V_{b,\alpha})\left|u_{0,\alpha}(t) + V_{b,\alpha}\right| \quad \textbf{(4.11)}$$

where $u_{0,\alpha}(t)$ is the orbital velocity above the wave boundary layer, $V_{b,\alpha}$ is mean current above the wave boundary layer, f_{cw} is the bottom friction factor.

The wind shear stress τ_α^S is given by a similar quadratic law:

$$\tau_\alpha^S = C_D\rho_a|W|W_\alpha \quad \textbf{(4.12)}$$

where C_D is the drag coefficient ρ_a is the air density and W_α is the wind velocity at the 10 meter elevation.

Steady streaming is included by adding an additional streaming shear, τ_{str} based on an approximation by Longuet-Higgins (1956).

$$\tau_{str} = \rho f_{cw}\frac{H}{h}(\max(u_{0,\alpha}))^2 \quad \textbf{(4.13)}$$

where H is the wave height and h is the water depth. The magnitude of the wave orbital velocity at the seafloor is shown as $\max(u_{0,\alpha})$ in the above equation. Since steady streaming is included in the current calculated by SHORECIRC which is input into the

boundary layer model, when SHORECIRC is used to calculate mean currents steady streaming is turned off in the boundary layer model.

4.2.2. Boundary Conditions

The offshore boundary is an absorbing-generating boundary where long waves and currents can be generated and are allowed to leave without reflection. Along the two lateral boundaries, which extend in the cross-shore direction, water fluxes can be specified. Knowledge of these fluxes requires either many measurements along the lateral boundaries or the results from another model with a larger domain. Another option is the periodic boundary condition where the flow at each point at one lateral boundary matches conditions at the corresponding point at the other boundary. This is applicable in conditions where the cross-shore profile may be assumed the same at the two lateral boundaries.

Both the longshore and cross-shore fluxes of water are zero at the shore boundary. The position of the shoreline changes as the bathymetry changes and it can move either onshore or offshore.

4.2.3. Numerical Scheme

The system of equations, describing conservation of mass, and x- and y-momentum equations, are solved with a predictor-corrector, central finite-difference scheme. The method is based on that of Wei and Kirby (1995). The predictor step is a third-order, explicit, Adams-Bashforth scheme, and the corrector step is a third-order, Adams-Moulton time-stepping scheme. The scheme is fourth-order accurate in space except for the dispersion terms, which are second-order accurate. The grid sizes can vary by direction, but they are constant in space. Various high-order filters with minimal artificial dissipation are also used to remove high-order numerical oscillations.

4.3. Wave Orbital Velocity

As the waves approach the shore they begin to "feel" the bottom and become more and more nonlinear. The crests of the waves become narrow and higher while the trough becomes wider and shallower. The wave orbital velocity under the waves also follows the same pattern (Figure 4.3). Predicting the shape of the orbital velocity is important for sediment transport calculation since sediment transport rate is non-linearly related to the velocity. A skewed wave creates a net sediment transport even in the absence of a mean current.

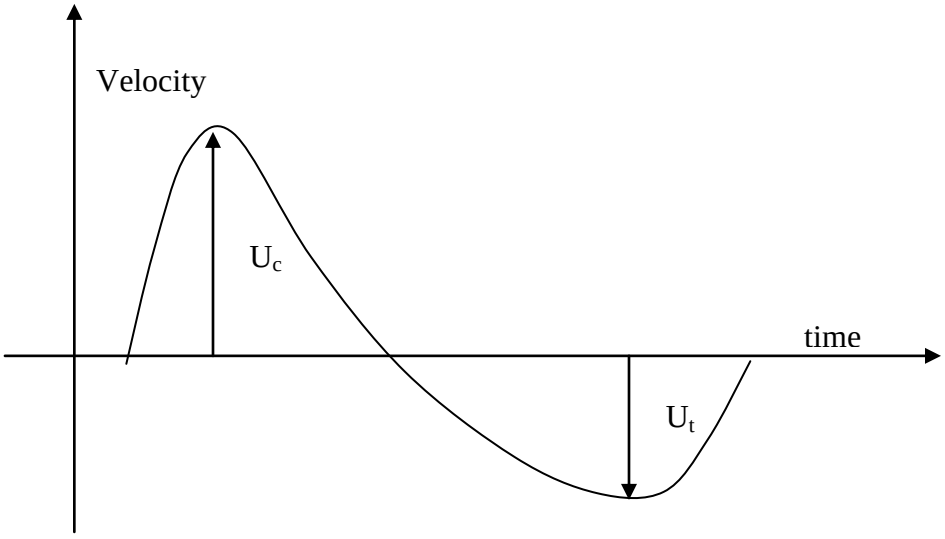

Figure 4.3. Skewed wave orbital velocities showing velocity magnitude under the crest (U_c) and under the trough (U_t).

Wave orbital velocity skewness may be defined quantitatively in several ways. One common way is to define velocity skewness S as:

$$S = \frac{U_c}{U_c + U_t} \tag{4.14}$$

where U_c is the bottom wave velocity under the crest and U_t is the velocity under the trough. However this is more appropriate for monochromatic waves where there are

clearly defined crest and trough velocities. A definition of skewness that is more appropriate for velocity under random waves is used here.

$$S = \frac{\overline{U^3}}{\left(U_{rms}\right)^3} \tag{4.15}$$

Using this definition the skewness of a linear wave is 0. Since REF/DIF does not solve for skewed nonlinear wave orbital velocities that occur in the nearshore, orbital wave velocities should be predicted using a different method. There are various methods for predicting a skewed orbital velocity at the bottom. Once this velocity is known its variation over the water column, which is generally small in the nearshore, can be estimated using linear wave theory.

Isobe and Horikawa (1982) predicted water particle velocities in the surf zone using fifth-order Stokes and third-order cnoidal wave theories in their applicable ranges. Approximate functions for skewness were derived from these theoretical solutions and modified to match measurements. The suggested model could predict wave amplitudes and wave asymmetry satisfactorily outside the surf zone, but its performance decreased with wave breaking.

Using three different data sets from the Netherlands and USA, Doering et al. (2000) parameterized wave orbital velocity skewness with genetic programming. Using Isobe and Horikawa's (1982) velocity profiles with their own skewness values, they modeled onshore sediment transport in cases where it could not be predicted with symmetric linear waves.

A more recent empirical model for predicting orbital velocities in the surf zone was proposed by Elfrink et al. (2006). The same data set used by Doering et al. (2000) was used to develop the model. The methodology predicts a near-bed orbital velocity for

individual waves using bottom slope, water depth, wave height, and wave period as calculated from zero-crossing analysis.

The method of Elfrink et al. (2006) was chosen in this study to predict orbital velocities since it was developed using a large data set using waves both inside and outside the surfzone. This model predicts a time series of bottom orbital velocity given wave height, wave period, water depth and bottom slope. However this formulation is based on measurements of individual waves. Application of this method requires a time series of wave data describing individual waves, which is not always available, especially for forecasting, and is computationally demanding. A formula in terms of burst-averaged properties is desirable.

Figure 4.4 gives a flowchart of methods for calculating and predicting skewness and U_{rms} from the measured water surface profile. The most straightforward way is to calculate skewness and U_{rms} from measured velocity time series. In the time series method, first individual wave parameters (wave height H, and period T) are calculated using the zero up-crossing method. The Elfrink method is applied to each individual wave giving a bottom velocity shape for each wave. The Elfrink method was developed for individual waves so this is the ideal way to apply the method, but it is not practically useful. These predicted velocities are added to create a velocity time series which can be used to calculate skewness. In the third method, burst-averaged properties are calculated (e.g. significant wave height H_s, mean period T_m) from the surface profile. Wave height computed from the wave spectra (H_{mo}) is used instead of the significant wave height (H_s). These average properties are then used to predict a velocity shape. This last method is desirable as explained above so its results were compared with the second method to decide on the burst averaged properties that give the best results. Comparison to skewness calculated directly (method one) is done later to investigate the performance of the model.

The burst-averaged properties investigated for method three were: significant wave height (H_s), root-mean-square (rms) wave height (H_{rms}), mean wave period (T_m), and peak wave period (T_p). All good data from all the instruments from the 2003 Myrtle Beach experiments were used for the figures and tables given here unless labeled differently. Skewness calculated by methods two and three is shown Figure 4.5 and the rms differences between the two methods are given in Table 4.1. The first data column gives the percentage difference in rms skewness the second column gives the percentage difference in rms velocities. Third and fourth columns are the biases for the same parameters. For example the percentage rms skewness difference for the H_s-T_m pair is calculated as $100*\text{rms}(sk_{HrmsTm}-sk_{timeseries})/\text{rms}(sk_{timeseries})$ and bias is calculated as $100*\text{mean}(sk_{HrmsTm}-sk_{timeseries})/\text{mean}(sk_{timeseries})$.

Velocities are compared in Figure 4.6. Using the H_{rms}-T_m pair for predictions leads to the closest match to the measured time series both in terms of skewness and velocity and was chosen for subsequent use. Velocities computed using H_s are significant velocities and are divided by $\sqrt{2}$ to convert to rms velocities assuming a Gaussian water level distribution.

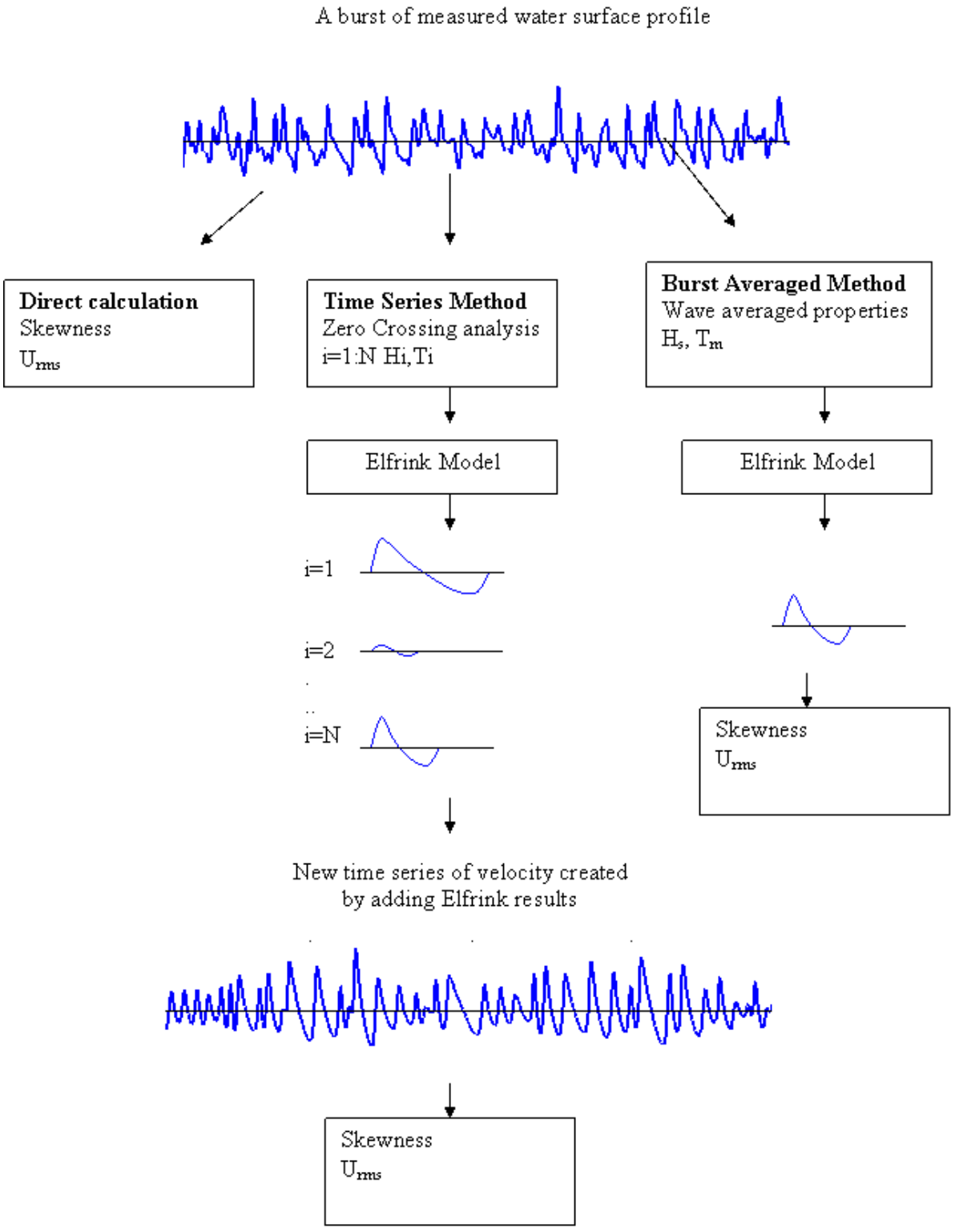

Figure 4.4. Methods of creating velocity time series and calculating skewness from measured surface profile. First method (left) calculates skewness directly from measured time series. Second method (center) recreates the time series using Elfrink method and calculates the skewness. The third method creates a representative wave using statistical wave parameters and calculates the skewness.

Table 4.1. Root mean square difference and bias in velocity skewness and u_{rms} calculated by using time series vs. using burst-averaged properties. Percentages are calculated by comparing to the time series values.

	% rms difference		% Bias	
Wave properties	Skewness	U	Skewness	U
H_{rms}-T_m	20.2	5.6	-9.6	-1.0
H_{rms}_T_p	40.3	20.2	-35.8	15.3
H_s_T_m	23.9	7.7	14.6	6.3
H_s-T_p	26.1	20.0	-15.2	15.1

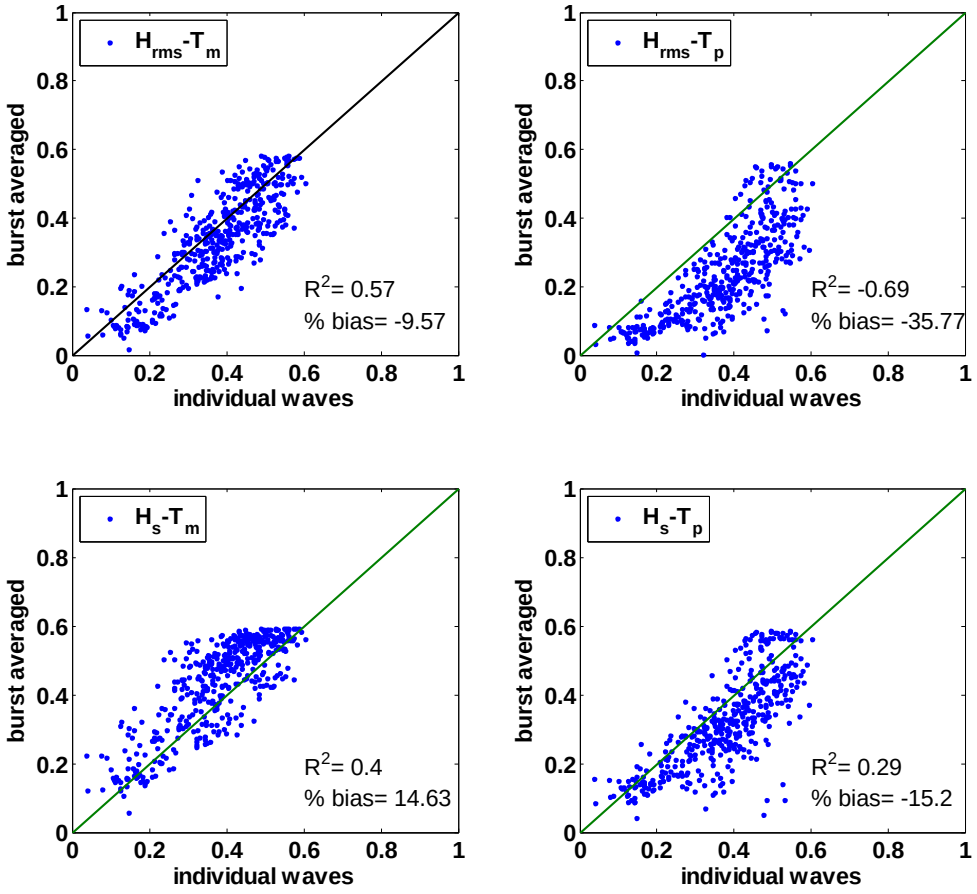

Figure 4.5. Skewness calculated by using time series of individual waves(x –axis) compared to skewness calculated using burst averaged properties (y-axis). Four plots show four different pairs of wave averaged properties.

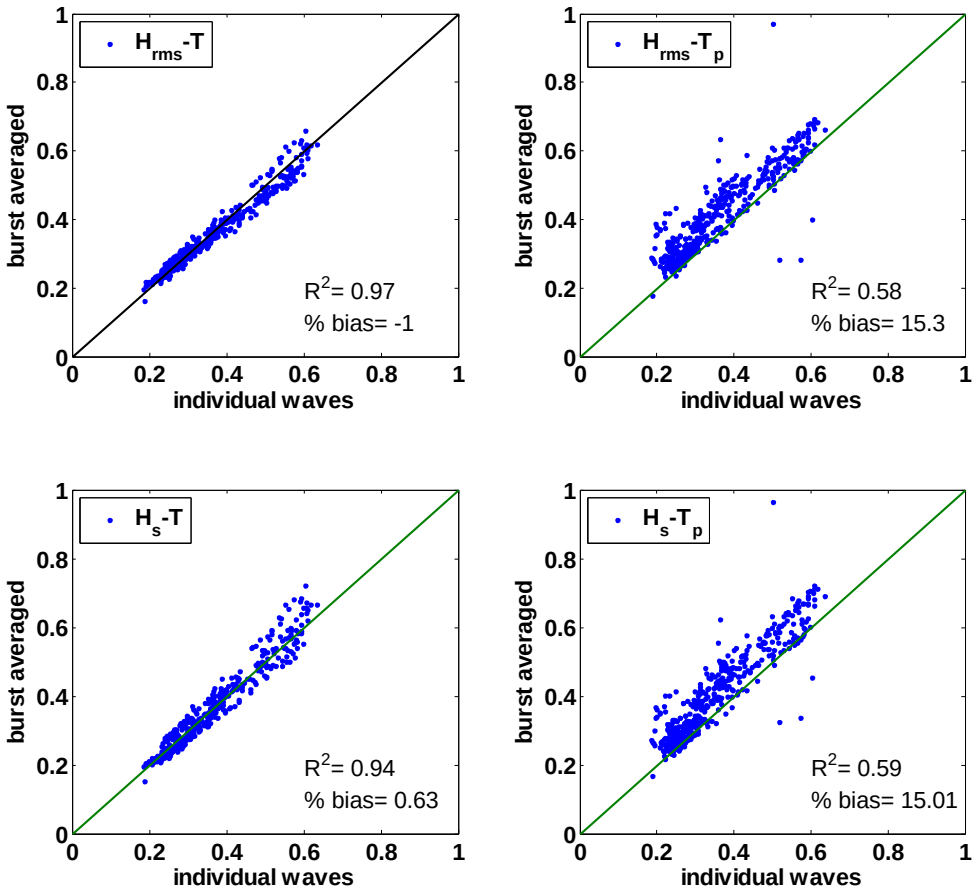

Figure 4.6. Velocity calculated by using time series of individual waves(x –axis) compared to velocities calculated using burst averaged properties (y-axis). Four plots show four different pairs of wave averaged properties.

Skewness and rms velocities calculated with both methods were compared with values derived from velocity measurements. The skewness calculated from the measured time series will be referred to as "measured skewness" even though it was not directly measured. A band-pass filter from 0.05-0.5 Hz was applied to measured velocities to make sure that data in the same frequency range from all instruments was used and only surface wave components were included (i.e. tidal and wind currents were filtered out). The top panel of Figure 4.7 compares skewness measured at the offshore Aquadopp (AQDC) with the Elfrink model. The model can capture the general trend of skewness successfully. There are a lot of fluctuations in the measurements that do not appear in the

model. This is due to measurement noise and physics not included in the model as arising from the presence of 3-D bathymetry and time history effects. The model does not take into account properties of the waves at previous time steps so the history of the flow is ignored. The measured skewness at ADV2 (Figure 4.7, middle panel) is the highest of all instruments. The model under-predicts these values. The skewness at the inshore instrument (bottom panel) is over-predicted when the measured values are low. The Elfrink model has a limited range and its performance decreases for very high and very low skewness. When the skewness is very high the waves are breaking or very close to breaking. The high level of turbulence might be introducing errors to measurements and/or the model performance decreases in this region. In the measurements the low skewness values are observed for small wave heights. The signal-to-noise ratio is low for these cases and this may be contributing to the errors. Applying the model on a wave-by-wave basis improves the overall fit only slightly.

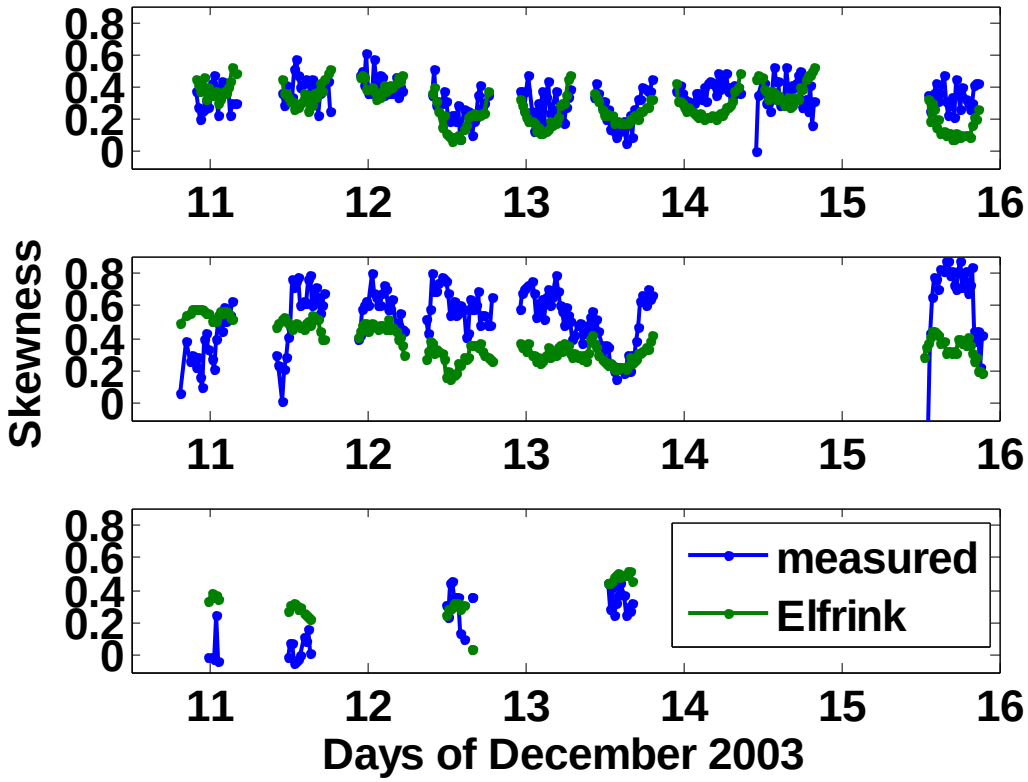

Figure 4.7. Elfrink skewness compared with measured skewness. Each panel shows one instrument. Top : AQDC (offshore), middleADV2, bottom ADV1 (inshore).

Figure 4.8 shows the measured wave orbital velocities compared with the Elfrink model results and linear wave theory. The fit is generally good except around day 14 and 15 for the offshore instrument (top panel). In this region the Elfrink predictions are lower than both the linear model and the measurements. The linear model generally performs better than the Elfrink model in velocity magnitude predictions.

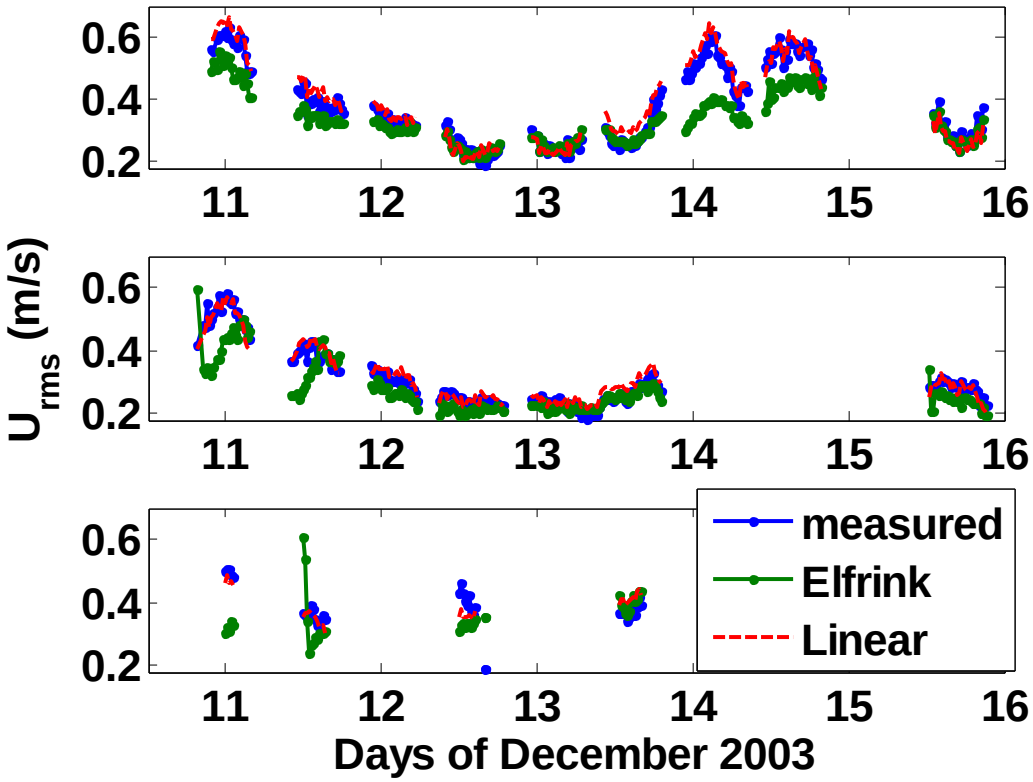

Figure 4.8. Measured wave bottom orbital velocities compared with Elfrink model and linear wave theory. Top : AQDC (offshore), middleADV2, bottom ADV1 (inshore).

Elfrink model utilizing burst averaged properties H_{rms} and T_m is used to predict skewed wave orbital velocities. It can predict the variation of skewness across the beach profile inside and outside the surfzone, but cannot predict high skewness values exceeding 0.6 measured in the field.

4.4. Boundary Layer Model

Potential wave theory breaks down near the seafloor, as the proximity to the bed begins affecting the flow. A wave boundary layer forms where viscous effects become important. This layer is important in terms of sediment transport, because sediment is made available for transport here and most of the sediment transport also takes place in this layer. The flow in this layer is solved in detail using a new and separate boundary layer model since SHORECIRC does not resolve the mean flow in this layer, nor does the

potential theory give any information on the oscillatory flow here. Figure 4.9 shows the velocity profile under waves, in the cross-shore direction. The velocities inside the wave boundary layer (below the dashed line) are solved by the boundary layer model. Velocities above this level are found from SHORECIRC, linear wave theory and the Elfrink method as explained above.

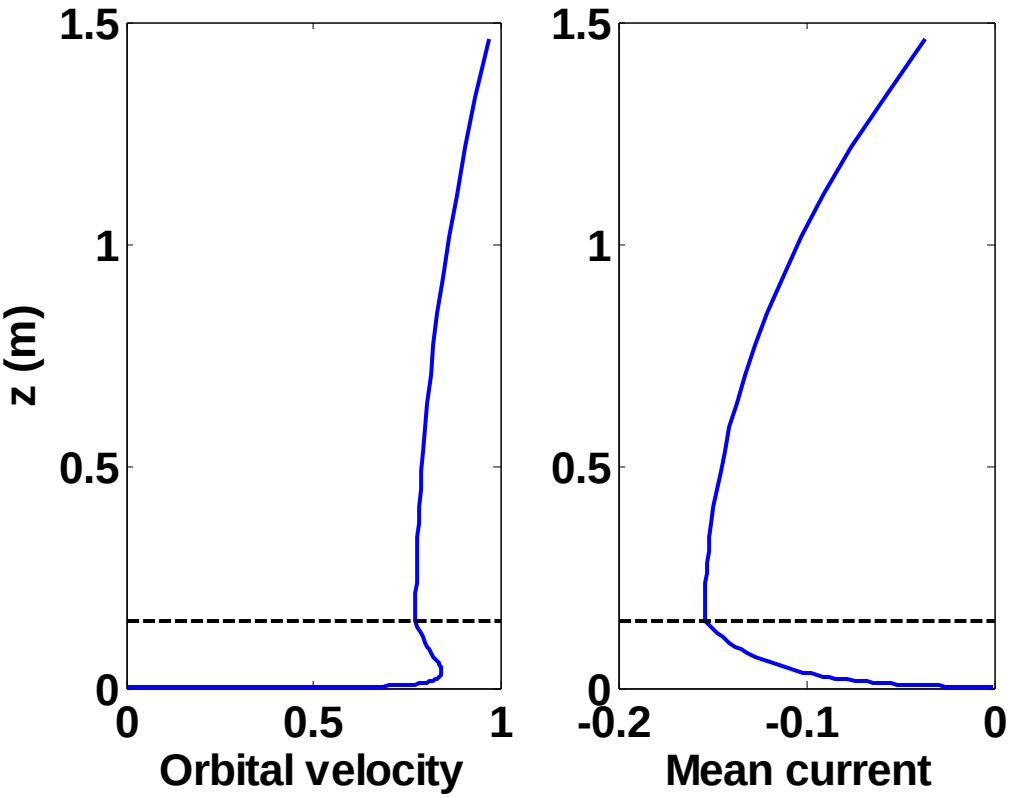

Figure 4.9. Sketch of the cross-shore velocity profile under waves. The dashed line shows the top of the wave boundary layer. The left panel shows the magnitude of the orbital velocity in (m/s), the right panel shows the mean current in (m/s). *H*=0.6 m *T*=6 seconds, around wave breaking.

In the presence of mean currents a current boundary layer also develops which is much thicker than the wave boundary layer and can in some cases extend up to the water surface. The currents above the wave boundary layer are solved by SHORECIRC. The effects of currents on the wave boundary layer are represented as a modification to the eddy viscosity. The mean currents inside the wave boundary layer are solved separately as explained later. In addition to the mean and oscillatory flows there is also steady

streaming created by the waves, which is another component of the velocity inside the boundary layer (Figure 4.10). It is in the wave propagation direction. This component is created by the interactions between horizontal and vertical velocities inside the wave boundary layer and discussed in section 4.4.2. Streaming velocity is zero at the bed and quickly increases to its maximum value. This maximum value is small compared to the oscillatory flow in magnitude (typically less than 10% in turbulent boundary layers, 9% in the figure), but may affect sediment transport rate significantly since it creates a shoreward mean flow very close to the bottom. Steady streaming is solved as a part of the mean flow inside the wave boundary layer. Table 4.2 summarizes the methods used to solve for the velocity over the water column.

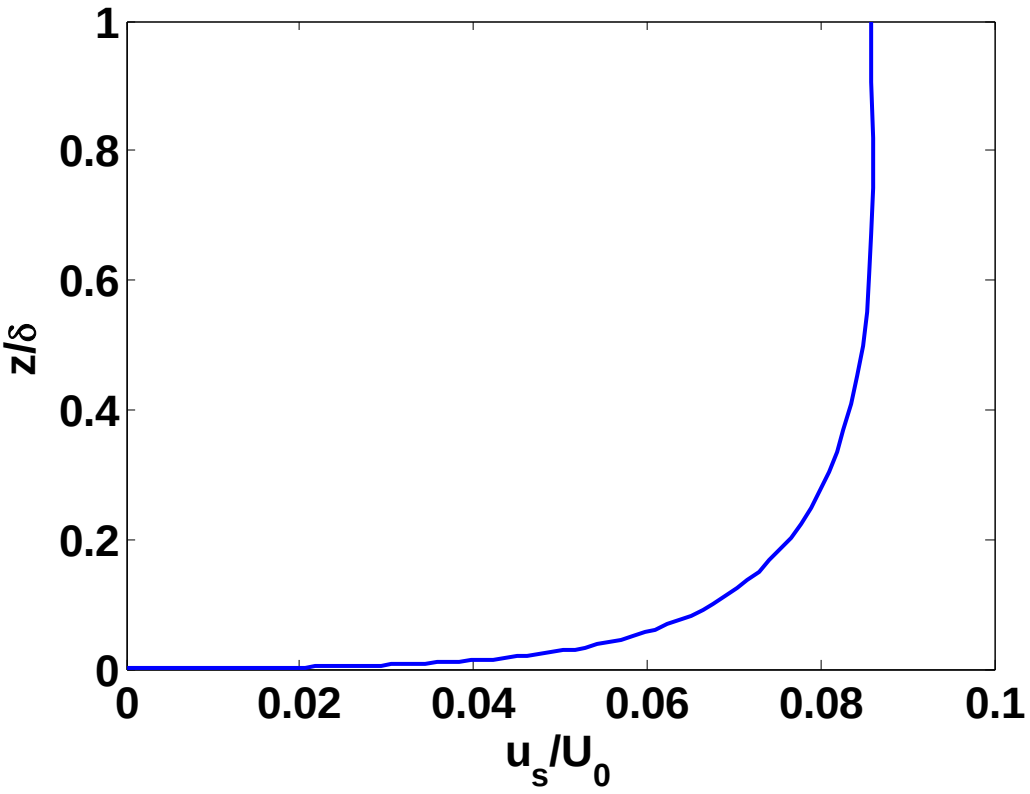

Figure 4.10. Streaming velocity u_s in the wave propagation direction normalized by the wave orbital velocity magnitude U_0 just outside the wave boundary layer. The y-axis shows the elevation normalized by the boundary layer thickness δ.

Table 4.2. Solution methods for velocity components in different portions of the water column. Numbers in parentheses indicate the section of this thesis where each is explained.

Location/ Type of Flow	Mean flow	Oscillatory flow
Outside wave boundary layer	SHORECIRC (4.2)	Skewed orbital velocity formulation (4.3)
Inside wave boundary layer	Logarithmic profile (4.4.4)	Boundary Layer Equations (4.4.1)

The Navier-Stokes equation with the boundary layer approximations are solved within the wave boundary layer. The thickness of the wave boundary layer δ is not a very well-defined quantity. Grant and Madsen 's (1979) expression that relates the boundary layer thickness to the shear velocity U_*, defined as $U_* = \sqrt{\frac{\tau}{\rho}}$, where τ is shear stress on the bed, is used.

$$U_{*wcm} = \max\left(\sqrt{\frac{\frac{1}{2}\rho f_w U_T(t)\left|U_T(t)\right|}{\rho}} \right) \tag{4.16}$$

$$\delta = n_{BL}\frac{\kappa U_{*wcm}}{\omega} \tag{4.17}$$

where U_{*wcm} is the maximum shear velocity corresponding to the maximum shear stress under a wave, $U_T(t)$ is the magnitude of the combined wave-current velocity just outside the wave boundary layer, f_w is the wave friction factor, ω is the wave angular velocity, κ is von Karman's constant taken as 0.4, n_{BL} is an empirical constant suggested to be between 1 and 2. It was chosen as 2 in this study.

4.4.1. Governing Equations for the Boundary Layer

The equations to be solved to describe the flow within the boundary layer consist of the horizontal momentum equation and the continuity equation. These equations, stated in the two dimensions collinear with the wave propagation direction are

$$\frac{\partial u}{\partial t} = u\frac{\partial u}{\partial x} + w\frac{\partial u}{\partial z} = -\frac{1}{\rho}\frac{\partial P}{\partial x} + \nu\frac{\partial^2 u}{\partial z^2} \quad \textbf{(4.18)}$$

$$\frac{\partial u}{\partial x} + \frac{\partial w}{\partial z} = 0 \quad \textbf{(4.19)}$$

where u and w are orbital wave boundary layer velocities in the wave direction x and vertical direction z respectively, P is the pressure and ν is the eddy viscosity. The mean part of the flow is solved for separately as explained later. Assuming that vertical variations and viscous effects are negligible the momentum equation just outside the boundary layer can be written as

$$\frac{\partial U}{\partial t} + U\frac{\partial U}{\partial x} = -\frac{1}{\rho}\frac{\partial P}{\partial x} \quad \textbf{(4.20)}$$

where U is the wave orbital velocity just outside the boundary layer. In keeping with the assumption that the vertical variation of horizontal pressure gradient inside the boundary layer is small, Equation 4.20 can be substituted into Equation 4.18, giving the momentum equation for the boundary layer

$$\frac{\partial u}{\partial t} + u\frac{\partial u}{\partial x} + w\frac{\partial u}{\partial z} = \frac{\partial U}{\partial t} + U\frac{\partial U}{\partial x} + \nu\frac{\partial^2 u}{\partial z^2} \quad \textbf{(4.21)}$$

A zero shear stress condition is applied at the top of the boundary layer. The no-slip bottom boundary conditions are also applied: $u=0$, $w=0$ at $z=k_N/30$, where k_N is the Nikuradse roughness. This theoretical bed level was found by the now-classical work of Nikuradse. He fit a logarithmic curve to the velocity and the location where the velocity is zero on this curve is defined as the theoretical bed level (Figure 4.11).

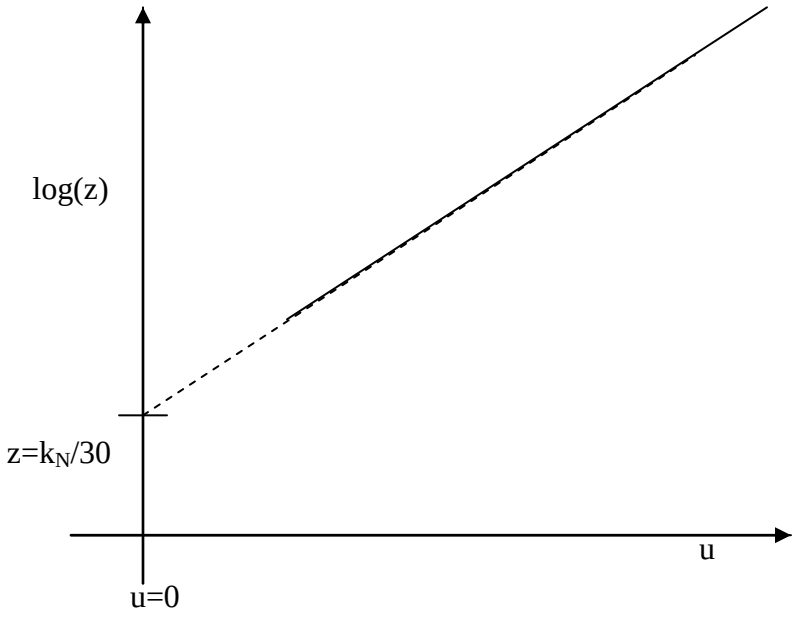

Figure 4.11. Logarithmic velocity profile showing the theoretical bed level at $z=k_N/30$.

Away from the bottom, the horizontal velocity u approaches U. The first-order approximation to this equation can be stated as:

$$\frac{\partial u}{\partial t} - \nu \frac{\partial^2 u}{\partial z^2} = \frac{\partial U}{\partial t} \qquad \textbf{(4.22)}$$

By dropping the convective terms from Equation 4.21, second-order effects are ignored. However the most important second-order contribution, steady streaming, is added explicitly as explained in the next section. Steady streaming is significant because it creates a mean flow, whereas other effects slightly modify the oscillatory flow without much effect on sediment transport. Equation 4.22 can be solved analytically for the

laminar flow case, where viscosity v is a constant or varies linearly with z. However a numerical solution is needed for the turbulent case, when v is a function of z except for some special cases. Equations 4.19 and 4.22 were solved numerically to find the velocities inside the wave boundary layer.

4.4.2. Steady Streaming

Steady streaming is a net flow velocity inside the wave boundary layer in the wave propagation direction. This phenomenon was first described by Longuet-Higgins (1956) and is also called the boundary layer drift (Nielsen 1992) or induced streaming (Fredsoe and Deigaard 1992). The interaction between horizontal and vertical velocities that create a non-zero time-averaged horizontal forcing is responsible for steady streaming. In an inviscid case these velocities are 90^o out of phase and have no net effect. This is a second-order contribution and is not captured by Equation 4.22. The streaming velocity u_s can be calculated separately by the use of Equation 1.19:

$$u_s = \frac{1}{\nu_t}\int_0^{\delta}((\overline{wu}) - \overline{(wu)}_{\delta})dz \qquad \textbf{(4.23)}$$

where δ refers to the top of the boundary layer. Horizontal velocity u is calculated using Equation 4.22. The continuity equation, (4.19), is used to calculate w, once u is known. The magnitude of streaming velocity is generally less than 10% of the orbital velocity magnitude in turbulent boundary layers.

4.4.3. Eddy Viscosity

A parabolic eddy viscosity profile that is not coupled with the boundary layer solution was chosen for use in this study, because of its simplicity and efficiency. Speed of computation differs significantly since a k-ω model can be 40 times slower than a

time-invariant model (Puleo et al. 2004). SHORECIRC uses a constant eddy viscosity for calculating the flow outside the boundary layer and its results are used to drive the boundary layer solution. Using a computationally expensive turbulent closure in the boundary layer solution when its input comes from a constant eddy viscosity model would not be an efficient way to improve model physics. The parabolic eddy viscosity used for turbulence closure may decrease the accuracy of the time variation and profile shapes for velocity and sediment concentration. The effects on sediment transport rate, which is the primary quantity of interest for this study, would be less since it is an integrated quantity and model tuning is done for sediment transport rate. Even if the sediment concentration high above the water column is not captured correctly, the effect of this on the sediment transport rate would be negligible since concentration decays very quickly with distance from the bed. This approximation makes it possible to apply this model to the temporal and spatial ranges desired.

The parabolic eddy viscosity formulation has been modified by Fredsoe et al. (1985) to have a continuous profile at the edge of the boundary layer. A slightly modified form of this formula (Qin and Svendsen 2003) was used in this study.

$$\nu_t = \kappa U_{*wcm} z\left(1 - m\frac{z}{\delta}\right)$$
$$\mathrm{m} = 1 - \frac{\mathrm{U}_{*\mathrm{c}}}{\mathrm{U}_{*\mathrm{wcm}}}\left(1 - \frac{\delta}{h}\right) \qquad \textbf{(4.24)}$$

where υ_t is the turbulent eddy viscosity, m is the correction included since the original work (Fredsoe et al. 1985) did not give an exact match. The maximum combined shear velocity U_{*wcm}, and current shear velocity U_{*c} are defined as

$$U_{*c} = \sqrt{\frac{\overline{|\tau_\alpha^B(t)|}}{\rho}}$$
$$U_{*wcm} = \max\left(\sqrt{\frac{\tau_\alpha^B(t)}{\rho}}\right) \quad \textbf{(4.25)}$$

The definition of shear stress is given by Equation 4.11. As discussed above, velocity is not very sensitive to time variance of the eddy viscosity, but concentration is more sensitive. To investigate the possible effects of time variation, a time-varying eddy viscosity $\nu_t'(t)$ was created by introducing a simple variation function *tv*

$$\nu_t'(z,t) = tv(z,t)\nu_t(z)$$
$$tv(z,t) = 1 + \left(\frac{\delta - z}{\delta}\right)\left(\frac{1 + \frac{|U(t)|}{\max(U)}}{\left(1 + \frac{|U(t)|}{\max(U)}\right)}\right) \quad \textbf{(4.26)}$$

The time average of the eddy viscosity does not change and the time variation is proportional to the change in free stream velocity *U*. By introducing the constant 1.0, the time dependence is damped and the unrealistic case of zero eddy viscosity such as found in the mixing length models is not encountered. Time variation of eddy viscosity is smoother as observed in measurements and predicted by higher order models. The time variation is maximum at the bottom, and at the top of the wave boundary layer the eddy viscosity is time invariant (Figure 4.12).

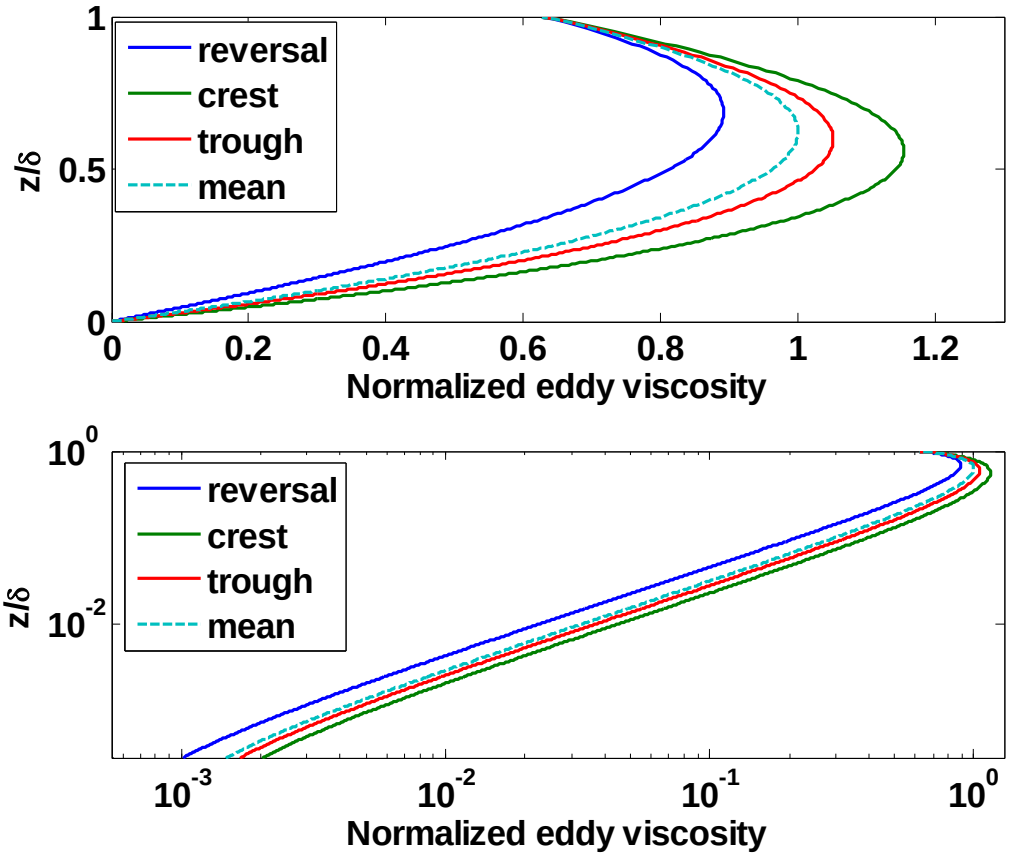

Figure 4.12. Time varying eddy viscosity inside the boundary layer normalized by the maximum time averaged eddy viscosity. Top: linear scale, bottom: logarithmic scale.

4.4.4. Mean Flow

The mean flow inside the boundary layer is solved separately from the oscillatory portion of the flow, instead of using a combined current-wave boundary layer model. The wave direction and the mean current direction are generally not the same. This simplification allows solving for both the mean and oscillatory part in one horizontal direction (each). The main reason for the separation is to be able to account for the increased apparent roughness felt by the mean flow. Nielsen's (1992) modeling approach is used for predicting the mean flow inside the wave boundary layer. The apparent roughness felt by the mean flow is higher than that felt by the oscillatory flow, and the

theoretical bed level of the current z_a is higher than the value of $z_0=k_N/30$, used for the wave boundary layer. Nielsen drives an expression for z_a.

$$z_a = a_N \frac{U_0}{\overline{u_*}} z_0 \tag{4.27}$$

where U_0 is the bottom orbital wave velocity amplitude, a_N is a constant and mean shear velocity $\overline{u_*}$ is defined as

$$\overline{u_*} = \left(\sqrt{\frac{\frac{1}{2}\rho f_w U_0(t)|U_0(t)|}{\rho}} \right) \tag{4.28}$$

Nielsen (1992) uses 0.44 for a_N. He also notes that this leads to underprediction of the theoretical bed level for the mean current for small roughness cases as shown in his figure 1.5.16. Sheet flow conditions generally are in this underpredicted region. The constant a_N was taken as 1.0 in this study to better represent sheet flow conditions.

In this model the eddy viscosity used for current ν_{tc} is

$$\begin{aligned} \nu_{tc} &= \kappa u_* z \quad z > l_c \\ \nu_{tc} &= \kappa u_* l \quad z < l_c \end{aligned} \tag{4.29}$$

This eddy viscosity (Figure 4.13) follows a logarithmic velocity profile for the upper part the figure and a linear velocity profile for the lower part. The location of the shape change l_c can be found by a matching condition $l_c=e\ z_a$.

The waves affect the current by the parameter z_a which is a function of the wave velocity. Nielsen (1992) argues that the effect of currents on waves might be neglected. In the model used here it has a small effect through the eddy viscosity formulation.

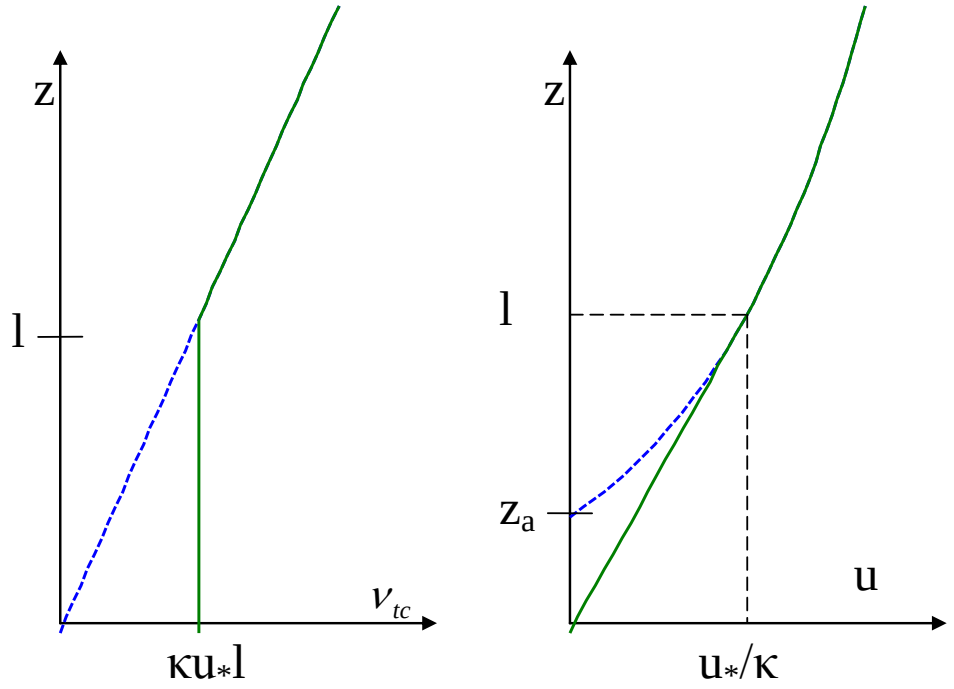

Figure 4.13. The assumed eddy viscosity (left) and mean velocity profile (right) in a combined wave-current boundary layer. Green solid lines show the actual eddy viscosity and velocity. Blue dashed lines show the extension of the expression used for z>l to the bottom. Adapted from Nielsen (1992) Figure 1.5.15.

4.4.5. Numerical Scheme

An implicit Crank-Nicholson scheme, forward in time and central in space, was used to solve for flow within the boundary layer:

$$\frac{u_i^{n+1}-u_i^n}{\Delta t}=\alpha_{CN}\left(\nu_i\frac{u_{i+1}-2u_i+u_{i-1}}{\Delta x^2}\right)^{n+1}+(1-\alpha_{CN})\left(\nu_i\frac{u_{i+1}-2u_i+u_{i-1}}{\Delta x^2}\right)^{n}+\frac{U_i^{n+1}-U_i^n}{\Delta t} \quad \textbf{(4.30)}$$

where *i* stands for grid location and *n* stands for time level. The parameter α_{CN} adjusts the relative magnitudes of the implicit and explicit terms in the solution scheme. When this value is zero the scheme becomes fully explicit, or fully implicit for a value of one. The scheme is second-order in space and second-order in time for α_{CN} =0.5. It is first-order in time for the fully explicit and fully implicit cases. This is a standard numerical method widely employed for the solution of the boundary layer and diffusion equations. It gives reasonable accuracy in time and space while being straightforward to implement, modify and debug. The same numerical scheme has also been used in solving the sediment diffusion equation.

4.5. Sediment Transport Modeling

Cross-shore sediment transport rates at every horizontal location within the model domain are calculated by integrating the sediment flux in each direction over the water column and averaging over a wave period, *T*.

$$q_\alpha = \int_{-(h+d_c)}^{0} \int_{0}^{T} u_{T\alpha}(z,t)c(z,t)dtdz \qquad \textbf{(4.31)}$$

where q_α is the sediment transport rate in direction α, $u_{T\alpha}$ is the total flow velocity in the same direction , *c* is the volumetric sediment concentration and d_c is the erosion depth which is the distance from the still bed to the bottom of the active transport layer (explained in Section 4.6) . The method to find *u(z,t)* was explained in the previous section. This section will explain the method used in predicting *c(z,t)*.

Equation 4.31 involves assuming that sediment velocity is the same as the fluid velocity in the horizontal direction. This is a reasonable assumption for sands in low concentrations. The assumption begins to break down at very high concentrations such as

the flow in the lower part of the sheet flow layer near the bed. For this reason, sediment transport in this region is solved by a separate sheet flow model.

4.5.1. Governing Equations for Sediment Suspension

The vertical distribution of the suspended sediment is modeled by the advection-diffusion equation.

$$\frac{\partial c}{dt} = (w_f - w)\frac{\partial c}{dz} - u_T \frac{\partial c}{dx} + \frac{\partial}{dz}\left(\varepsilon_s \frac{\partial c}{dz}\right) + \frac{\partial}{dx}\left(\varepsilon_s \frac{\partial c}{dx}\right) \quad \textbf{(4.32)}$$

where w_f is the fall speed of the suspended sediment and ε_s is the diffusion coefficient. The first term on the right-hand-side of the equation is the vertical advection due to net vertical velocity, accounting for sediment settling. The second term on the right-hand-side is the horizontal advection. The last two terms are the vertical and horizontal diffusion terms.

The main assumption implicit in this equation is that the movement of the sand grains can be modeled as a diffusive process. This assumption has some theoretical shortcomings, but has been successfully used in sediment transport predictions as discussed in the literature review.

The concentration gradients in the vertical are typically much higher than the horizontal concentration gradients in the coastal environment. In the nearshore region, the vertical length scale, which is proportional to the water depth, is much smaller than the horizontal length scale, which is proportional to the wavelength. Dimensional analysis shows that if vertical diffusion is order one, advection terms due to fluid velocities are second-order and the horizontal diffusion is third-order. As a result, the horizontal diffusion term is typically ignored.

The first-order approximation to the advection-diffusion equation is one-dimensional and given as

$$\frac{\partial c}{dt} = (w_f)\frac{\partial c}{dz} + \frac{\partial}{dz}(\varepsilon_s \frac{\partial c}{dz}) \quad \textbf{(4.33)}$$

Including second-order terms makes the equation two-dimensional. A method to keep the equation one-dimensional while including the second-order terms is to define horizontal derivatives in terms of time derivatives (e.g. Deigaard et al. 1999).

$$\frac{\partial}{\partial x} = -\frac{1}{C_p}\frac{\partial}{\partial t} \quad \textbf{(4.34)}$$

where C_p is the wave phase velocity. This assumes that the wave has a permanent form, moving without changing form. Using this approach and including the second-order terms, the equation becomes:

$$(1-\frac{u}{C_p})\frac{\partial c}{dt} = (w_f - w)\frac{\partial c}{dz} + \frac{\partial}{dz}(\varepsilon_s \frac{\partial c}{dz}) \quad \textbf{(4.35)}$$

The terms $w\frac{\partial c}{dz}$ and $u\frac{\partial c}{dx}$ are of the same order so they should be included or excluded together. However sometimes one has been included, while the other is left out (e.g. Qin and Svendsen 2003). The effects of these two terms on the solution of the diffusion model are investigated and quantified in the results section.

4.5.2. Sediment Diffusion Coefficient

The sediment diffusion coefficient is generally related to the eddy viscosity with a simple proportionality constant β. The inverse of this constant is sometimes called the Schmidt number.

$$\varepsilon_s = \beta \upsilon_t \tag{4.36}$$

where β is generally taken as 1.0, mostly due to the lack of better information. However, various values in the range 0.5-4 have also been used. Malarkey et al. (2003) investigated the data of Dohmen-Janssen et al. (2001) and suggested that β is a function of sediment size, recommending values of 0.5,1, and 3 for fine (0.13 mm), medium (0.21 mm) and coarse (0.32 mm) sand, respectively. Davies and Thorne (2005) indicate that $\beta = 4$ gave the best fit to their data, obtained using medium sand (0.175-0.23 mm). Davies (1995) gives a review of various values used for the parameter β.

SHORECIRC employs an eddy viscosity profile that is constant over the depth to enable analytical integrations of the momentum equation to calculate velocity profiles. No such limitation is present for the solution of the advection-diffusion equation, so parabolic profiles for sediment diffusion coefficient are used both inside and outside the boundary layer. The diffusion coefficient is the same as the eddy viscosity inside the wave boundary layer, and outside the boundary layer its average value is equal to the value of eddy viscosity used by SHORECIRC.

Wave breaking creates additional turbulence and increases the sediment diffusion coefficient. Roelvink and Stive (1989) included a stirring effect due to wave breaking, which improved their sediment transport predictions. Deigaard et al. (1986) modeled the production of turbulence by breaking waves using a bore model, its diffusion over the

depth and its dissipation improving concentration profile predictions. The wave breaking did not change the concentrations close to the bed.

The effect of wave breaking has been included as an increase in eddy viscosity above the wave boundary layer. The expression used in Qin and Svendsen (2003) has been employed where the additional stirring effect has been related to the wave energy dissipation due to wave breaking, D [kg/s^3]. The time-averaged diffusion coefficient is given as

$$\varepsilon_s = \begin{cases} \beta\kappa u_{*wcm} z(1 - m\frac{z}{\delta}) & z < \delta \\ \beta\kappa u_{*c} z(1 - \frac{z}{\delta}) + \alpha_{ML}\frac{3}{5}\sqrt{\frac{z-\delta}{h}}h(\frac{D}{\rho})^{\frac{1}{3}} & z > \delta \end{cases} \quad \textbf{(4.37)}$$

where α_{ML} is the ratio of the mixing length l, to water depth ($l=\alpha h$) taken as 0.25. The diffusion coefficient defined this way is proportional to the eddy viscosity by β, the proportionality constant. Extending this proportionality further, the time variation of the diffusion coefficient *tv* is chosen the same as the time variation of eddy viscosity given in Equation 4.26.

$$\varepsilon_s^{'}(t) = \mathrm{tv}\varepsilon_s \quad \textbf{(4.38)}$$

This way eddy viscosity and sediment diffusion coefficient are in phase and related by a constant factor, β.

4.5.3. Boundary Conditions for Sediment Diffusion Equation

There is no sediment flux across the water surface. The surface boundary condition is thus defined as no sediment flux at the mean water level $\overline{\zeta}$.

$$(w_f - w)c + \varepsilon_s \frac{\partial c}{\partial z} = 0 \qquad z = \bar{\zeta} \tag{4.39}$$

Applying the no-flux boundary condition at the mean water level rather than the instantaneous water surface is an approximation used most of the time since the sediment concentration close to the surface is negligible. This simplifies the numerical scheme since the length of the numerical domain does not change.

For the bottom boundary condition a hybrid reference concentration formulation was created where the Zyserman reference concentration (Equation 2.11) is used for high shear stress values and the Fredsoe expression (Equation 2.10) is used for lower stress values. The switch was chosen to be at θ=0.328 where the two expressions give the same value. This hybrid reference concentration was cast in terms of a pick-up function (Equation 2.16) giving the rate of sediment entrainment instead of the sediment concentration.

4.6. Sheet Flow Layer Model

Sediment transport also occurs below the reference concentration or pick-up level, defined at $2d_{50}$. A new method is presented here to model the sediment transport in this region. The sediment transport below this level will be defined as bed load transport for convenience. The top of the sheet layer defined as c=0.08 can be below or above the reference level during various phases of the flow. The concentration is very high in this region and diffusion concepts no longer apply. Two-phase flow models where the fluid and sand interact would be the ideal approach. In some studies sediment transport below the reference level has been ignored. Bed load formulations have also been used to take this portion of the sediment transport into account. All these options have been discussed in the literature review section.

The sediment transport was calculated by assuming empirical shapes for the concentration and velocity profile below $2d_{50}$ in this study. A two-layer approach was used by Kaczmarek (1991) combining a diffusion model with a collision model. Kaczmarek and Ostrowski (2002) added a third transition layer where both collision and diffusion where important. Malarkey et al. (2003) used a two-layer approach where empirical velocity and concentration profiles were assumed. In this study the reference level for the suspension model was defined at varying elevations with a constant concentration of 0.08. This study differs from Malarkey et al. (2003) by using a reference concentration formulation at a fixed elevation instead of a fixed reference concentration at a changing elevation given by a sheet flow layer thickness formulation. Sumer et al. (1996) observed that in steady flow, the concentration profile was linear in the lower part of the sheet flow layer, while it could be described by a logarithmic profile in the upper half. The model used in this study resembles this observation more than the Malarkey et al. (2003) model.

When there is no flow the bed is stationary at the initial bed level ($z=0$). When the flow begins, some sediment goes into suspension and the sediment inside the bed begins moving, down to an erosion depth d_c which is the new stationary bed level. The concentration below the reference level is given by

$$c = c_0 - (c_0 - c_a)\left(\frac{d_c + z}{d_c + 2d_{50}}\right)^n \qquad -d_c \le z \le 2d_{50} \tag{4.40}$$

where c_r is the concentration at the reference level and n is a parameter controlling the shape of the concentration profile. Figure 4.14 shows the concentration profile for n=1.

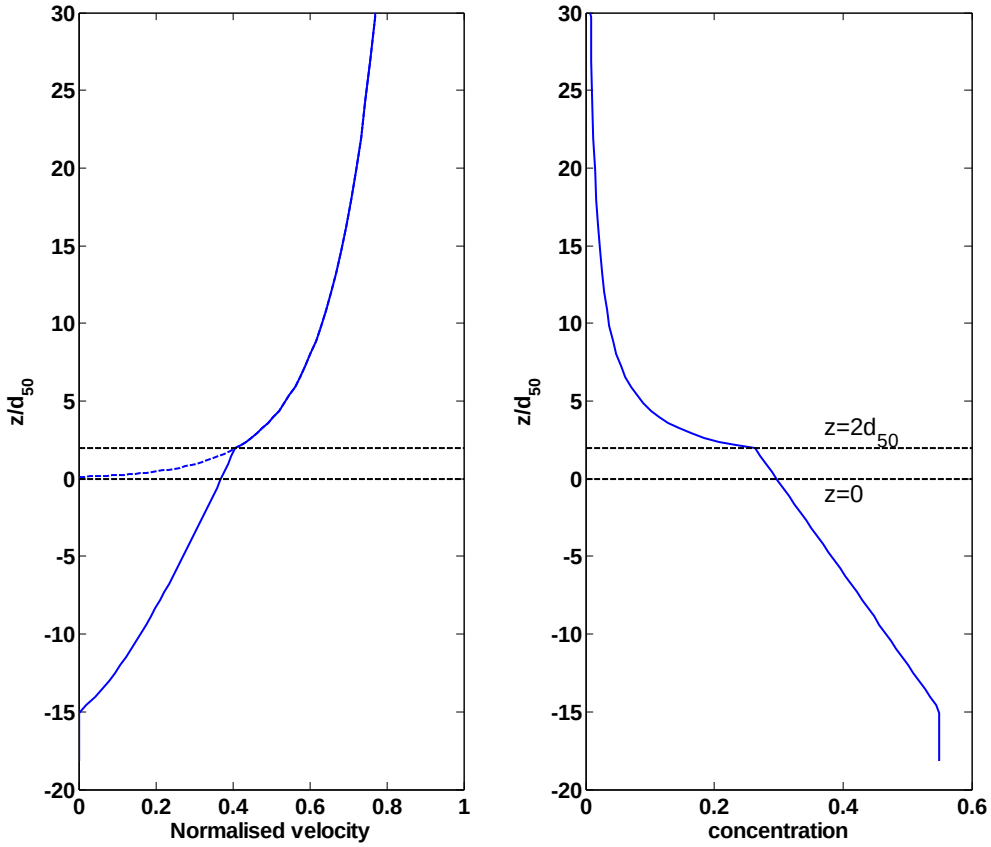

Figure 4.14. Sketch of Velocity and concentration profiles in the sheet flow layer. Velocity is normalized by its value at the edge of the boundary layer. Horizontal dashed lines show initial bed level z=0 and reference level $z=2d_{50}$. Dashed curve shows the velocity from the boundary layer solution.

The velocity profile is defined in a similar fashion to the concentration profile as

$$u = u_r \left(\frac{d_c + z}{d_c + 2d_{50}} \right)^m \qquad -d_c \le z \le 2d_{50} \tag{4.41}$$

where u_r is the velocity at the reference level and m is the shape parameter. The solution for velocity between $z=k_N/30$ and $2d_{50}$ found from the boundary layer model (shown with dashed lines in Figure 4.14) is replaced by the velocity expression for the sheet flow layer.

Conservation of mass is given by:

$$\int_{-d_c}^{0} c_0 dz = \int_{-d_c}^{2d_{50}} c dz + \int_{2d_{50}}^{h} c dz \qquad \textbf{(4.42)}$$

where c_0 is the bed concentration level. The total volume of suspended sediment M_{sus} ($\int_{2d_{50}}^{h} c dz$) is known from the solution of the diffusion equation. Using equations 4.42 and 4.40 erosion depth can be found as:

$$d_c = \left(\frac{M_{sus} + c_0 2d_{50}}{c_0 - c_r} \right)(n+1) - 2d_{50} \qquad \textbf{(4.43)}$$

Note that d_c never goes below $2d_{50}*n$ even if M_{sus} and c_0 both go to zero.

A sketch of the time variation of the sheet flow layer is shown in Figure 4.15. Erosion depth and sheet flow layer thickness change as a function of the flow. The top of the sheet flow layer is shown only for illustrative purposes. The definition is not used in the model itself.

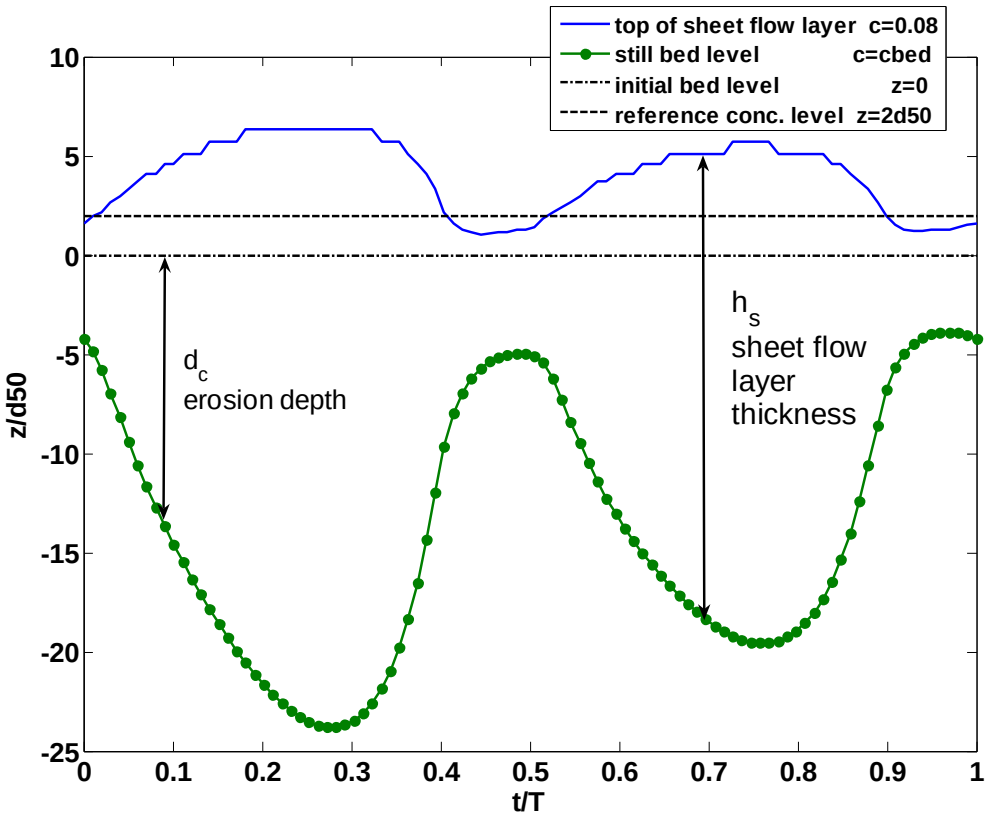

Figure 4.15. Sketch of time variation of sheet flow layer.

Malarkey et al. (2003) chose *n* in Equation 4.40 as 2.0 based on oscillatory water tunnel data (Horikawa et al. 1983). For steady flow data a linear profile (n=1) gave the best fit (Sumer et al. 1996). Hanes and Bowen (1985) and Wilson (1987) also used n=1. More recent concentration measurements under oscillatory flow (McLean et al. 2001) can be better represented by a linear profile rather than a convex up (n=2) profile. A linear profile averaged over time would also be convex in shape because of the changing erosion depth. The definition of the still bed level complicates finding the shape of the concentration profile, too. The top part of a convex up profile can easily be fitted with a linear profile, given the scatter in measurements. The concentrations do not change significantly when the shape of the profile is changed, since the erosion thickness is also changing to conserve mass. However the erosion depth is directly proportional to *n* (Equation 4.43). Velocity is sensitive to erosion thickness, as is the sediment transport

rate. Inspection of the Horikawa et al. (1983) data shows that the level where velocity goes to zero and concentration goes to the bed level value are not always the same. In the model both of these levels are at $z=-d_c$. If a linear profile is chosen the sediment transport would be less sensitive to d_c, which is not easily measured or predicted. As a result the value of n was chosen as 1.0.

Malarkey et al. (2003) used m=1 in Equation 4.41 Sumer et al. (1996) suggested m to be 0.75, which is very close. The value of m is chosen as 0.75 for this study.

This model gives time-varying, continuous predictions of velocity and concentration profiles down to the still bed level. It does not use an artificial distinction between suspended and bed load and the sediment is modeled continuously. This approach is physically more realistic than assuming that the sediment transport can be explained by diffusion everywhere or neglecting the sediment transport below the reference concentration level. Empirical shape functions were chosen for the velocity and concentration profiles according to the data available in the literature.

4.7. Bathymetry Updating

A conservation of sediment mass equation is solved to find the change in bathymetry, given as

$$\frac{\partial z}{\partial t} = -\frac{1}{1-p}\left(\frac{\partial q_x}{\partial x} + \frac{\partial q_y}{\partial y}\right) \tag{4.44}$$

where p is the bed porosity, q_x and q_y are volumetric sediment transport rates in the x and y directions, respectively. Following Johnson and Zyserman (2002) the conservation of mass equation can be written as an advection equation:

$$\frac{\partial z}{\partial t} = C_x(z)\frac{\partial z}{\partial x} + C_y(z)\frac{\partial z}{\partial y} \quad \textbf{(4.45)}$$

where $C_x(z)$ and $C_y(z)$ are the celerity of the bed level oscillations equal to $\partial q_x/\partial x$ and $\partial q_y/\partial y$ respectively. As particle velocities approach the celerity of the bed level oscillations, discontinuities or shocks appear. Numerical schemes that can capture these discontinuities are called shock-capturing schemes. A popular scheme used for updating of morphology is the Lax –Wendroff scheme (Long et al. 2006). However, spurious high-order oscillations occur around the shock. Filters are required to remove these high-order oscillations (Johnson and Zyserman 2002). Correct choice of these filters becomes critical in order to remove high-order oscillations without smoothing of real physical features such as sand bars.

Schemes that do not create spurious oscillations are called monotonicity-preserving. Total Variation Diminishing (TVD) schemes can be high-order accurate and preserve monotonicity, but they require calculation of velocities at intermediate time steps. An Euler-Weighted Essentially Non-Oscillatory scheme is implemented by Long et al (2006) in the NearCom model. This method uses flux splitting, choosing the direction of derivatives (forward vs. backwards) depending on the local celerity and uses weighted average among possible finite difference approximations. This method is fifth-order accurate in space and first-order accurate in time and is shown not to create oscillations without significantly increasing the calculation requirements. This method is accurate and stable. Its capability to smooth out numerical oscillations without using filters that need tuning makes it an ideal method.

A no-flux boundary condition for sediment is used at the offshore boundary. The sediment transport rate is likewise set to zero at the shoreward boundary.

5. RESULTS I: SEDIMENT TRANSPORT MODEL

This chapter covers the boundary layer model for the water, and the diffusion and sheet flow layer models for the sediment. These models solve for the velocities inside the wave boundary layer, given the velocities outside the wave boundary layer. Volumetric sediment concentration and its change within a wave period and vertically through the water column are resolved. Sediment movement within the bed is also modeled, so that the model describes both the suspended and bed load contributions to sediment transport, without specifically defining the distinction between them. All of these models were developed for this study and are used to predict the local sediment transport rate for given local flow conditions. These models can be run independently of the rest of the modeling system. In this section the model components are described, numerical properties of the model are optimized, and the effects of various physical processes are investigated. Concentration and velocity profiles and sediment transport rates are calibrated by comparison to existing data.

5.1. Grid and Temporal Spacing

The same vertical grid is used for both the boundary layer and the diffusion models. The grid for the diffusion model extends to the water surface while the other ends at the top of the wave boundary layer. A logarithmic grid is used such that vertical grid spacing is uniform on a semi-logarithmic plot. This way the grid spacing is much finer close to the bed where the gradients in velocity and sediment concentration are largest. The sediment concentrations plotted are volumetric sediment concentrations with units of m^3/m^3 unless otherwise stated. The number of vertical grid points, *Nz*, is kept constant throughout the model domain, regardless of the water depth. Grid spacing is greater for deeper parts of the domain, but the sediment transport rate is also much smaller in these areas, requiring less resolution.

The error due to resolution in a numerical solution is often defined as the difference from a known analytical solution. Since there is no analytical solution for the boundary layer or the diffusion models, the error will be defined as the normalized rms difference from the solution with the highest number of grid points. A test case with the following parameters is used. Wave crest speed (U_c) =1 m/s, trough speed (U_t) = 0.8 m/s, mean velocity U_m= -0.1 m/s at the edge of boundary layer, h=3.5 m, T=6.5 sec, d_{50}=0.21 mm. This is a typical case that can be observed in the nearshore environment. The velocity under the wave crest is assumed to be in the onshore direction and the mean velocity is directed offshore. Figure 5.1 shows the effect of grid size on numerical error. "Steady" state velocity *u(z,t)* and concentration *c(z,t)* solutions and the total sediment transport rate are compared to the solution with 2000 grid points. For example the normalized error for concentration for Nz=100 is defined as

$$Errc(Nz=100)=\sqrt{\frac{\sum_{i=1}^{100}\sum_{j=1}^{Nt}\left(c_{Nz=2000}(i,j)-c_{Nz=100}(i,j)\right)^2}{\sum_{i=1}^{100}\sum_{j=1}^{Nt}\left(c_{Nz=2000}(i,j)\right)^2}} \qquad \textbf{(5.1)}$$

Note that the solution with Nz=2000 is interpolated to the grid locations of Nz=100 before the above calculation. The error is calculated similarly for other computational grid sizes and for velocity. Sediment transport rate is defined by Equation 4.31, and the error for it is defined similarly, but without summation since it is already integrated over time and space. All lines have a slope of two in Figure 5.1 since the numerical scheme is second-order accurate in space.

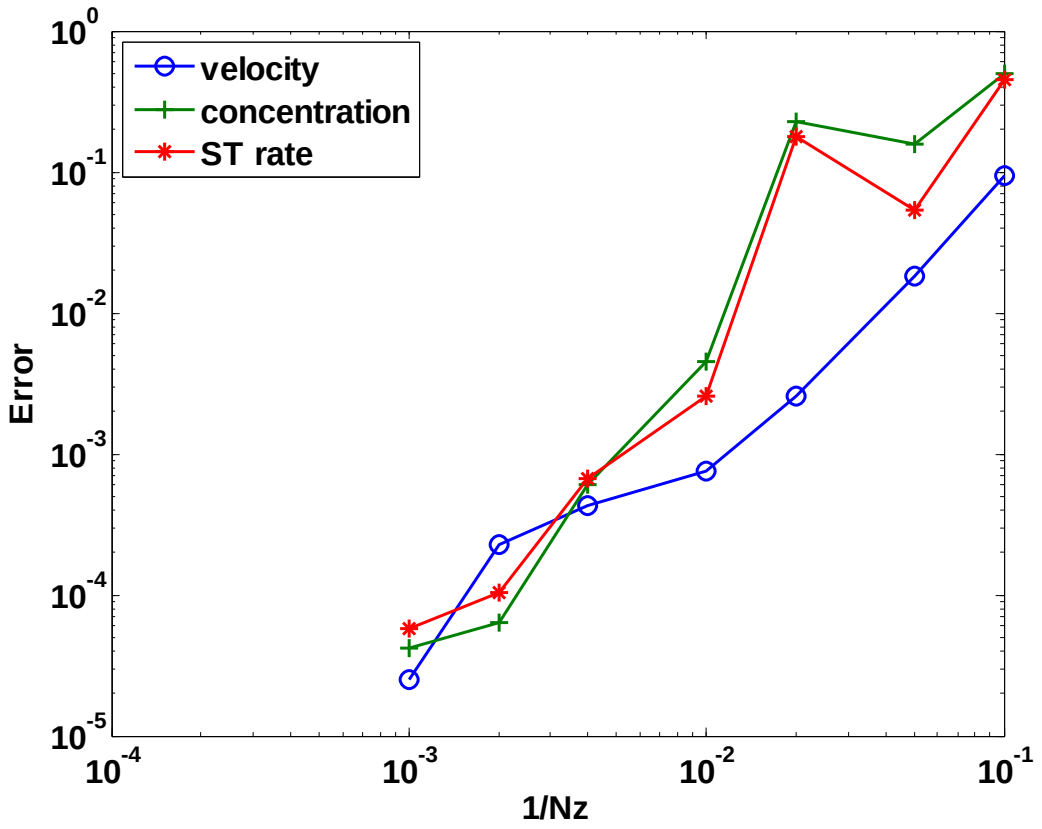

Figure 5.1. The effect of grid size on numerical error. Error is defined as normalized rms difference from the case with the largest number of nodes (*Nz*=2000). h=3.5 m, *U* crest (U_c)=1m/s, *U* trough (U_t)=0.6 m/s, U_m=-0.1 m/s, *T*=6.5 sec *Nt*=100.

The influence of temporal resolution on calculated results is shown in Figure 5.2. The number of points in one wave period is defined as $Nt=T/dt$. The Crank-Nicholson numerical scheme used for the temporal solution of the equations is theoretically second-order when the parameter controlling the influence of the implicit part of the solution, α_{CN}, is 0.5 (Equation 4.30). However the solution is marginally stable for this value. It is first-order accurate for α_{CN} =0 and α_{CN} =1. To improve stability, α_{CN} was chosen as 0.6. By observing the slope of the lines in Figure 5.2 it can be seen that the solution is slightly better than first-order.

Based on the results of the tests shown in Figure 5.1 and Figure 5.2, the number of grid points, *Nz*, was chosen as 110, and the number of points in a wave period, *Nt*, was chosen as 100. The resulting error in sediment transport rate due to the resolution

limitations is around 1%, which is negligible compared to the errors in measurements and other errors in the model.

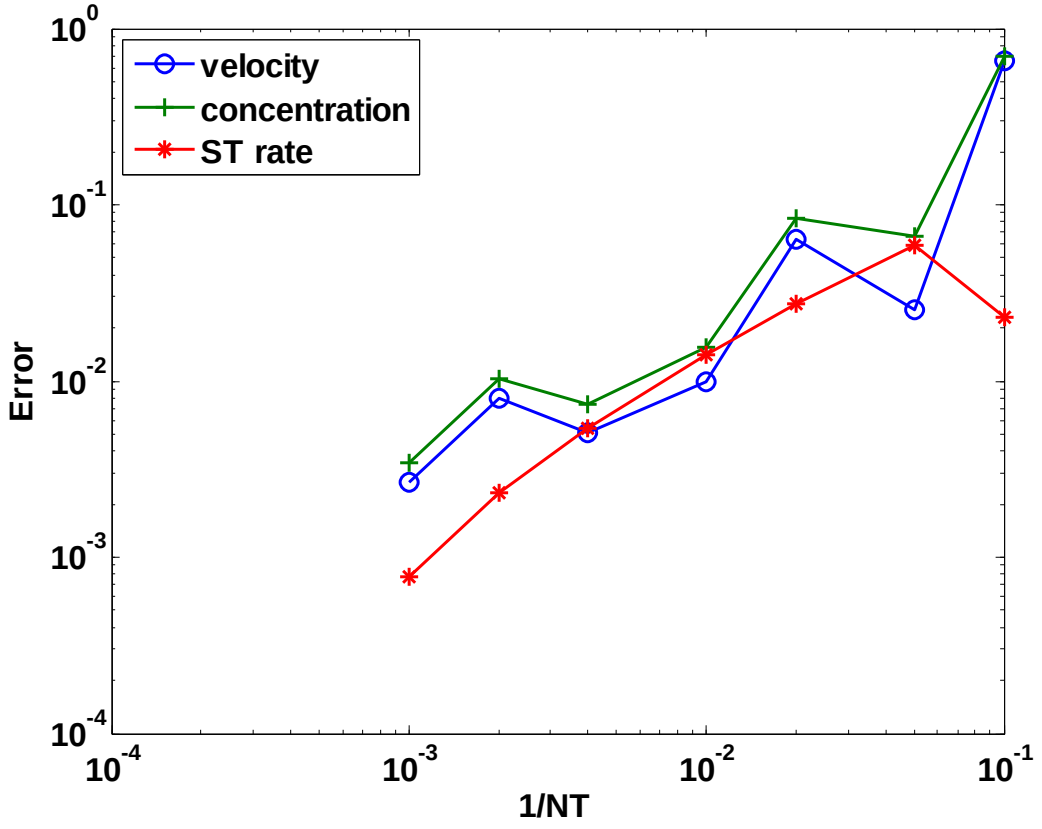

Figure 5.2. The effect of temporal spacing on numerical error. Error is defined as normalized rms difference from the case with highest number of points (Nt=2000). U_c=1m/s, U_t=0.6 m/s, U_m=0.1 m/s, T=6.5, Nz=100.

5.2. Equilibrium Sediment Transport

When the flow or bathymetric conditions change, and the sediment transport model is called, the velocities in the boundary layer and sediment concentrations respond to this and change. After some time, the velocities and sediment concentrations at a specific wave phase reach a dynamic equilibrium state where they do not change from one wave period to the next for the representative monochromatic wave. The simulations are stopped at this point and sediment transport rate is assumed constant until the next call to the sediment transport model, i.e. after "significant" bathymetric change occurs. If

the wave conditions are updated hourly and there is no significant bathymetric change in this period, the sediment transport model is run for only several wave periods instead of the whole hour, decreasing the run time of the model significantly.

The equilibrium is assumed to be reached when the normalized change in sediment transport rate is less than $4*10^{-3}$. This value which has been found by trial and error ensures that the "equilibrium" solution chosen is no more than 2% different than the solution found after hundreds of iterations. The normalized change *STdiff* is defined as

$$STdiff = \frac{\sqrt{\left(ST_x(i) - ST_x(i-1)\right)^2}}{\max\left(\left|ST_x(i)\right|, 10^{-6}\right)} \quad \textbf{(5.2)}$$

where $ST_x(i)$ is the depth integrated, wave-averaged sediment transport rate at wave period *i*. A lower limit of 10^{-6} is imposed on the normalization value so that the model spends little time at locations and instances where the sediment transport rate is negligible. This value was optimized for field conditions. It has to be adjusted for small-scale lab studies. The model is run for at least three wave periods regardless of the computed value of *STdiff*. Figure 5.3 shows the temporal variation in sediment transport rate and *STdiff* at a location as a function of wave periods. The solution reaches steady state very fast; within a couple of wave periods for the wave-dominated cases as shown. The limiting case of a minimum of three wave periods is used in many cases. For current-dominated cases, the convergence is much slower and it may take tens of wave periods to reach the pseudo-steady-state condition.

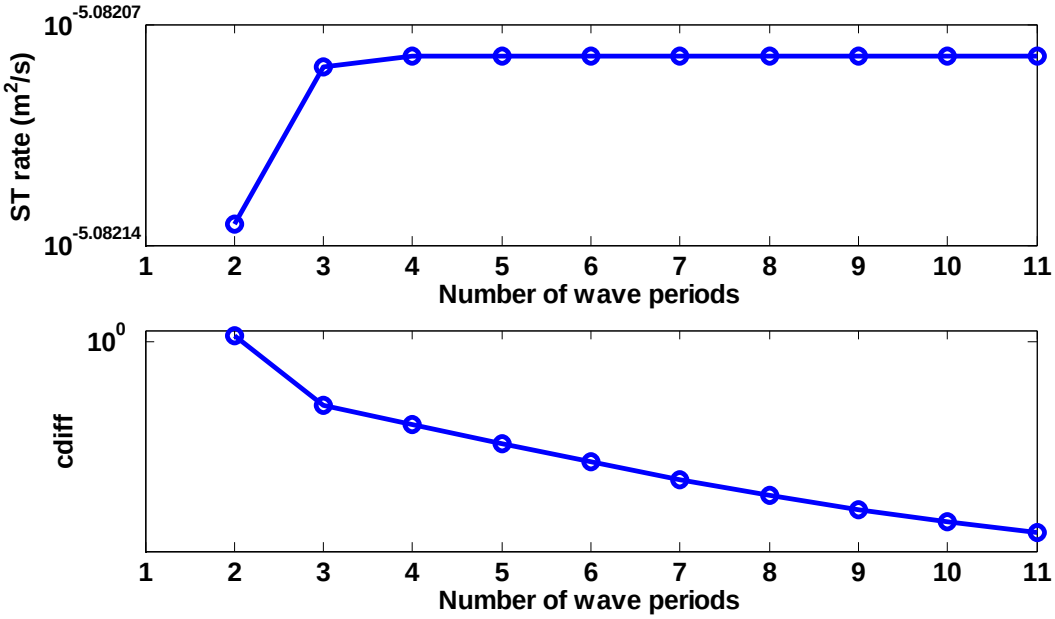

Figure 5.3. Solution reaching equilibrium state. Net sediment transport rate (top) and change in sediment transport rate, *STdiff* (bottom) as a function of number of wave periods. h=3.5 m, U_c=1m/s, U_t=0.6 m/s, U_m=-0.1 m/s, T=6.5 sec.

5.3. Effects of Vertical Velocity and Convective Accelerations

The vertical velocity and convective acceleration terms are often ignored when solving the sediment diffusion equation. Their importance is investigated here. The equation describing sediment diffusion is given here again for convenience.

$$(1-\frac{u}{c_p})\frac{\partial c}{dt} = (w_f - w)\frac{\partial c}{dz} + \frac{\partial}{dz}(\varepsilon_s \frac{\partial c}{dz}) \qquad \textbf{(5.3)}$$

The vertical (water) velocity acts in the same fashion as the sediment fall velocity, so it is worthwhile to investigate their magnitudes. The vertical velocity is zero at the bed and increases slowly with elevation, compared to the horizontal wave-induced velocity (Figure 5.4). For the conditions assumed here, the maximum vertical velocity reaches 10% of the fall velocity 15 mm above the still bed. Horizontal velocity increases much faster with elevation above the bed than does the vertical velocity. Inside the boundary

layer the horizontal velocities are a couple of orders of magnitude larger than the vertical velocity (Figure 5.4).

Vertical velocity is almost 90 degrees out of phase with horizontal velocity (linear wave theory predicts exactly 90 degrees difference). When horizontal velocity is zero and about to increase, the vertical velocity is close to its maximum in the upwards direction (Figure 5.4 bottom panel). Upwards velocities enhance suspension and increase sediment concentrations and downwards velocities enhance settling and decreases sediment concentrations. This can be observed in Figure 5.5 at altitudes 80 and 100 mm above the bed. The effect of the vertical velocities at lower elevations is negligible, as seen in the bottom panel of the figure. In general, the vertical velocity modifies concentrations only at elevations where the concentration is very low. As a result, the change in both instantaneous and net sediment transport rate when vertical velocity is included is negligible. The effect of vertical velocity would be more significant in cases with fine sediments where the fall velocity is small.

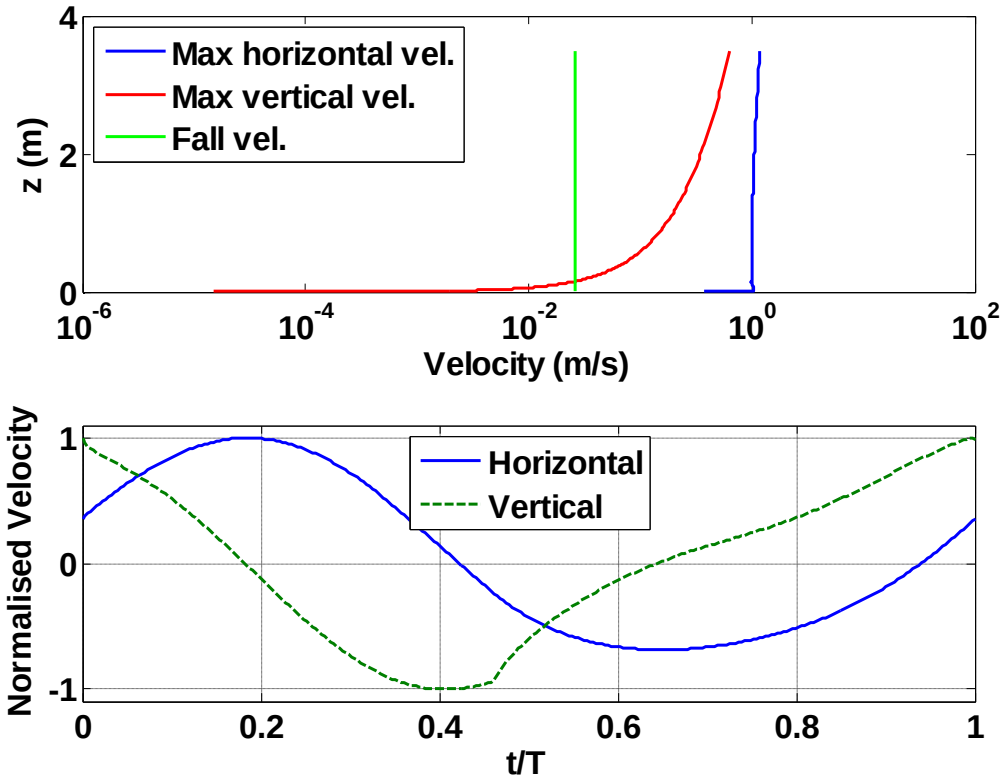

Figure 5.4. Top: Maximum horizontal and vertical velocities and fall velocity of the sand. Bottom: Normalized horizontal and vertical velocities inside the boundary layer 1.0 mm above the bed. U_c=1 m/s, U_t= 0.8 m/s, U_m=-0.1 m/s at 1m, h=3.5 m, T=6.5 sec, d_{50}=.21 mm.

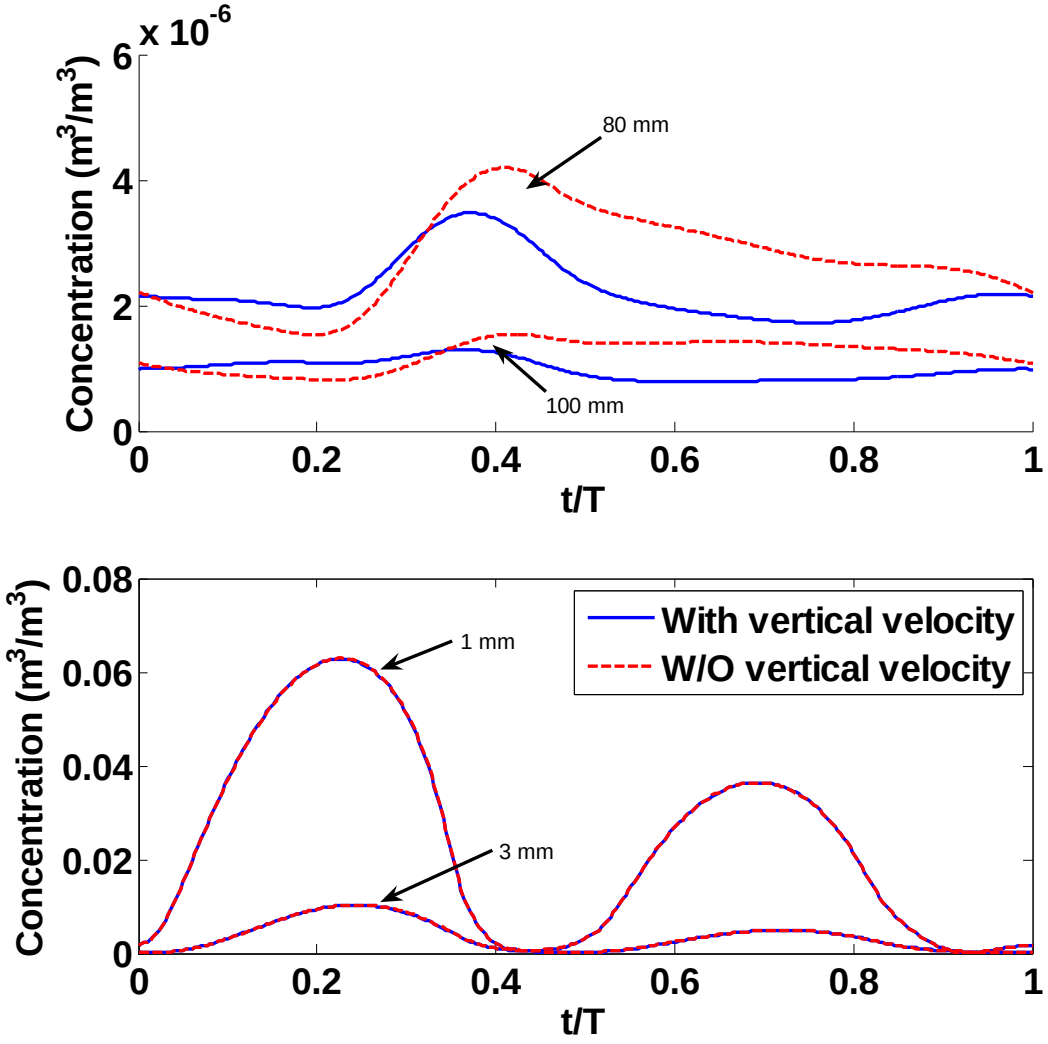

Figure 5.5. Effect of vertical velocity on the volumetric sediment concentration. Labeled lengths indicate elevation above still bed level. Legend applies to both panels. Model parameters same as Figure 5.4.

The convective term in the sediment model is represented by the term u/c_p in Equation 5.3. This term acts in phase with the horizontal velocity u. It increases sediment concentration when u is directed onshore (positive) and decreases the concentration when it is directed offshore (negative). Its effect is negligible very close to the bed. It becomes significant higher in the water column (Figure 5.6). The contribution of the convective term on sediment transport is also negligible, for the same reason that the influence of

vertical velocity is negligible: it becomes important only where the sediment concentrations are very low.

For the investigated cases convective term and vertical velocity do not have significant effects on net sediment transport rate. They have some effect on the time variation of sediment concentration away from the bed. However their effects counteract each other since one is in phase with the horizontal velocity, while the other is in phase with the vertical velocity. For cases where the shear stresses are more and/or sediment diameter is less, sediment concentration would be more at higher elevations and these terms would have more influence. The diffusion equation is solved including these terms for completeness.

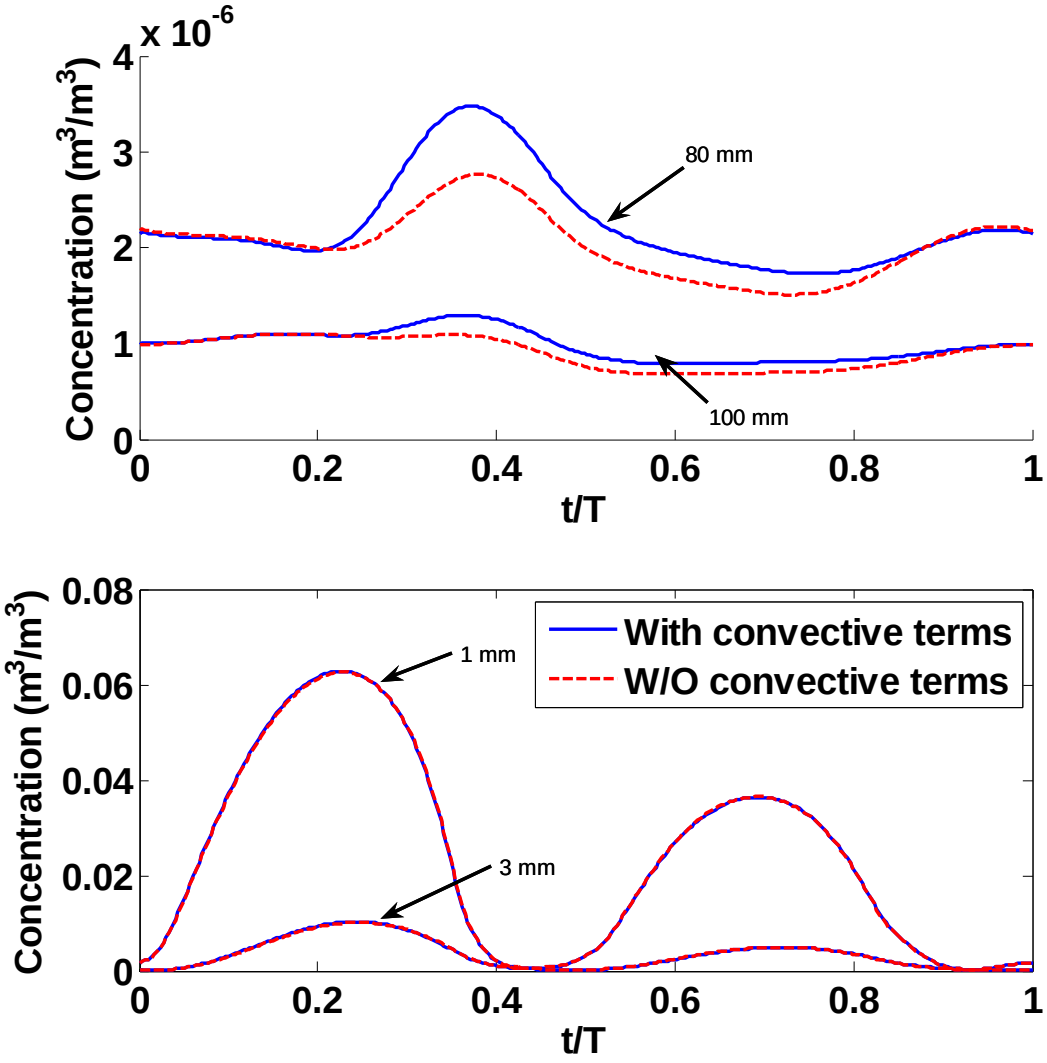

Figure 5.6. Effect of convective terms on the volumetric sediment concentration. Altitudes show elevation above still bed level. Both panels show concentration at different elevations. Legend applies to both panels. Model parameters same as Figure 5.4.

5.4. Effect of Boundary Layer Streaming

Boundary layer streaming is also a second-order effect, like the vertical velocity and convective terms. Its impact was investigated by removing the streaming velocity from the same test case. The time-averaged horizontal velocity is shown in Figure 5.7. The magnitude of the streaming velocity is about 10% of the maximum orbital velocity at the outer edge of the boundary layer. This is about the same magnitude as the time-

averaged velocity. However it is stronger close to the bed and creates a net positive (onshore) mean flow.

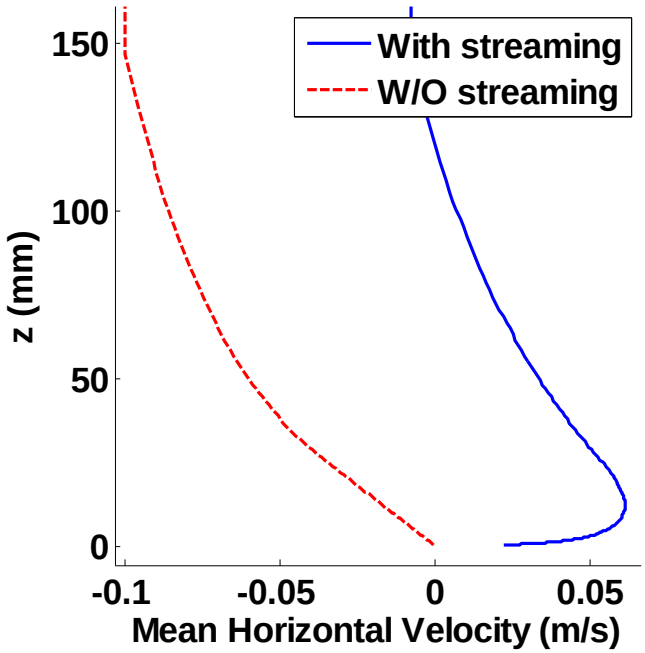

Figure 5.7. Effect of boundary layer streaming on the mean horizontal velocity. Time-averaged velocity is shown with and without the boundary layer streaming. Model parameters same as Figure 5.4.

The streaming velocity is directed onshore and changes both the bottom shear stress and the sediment pick-up rate. When the orbital velocity is onshore, streaming adds to it, increasing the velocities and the pick-up rate. It decreases the velocity and the pick-up rate when the orbital velocity is offshore. This can be observed clearly in the bottom panel of Figure 5.8. This effect is harder to distinguish higher in the water column (top panel) as the sediment concentration peaks shift and smooth out.

The change in sediment transport rate caused by boundary layer streaming is mainly due to the change in velocity, not due to concentration change. The streaming velocity, even though small in magnitude, can increase sediment transport rate 2-4 times in the absence of a strong mean current (Figure 5.9). In cases with linear, symmetric

waves without any mean currents, sediment transport rate is zero without the inclusion of boundary layer streaming.

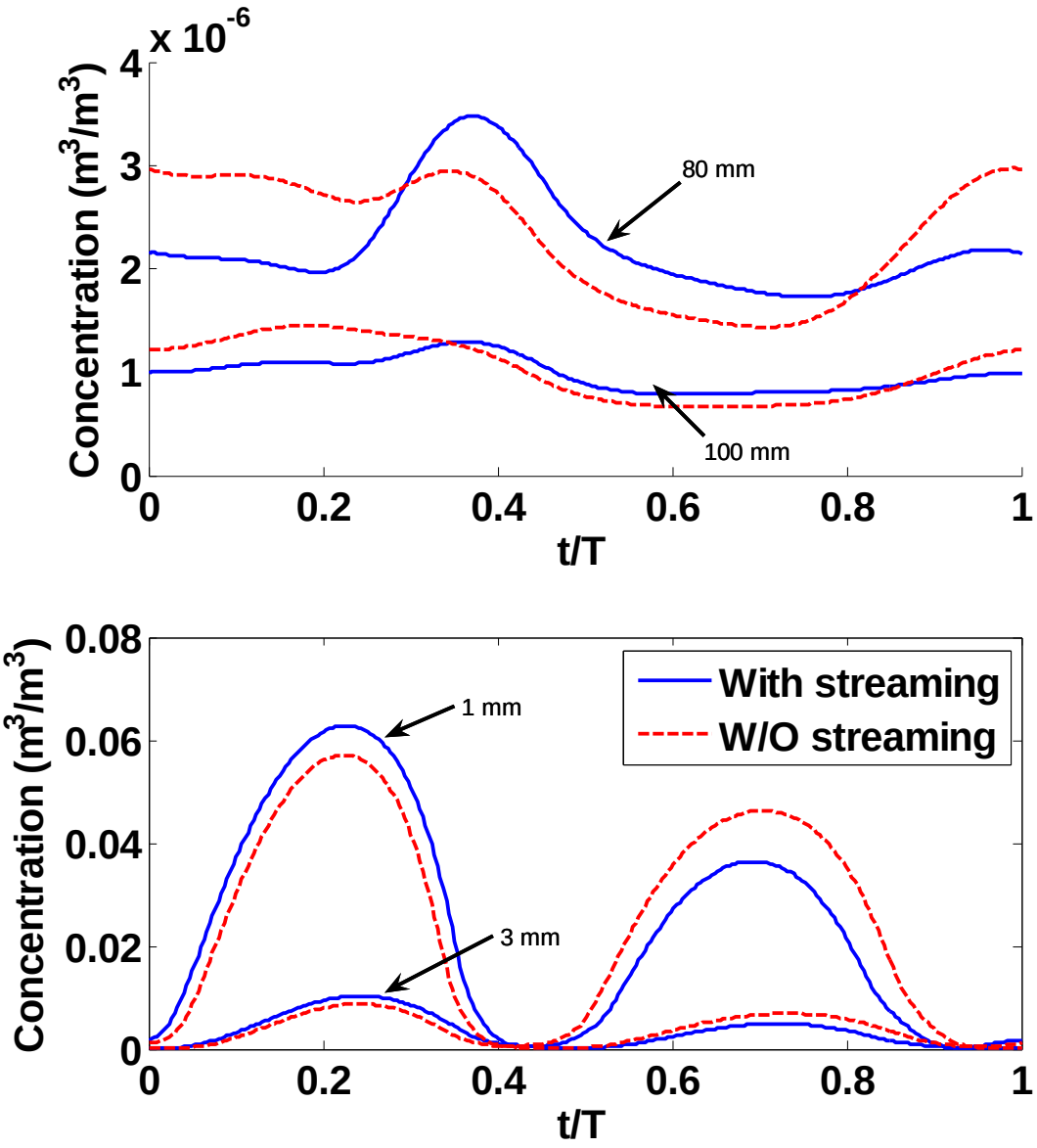

Figure 5.8. Effect of boundary layer streaming on the volumetric sediment concentration. Labeled lengths are elevations above still bed level. Both panels show concentration at different elevations. Legend applies to both panels. Model parameters same as Figure 5.4.

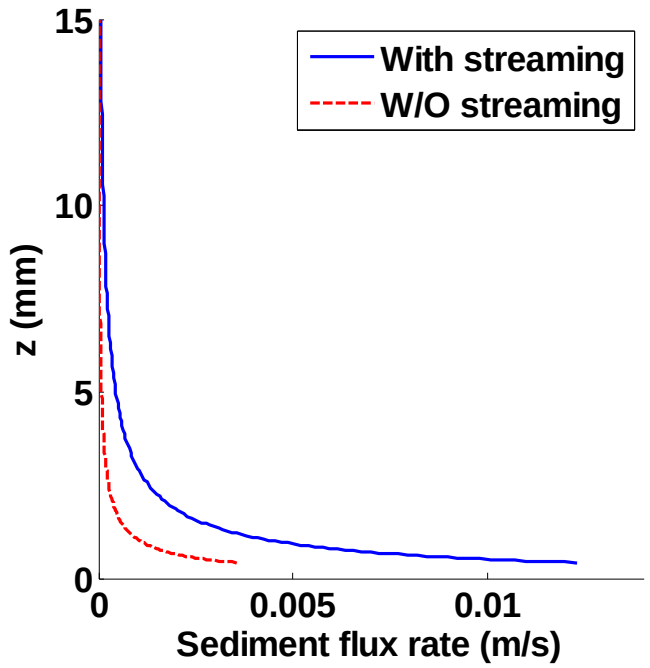

Figure 5.9. Effect of boundary layer streaming on sediment flux ($c(m^3/m^3)*u(m/s)$) rate. Model parameters same as Figure 5.4.

5.5. Reference Concentration vs. Pickup Function

The bottom boundary condition for the sediment diffusion equation can be defined as a reference concentration or a pick-up function. The two approaches are compared in Figure 5.10. The reference concentration is a function of the instantaneous shear stress at the bottom and it goes to zero as the shear stress changes direction. The concentration is discontinuous for the reference concentration plot since zero concentration can't be shown on the logarithmic plot. The pickup function does not state the concentration, but rather it's gradient. Even when the shear stress is zero the concentration does not go to zero due to sediment settling from above. This way the sediment concentration at the reference height is also affected by the time history of shear stress. This results in a very small phase shift in sediment concentration which is not distinguishable in the figure. A pick-up function was used in this study since it represents the physical process better.

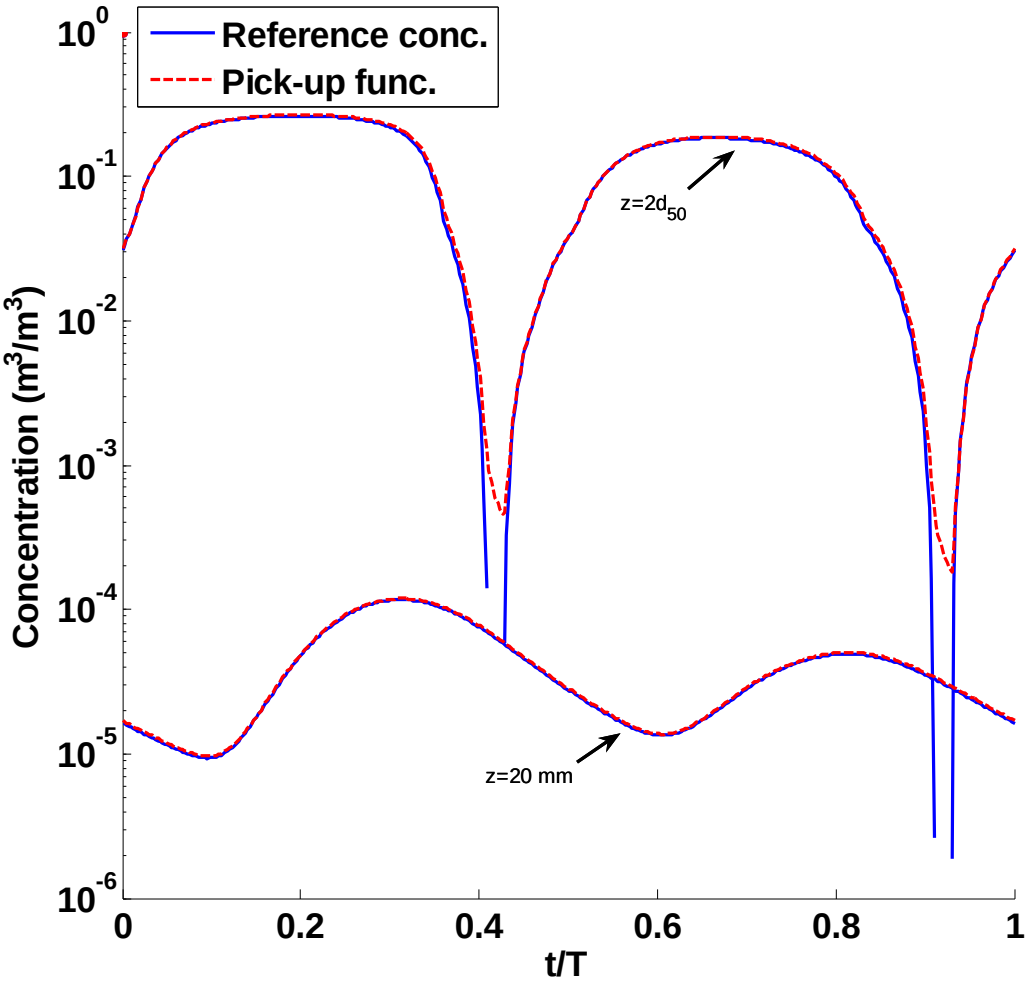

Figure 5.10. Comparison of suspended sediment concentrations when reference concentration and pick-up function are used. Concentration at the reference level (z=2d_{50}) and at 20 mm are shown.

5.6. Phase Lags in the Boundary Layer

The velocities inside the boundary layer have a phase lead over the free stream velocity. The phase lead was found by comparing the time of maximum velocity at each elevation to the time of the peak free stream velocity (Figure 5.11). For the case plotted it reaches a maximum value of 21 degrees at the bottom, from zero at the top of the boundary layer. Most of the change in phase occurs close to the bottom where the change in velocity is also larger. Shear stresses also have a different phase structure. Bottom

shear stress has a phase lead of 16 degrees over the free stream velocity. Reference concentration is in phase with the bottom shear stress.

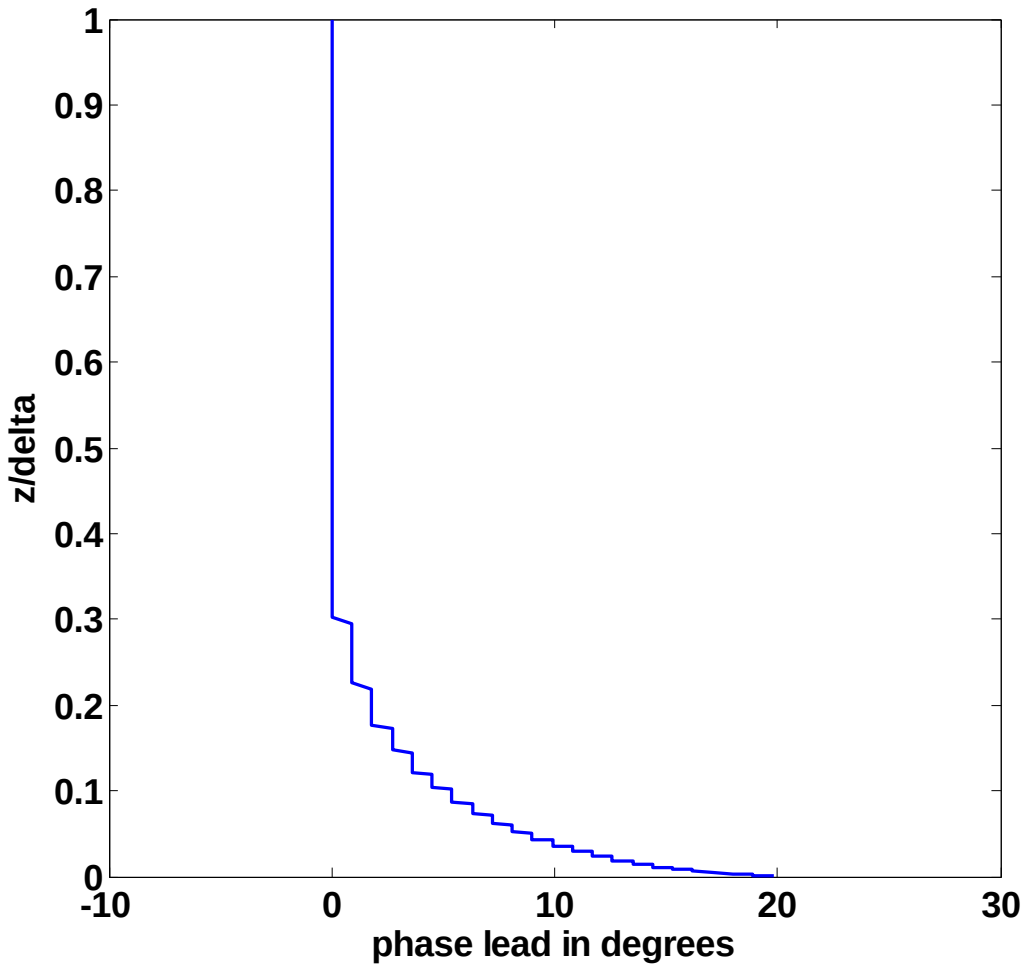

Figure 5.11. Phase lead of velocities inside the boundary layer compared to the free stream velocity. Elevation normalized by boundary layer thickness. The plot is discontinuous due to the temporal and spatial resolution of the numerical grid.

Concentrations also have a varying phase structure over the water column. Figure 5.12 shows concentrations at various elevations and the vertical dashed lines follow the phase for maximum and minimum concentrations. The phase lags of concentrations compared to the bottom concentration are plotted in Figure 5.13. The three lines correspond to the three dashed lines in Figure 5.12. The phase lead at the bottom due to the phase lead of the bottom shear stress quickly becomes a phase lag away from the

bottom. Even before reaching the top of the boundary layer the phase lags exceed 90 degrees, the concentrations decrease, the original peaks disappear and a phase can no longer be defined clearly.

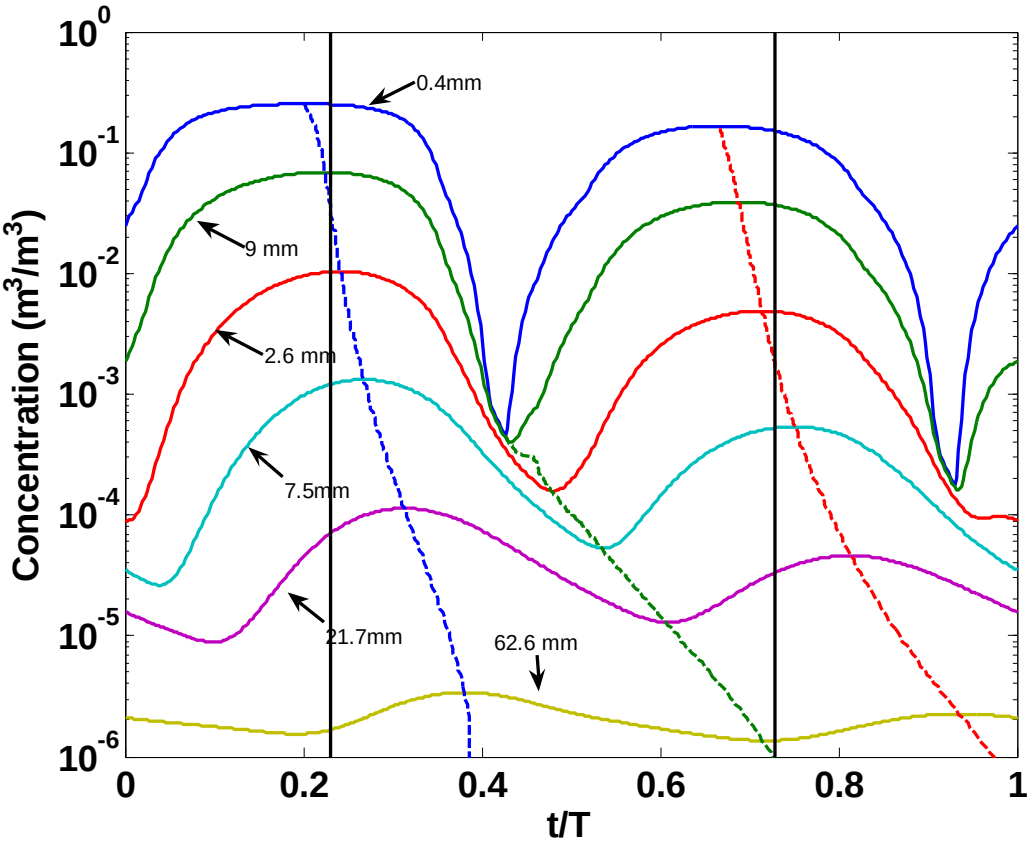

Figure 5.12. Sediment concentrations inside the boundary layer showing phase shift. Solid lines show concentrations at various elevations. Vertical dashed lines follow the peak for maximum and minimum concentrations. Vertical solid lines the times of the crest and trough of the wave.

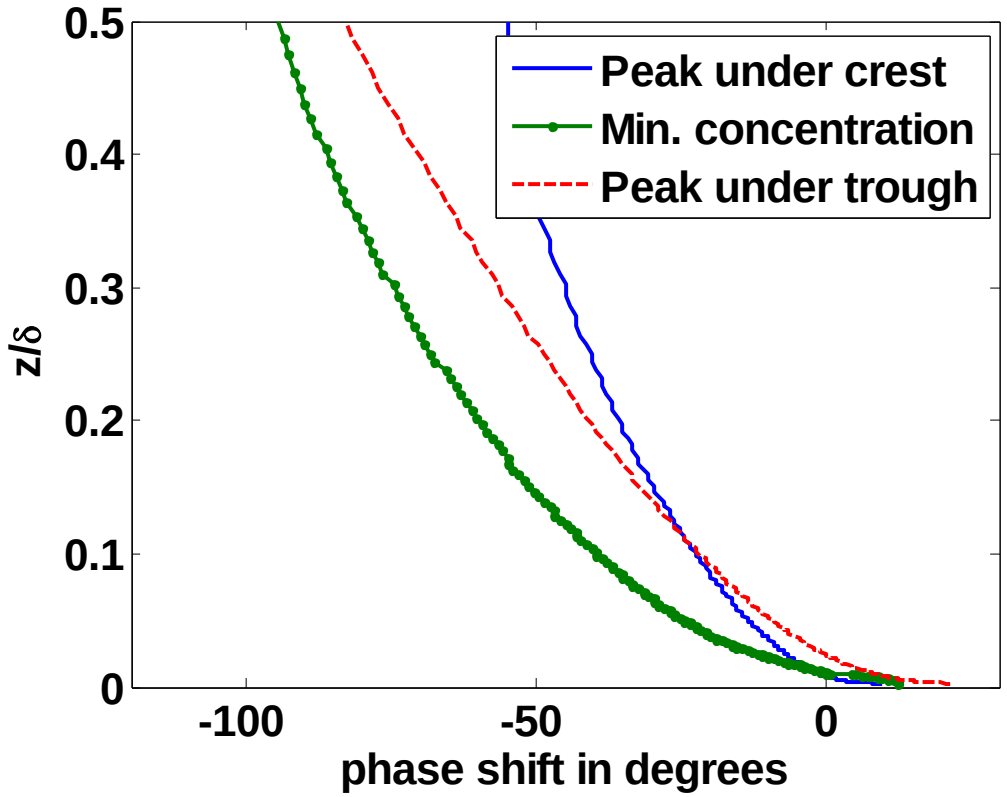

Figure 5.13. Phase shift in concentration inside the BL. Elevation normalized by wave boundary layer thickness. The three lines correspond to the three dashed lines in Figure 5.12.

5.7. Sediment Transport Rate Calibration

There are many parameters used in this model that can be modified to fit the model results to the measurements. The parameters most commonly modified to force a model of this type to fit data are roughness height, turbulence damping parameter and the ratio of eddy diffusivity to eddy viscosity. These parameters are modified to fit the data, because it is hard to measure them directly and there is a range of parameters used for them in literature. A good fit to any specific data set can be achieved by modifying one or more of these parameters.

Roughness height is chosen as $10d_{50}$ in this study and was not used as a calibration parameter. This is within the range used in the literature varying from $2.5d_{50}$ to sheet flow layer thickness which can exceed one cm. The same roughness height was used both for sheet flow and rippled flow. Form roughness was not included explicitly

and the roughness height is underpredicted for fully formed ripples. As roughness height increases friction factor, shear stress, reference concentration, eddy viscosity and the elevation of the theoretical bed level increase. These result in increased concentrations and decreased velocities. The net effect on sediment transport depends on the relative changes in sediment transport and concentration. In various tests both increase and decrease in sediment transport rates were observed as roughness heights were increased. Increasing the roughness height from $2d_{50}$ to 50 d_{50} sediment transport rates changed within 20% to 500% depending on hydrodynamic conditions. A 25 fold increase in roughness height results in maximum 5 fold change in sediment transport rate.

The ratio of sediment diffusivity to eddy viscosity is a parameter about which little is known, and it is often taken to be equal to unity (e.g. Davies and Villaret 2002). It is chosen as 1.0 in this study and is not modified.

The presence of sediments in the flow creates a stable stratification. This reduces turbulence since some energy is spent on moving sediment against gravity instead of mixing the fluid (Li and Davies 2001). This damping of turbulence is represented by a constant turbulence damping parameter, βt. It is multiplied by eddy viscosity to modify its value. Since this parameter is used as the only parameter to calibrate the sediment transport model, its value will incorporate all the processes not included and uncertainty in other parameters such as roughness height. It should be thought of as a calibration parameter rather than strictly as a measure of the turbulence damping, so it will be called the correction factor.

Sediment transport rate data from the literature were used to calibrate the model. Data sources include Dohmen-Janssen et al (2002) (DJ02), (Dohmen-Janssen and Hanes 2002) (DJ&H02), (McLean et al. 2001) (McL01), and (Ribberink and Al-Salem 1994) (R&AS94). Similarly this study is abbreviated as HD07. All of the previous studies are lab studies at prototype or near-prototype scale. The DJ&H02 experiments were conducted in a wave flume, while the others were conducted in oscillatory wave tunnels.

No field data were used in the calibration process because there are many uncontrolled parameters and measurements are fewer, and noisier. Hydrodynamic conditions change and there are three-dimensional effects that are not always captured in the measurements. Sediment transport rate is generally inferred from bathymetric changes. This would give a mean sediment transport rate over a time with changing hydrodynamic conditions. Since most of the time not all the required hydrodynamic parameters are measured directly, hydrodynamic models would be required. This would introduce errors due to the hydrodynamic models. Due to the lack of detailed measurements in field experiments and additional problems it will create as explained above, field data were not used for the testing and calibration of this part of the model.

Both monochromatic and JONSWAP-type random waves were used in the experiments described in R&AS94. The median grain diameter was 0.21 mm. There were no mean currents except weak residual currents. McL01 and DJ02 focused on sheet flows, but used a range of grain diameters. The experiments simulated combined wave-current conditions with monochromatic waves. DJ&H02 investigated sheet flows under monochromatic waves with real waves in a wave flume.

In the HD07 model, the correction factor, βt, was calibrated to a value of 0.40 using the cases with grain diameters greater than 0.2 mm. The calibration was done by minimizing the rms error excluding the cases with low sediment transport rate for R&AS94. Figure 5.14 shows the comparison of computed and measured transport rates. Most of the model predictions are within a factor of 2 except for five cases from R&AS02 at lower sediment transport rates.

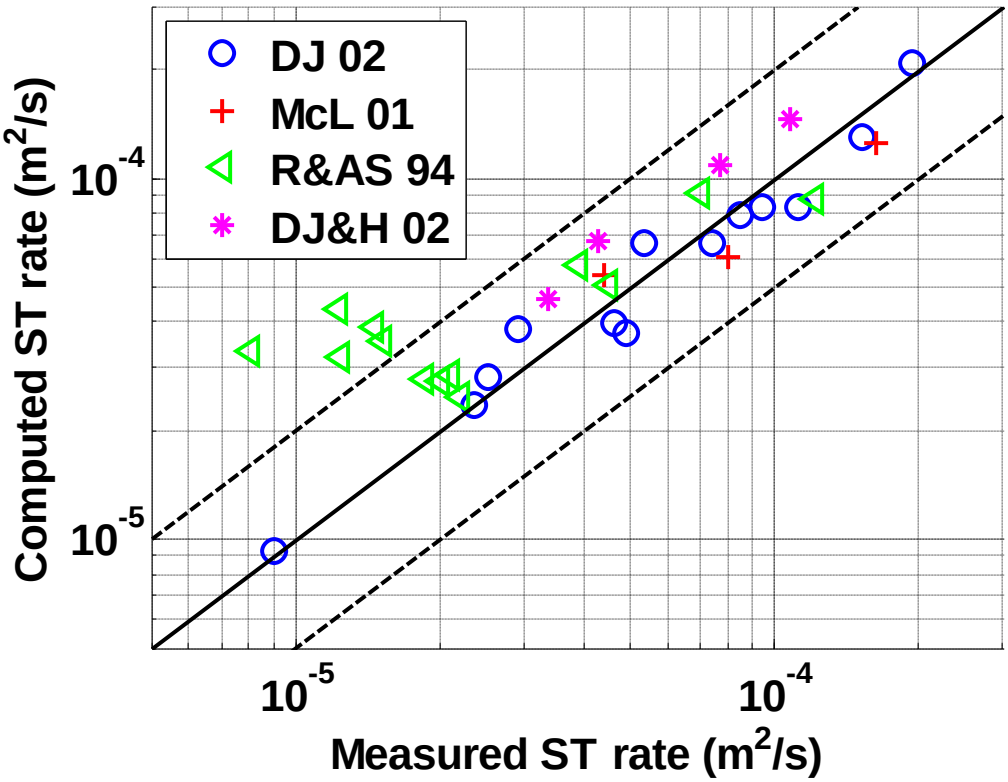

Figure 5.14. Comparison of computed sediment transport rates with measured sediment transport rates for d_{50}>0.2 mm. The solid line in the middle shows the perfect fit. The dashed lines on either side show factor of 2 bands (50% and 200%).

Cases with fine sands were calibrated separately to a βt value of 0.26. The performance is similar to the cases with coarser sands. The optimum βt values found here are comparable to the values found by fitting to concentration and velocity profiles (Dohmen-Janssen et al. 2001). The βt values were 0.22, 0.44, and 0.78 for d_{50} values of 0.13, 0.21 and 0.32 mm respectively. It should be noted that the roughness heights used by Dohmen-Janssen et al. (2001) were significantly higher than the roughness heights used in this study.

Only DJ&H02 used real waves and boundary layer streaming was included only for this case. The inclusion of boundary layer streaming increased sediment transport rates 2 to 4 times. Its effect was more for smaller sediment transport rates.

The fit of the model to the data is worse for smaller sediment transport rates. Net sediment transport rate is the result of small differences between forward and backward sediment transport rates during one wave period. The errors in the model might be bigger for small net transport rates, especially if the half-cycle sediment transport rates are not proportionally small. The errors in measurements are also expected to be larger for smaller sediment transport rates. The values of βt optimized for sediment transport rate are the "standard" parameters for this model. These standard parameters will be used while investigating details of the velocity and concentration profiles unless stated otherwise.

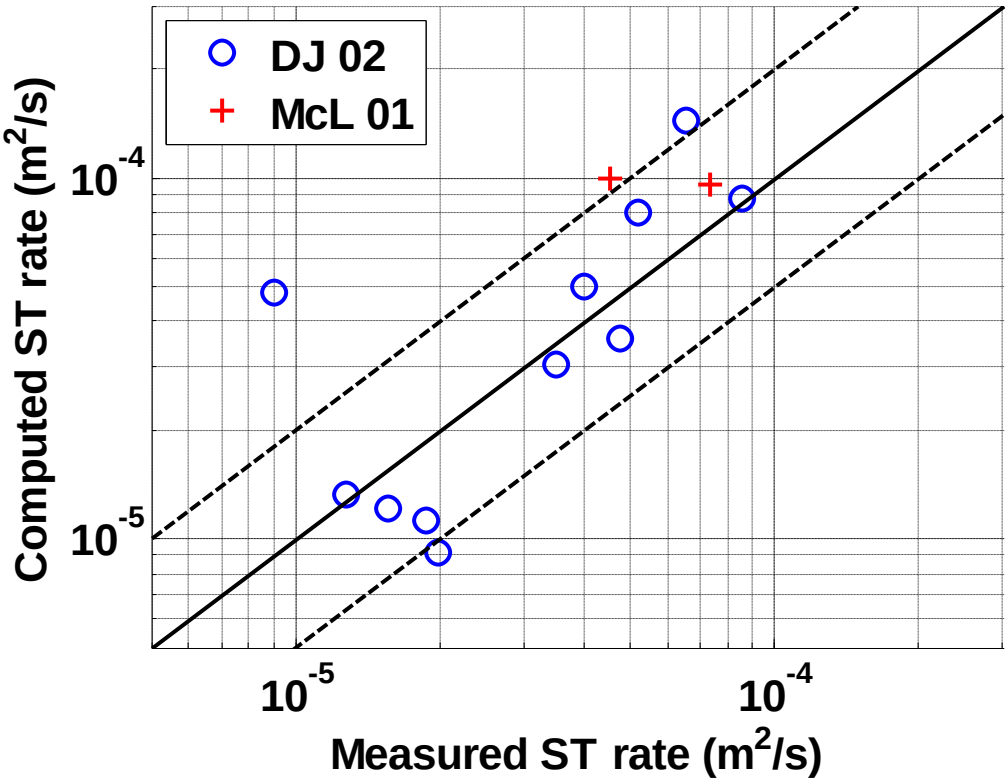

Figure 5.15. Comparison of computed sediment transport rates with measured sediment transport rates for d_{50}<0.2 mm. The solid line in the middle shows the perfect fit. The dashed lines on either side show factor of 2 bands (50% and 200%).

R&AS94 combined their measured data with four other data sets and came up with a sediment transport formula for sheet flow. This model is compared with that

formula in Figure 5.16 since the data for all the other data sets is not available. The fit to their formula is much better than the fit to the measurements, especially for the lower part of the plot (i.e. lower sediment transport rates). Since the R&AS 94 formula was based on a larger data set it might indicate some inaccuracies in the measurements of R&AS 94 for small sediment transport rates.

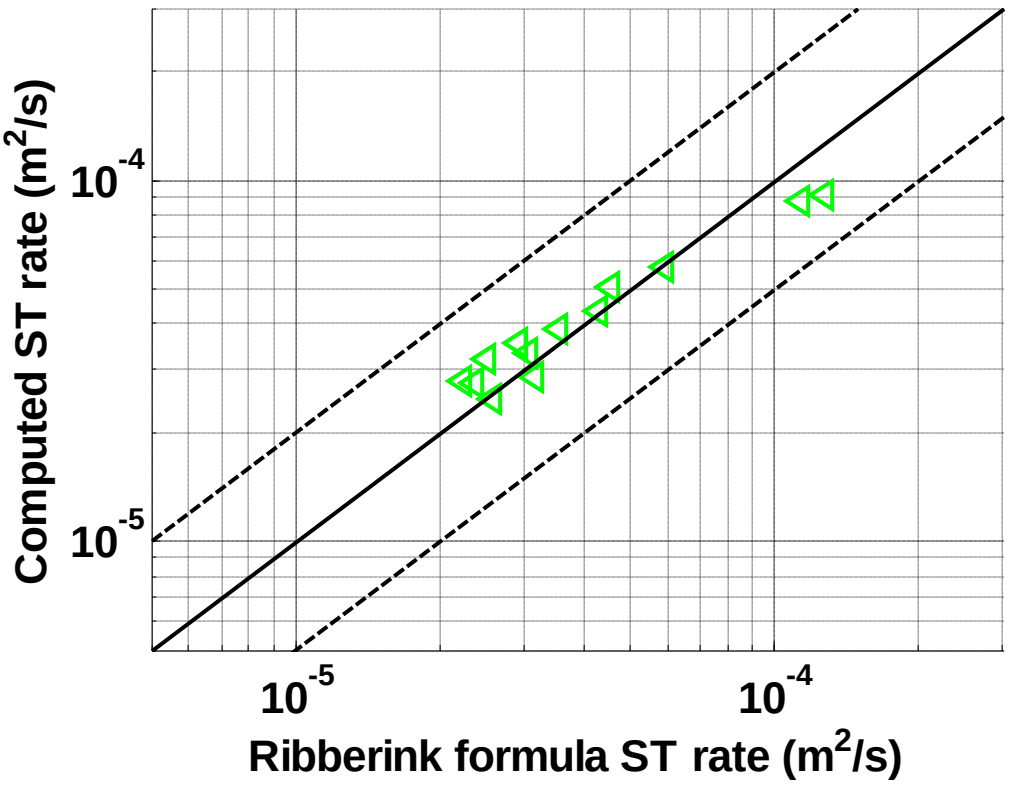

Figure 5.16. Comparison of computed sediment transport rates with R&AS 94 sediment transport formula. The solid line in the middle shows the perfect fit. The dashed lines on either side show factor of 2 bands (50% and 200%).

The sediment transport rate predictions of the new model have also been compared to measurements over rippled beds by R&AS94 in Figure 5.17. The model overpredicts sediment transport rates and the fit is not very good (Sediment transport is predicted within a factor of two in one out of five cases). However a similar result has been observed for flow over planar beds, too, for similarly small sediment transport rates as discussed above. Figure 5.17 compares the model results also to the R&AS 94

sediment transport formula. The performance of the model is much better in that case (within a factor of two in four out of five cases). The reference concentration formulas used in this study (Equations 2.10 and 2.11) were developed for both plane and rippled beds. Diffusion-type models have been employed in predicting sediment transport concentrations over rippled beds, too (e.g. Davies and Villaret 2002). The roughness of rippled beds is typically larger than $10d_{50}$ and is a function of ripple size. The model explaining the sediment transport below the reference concentration flow has been based on sheet flow conditions. Even though the sediment transport model has been developed for sheet flow conditions, its performance for rippled bed cases is still reasonable and can capture the general trends. However the model is not expected to capture the details of sediment transport for rippled cases such as time variation of concentration profiles

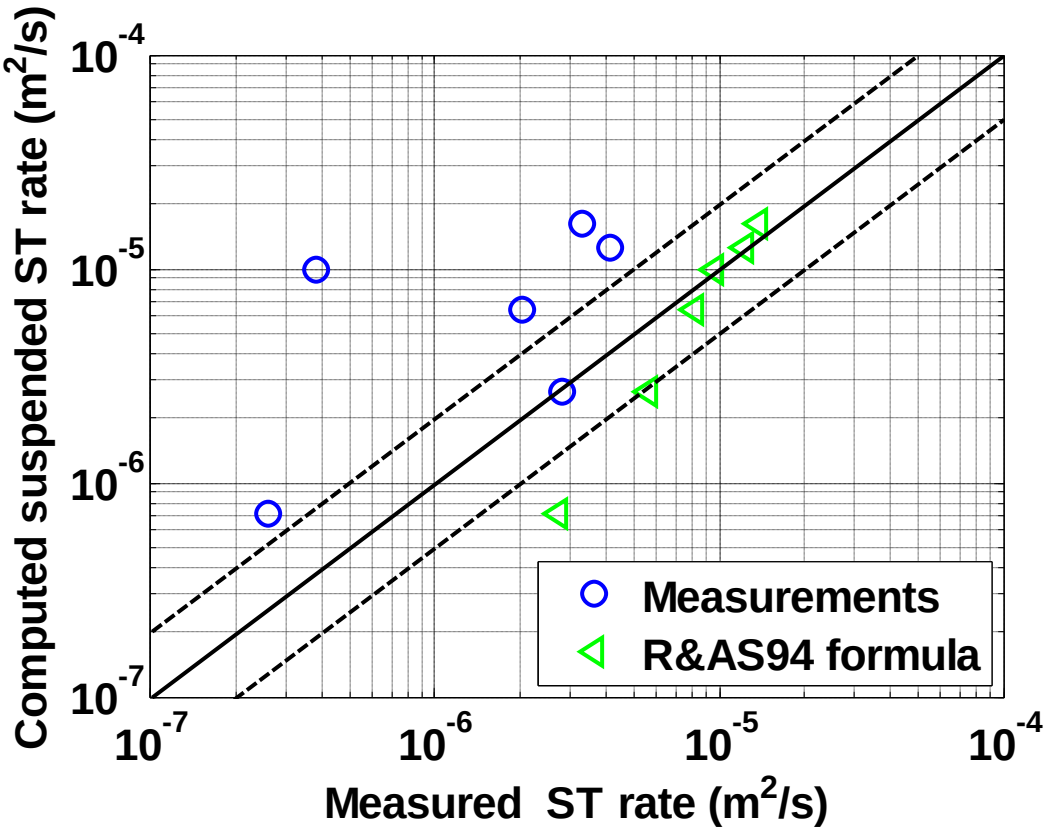

Figure 5.17. Comparison of the computed sediment transport rate to R&AS94 measurements and R&AS94 sediment transport formula for flow over rippled bed.

5.8. Velocity and Concentration Profiles

Dohmen-Janssen et al. (2001) provided detailed measurements of mean velocity and concentration for three cases included in DJ02. Velocities were measured with an acoustic Doppler velocimeter (ADV) close to the bed and with a laser Doppler anemometer (LDA) away from the bed. Time averaged sediment concentrations were measured with a transverse suction system with 10 intake nozzles at different heights. An optical concentration meter was used to measure time variation of concentration above the bed. A Conductivity Concentration Meter system (CCM system), which measures high sediment concentrations using electrical conductivity, was placed inside the sand to measure the high sediment concentrations within the sheet flow layer.

Figure 5.18 through Figure 5.20, which show the measured mean currents inside the boundary layer, are reproduced from Figure 10 of Dohmen-Janssen et al. (2001). The figures also show the results of the Ribberink and Al-Salem (1995) (RA95) diffusion model with standard parameters and modified parameters to fit each plot individually. The results of the HD07 model are also plotted with standard parameters without any individual modification. For d_{50}=0.13 and 0.22 mm the HD07 model can predict the measured mean velocities very successfully with the standard parameters. The same level of success was achieved by modifying roughness height and turbulence damping coefficient, βt, individually for each case with the RA95 model by Dohmen-Janssen et al. (2001). For d_{50}=0.32 mm this model underpredicts the mean velocity. However it is still as good as the standard RA95 model. One parameter was used both for medium and coarse grained sands. The difference in results between medium and coarse sand was not as big as the difference between results for fine and medium sands, so the former two were grouped together. The results would improve if two parameters had been used especially for the coarse grained sands. The optimization is biased towards medium grain sizes since more of that size was used in calibration. These results show that the mean flow inside the boundary layer can be predicted successfully by the model.

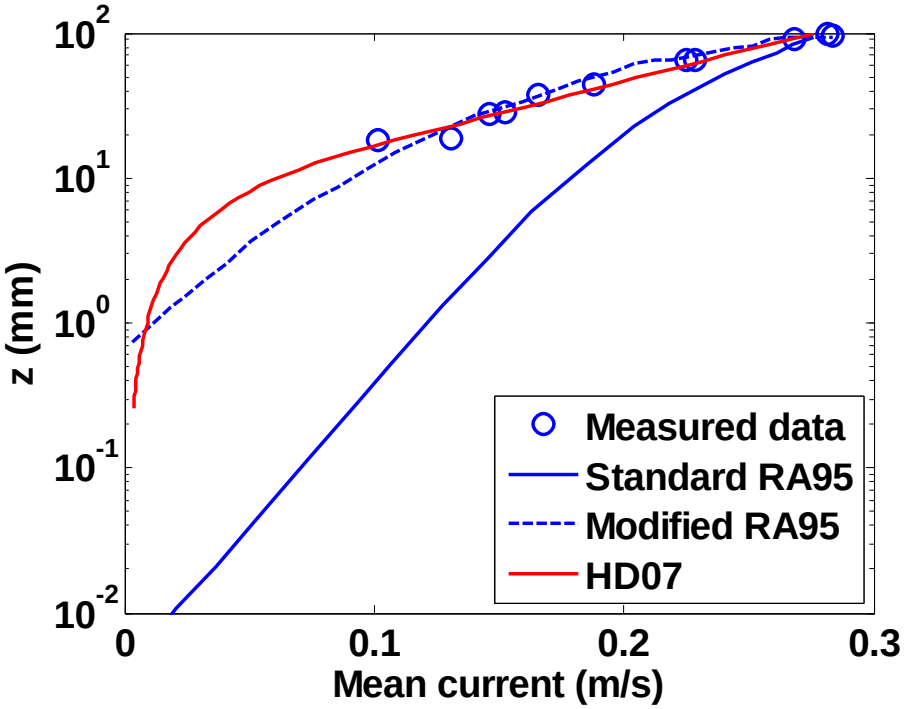

Figure 5.18. Measured and modeled mean velocities inside the BL for d50=0.13 mm. Data and RA95 model results reproduced from Dohmen-Janssen et al. (2001) figure 10.

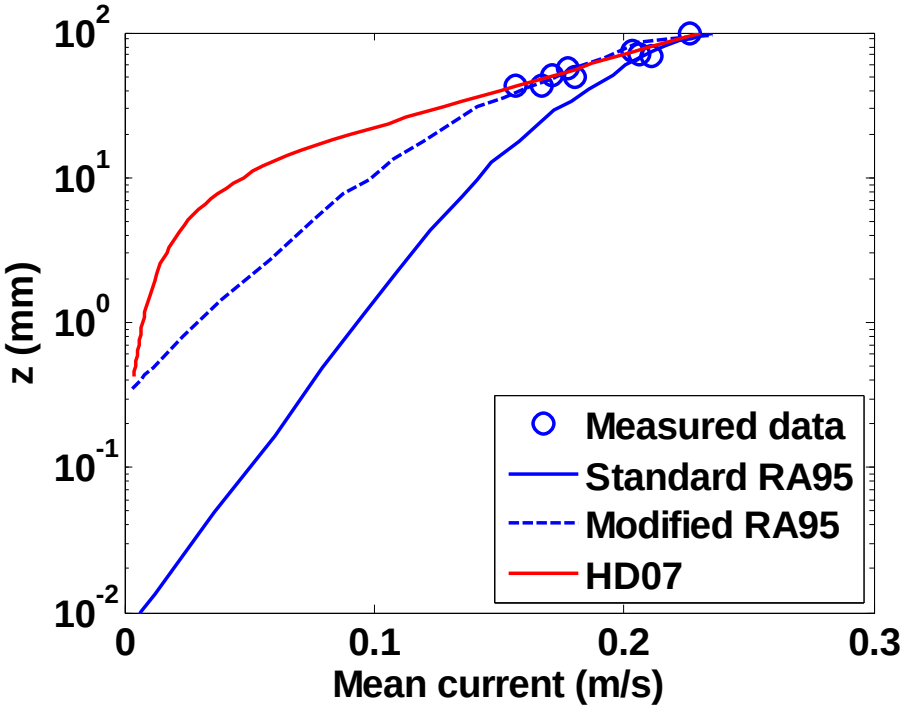

Figure 5.19. Measured and modeled mean velocities inside the boundary layer for d50=0.21 mm. Data and RA95 model results reproduced from Dohmen-Janssen et al. (2001) figure 10.

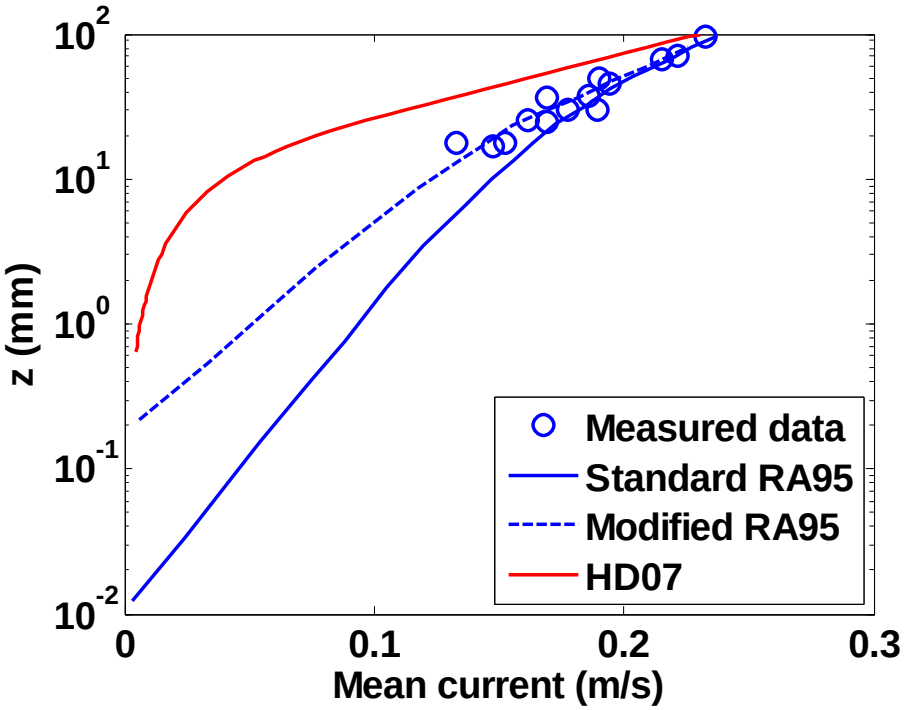

Figure 5.20. Measured and modeled mean velocities inside the boundary layer for d50=0.32 mm. Data and RA95 model results reproduced from Dohmen-Janssen et al. (2001) Figure 10.

Time-averaged concentrations for the three cases discussed above are given in Figure 5.21 and Figure 5.22. For medium and coarse grains the model can predict the magnitude and shape of the mean concentration profile very successfully inside the sheet flow layer, above this layer (Figure 5.21), and higher in the water column (Figure 5.22). For fine sand the model is successful in predicting concentrations above an altitude of 20 mm, but fails below this level. The maximum concentration inside the bed is prescribed to a constant value of 0.55 by the model. However, in this experiment, the maximum measured concentration for fine sand is unusually low and the model overpredicts the concentration inside the sheet flow layer. Above the reference concentration level the concentrations are much higher than the model results. The general shape of the concentration profile does not follow the logarithmic shape predicted by the diffusion model either. For fine sands there are sometimes strong sediment ejection events around flow reversal that can't be explained by the diffusion model and this might explain the underprediction by the model.

Overall the model was successful in predicting both the mean velocity and concentration profiles, with the exception of the finest sediments (d_{50}=0.13 mm). This was achieved using a standard set of parameters without any fine tuning.

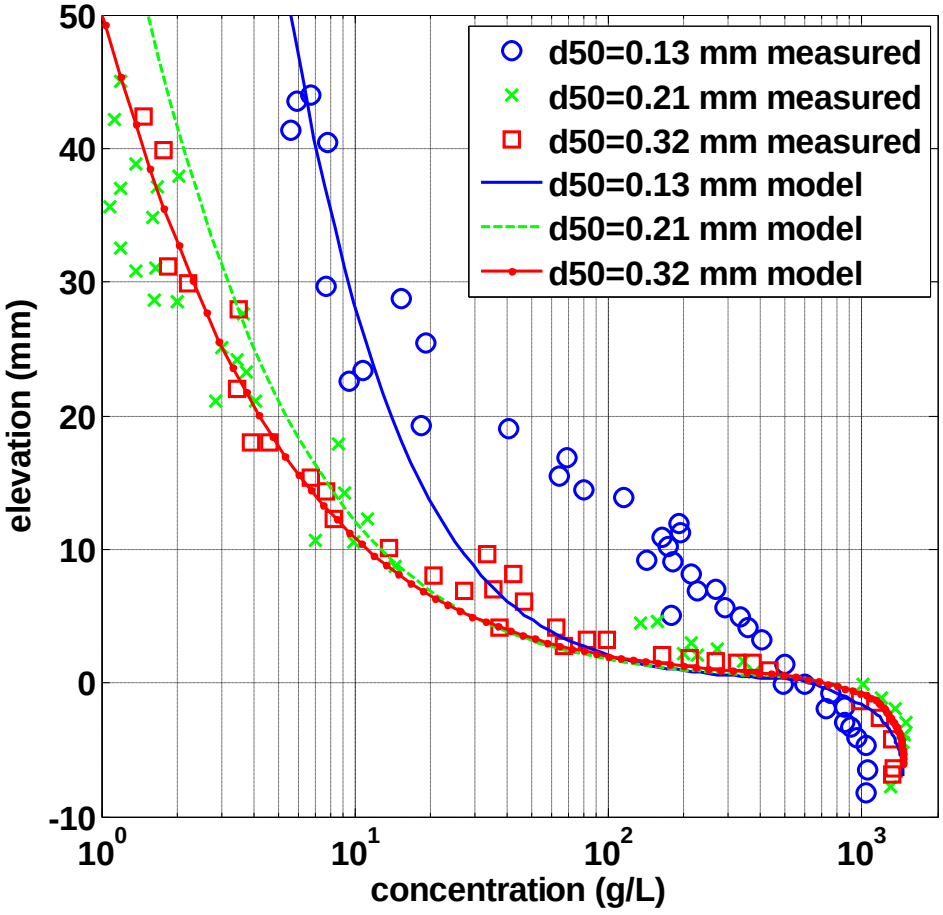

Figure 5.21. Measured and modeled time-averaged concentration profiles for three different grain diameters. Data reproduced from figure 4 of Dohmen-Janssen et al. (2001).

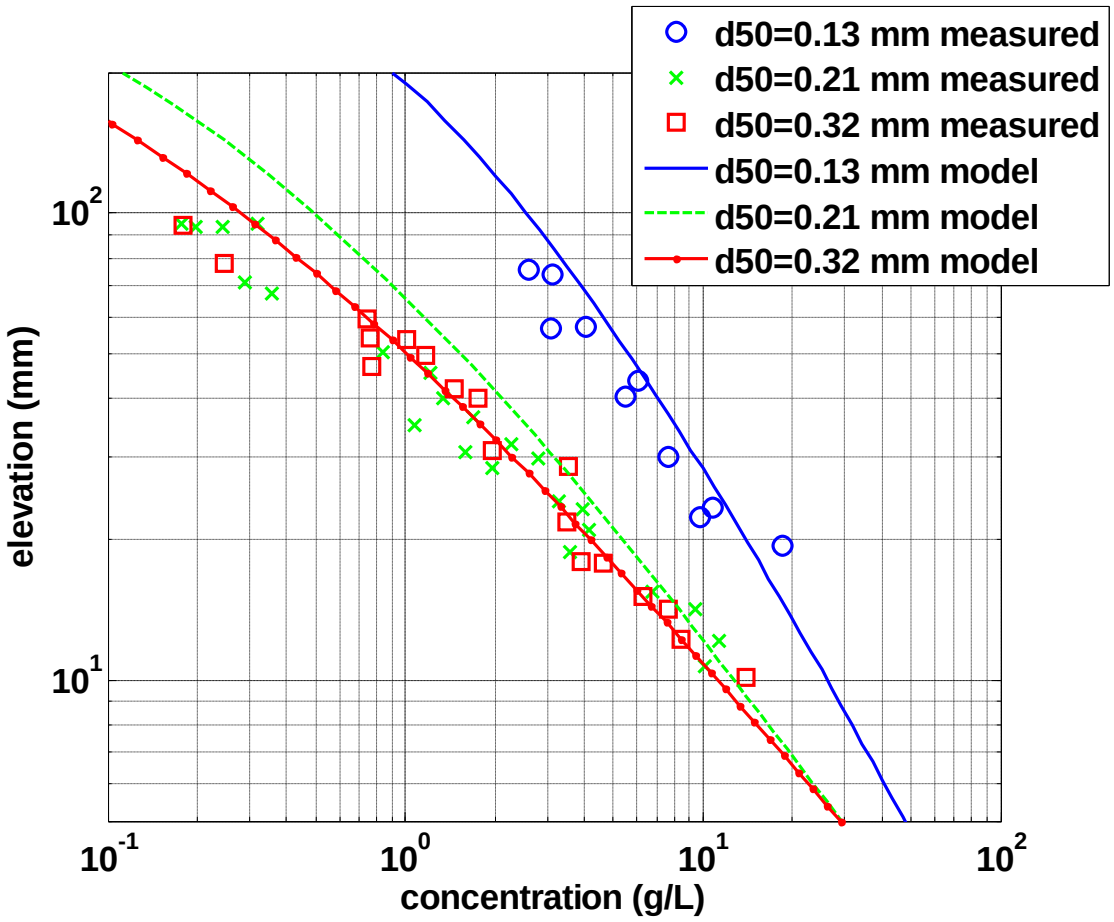

Figure 5.22. Measured and modeled time-averaged concentration profiles for three different grain diameters. Data reproduced from figure 8 of Dohmen-Janssen et al. (2001).

5.9. Erosion Depth and Sheet Flow Layer Thickness

One feature of the new model is that it predicts the erosion depth, d_c directly without using an empirical expression. Erosion depth predictions are compared to measurements in this section. Dohmen-Janssen et al. (2001) (DJ01) measured erosion depth visually by observing video camera recordings with a reported uncertainty of ±0.25 mm. In a later work (Dohmen-Janssen et al. 2002) (DJ02) detailed concentration measurements are published for three cases from the previous work. Figure 14 of DJ02 shows time-dependent sediment concentrations within the bed at various elevations. By looking at this figure an erosion depth can found for each case. The erosion depth found by observing the concentration time series is what the HD07 model is predicting. The

comparison of erosion depth measured by the two methods is given in Table 5.1. The visual observation method gives 1.4 to 2.0 times smaller erosion depths than are obtained by concentration measurements. The erosion depths predicted by the model are compared to the measurements from DJ01 keeping this in mind (Figure 5.23). The model predictions are about twice the measurements by DJ01. Taking into account that the DJ02 measurements are also up to two times more than DJ01, it can be concluded that the HD07 model slightly overpredicts erosion depth.

Table 5.1. Erosion depth measured by DJ01 by visual observation and by DJ02 by concentration measurements.

Case no/ Paper	d_c from DJ01 (mm)	d_c from DJ02 (mm)	$d_{c2/}\, d_{c1}$
D1	2.8	4.0	1.4
D2	2.0	3.5	1.75
D3	2.0	4.0	2.0

DJ01 provides sheet flow layer thickness for five cases with a reported uncertainty of ±1 mm; three of them are discussed in section 5.8. The model predictions for medium and coarse grained sands are very good. Sheet flow layer thickness for fine sand is underpredicted. These results are consistent with the observations made for concentration profiles in Figure 5.21.

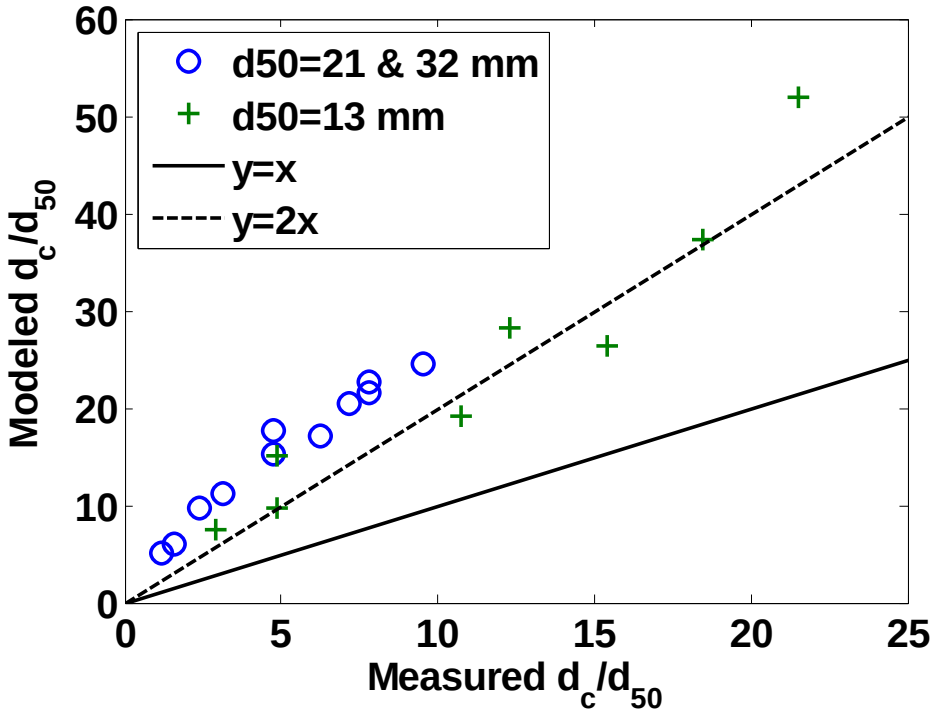

Figure 5.23. Modeled erosion depth compared to measurements. Data from DJ01.

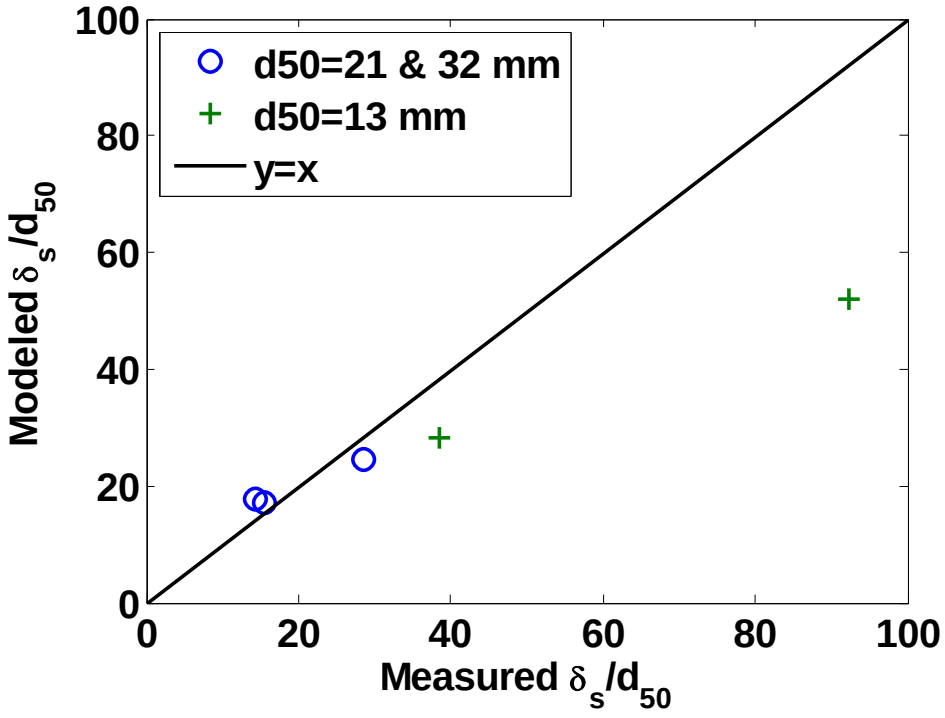

Figure 5.24. Modeled sheet flow layer thickness compared to measurements. Data from DJ01.

5.10. Sheet Flow

Detailed measurements of sediment concentration and velocity within the sheet flow layer under oscillatory flow are hard to make and this type of data is scarce in the literature. One such data set is by Dohmen-Janssen and Hanes (2002) (DJ&H02). Measurements were made in an oscillatory wave tank using prototype scale waves. An acoustic backscatter (ABS) and Transverse Suction system was used to measure suspended sediment concentrations. Two CCM probes were placed along the flow direction. The sediment speeds were measured by looking at the correlation between the two probes. The fluid velocity above the sheet flow layer level was measured using ADV.

Results of case *mh* from the study are used for comparison. This case was designed to simulate a monochromatic second order Stokes wave with a height of 1.6 meters, T=6.5 s, U_c=1.09 m/s, U_t=-0.72 m/s, U_m=-0.037 m/s. This case is simulated twice using standard parameters (βt=0.40, k_r=10d_{50}) and parameters optimized for this case (βt=0.6, k_r=10d_{50}). Only βt is modified. Roughness height k_r could also be modified to get a better fit, but the goal is to compare the general characteristics of the model to available data. Figure 5.25 shows the time-averaged sediment concentrations as measured by Conductivity Concentration Meter system (CCM) and acoustic backscatter (ABS). The concentration predicted by the standard model is mostly within the error bands of the measurements which are about ±1-2 mm for elevation and ±0.5 (m^3/m^3) for concentration. The model underestimates the concentrations above the still bed level, which causes an underestimation of erosion depth and an overestimation of concentration below still bed level. The optimized case has a very good fit to the data showing the ability of the model to correctly predict the concentration profile shape.

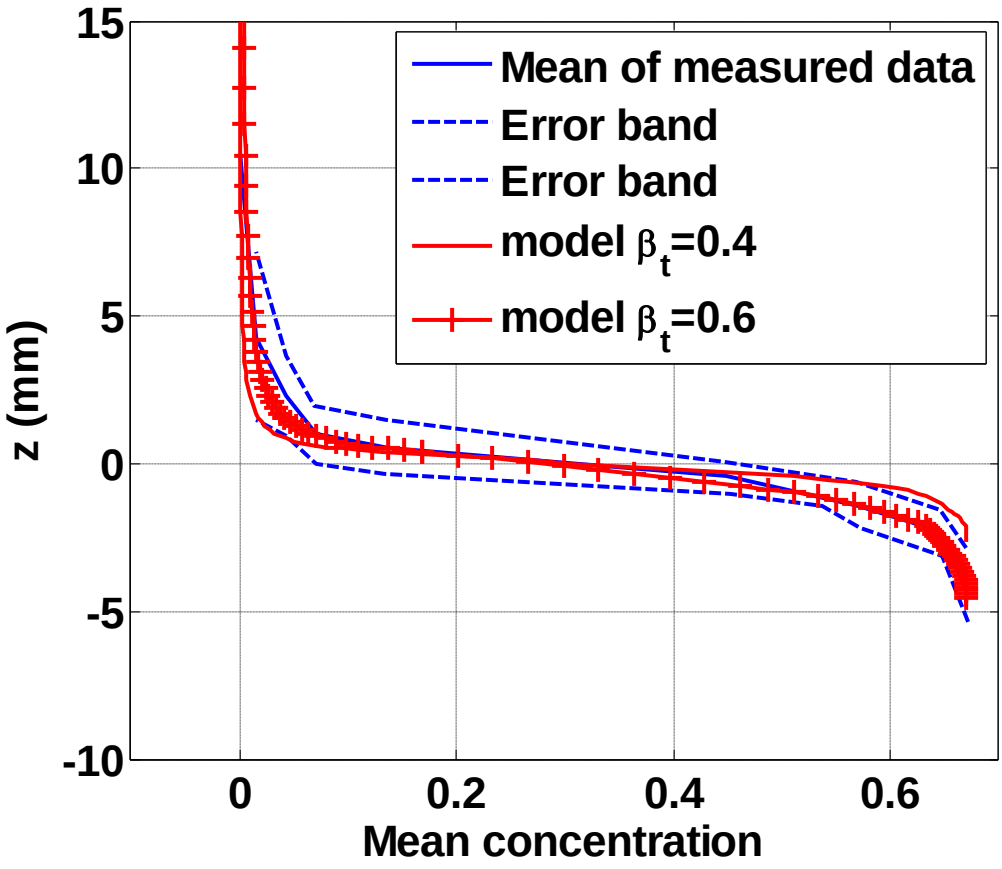

Figure 5.25. Measured time-averaged sediment concentration compared with model results. (Data reproduced from DJ&H 02 figure 7).

Instantaneous concentration under the crest is plotted in Figure 5.26. In addition to the two new model results (HD07) plotted previously it has two different model results. One is a two-phase flow model that is used to model the flow of sediment and water inside the sheet flow layer (Jenkins and Hanes 1998, JH98). The other is a diffusion-type model developed by Ribberink and Al-Salem (1995, RA95). This model is run for two different roughness values ($2.5d_{50}$ and sheet flow layer thickness). These two models were run for this case by Dohmen-Janssen and Hanes (2002) to compare two different approaches to modeling the sheet flow. The approach used in this study is somewhere in between. The diffusion model is used for low concentrations and the high concentration area where a two-phase model is more appropriate is simulated by using empirical velocity and concentration profiles. The RA95 model can't predict erosion

depth and can predict concentration above the reference level at $2d_{50}$. The results were shifted 4 mm to match the measured erosion depth. It should be noted its performance can't be compared directly to the other models since it uses measured data for parameters that the other models are predicting.

Both the JH98 model and the HD07 model can predict the concentration in the lower part the sheet flow accurately. At the top of the sheet flow the JH98 model underpredicts concentrations, while the performance of HD07 is still good. RA95 performs poorly inside the sheet flow layer, but improves for the suspension layer. The HD07 model is overestimating the concentration for the lower part of the suspension layer, but gives improved results higher in the water column. The HD07 model, optimized for the mean concentration (red dashed line) is actually worse than the standard model for this instantaneous plot. Overall, the HD07 model can predict the concentrations as well as the much more complex two-phase flow model (JH98) inside the sheet flow layer.

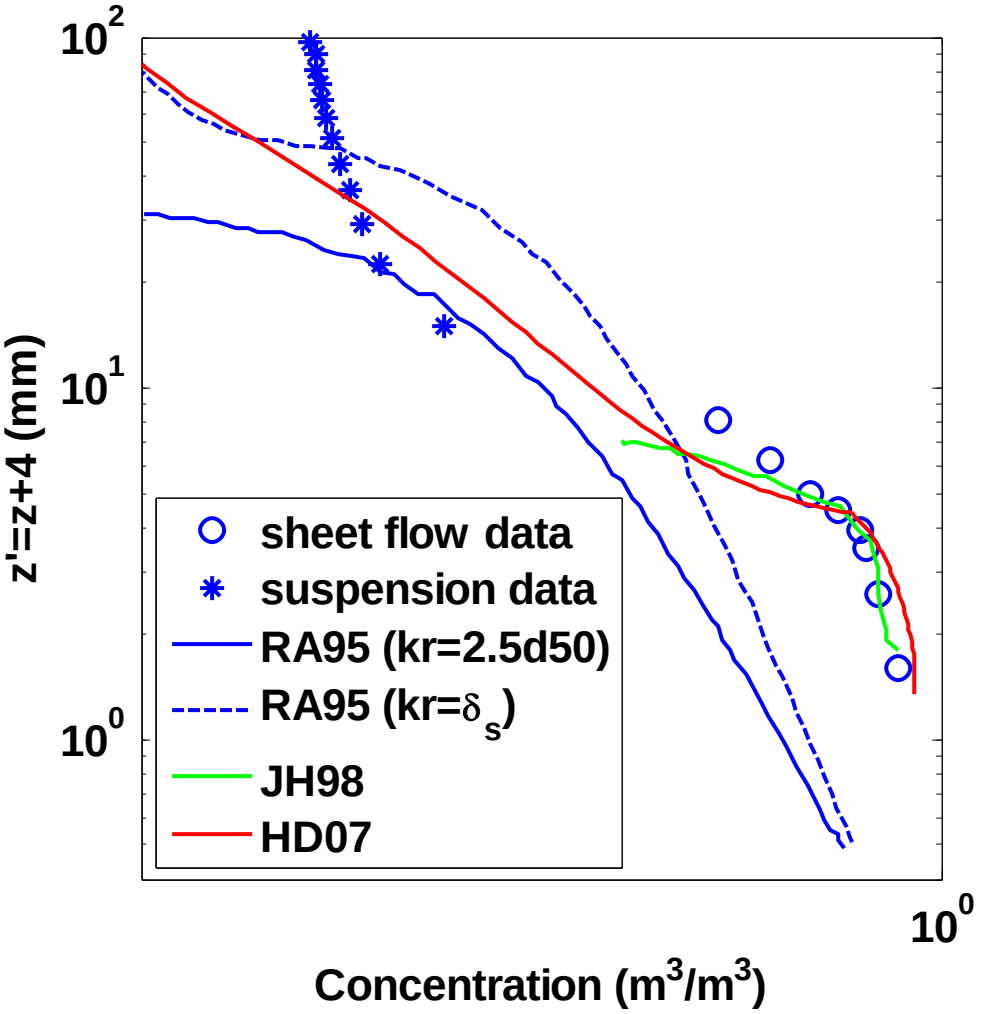

Figure 5.26. Measured instantaneous concentration profile below the wave crest compared with models results. The y axis is shifted 4 mm to be able to show negative elevations on logarithmic scale (Data and model results for RA95 and JH98 are reproduced from DJ&H02 figure 14).

The velocity is compared in Figure 5.27. JH98 models sediment and fluid velocity separately. The difference between the two is very small, supporting the approximation that the sediment moves with the fluid inherent in the other two models. Both JH90 and HD07 underestimate the velocity close to the bottom and give improved results towards the top. The RA95 model run, which uses the sheet flow layer thickness as the roughness height predicts the velocity the best. The performance of HD07 is comparable to JH98.

HD07 underestimates sediment flux in the lower part of the sheet flow layer region because it underestimates the velocity (Figure 5.28). However the results are

comparable to JH98 and better than RA95. HD07 overestimates sediment flux in the suspension layer, but its affect on the sediment transport rate is minor since the concentrations are small. Velocity and concentration both contribute to the sediment flux. However improving the concentration profile is more important since the range of errors in the concentration profile can be one or two orders of magnitude, while the velocity errors are typically much more limited. As a result HD07 and JH98 models could improve sediment flux predictions without improving the velocity predictions.

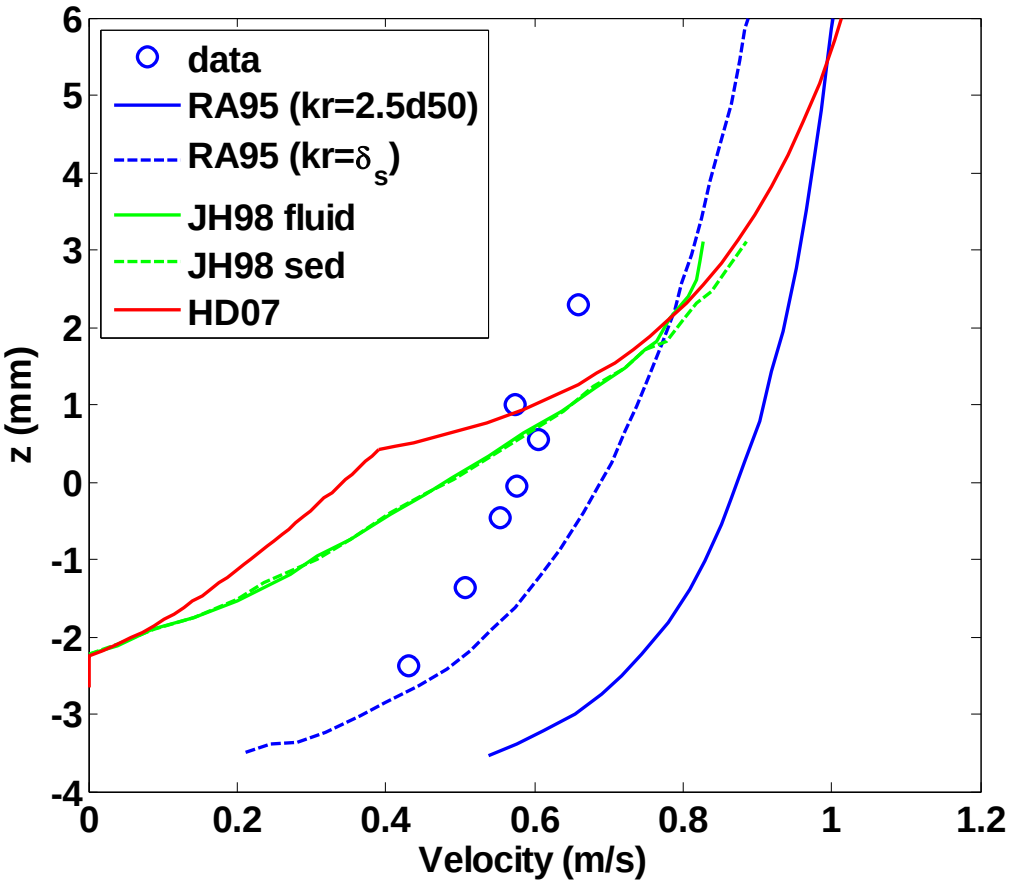

Figure 5.27. Measured instantaneous velocity profile below the wave crest compared with results from other models. (Data and model results for RA95 and JH98 are reproduced from DJ&H02 figure 13).

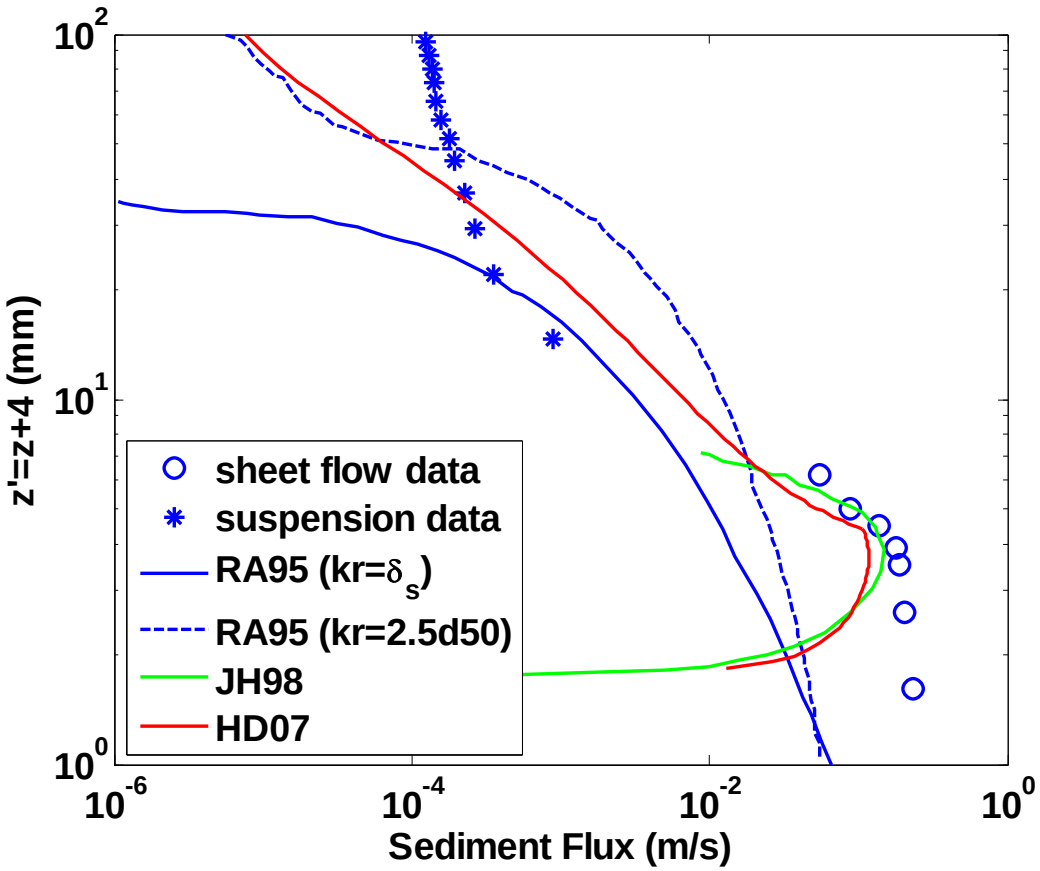

Figure 5.28. Measured instantaneous sediment flux profile below the wave crest compared with results of other model. The y axis is shifted 4 mm to be able to show negative elevations on logarithmic scale (Data and model results for RA95 and JH98 are reproduced from DJ&H02 figure 15).

5.11. Time Variation of Sediment Concentration

DJ&H02 made detailed measurements of the time variation of concentration inside the sheet flow layer. Figure 5.29 is reproduced from Figure 9 of DJ&H02. The erosion depth is 4 mm for this case. The region between z=0 and z=-4 mm is the pickup region. When shear stress increases (e.g. under the wave crest, for t/T=0.2) the concentrations in this region decrease since the sediment is picked up and entrained into the flow. Sediment concentration above this region increases. The sediment entrainment under the crest is very clear, but the sediment entrainment under the trough of the wave (t/T=0.7) is much milder.

Model results for the same case are given in Figure 5.30. The model uses the standard parameters except bed concentration level which was taken as 0.67 to match the measured value. The model can capture the major features of the time dependence in the sediment concentration successfully. The predicted erosion depth is smaller than the measured erosion depth. The measured concentrations at -2.4 mm are comparable to modeled concentrations at -1.4 mm. However it should be noted that the vertical thickness of the measurement volume is itself 1-1.5 mm. The magnitudes of the concentration peaks above z=0 mm are predicted accurately. The concentrations around flow reversal (t/T=0.4) decrease sharply in the model, since shear stress goes to zero (top figure). The decrease is much milder in the measurements. The concentration peak under the trough appears more pronounced in the model, because of this. Modeled magnitudes of concentration under the trough are close to the measurement.

Higher in the water column (bottom figures) the maximum concentration is predicted accurately. In the model the peak sediment concentration under the crest becomes more dominant. The measurements show that the peak occurs between the crest and trough at higher elevations. This is related to the secondary peak near the flow reversal discussed in section 2.7.6.

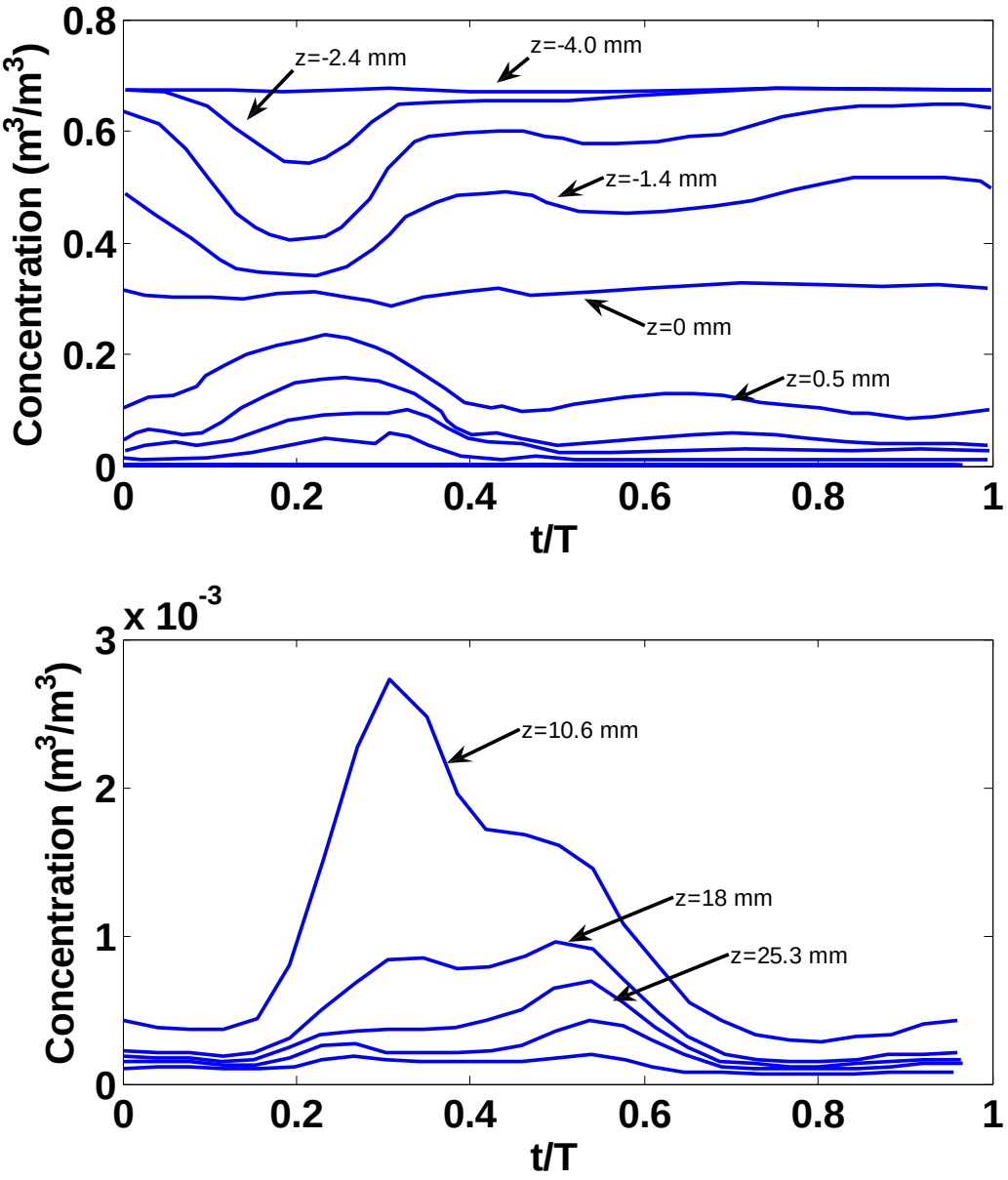

Figure 5.29. Measured time variation of sediment concentration inside the sheet flow layer at various elevations. Top plot: (-4, -2.4, -1.4, -0.4, -0.2, 0,0.5 1 2.3 4.2) mm, Bottom plot (10.6, 18, 25.3, 40.1, 77, 202) mm. Reproduced from DJ&H02 figure 9.

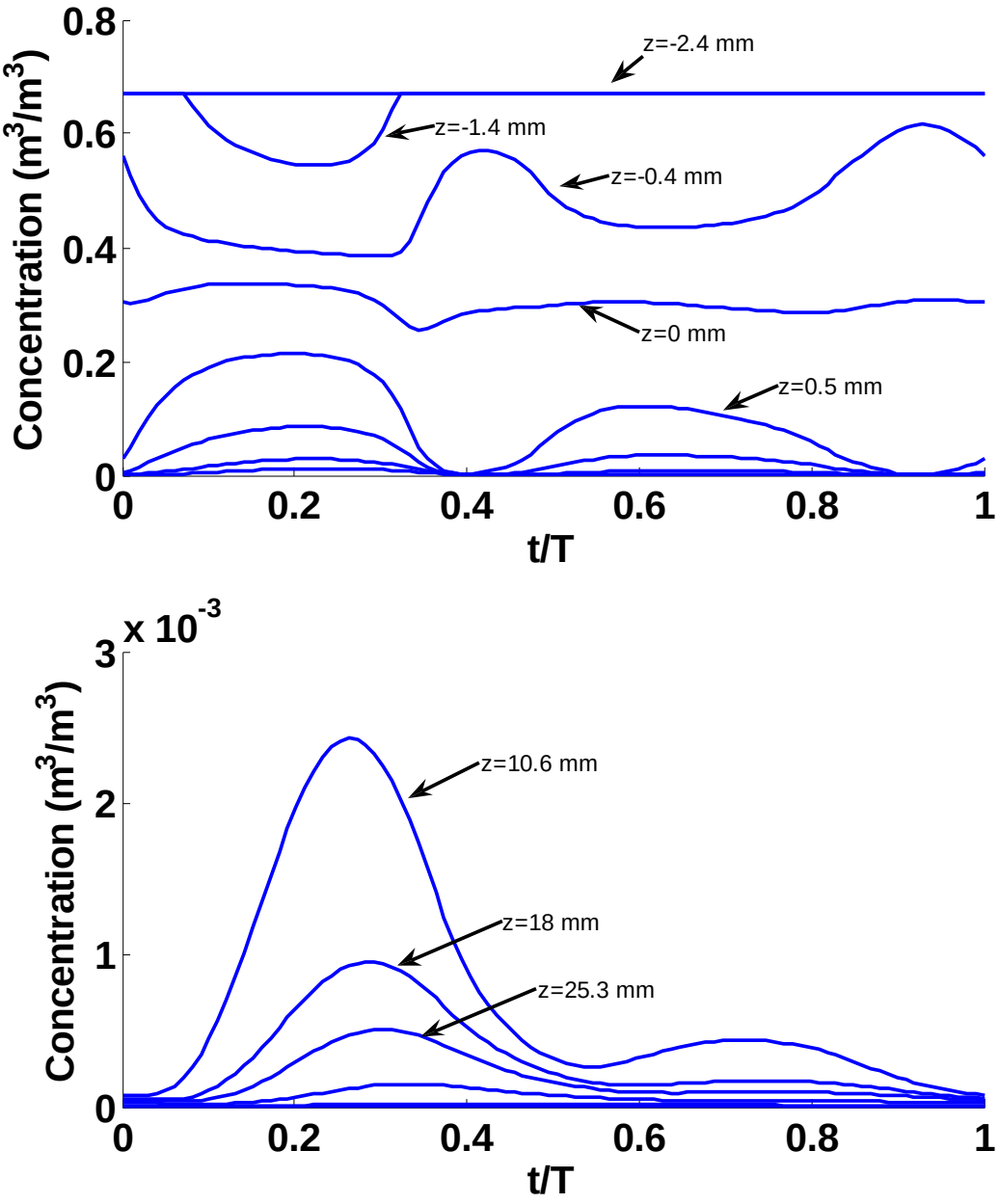

Figure 5.30. Modeled time variation of sediment concentration inside sheet flow at various elevations. Top(-4, -2.4, -1.4, -0.4, -0.2, 0,0.5 1 2.3 4.2) mm, Bottom (10.6, 18, 25.3, 40.1, 77, 202) mm

In summary, a new sediment transport model was developed which can predict time-varying sheet flow thickness and sediment transport within the bed as well as in the suspension layer. The main purpose of the developed model is to predict sediment

transport rate. It could predict the sediment transport rate within a factor of two for prototype scale lab data from four different studies. This success rate is typical of sediment transport models compared to laboratory data. It could also predict mean concentration profile shapes inside and outside the sheet flow layer and the time variation of concentration successfully. Mean velocity profile calculations were also good. However the instantaneous oscillatory velocity is underestimated in the sheet flow region, but still its success is comparable to more complex models. All the detailed comparisons with measurements were conducted using standard model parameters without fine tuning for individual cases.

6. RESULTS II: MORPHODYNAMIC MODEL

The sediment transport model described in the previous chapters was applied to find profile evolution in laboratory and field scenarios. The modeling system is optimized for computational speed, the hydrodynamic model results are tested with measured data, and morphological changes are predicted and compared to measurements. Three laboratory studies from the literature are considered: 1) bar formation, 2) an accretive wave case with onshore bar movement, and 3) an erosive wave case with offshore bar movement. The model is also applied for one field scenario, a short-term experiment at Myrtle Beach, South Carolina.

6.1. Model Optimization

Model grid size and time step are defined explicitly in the master program, but each sub-model can use a finer module time or space step as required by the numerical method. The wave transformation model REF/DIF-S requires spatial resolution yielding at least 5 points per wavelength and uses sub-grids if this condition is not fulfilled. The circulation model SHORECIRC implements a Courant number criterion and generally uses time steps smaller than 1 second. Not all models are run at each time step, but they are run at specified interval time steps. For example bathymetry can be updated at every time step, SHORECIRC can be called at every other time step and REF/DIF-S at can be called at every tenth time step. Choice of these intervals plays a major role in the performance and cpu time of the model. Various simulations showed that circulation is much more sensitive to changes in wave forcing compared to changes in bathymetry. Taking this into account, the circulation and wave models are always updated simultaneously. Morphology update is the fastest of all modules and using a time step sufficiently long to create “significant” bathymetric change is an obvious method to improve model speed. Optimum update intervals can be found to give the best result, but

this optimum would be a function of bathymetry and wave conditions. To overcome this, the NOPP model was modified to update circulation and wave models only after a specified amount of bathymetry change (tolerance) occurs. Change in bathymetry is defined as the maximum change in elevation at any point since the last hydrodynamic update. Maximum change is more appropriate than a mean change since a local error can affect the whole domain pretty quickly and the areas of maximum change are generally the areas of greatest interest.

Many simulations with different tolerances were done to see the effect of the chosen tolerance on results and speed. 1 cm was chosen as the optimum tolerance value to be used. It should be noted that if the scale of the problem changes as in the case of some lab experiments the tolerance value should be decreased accordingly.

6.2. Bar Formation

Many beaches have one or more longshore bars and they interact with hydrodynamic and sediment transport processes significantly. The ability of the morphodynamic model to simulate the bar formation is an important factor in evaluating its performance. The results of this model are compared with the laboratory measurements of Roelvink and Stive (1989) in which a bar was formed on an initially plane beach. This data set was chosen because it includes wave height and velocity measurements at a high spatial resolution across the beach profile. In their study a small-scale plane beach with a slope of 1:40 (v:h) was subjected to normally incident random group waves for 12 hours. In their "case 1" that is discussed below, the peak frequency was 0.50 Hz and the rms wave height was 12.3 cm. A JONSWAP-type spectrum with a peak enhancement factor of 3.3 was used. Waves were generated by a piston-type wave maker and an active wave absorption system was used to minimize the re-reflection of waves reflected from the beach. A sand diameter of 0.1 mm was used. Sheet flow conditions prevailed in the wave flume except at the offshore end where steep ripples

were observed. Velocity measurements were made with an Acoustic Sediment Transport Meter (ASTM) with an estimated inaccuracy of ±1 cm/s 5 cm above the bottom.

The numerical modeling of the flume scenario was done using a horizontal grid spacing of 1 m and hdiff (maximum change in depth allowed before hydrodynamics update) was decreased to 3 mm from its default 1 cm value since the scale is small in the laboratory scenario. Figure 6.1 shows the measured and modeled rms wave height, H_{rms} and horizontal mean velocity 5 cm above the bottom, *U*. Wave height predictions from the model, made using breaking parameter γ=0.55, are excellent. The breaking parameter was chosen by trial and error to give the best wave breaking pattern. Mean, near-bottom velocity predictions made using the default model parameters were 50% less than the measured values. The parameter σ_r controlling the mass flux due to the roller was changed from its default value of 10, to 2. The resulting mean velocity predictions are generally good. Inclusion of roller delay shifts the undertow velocities onshore by about 0.5 meters. The roller delay does not improve undertow predictions for this case, but causes the results to deteriorate by a small amount.

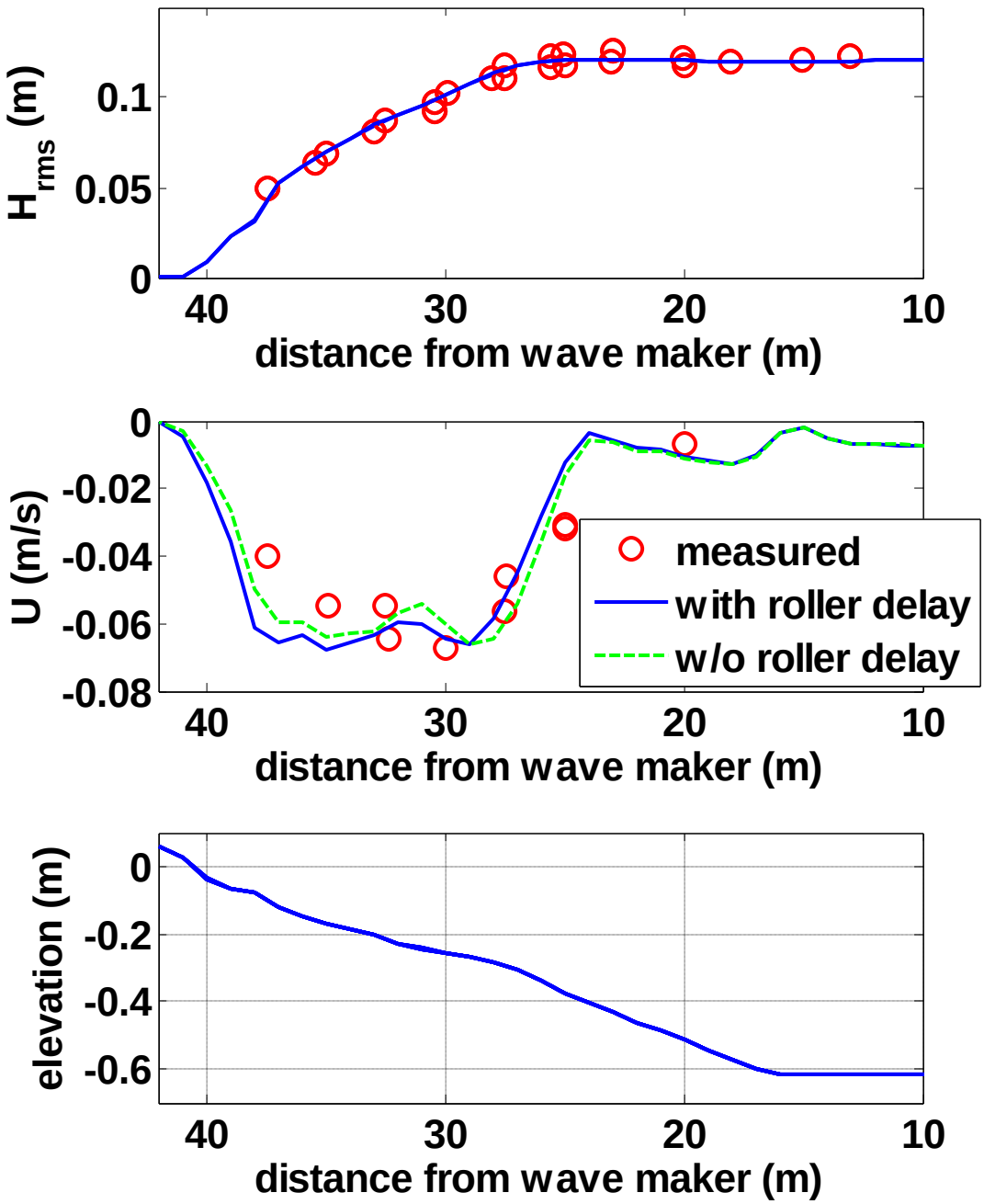

Figure 6.1. Top: Measured (circle) and modeled (blue solid line) H_{rms}. Middle: Measured (circle), modeled (blue solid line) mean near-bottom horizontal velocity. Bottom: Bathymetry. Data from Roelvink and Stive (1989).

Velocity moments are a good indicator of forces controlling sediment transport. Wave-averaged third and fourth velocity moments are given in Figure 6.2. Predicted moments of the oscillatory flows are very good. Orbital velocity and skewness predictions are good. Moments of the total velocity are less than measured values offshore of x=30 m even though the undertow velocities were predicted successfully. The location of the maximum velocity moment, which was measured near x=30 meters, is predicted slightly offshore by the model. Wave groups and associated bound long waves are not simulated by the models; this might explain some of the differences between the model and the measurements. The trends in the fourth moments of the velocity are similar to the third moments, but the differences in model and measurements are more as expected.

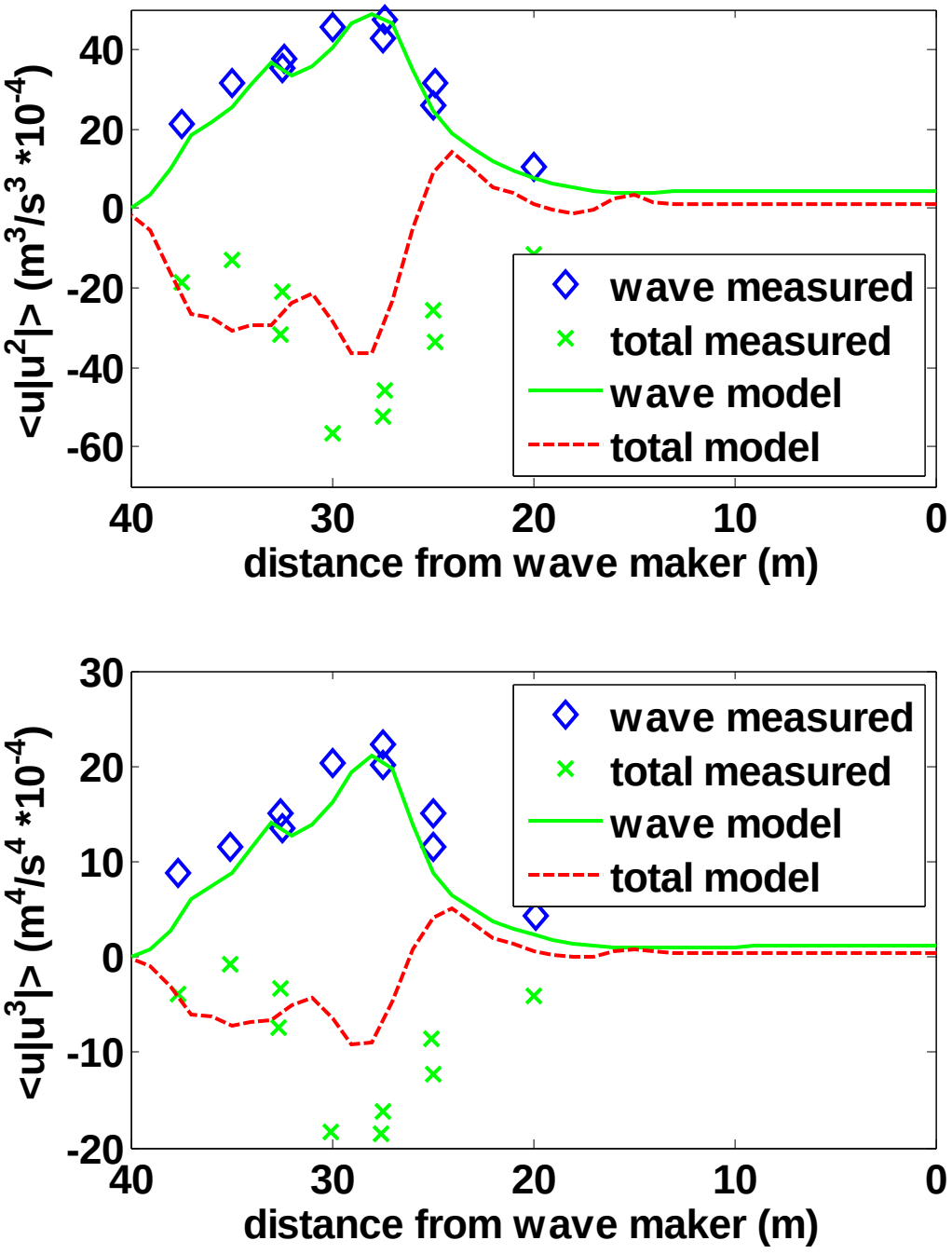

Figure 6.2. Measured and modeled wave-averaged third (top) and fourth (bottom) velocity moments. Total moments are calculated using the total measured velocities. Wave moments are calculated using orbital velocities found by removing mean flow and oscillations at scales larger than the wave period. Data from Roelvink and Stive (1989).

The mean sediment transport rate for the 12-hour simulation was calculated from the beach profile deformation. Zero sediment transport at the dry end of the domain (which is 3-4 grid points inshore of the shoreline) was taken as the boundary condition for sediment transport rate. The computed sediment transport rate is plotted in Figure 6.3 along with two model results computed using correction factors, βt equal to 0.80 and 0.90. These correction factors are significantly larger than the optimum correction factor of 0.26 for fine sand found in the previous chapter using data from oscillatory wave tunnels. Oscillatory wave tunnels do not have a free surface and they damp turbulence more (Dohmen-Janssen and Hanes 2002). This is one factor in this increase. This laboratory test was performed at reduced scales. The sand would correspond to coarser sand which requires larger correction factors at prototype scales. Those studies also did not include breaking waves. The eddy viscosity formulation used in this study takes into account the effect of wave breaking, but its effect might be more than predicted by the model. Also the breaking waves increase the eddy viscosity only in the current boundary layer, not the wave boundary layer. The wave boundary layer might be affected by the breaking waves due to the small scale of the experiment.

The location of the maximum negative (offshore) sediment transport rate is predicted offshore of the measured location. This is consistent with the difference in measured and modeled velocity moments. The measurements show a positive peak at the shoreline. Even though the third and fourth moments of the velocity are negative throughout the domain, the model can predict positive sediment transport rates on either side of the domain. In such cases positive sediment transport cannot be predicted by simpler instantaneous response models such as BBB (Bagnold 1966; Bailard 1981; Bowen 1980) since sediment transport rate is proportional to velocity moments (Roelvink and Stive 1989). As a result of the shift in the sediment transport rates both the shoreface erosion and the offshore bar shift offshore. The model run using βt=0.90 predicts the bar shape better, and the model run using βt=0.80 predicts the shoreface erosion better. The

sediment transport rates are very sensitive to the correction factor. At x=20 a positive peak in sediment transport rate is observed. The model captures that peak successfully even though it is wider than the measured peak. Steep ripples are present in this region in the laboratory, but the model still captures the basic characteristics of the sediment transport.

Suspended sediment flux profiles at a location where the sediment transport rate is strongly offshore (x=27 m, left) and at another location where the transport is onshore (x=38 m, right) are shown in Figure 6.4. The sediment is directed onshore close to the bed and offshore directed above 1.5 and 3 mm for left and right panels respectively. The waves dominate the velocity close to the bed and create onshore sediment transport due to their skewness even in cases with net offshore sediment transport rate. This behavior was observed by Vincent and Green (1990) in the field for flow over rippled bed.

The effect of frequency spread of the spectrum was investigated by using different peak enhancement factors for the JONSWAP spectrum. Velocities and sediment transport rates were insensitive to the changes in the spectrum spread. This agrees with the conclusion of (Rakha et al. 1997) who also investigated different spectrum shapes.

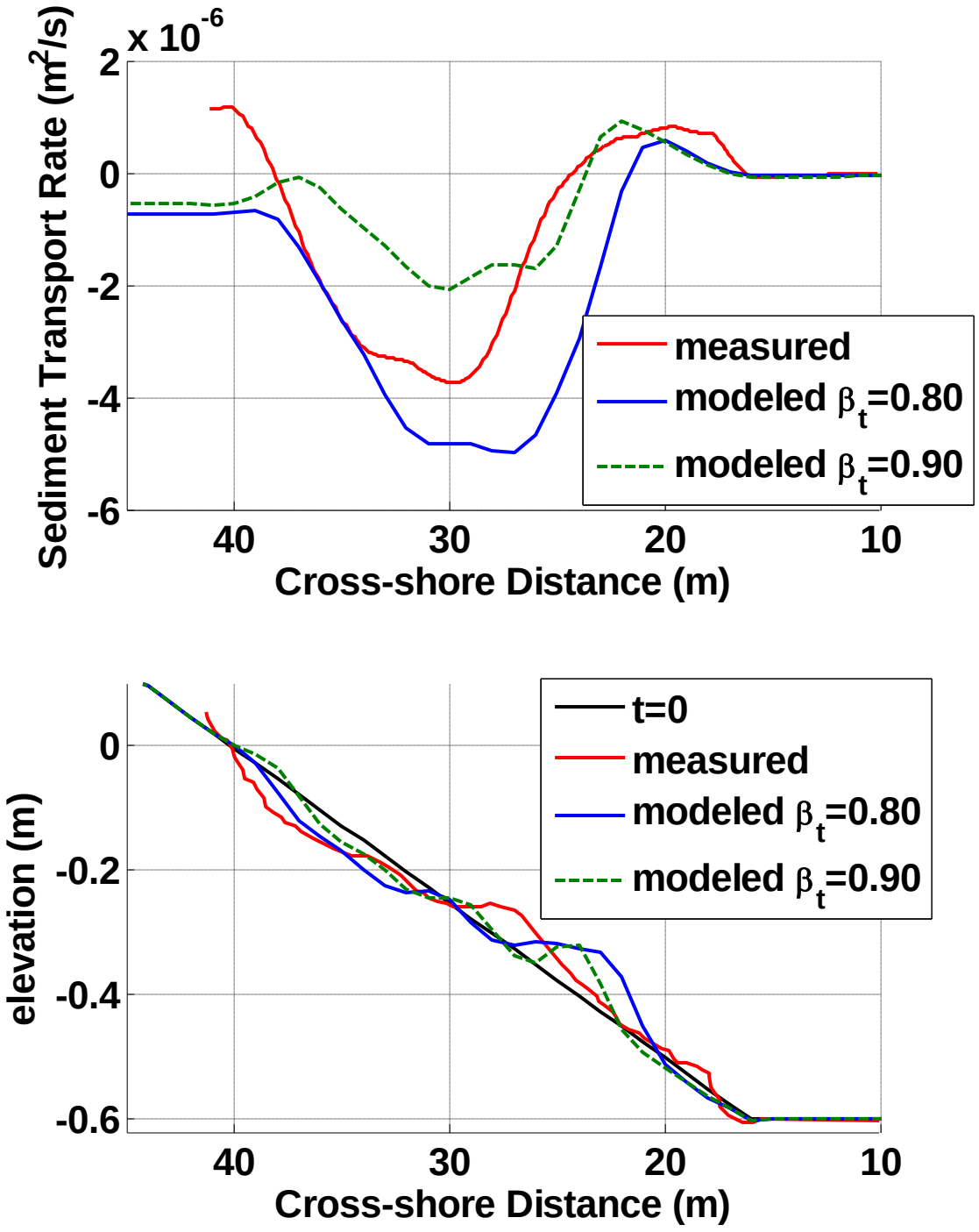

Figure 6.3. Top: Sediment transport rate calculated from bathymetry change. (Positive sediment transport is directed onshore) Bottom: Bathymetry change after 12 hours showing measurement and model results with two different correction factors, *βt*. Data from Roelvink and Stive (1989).

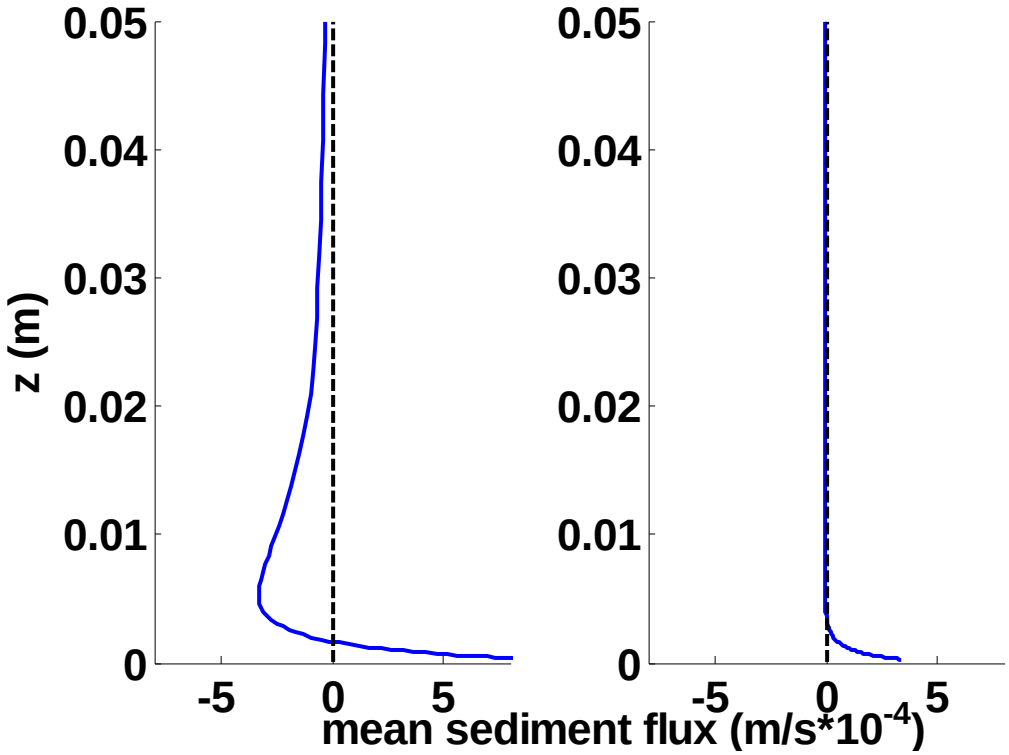

Figure 6.4. Wave averaged suspended sediment flux profile at x=27m (left) and x=38 m (right). Onshore sediment flux is positive.

6.3. Onshore-Offshore Sediment Transport

The ability of the model to predict both onshore and offshore sediment transport and accompanying profile changes was tested and results are described in this section. The data set used for this are from the Delta Flume 93 experiment conducted in the Delft Hydraulics large-scale flume (Roelvink and Reniers 1995). Narrow-banded random waves with normal incidence were used in all experiments. The median sand diameter was 0.2 mm. Wave heights were measured with ten pressure sensors attached to the flume wall. Velocities were measured with 5 electromagnetic velocity meters attached to a carrier at various elevations with a speed accuracy of ±2 cm/s. Bathymetry was measured with a PROVO profiler that uses an echo sounder for underwater measurements and rod displacements for dry land with an accuracy of 0.2 cm

A highly erosive (Test 1b) wave condition (H_{mo}=1.4 m, T_p=5 s) and a strongly accretive (Test 1c) wave condition (H_{mo}=0.6 m, T_p=8 s) were used for comparison. The

results for the strongly accretive case (Test 1b) are shown in Figure 6.5. Wave heights were satisfactorily modeled with breaking parameter γ=0.5, but not as well as in the previous case with the initially plane beach. As the geometry gets more complex the model performance decreases, as expected. Bottom velocities were overpredicted 30% with σ_r =1.6 so this parameter was increased to 6 to give the results shown. The location of peak velocity over the offshore bar was predicted offshore of the measurements even with the roller delay. The case without roller delay was also investigated (not shown here) and it was seen that the roller delay does not shift the velocities onshore at all for this case. The velocity profiles at four locations are shown in Figure 6.6. There are not grid points at x=65 and x=145 for the numerical model. The model results one meter on either side of these points are shown. The model results match the measurements at x=65. At x=102 meters the model overpredicts the velocities close to the bottom, but still reasonable. At x=138 meters even though predicted near bottom velocity is close to the measurements, the shape of the velocity profile is wrong. At x=165 meters neither the shape nor the magnitude of the velocity profile is predicted reasonably by the model.

The sediment transport rates calculated using βt=0.40 and βt=0.70 are shown in Figure 6.7. The location of the peak transport near the bar is predicted correctly, but the peak is wider than is evident in the measurements. Significant sediment transport is predicted onshore of the bar, while the measurements show very little. There are no wave height and velocity measurements available for this region, so the reason for the discrepancy is not clear. The growth and onshore movement of the bar is successfully predicted. The amount of movement predicted is less than seen in the measurements since the strong gradients in sediment transport rate onshore of the bar are smoother in the model. The onshore bar movement can be predicted even though the undertow predictions are not good since the onshore sediment transport cases are dominated by wave velocities rather than the undertow.

Unlike the bar formation case (Figure 6.3), which was an erosive case, the sediment transport rate is not sensitive to the value of βt for the accretive case. The bathymetric results hardly change at all for βt=0.40 vs. 0.70. This might be explained by the shape of the sediment flux profile (Figure 6.4). Increasing βt decreases the amount of sediment being suspended at higher altitudes above the bed. The offshore sediment transport is taking place mostly away from the bed, so erosive cases with offshore sediment transport rate are sensitive to the value of βt. On the other hand, accretive cases are not sensitive to this calibration parameter, since the onshore sediment transport is taking place mostly close to the bed.

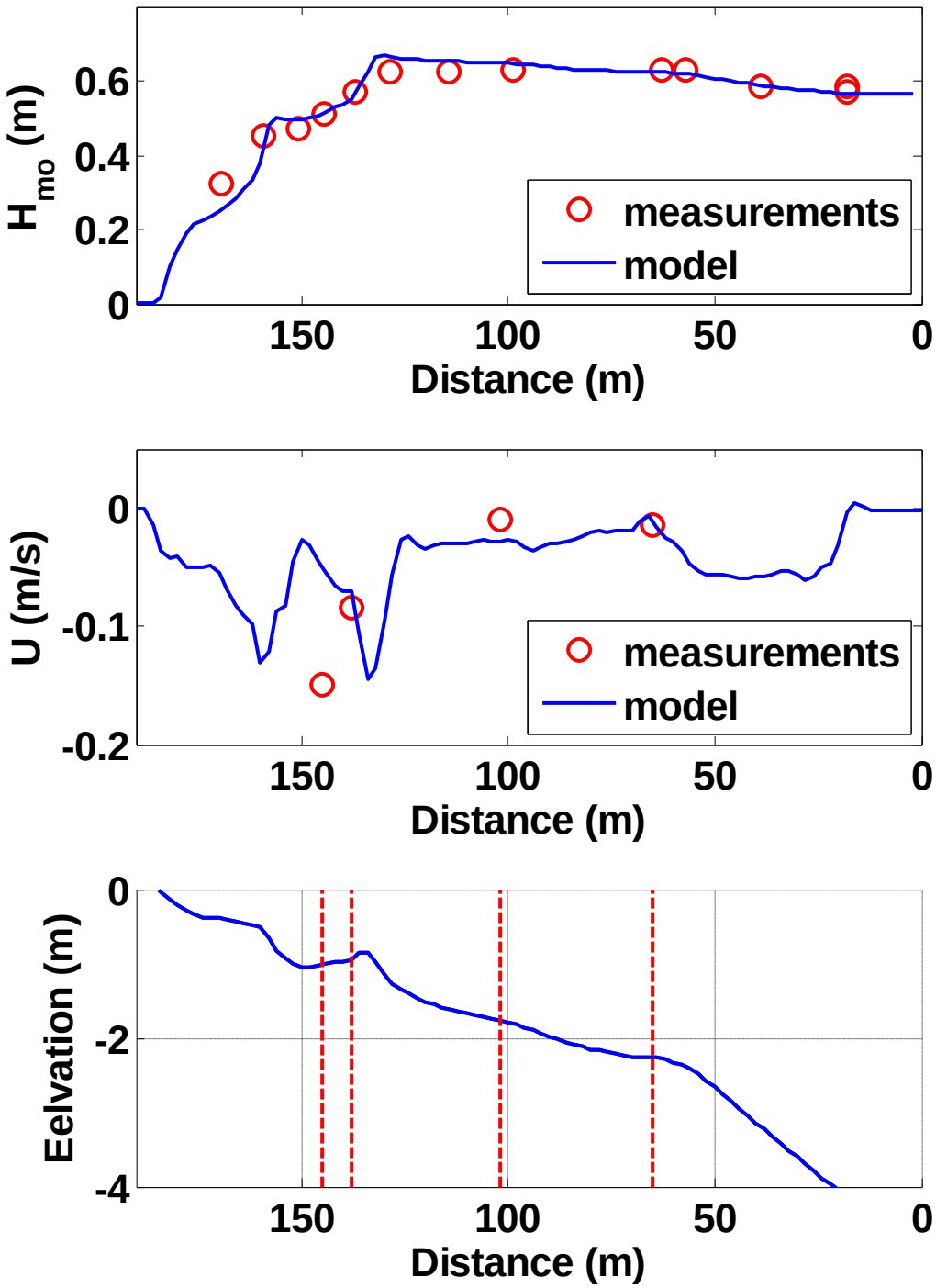

Figure 6.5. Test 1b, accretive case. Top: Measured and modeled wave heights, H_{mo}, breaking parameter γ=0.5. Middle: Measured and modeled mean near-bottom cross-shore velocities, U. Bottom: Bathymetry. Vertical dashed lines show locations of velocity measurements. Data from Rakha et al. (1997).

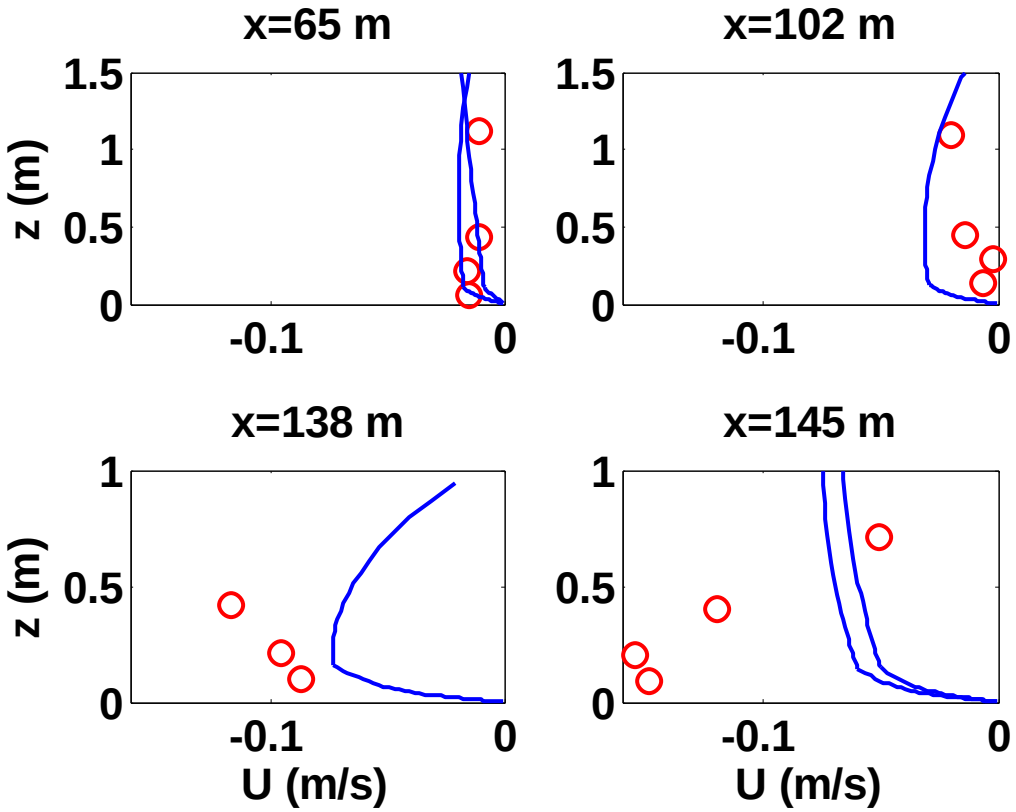

Figure 6.6. Velocity profiles for Test 1b. Red circles show measurements, blue lines show model results. There are 2 model results for x=65 and x=145 since there is not a numerical grid point at those locations. Data from Rakha et al. (1997).

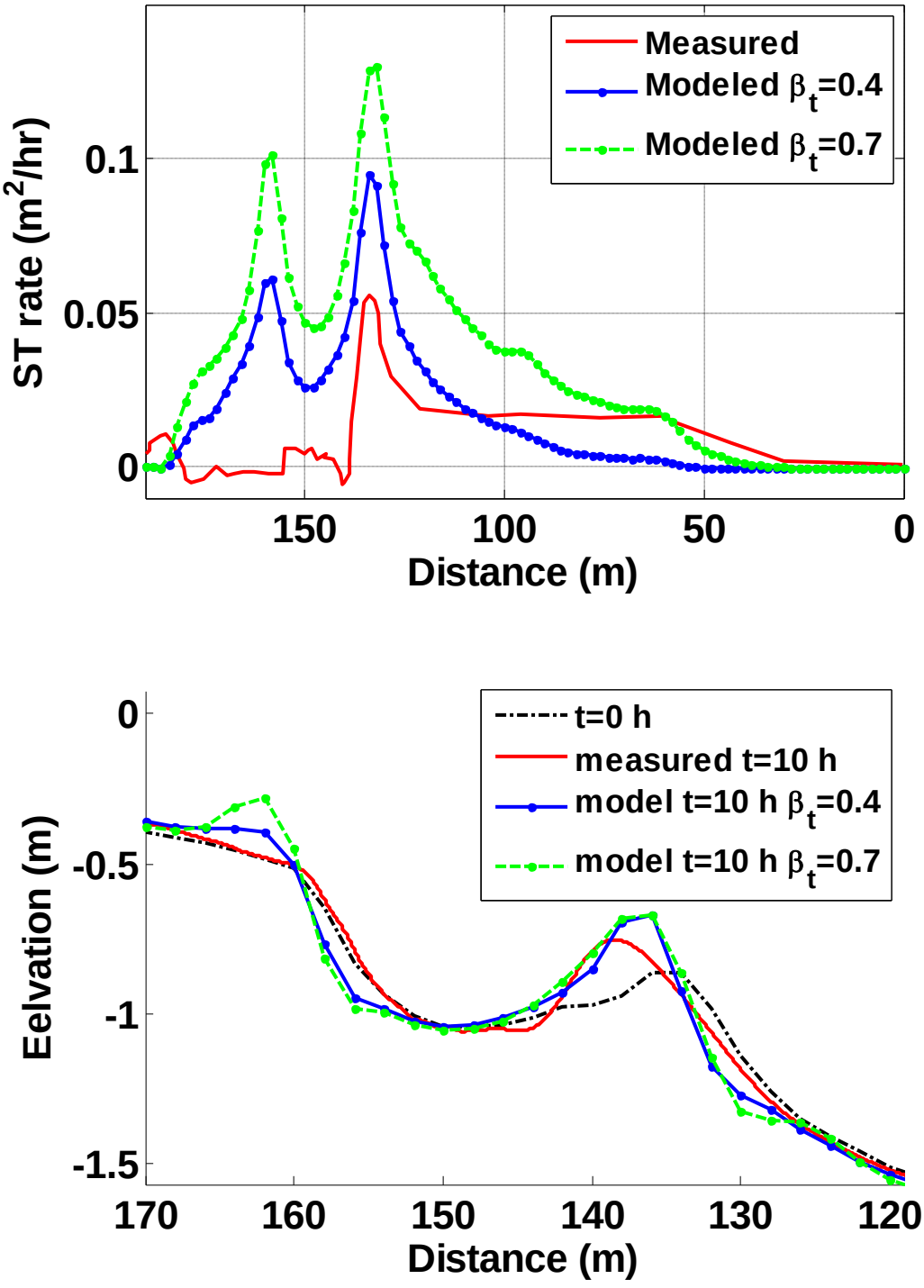

Figure 6.7. Test 1b, accretive case. Top: Sediment transport rate inferred from profile change in 20 minutes (Rakha et al. 1997 fig 7) and initial sediment transport rate. Bottom: Initial bathymetry, measured and modeled bathymetry after 10 hours. Data from Roelvink and Reniers (1995).

Figure 6.8 shows the wave heights, bottom velocities and the bathymetry for the erosive case with steep waves (Test 1b). Wave height predictions (γ=0.6) are good. Wave heights are overpredicted around x=60 meters and underpredicted close to shore. Wave energy dissipation has two peaks: one over the bar at x=140 m and one at the end of the steep slope at x=165 m. These are not easily identified from the changes in wave height, but appear as peaks in the undertow velocity. A roller angle, σ_r, of 1.6 degrees was used for this simulation. The undertow velocity above the bar is predicted well. The velocity around x=60 and x=100 meters is overpredicted. Figure 6.6 shows the velocity profiles at these locations. The shape of the velocity profile is captured successfully at all four locations. The magnitudes are overpredicted up to 0.1 m/s at all locations except x=145 m. The measurements at x=60 were done twice. The difference between the two gives an idea about the variability in measurements. At x=145 model results for x=144 and x=146 meters are shown. Both velocity magnitude and shape change sharply within 2 meters.

The test was run was run for 12 hours. The sediment transport rate inferred from the first 20 minutes of profile deformation is plotted in the top part of Figure 6.10. A correction factor, βt, value of 0.60 was used to match the measured bathymetric change. The initial sediment transport rate is less than the measured values, but the derivative of the sediment transport rate is what controls the bathymetric changes and they match better. The sediment transport rate also increases as the bar grows and moves onshore. The onshore sediment transport on either side of the bar is also captured. The onshore sediment transport at the shoreline is not predicted by the model since swash zone physics are not taken into account in the model. Growth and offshore movement of the bar is predicted by the model (Figure 6.10 bottom). The amount of bar growth is the same as the measured growth, but the model predicts that the bar moves further offshore than is observed. The modeled trough is also shallower than the measured bar trough.

The effect of including the roller delay is seen as a small onshore shift in near-bottom undertow which improves the fit to the measurements (Figure 6.8). However this small shift creates a very significant change in profile evolution. When the roller delay is not included, the bar dissipates instead of moving offshore (Figure 6.10). Offshore bar movement is very sensitive to the undertow profile since it is controlled by undertow.

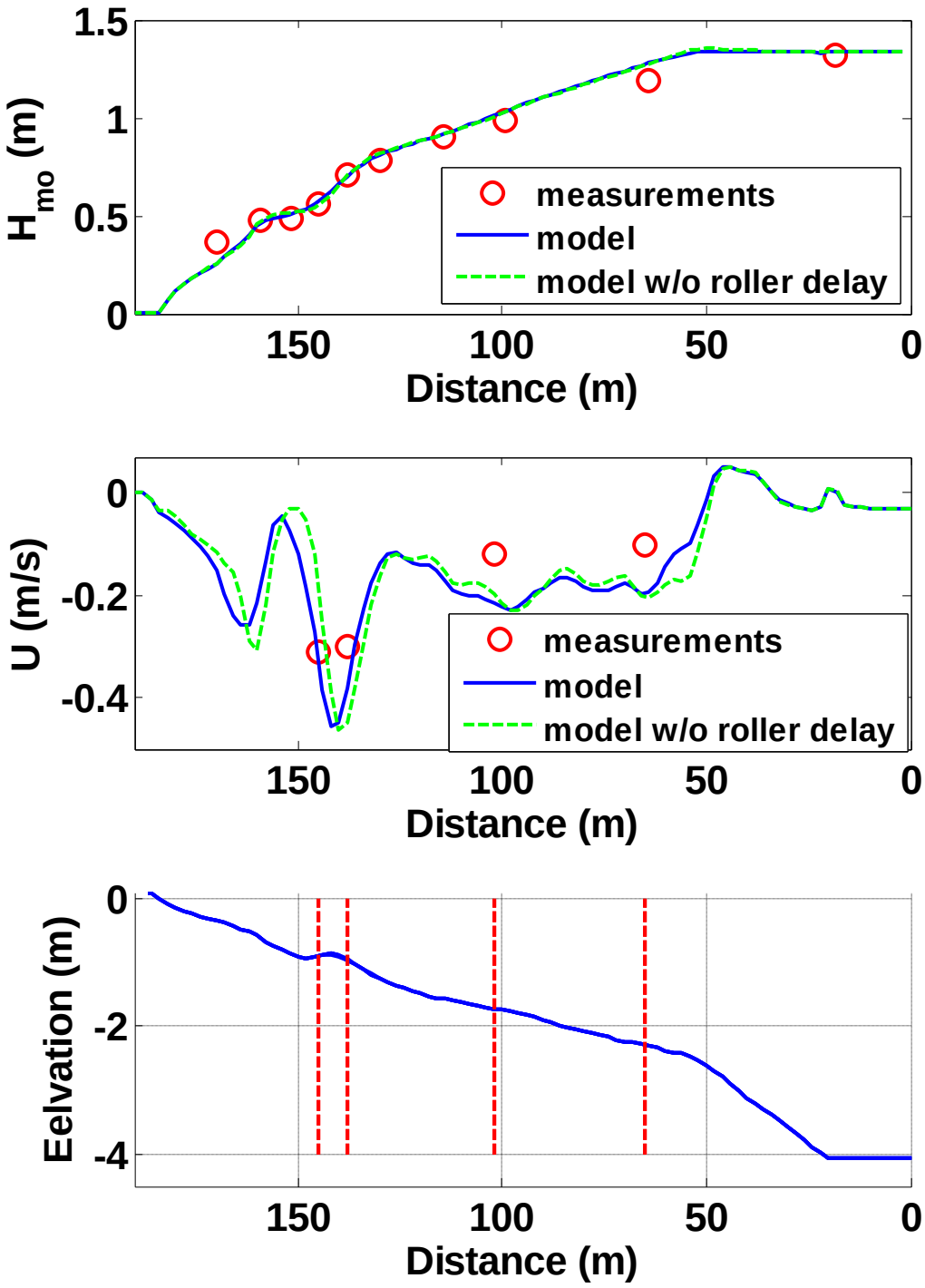

Figure 6.8. Test 1c, erosive case. Top: Measured and modeled wave heights, H_{mo}, breaking parameter γ=0.6. Middle: Measured and modeled cross-shore near bottom velocities, U. Bottom: Bathymetry. Vertical dashed lines show locations of velocity measurements. Data from Rakha et al. (1997).

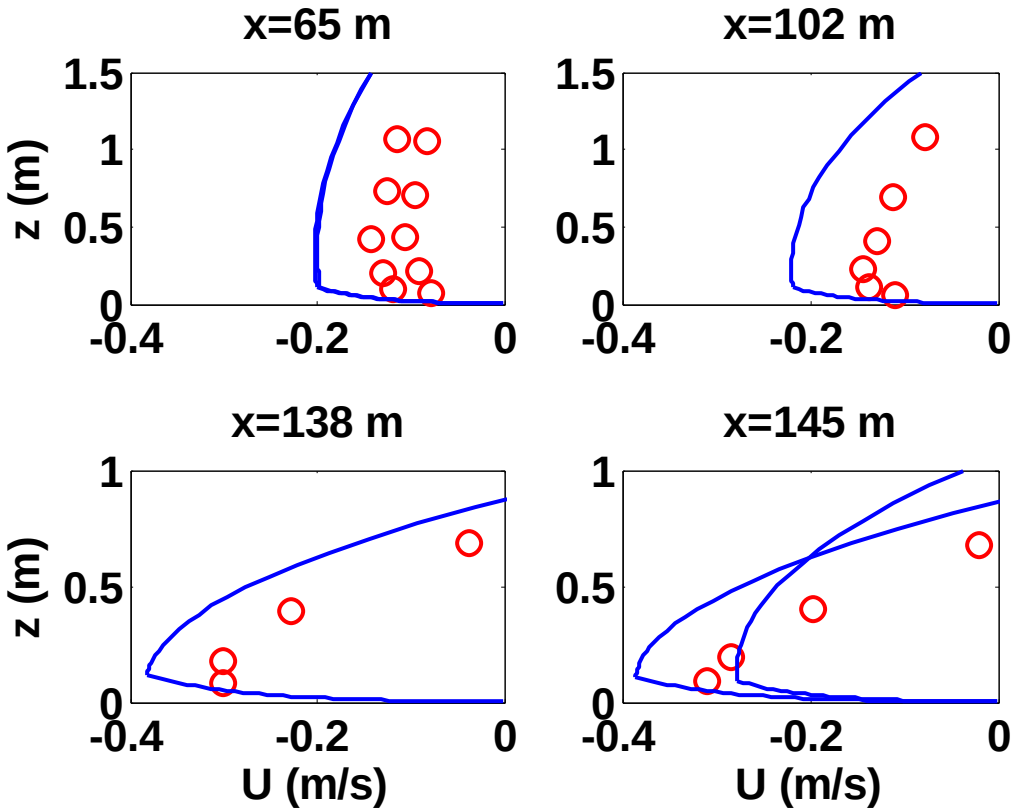

Figure 6.9. Velocity profiles for Test 1c. Red circles show measurements, blue lines show model results. There are 2 model results for x=65 and x=145 since there is not a numerical grid point at those locations. Data from Rakha et al. (1997).

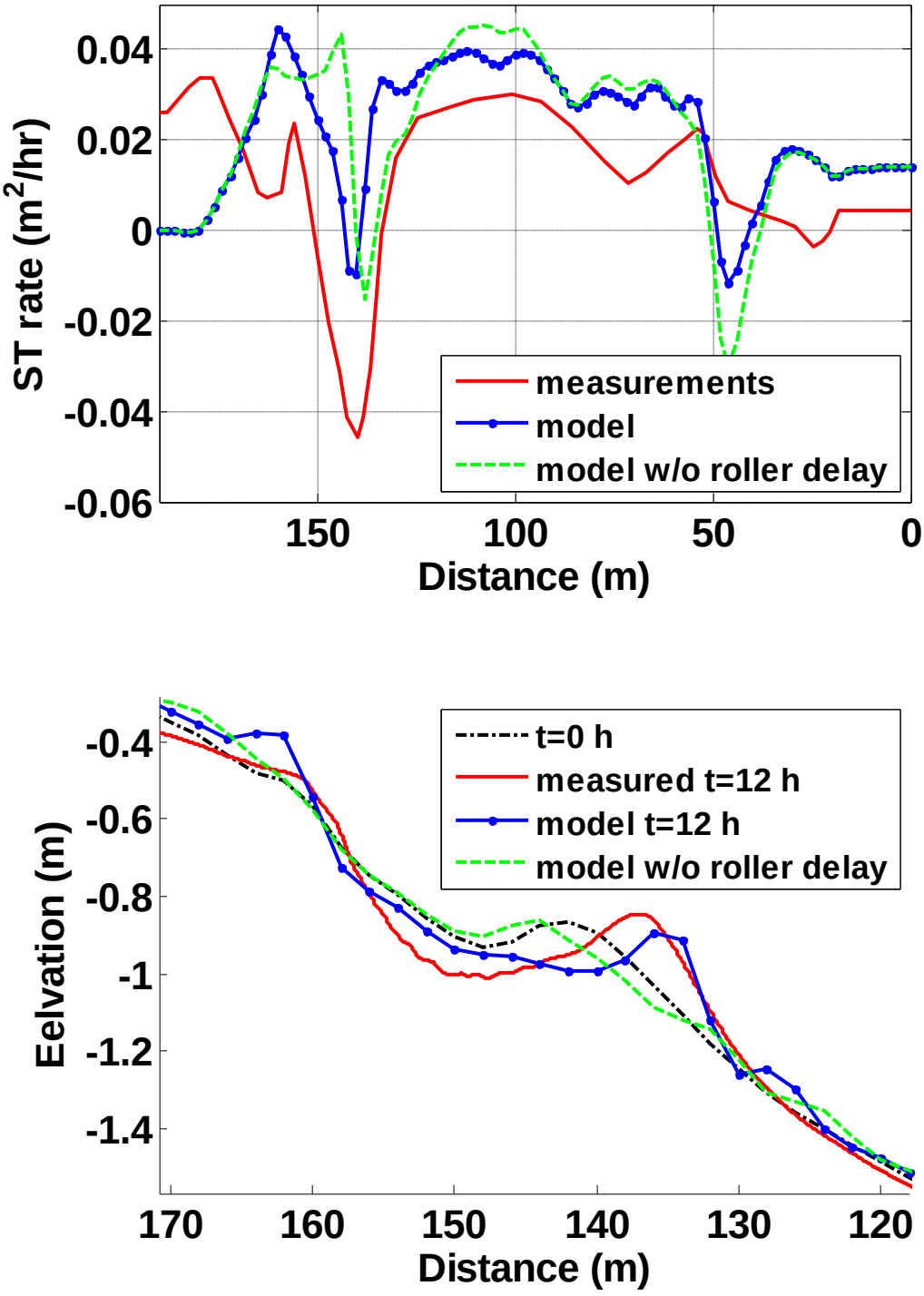

Figure 6.10. Test 1c erosive case. Top: Sediment transport rate inferred from profile change in 20 minutes ((Rakha et al. 1997 fig 6) and initial Sediment transport rate. Bottom: Initial bathymetry, measured and modeled bathymetry after 18 hours. Data from Roelvink and Reniers (1995).

6.4. 2005 Myrtle Beach Nearshore Experiment

Wave transformation and hydrodynamics at a site in North Myrtle Beach, South Carolina are modeled and compared to measurements made during the 2005 Myrtle Beach Nearshore Experiment. This experiment involved wave height and current measurements along a cross-shore profile with four instruments and bathymetric measurements extending approximately 500 meters on either side of this transect. The bathymetric profile and the location of instruments are plotted in Figure 6.11. Note that the coordinate system is different from the local coordinate system used in Chapter 3. The origin is at the offshore boundary and the x-coordinate is increasing towards the shore as required by the numerical model. As explained in section 3.2.2 four instruments measuring pressure and velocity were placed along a cross-shore profile. Directional wave spectra and mean currents were calculated for each instrument from these measurements.

A longshore-uniform bathymetry was created using the measured profile along the instrument transect. A longshore uniform bathymetry was used firstly because the longshore variations were small (Figure 3.14). Since all the measurements were conducted at one cross-shore profile there is no way to test longshore variations in flows and waves. Lastly, symmetric boundary conditions were used for lateral boundaries in the hydrodynamic model. This boundary condition cannot be applied for longshore varying bathymetry where the bathymetric profiles are different at the two lateral ends. Another option for lateral boundary conditions is specifying flux conditions, but these are not known, as they were not measured in the field.

The computational grid begins at the most offshore instrument (RDI) and extends to the dry beach, covering 510 meters in the cross-shore direction. The measured spectra at the offshore instrument are used to define the offshore boundary conditions for the wave transformation model. The grid spacing is 5 m in both horizontal directions. The tide level is taken from the pressure measurements taken at the offshore Nortek

instrument. The simulations are done for the period between 13-Dec-2005 19:00 (day=13.79) and 16-Dec-2005 21:00 (day=16.88), corresponding to the period when the RDI collected data.

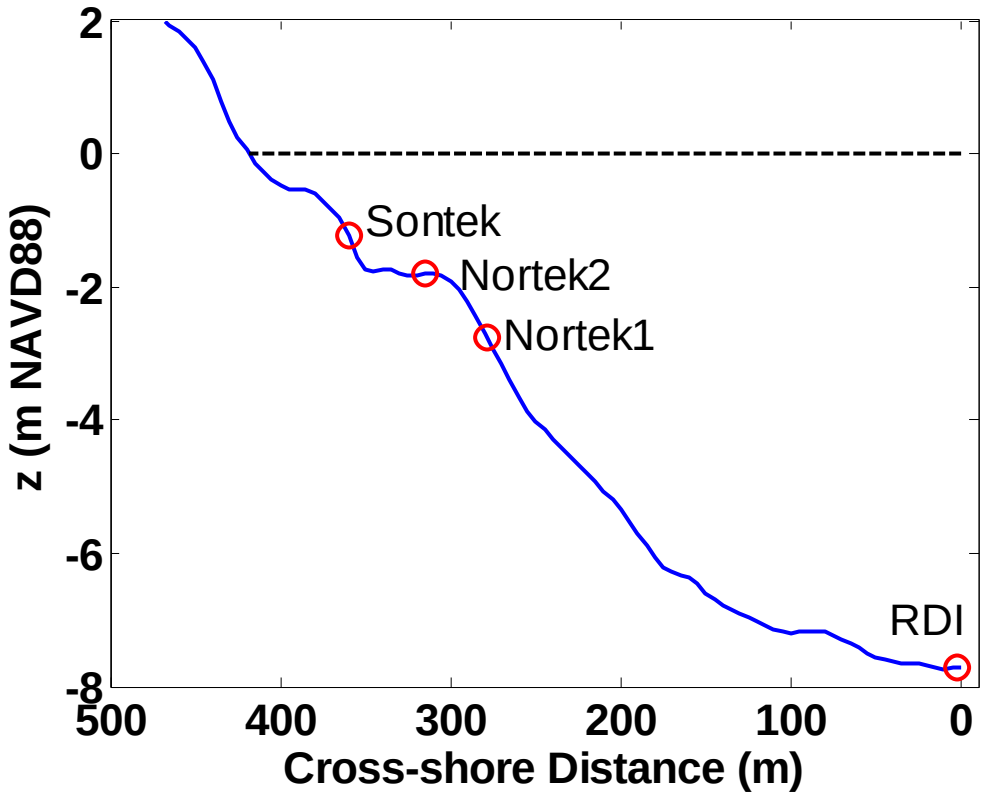

Figure 6.11. Instrumented profile showing location of instruments. The offshore boundary was chosen to coincide with RDI instrument location. The horizontal dashed line shows *z*=0 in NAVD88 coordinate system. All the instruments measure pressure, depth, velocity profiles, and directional wave parameters.

Forty-six directional bins extending 65 degrees on either side of shore normal, and 20 frequency bins covering the range from 1/15 to 0.35 Hz were used to simulate the measured directional spectra in REF/DIF S. REF/DIF S can simulate only waves within ±65 degrees of shore normal, so wave energy outside this region was not included in the simulations which typically did not exceed 10%. When wave heights predicted by the model are compared to measurements, only the energy in this range is considered.

Modeled and measured wave heights, H_{mo}, are shown in Figure 6.12 for all instruments from offshore to inshore. The wave breaking parameter γ was chosen as 0.33 for these simulations. This value is lower than the values used for the lab experiments in the previous section, but γ values as low as 0.24 have been used for field conditions (Lippmann et al. 1996). The most offshore instrument is used to define the boundary condition for the model so the model results are the same as the measurements at that location. Wave height transformation is modeled successfully. However, the wave heights are underpredicted at all instruments between days 15.7 and 16.2. Wave steepness is highest in this time period. Using a higher wave breaking parameter value shifts the location of wave breaking inshore and increases wave heights at all inshore instruments. This improves the results for this period, but the results deteriorate for other times. This is consistent with the findings of Lippmann et al. (1996), who observed that wave breaking parameter increases with wave steepness. Similarly to what was seen in section 6.3, the erosive case with steep waves was modeled using a higher wave breaking parameter (γ=0.6) than the accretive case with smaller wave steepness (γ=0.5). Even though using a different wave breaking parameter for different times would improve the model results for the Myrtle Beach data set, the wave breaking parameter of 0.33 was kept constant for the whole simulation period.

At the innermost instrument (Sontek) the model predictions for wave height are higher than the measurements for low tide levels. The wave heights are measured using a pressure gage on the instrument. When the water level decreases the pressure gage is going to be dry part of the time when the trough of the waves are below it even though the mean water level is above the pressure gage. This would cause the measured range of pressures to be smaller and wave heights to decrease. This might explain the difference between the model results for wave height from the measurements at the Sontek instruments for low water levels. The measured data cannot easily be filtered for these

events without being too conservative since drying contaminates both the wave height and depth measurements.

The normalized percentage rms error in wave height for three days of simulations at all instruments is slightly more than 10% (Table 6.1). The error is defined as $\sqrt{mean(Modeled - Measured)^2 / mean(Measured)^2}$. These numbers include the time period with steep waves discussed above with errors in wave height exceeding 30%. The errors in wave height at the Sontek instrument are higher than at the two Nortek instruments due to the low water level periods close to drying.

Table 6.1. Percentage rms error normalized by mean measured values for hydrodynamic simulations at Myrtle Beach.

	Wave Height H_{mo}	**Wave angle**	**Near bottom cross-shore current**
Nortek1	11.9	25.3	166.9
Nortek2	11.0	32.3	239.9
Sontek	12.9	104.2	240.0

Figure 6.13 shows the wave angles for the inner three instruments. The model slightly underpredicts wave angles for Nortek1 and Nortek2 instruments. However for the Sontek instrument the modeled wave angles are up to 20 degrees smaller than the measurements. The measured wave angles at Sontek1 increase compared to Nortek2. This is not expected since normally wave angles decrease as the waves approach the shore due to refraction. Wave reflection from the shore might be a reason for increase in wave angles. Another possibility is measurement errors. The Sontek instrument was placed hanging from a tripod in a downward looking position. The obstruction from the tripod to the flow might have contaminated the directional measurements. The percentage rms errors for the wave angles are given in Table 6.1 for consistency. However the rms errors that are not normalized by the mean value might give better

insight for errors in wave angles. The mean rms errors are 3.6, 3.7 and 11.7 degrees for Nortek1, Nortek2 and Sontek respectively.

Wave roller angle, σ_r, was taken as 1.0 for these simulations. The eddy viscosity coefficient in SHORECIRC was increased 10 times from its default value to smooth out the numerical instabilities at the offshore region. This has very little effect on the model results inside the surfzone since eddy viscosity is dominated by wave breaking here. Measured and modeled near-bottom mean cross-shore currents are plotted in Figure 6.14. Velocity measurements closest to the bottom were used for all instruments. These are 1.4, 0.6, 0.6 and 0.15 m for the RDI, Nortek1, Nortek2 and Sontek respectively. Even though the Nortek instruments measure velocity 60 cm above the bottom, model results show that mean cross-shore current is not very different than its value above the wave boundary layer at the instrument locations. The measured velocities are compared with circulation model results above the wave boundary layer. The offshore instrument is not included in the plot, since both the modeled and measured currents are very small there. The trends of the undertow are captured by the model at Nortek1 and Nortek2, but the model results and measurements are very different at Sontek. As discussed above for waves, directional measurements for currents at this instrument might be wrong too. The currents are generally underpredicted at Nortek1 and Nortek2 except for a brief period around day 15.75 when the model overpredicts the currents at Nortek1. The normalized rms errors are very high exceeding 200% for the inner two instruments. However some trends apparent in Figure 6.16 are lost in these statistics. The trends of cross-shore velocity at Nortek2 are captured by the model, but the model fails to reproduce the currents at Sontek completely, yet the error for those two instruments are the same.

Measured and modeled near-bottom mean longshore currents are shown in Figure 6.15. The measured variations at the offshore instrument show the tidal signal. The model does not include tidal velocities so longshore currents are close to zero at this instrument. The model can predict longshore currents at the two Nortek instruments successfully

especially for strong current cases which are more important. However at Nortek1 the direction of the current is predicted wrong for small current cases. The longshore current changes direction offshore of the bar due to shoaling in the model. This is not observed in the measurements. The model and the measurements do not agree at Sontek instrument as discussed above.

Figure 6.16 shows the variation of wave heights and near-bottom, mean cross-shore velocity across the profile, inside the surfzone. Note that the velocities are multiplied by two in the figure, for better visibility. Three conditions were chosen to reflect different wave conditions and different success rates of the models. On day 14.65 the wave height is low and not much wave breaking occurs over the bar. The wave height does not change much from Nortek1 to Nortek2 and the mean flow is almost zero. The model predicts wave breaking inshore of the region suggested by the Sontek measurement. The current is underpredicted in this region.

On day 15.9 wave heights are underpredicted everywhere. This is a steep wave case where the model would improve with a higher breaking coefficient. The waves begin to break over the bar and a strong offshore current forms there. The current at Nortek2 is underpredicted significantly. However the maximum current predicted over the bar is not much different than the measured value. The differences between measured and modeled currents are usually arising from a shift in the location of the maximum rather than an error in prediction of maximum velocity. This explains a lot of the errors seen in Figure 6.14. In contrast, the errors at Sontek1 are due to the differences in the value of the current there. Day 16.12 is an example where the model can predict both the wave heights and currents accurately at all instruments.

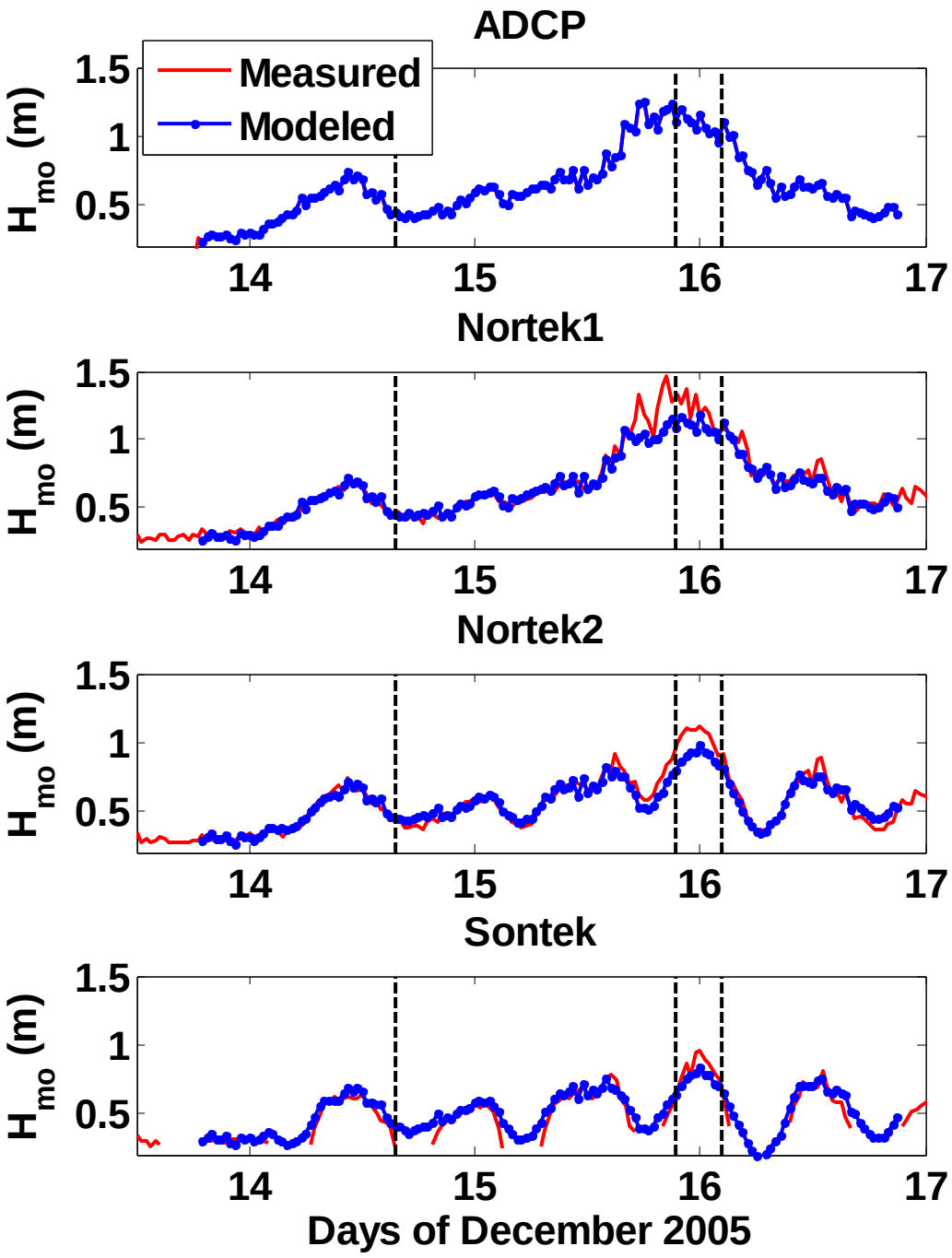

Figure 6.12. Measured (red line) and modeled (blue line & dot) wave heights, H_{mo} for North Myrtle Beach site. Vertical dashed lines show the times plotted in Figure 6.16.

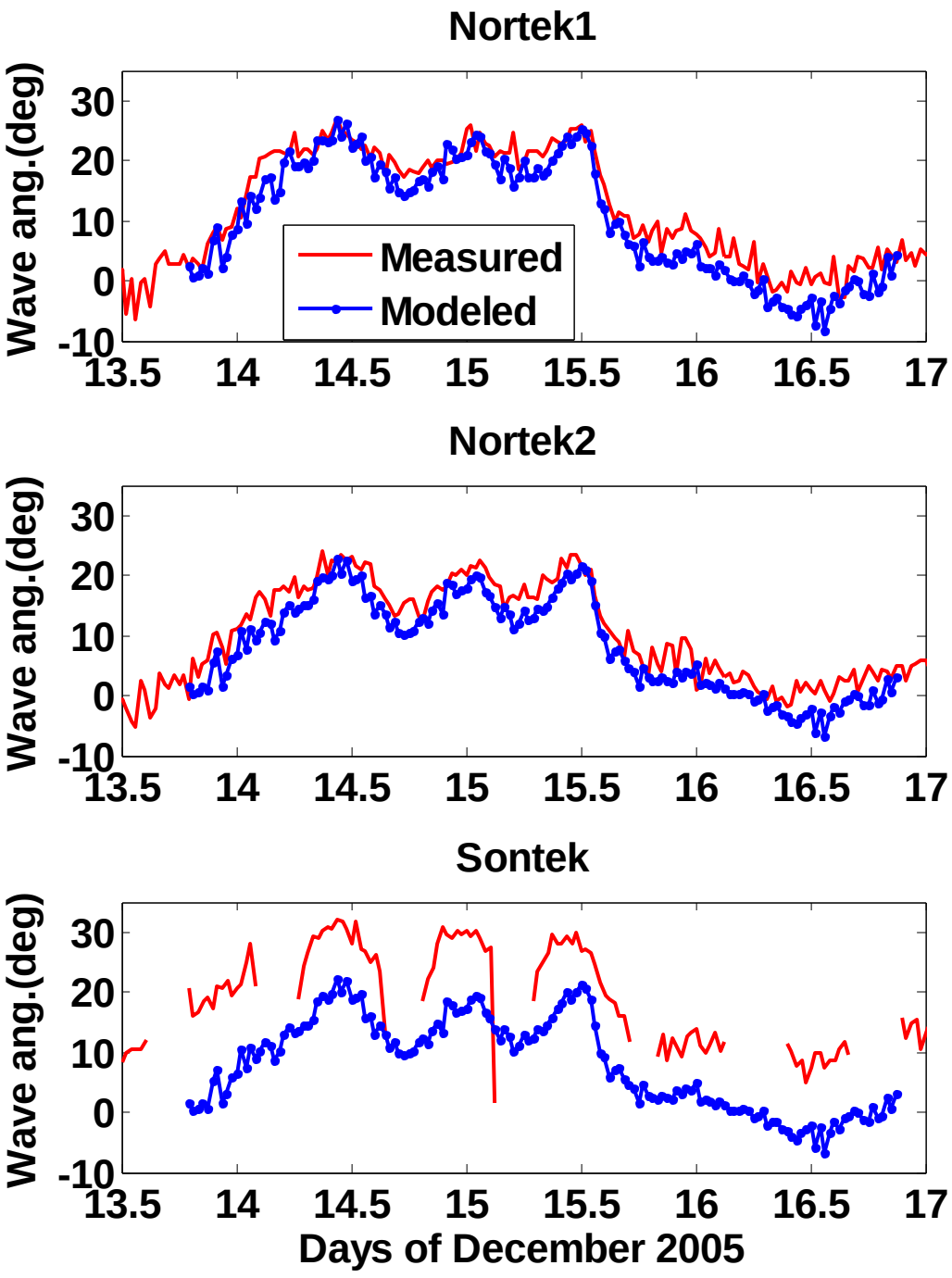

Figure 6.13. Measured (red line) and modeled (blue line & dot) wave angles for North Myrtle Beach site.

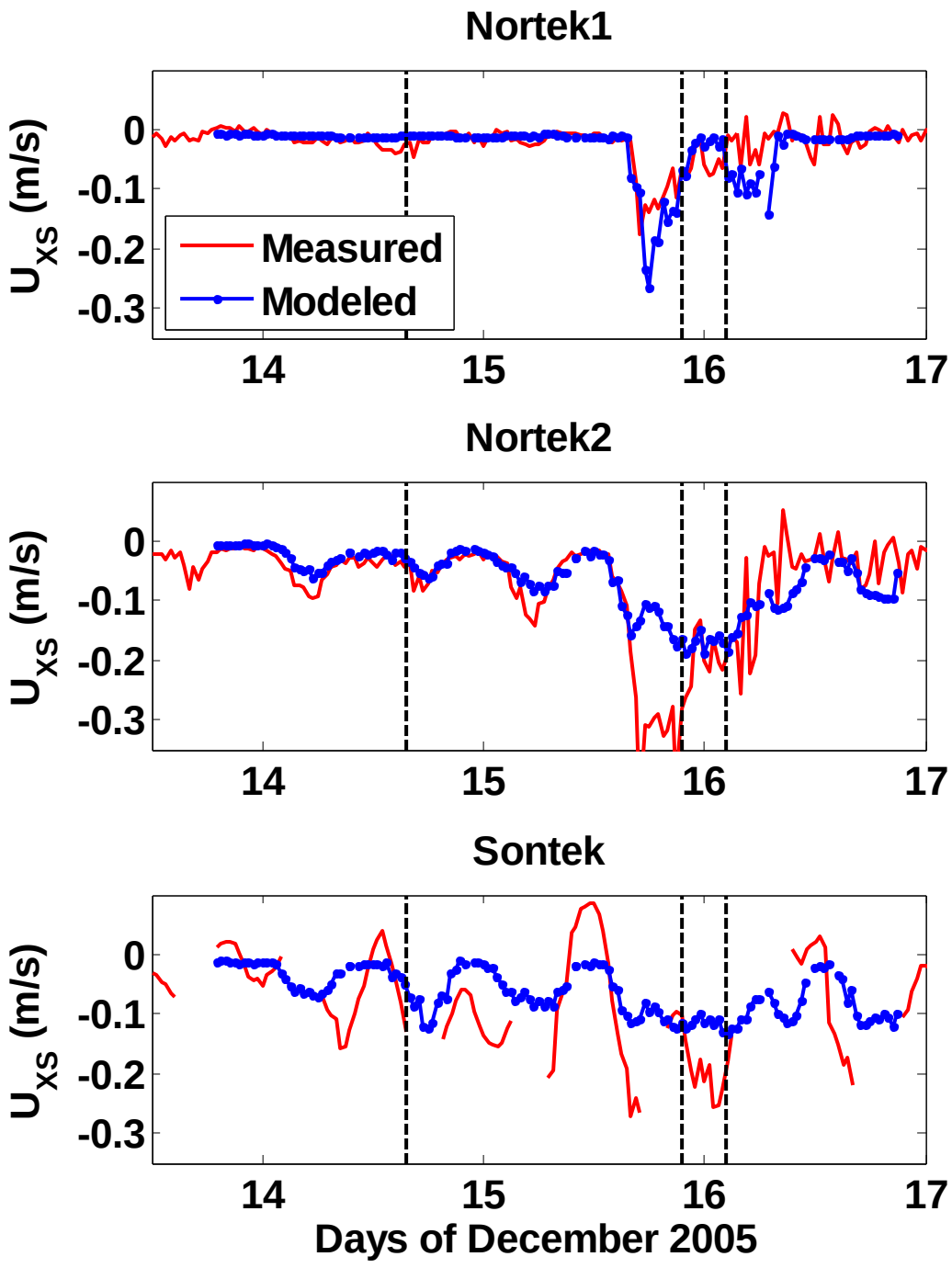

Figure 6.14. Measured (red line) and modeled (blue line & dot) near bottom cross-shore velocities for North Myrtle Beach site. Negative values show offshore directed flow. Vertical dished lines show the times plotted in Figure 6.16.

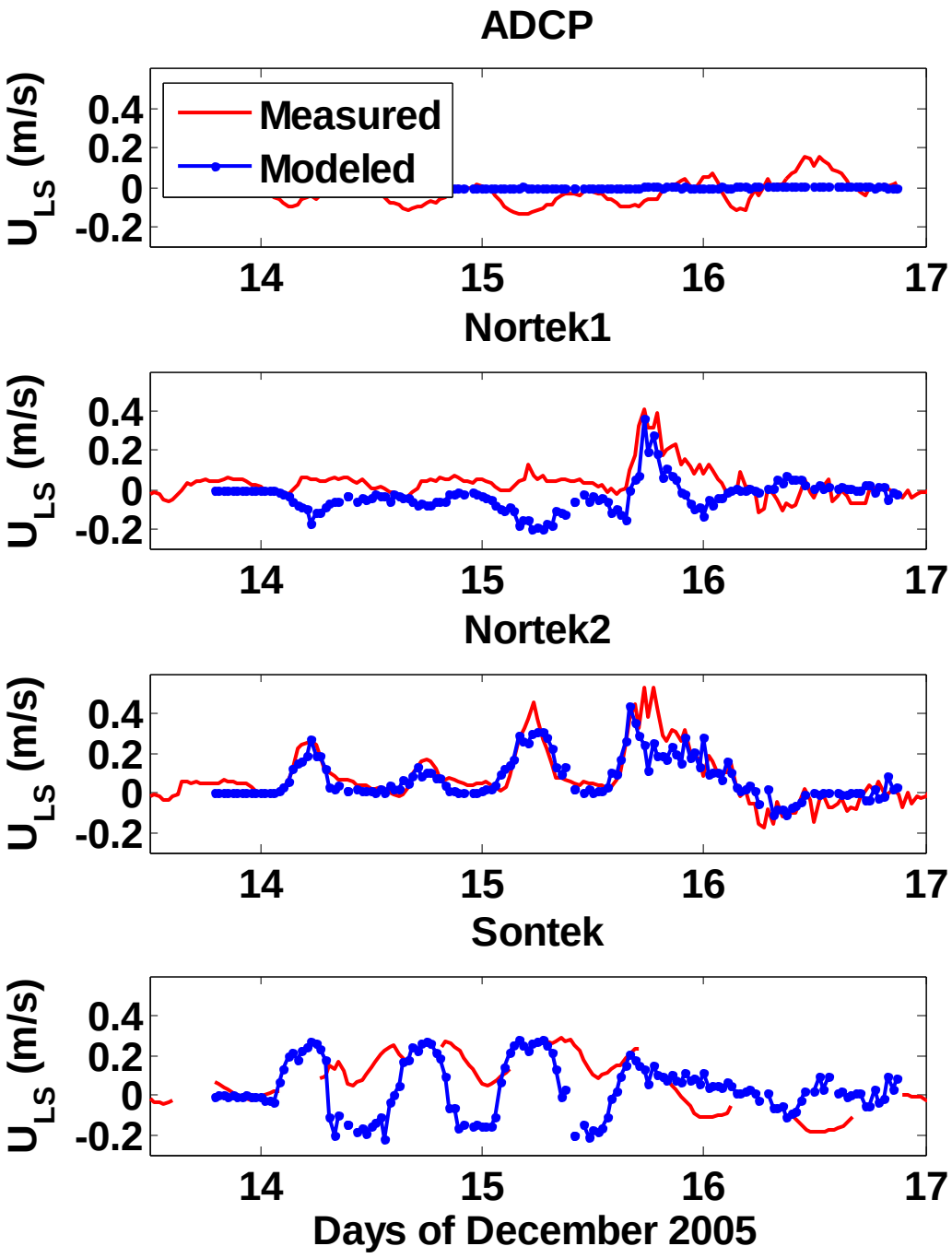

Figure 6.15. Measured (red line) and modeled (blue line & dot) longshore currents for North Myrtle Beach site.

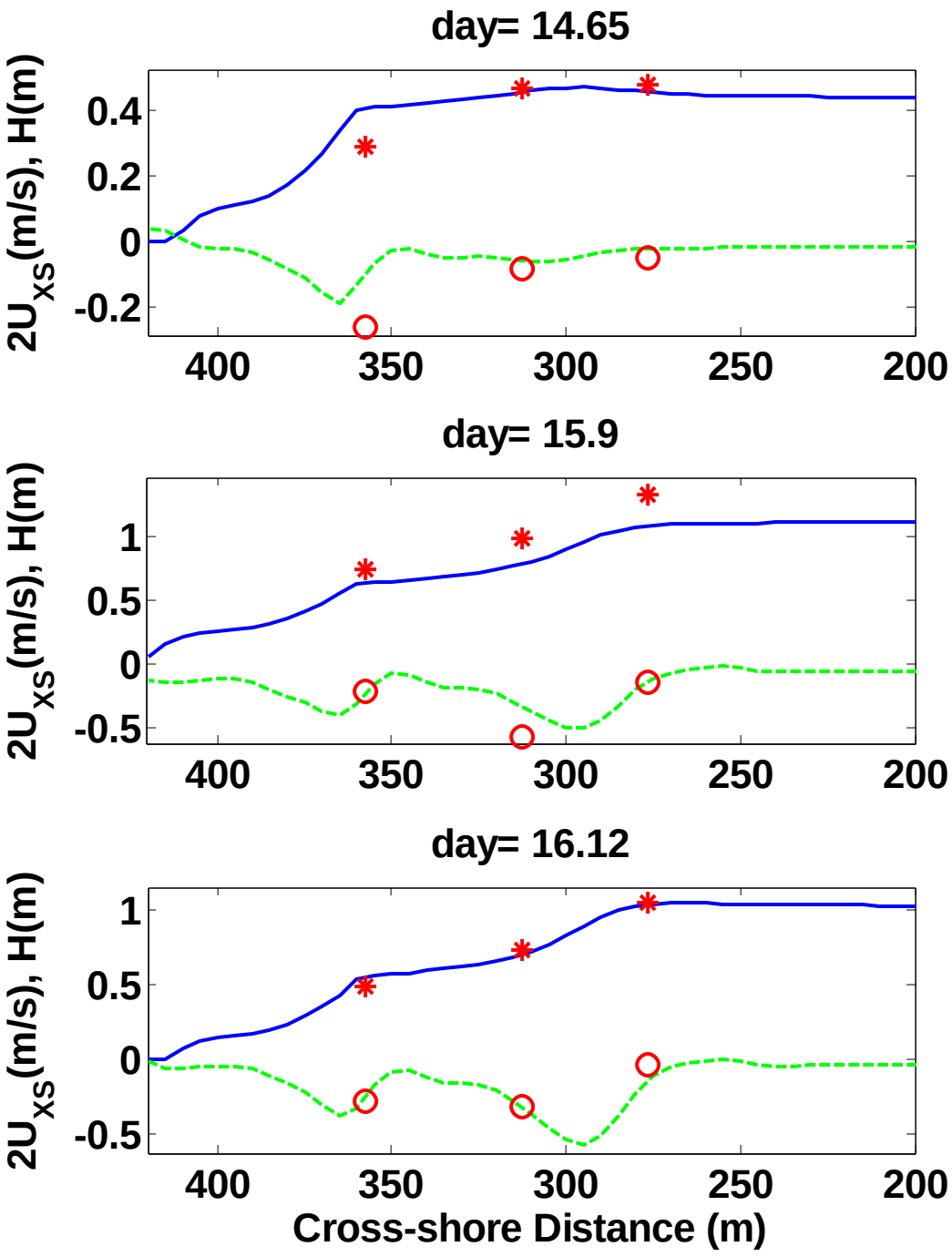

Figure 6.16. The variation of wave height H_{mo} and, 2*cross-shore velocity U_{XS} across the profile for days 14.65, 15.90 and 16.12. Note the velocity is multiplied by two for better viewing. Modeled H_{mo} (blue solid), U_{XS} (green dashed), Measured H_{mo} (red star), U_{XS} (red circle).

6.4.1. Bathymetric changes

The model was run for three days for the North Myrtle Beach scenario, updating the offshore boundary condition every thirty minutes with measured wave spectra. Bathymetry was updated at every time step. In a second simulation, the bathymetry was not updated. Since the total bathymetric change was small, it did not modify hydrodynamics significantly and the mean sediment transport rates calculated by the two methods were very close. Further simulations using different parameters were done without updating the bathymetry.

The measured median grain diameters vary between 0.2 to 0.4 mm across the sampled portion of the profile. Grain diameters 0.2 and 0.3 mm were used in simulations since 0.4 mm was mostly observed on the dry beach. The correction factor βt values of 0.4 and 0.7 were used in the simulations. The mean sediment transport rate and the resulting bathymetric changes are shown in Figure 6.17. Changing the grain diameter and βt changes the magnitude of the mean sediment transport rate, but has little effect on the shape of the cross-shore distribution of sediment transport. The mean sediment transport is everywhere directed onshore and there are two peaks in sediment transport rate over the two bars. The maximum change in bathymetry occurs between these two peaks, which is erosion of 5-15 cm, depending on chosen sediment diameter and βt. The uncertainty in bathymetric measurements is close to these values in this region and the predicted change can't be meaningfully compared to the measurements.

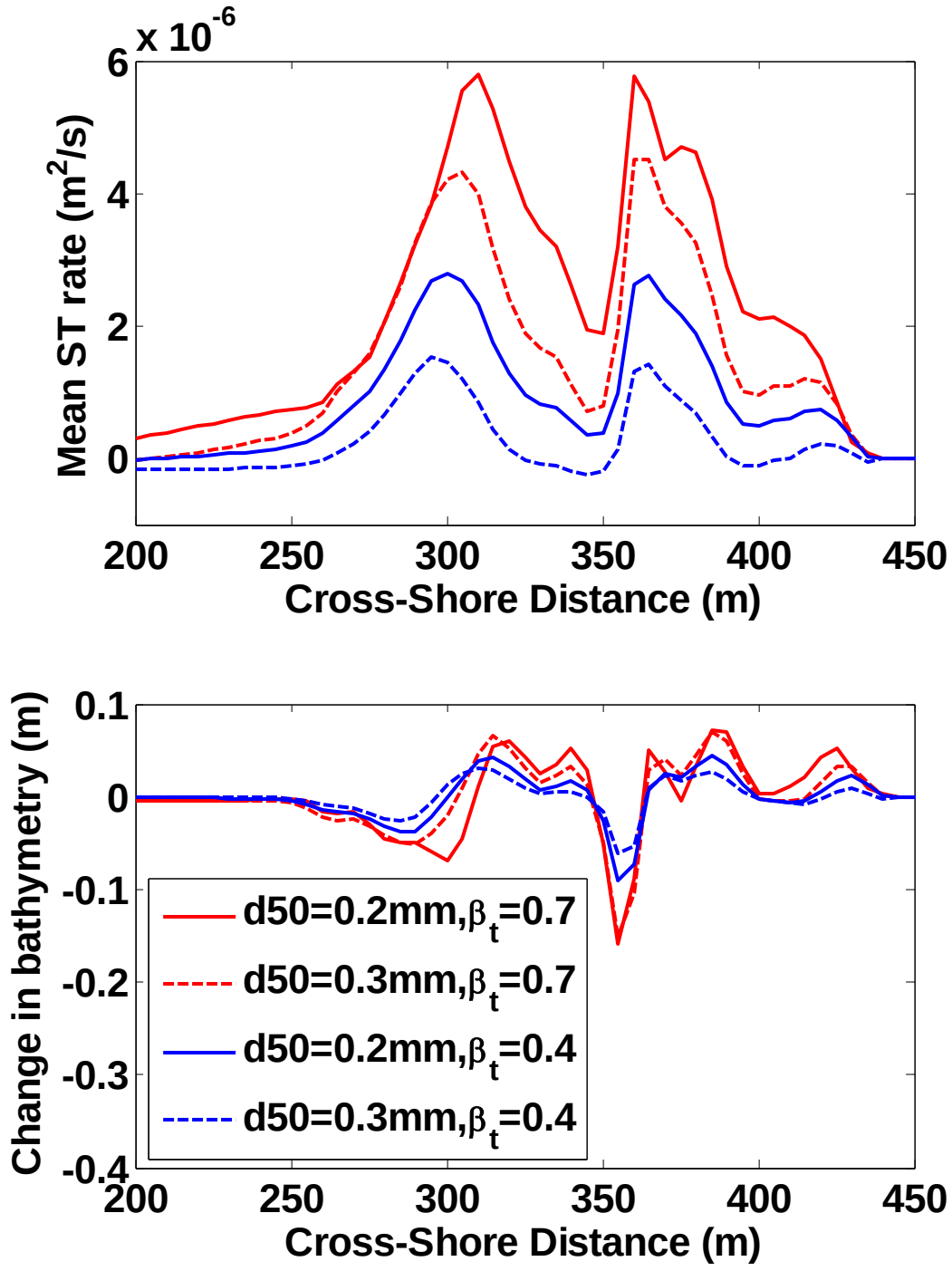

Figure 6.17. Top: Mean sediment rate for the 3 day simulation period excluding slope effect. Bottom: Total change in bathymetry. Negative values show erosion.

Sediment transport rates for different days are shown in Figure 6.18 for the two cases with maximum and minimum mean sediment transport rate in the previous figure.

On day 14.0 wave height is very small (0.3 m) and the water level is high. The wave passes over the bars without much change, and breaks close to the shore where the majority of sediment transport occurs. The two cases have opposite sediment transport rate.

On day 15.73 wave height is large and most of the sediment transport occurs over the offshore bar. The case with d50=0.2 mm is very similar to the case in the previous section with offshore bar movement. The sediment transport is onshore except within a narrow offshore region over the bar. The offshore transport is not observed for the case with d50=0.3 mm.

On day 15.98 the sediment transport profile has peaks over the two bars for both cases. Figure 6.18 shows that the shape of the sediment transport rate is seldom like the average sediment transport rate, due to variations in wave conditions and water level. The two cases investigated also may differ a lot for individual cases. However when averaged over a long period of time with various conditions, the shapes of the sediment transport profiles are very similar, even though the magnitudes are different.

Longshore currents may significantly increase cross-shore sediment transport rate by increasing the bottom shear stresses. Cross-shore sediment transport rate was recalculated by setting the longshore current to zero for day 14.52. This period was chosen for its strong longshore currents reaching 0.4 m/s (This is not apparent in Figure 6.15 since the maximum longshore currents occurs inshore of the instruments due to high tide). Figure 6.19 shows the cross-shore sediment transport rate for day 14.52 with and without the effects of longshore currents. The longshore current enhances cross-shore sediment transport rate as much as three times.

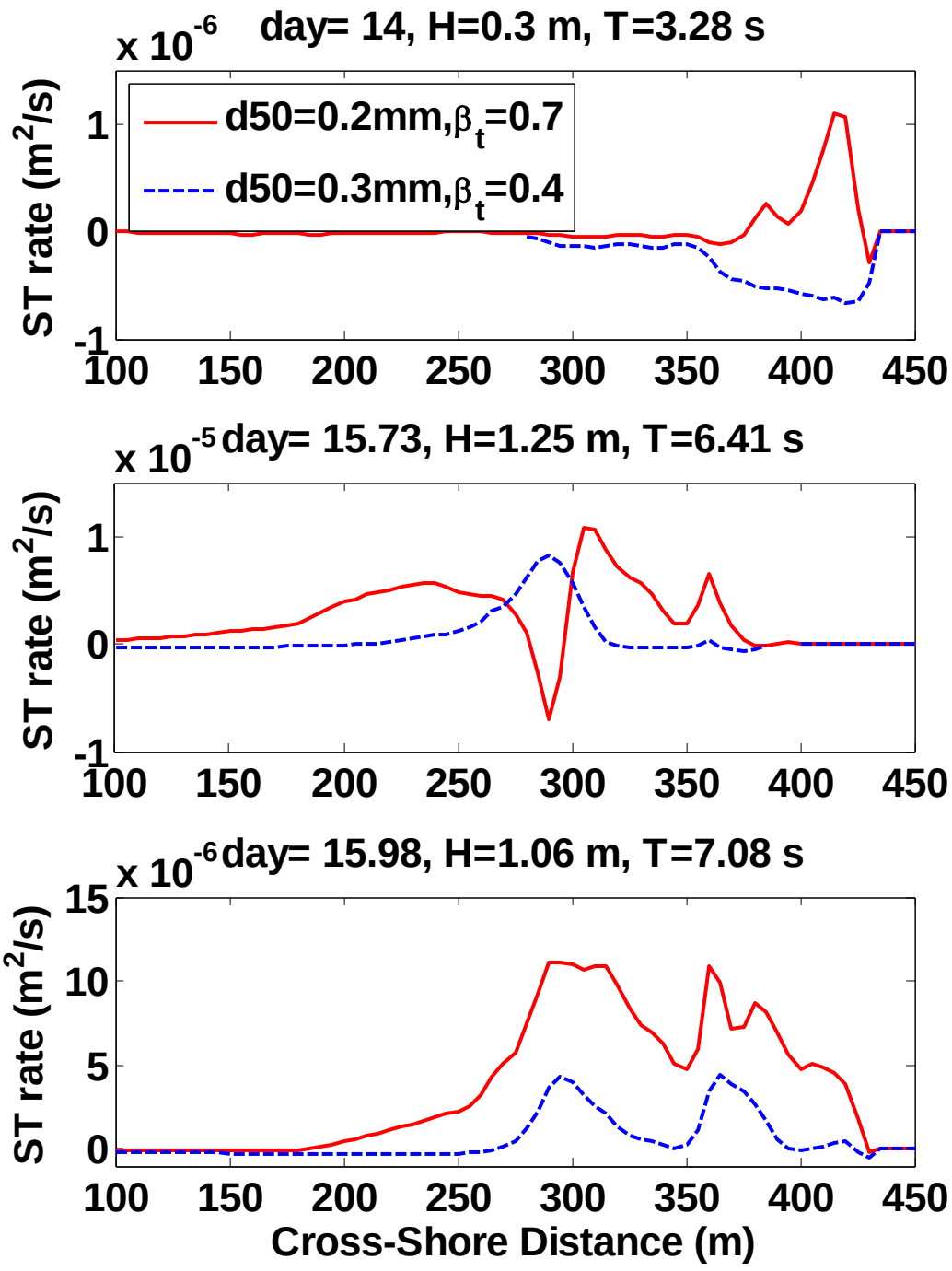

Figure 6.18. Sediment transport rate for days 14, 15.73 and 15.98 for d50=0.2 mm βt=0.7 (red solid line) and d50=0.3 mm βt=0.4 (blue dashed line).

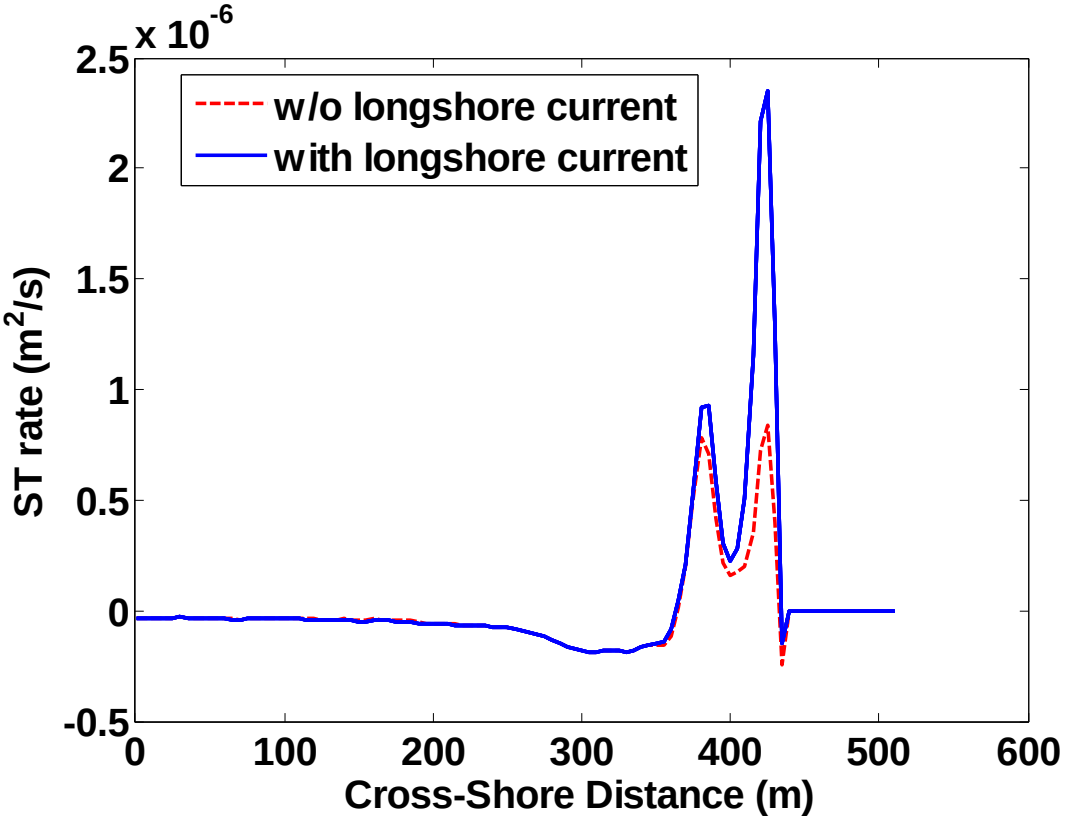

Figure 6.19. Effects of longshore currents on cross-shore sediment transport rate for day 14.52.

Hydrodynamics and morphological changes were modeled for a three-day period at Myrtle Beach. The modeled wave heights and currents were compared to the field measurements and found to be satisfactory considering the simplifications made in the model and the natural scatter in the data. No bathymetric changes exceeding the measurement uncertainty were observed in the field. The bathymetric changes predicted by the model using various parameters were small and within measurement uncertainty.

7. CONCLUSION

Beach profile evolution models are used to predict effects of storms, sea level rise, beach nourishment and to improve the understanding of physical processes in and near the surf zone. The processes governing the beach profile evolution and their interactions are complex and models predicting these represent an area of active research. A system of numerical models was used to resolve these processes and predict beach profile evolution. Sediment transport and boundary layer models developed for use in this thesis were coupled with existing spectral wave transformation, nearshore circulation and bathymetry update models. These models were applied to field and laboratory cases at storm time scales ranging from a couple of hours to three days and for depths up to 10 meters.

As waves approach the shore their heights increase due to shoaling, and may also be modified by refraction, winds, and bottom friction. At some point they begin to break and decrease in height. The momentum fluxes created by these waves, called radiation stresses, drive longshore and cross-shore currents. The magnitude of the mean cross-shore currents, called undertow, which are generally offshore directed, is controlled by the amount of onshore flux due to waves and due to rollers of breaking waves. The orbital wave velocities become skewed close to shore; the onshore velocities are larger than offshore velocities, but the velocities are offshore directed for longer periods. The cross-shore sediment transport is mainly controlled by the relative strengths of the undertow moving sediment offshore and the skewed wave orbital velocities moving sediment onshore.

Wave refraction, shoaling, breaking, rollers and skewed wave orbital velocities were solved by the numerical models used. Depth varying longshore and cross-shore currents, wave set-up, set-down, tides and boundary layer streaming were also included.

Wave heights could be modeled very successfully when the empirical breaking parameter was calibrated individually for different cases. Larger values of the breaking parameter (ratio of wave height to water depth at breaking) were needed to simulate cases with larger wave steepness. This is consistent with the findings in the literature. Wave breaking parameters used in this study were between 0.33 and 0.6 which are in the range used in previous studies. No clear evidence was found to support the need for a locally varying breaking parameter across the profile. Predictive capabilities of the model will improve if a formulation can be built into the wave breaking model that can estimate the breaking parameter as a function of incident wave parameters and bottom slope.

Skewed wave orbital velocities were modeled using an empirical equation. The equation could predict the variation of velocity skewness across the profile for a laboratory case. The performance of the equation decreased when compared to field data from Myrtle Beach, especially for high skewness cases.

Using standard parameters for the circulation model resulted in underprediction of the undertow. The undertow predictions were improved by increasing the onshore mass flux due to rollers. Wave roller angle $\sigma_{r,}$ the parameter controlling the mass flux due to rollers, was varied between 1.6 and 6 degrees. This range of parameters changed the undertow by 30%. The circulation model has numerical instabilities in the offshore region. Increasing the eddy viscosity coefficient ten fold removed these instabilities, without changing the velocities inside the surf zone since the dispersion is controlled mostly by wave breaking in that region.

A 1D vertical, advection-diffusion sediment model was developed to predict vertical and temporal variations of sediment concentration within a wave period and calculate sediment transport rate. This was combined with a new model that computes sediment transport below the suspension level. A standard, time-invariant, parabolic description of eddy viscosity was modified to include time variation, without increasing computational requirements. The bottom boundary condition for the sediment

concentration model was cast in terms of a pick-up function using reference concentration formulas from the literature. Bottom roughness height was taken as a constant equal to ten times the median grain size. A factor that is multiplied by the eddy viscosity was used as the only calibration factor for the sediment transport model. The sediment transport rates for a range of sheet flow conditions could be predicted within a factor of two. The performance for rippled bed conditions decreased, but still captured general trends.

The roughness height was taken as a constant in both space and time throughout this study. Roughness height can vary across the profile. Using variable roughness height across the profile in numerical models was shown to improve morphological results in the literature. However the uncertainties in prediction of the roughness height both in sheet flow conditions and rippled bed conditions are still very large, especially in field conditions. As a result, frequently roughness height is used as a fitting parameter. An eddy viscosity correction factor, which is the only calibration parameter for sediment transport in this study implicitly includes the effects of variations in roughness height, too.

A new model that uses empirical functions for velocity and concentration profiles within the bed was developed for describing sediment transport below the reference concentration level, thus including what is normally referred to as bed load. This is a thin layer on the order of millimeters that is dominated by gravity and inertia forces rather than turbulence. A linear concentration profile and a slightly concave (proportional to the 0.75 power of distance from still bed) velocity profile was used. The profile shapes predicted by the model compared favorably with measured data and physically more correct two phase flow model results. The model predicts erosion layer thickness and sheet flow layer thickness and their variation during a wave period reasonably well based on mass conservation. It also predicts the time variation of concentrations within the

sheet flow layer successfully. The sediment flux within the bed is computed as well as a two-phase flow model.

Including vertical velocity and convective acceleration did not change the net sediment transport rate. Defining the bottom boundary condition in terms of a pick-up function rather than a reference concentration created a more realistic sediment concentration time series close to the bottom, but did not significantly affect the net sediment transport rate. Inclusion of boundary layer streaming, on the other hand, increased the sediment transport rate 2-4 times.

Bar formation on an initially plane beach was successfully simulated, although the location of the computed bar was offshore of the location observed in laboratory situations. Errors in predicting the location of maximum undertow, and the presence of long waves, which were not simulated in the model, are potential reasons for the error in the location of the bar.

Offshore bar movement was successfully predicted for a laboratory case. Modeling the undertow was shown to be critical in predicting the offshore movement of the bar. Inclusion of roller delay was required to get the correct undertow over the breaking bar.

Growth and onshore movement of the breaking bar was also successfully computed even though the undertow could not be predicted successfully for this case. The undertow is not as important in cases with onshore sediment transport since the sediment transport is dependent more on wave orbital velocities.

The sediment transport calibration factor for medium and coarse sand was varied between 0.4 and 0.7 to give the best fit to different cases. This changed the sediment transport rate within a factor of two which is in the range of uncertainty for sediment transport rate predictions. The calibration factor for fine sand was found as 0.24 in the initial calibration. When modeling the bar formation case with fine sand a calibration factor of 0.9 was used. However this test case was a scaled down laboratory case and

corresponds to coarser sand at prototype scale, so these two factors can't be compared directly.

Field data was collected at Myrtle Beach, SC, during two one-week experiments in 2003 and 2005. Bathymetry was measured using a Total Station, differential GPS, a digital fathometer, boat and ATV with equipment deployed by foot, on an ATV (all-terrain vehicle) and on a small boat. Wave and current measurements were made along cross-shore profiles using bottom mounted acoustic sensors. Sand samples were taken and video images of the surf-zone were recorded. These experiments provided wave, current and bathymetric data for testing and calibration of the numerical models.

When the model was applied to field conditions for a three-day simulation, the performance of wave height predictions decreased compared to the laboratory cases, in part because a single wave breaking parameter was used for a variety of wave conditions. The magnitude of undertow could be captured reasonably well after tuning, but the location of maximum undertow caused by wave breaking over the offshore bar was predicted to be offshore of the measured location. The wave breaking was strongest on the inshore or offshore bar depending on the tidal level. This created a time averaged sediment transport rate with two peaks on each of the bars. Using different sediment sizes changed the magnitude of the time averaged sediment transport rate not its shape.

The model system can be improved by using a predictor for the breaking wave parameter as a function of incident wave conditions and beach profile, and using a better description of rollers in the circulation model. Improving wave orbital velocity skewness and bed roughness predictions would benefit all morphological models in general. The predictive capability of this morphological model and all models in general will improve when the requirements for tuning the model parameters for individual cases are decreased.

REFERENCES

Aagaard, T. (1988). "A study on nearshore bar dynamics in a low-energy environment; northern Zealand, Denmark." *Journal of Coastal Research*, 4(1), 115-28.

Aagaard, T., Black, K. P., and Greenwood, B. (2002). "Cross-shore suspended sediment transport in the surf zone: a field-based parameterization." *Marine Geology*, 185(3-4), 283-302.

Aagaard, T., Nielsen, J., and Greenwood, B. (1998). "Suspended sediment transport and nearshore bar formation on a shallow intermediate-state beach." *Marine Geology*, 148(3-4), 203-225.

Bagnold, R. A. (1956). "The flow of cohesionless grains in fluids." *Proc. R. Soc. Lond.* , A 249, 235-297.

Bagnold, R. A. (1966). "An approach to the sediment transport problem from general physics. ." Tech. Rep. 422-I. US Geological Survey professional paper.

Bailard, J. A. (1981). "An Energetics Total Load Sediment Transport Model For A Plane Sloping Beach." *Journal Of Geophysical Research-Oceans And Atmospheres*, 86(NC11), 938-954.

Bakker, W. T. (1974). "Sand concentration in an oscillatory flow." Proc. 14th Int. Conf. on Coastal Engineering, ASCE, Copenhagen, 1129-1148.

Berkhoff, J. C. W. (1972). "Computation of combined refraction-diffraction." Proc. 13th International Conference on Coastal Engineering., ASCE, 471-490.

Bijker, E. W. (1968). "Littoral drift as a function of waves and current." Proc. 11th Coastal Engineering Conference, London, 415-435.

Black, K. (1994). "Suspended sediment load during an asymmetric wave cycle over a plane bed " *Coastal Engineering*, 23, 95-114.

Black, K. P., Gorman, R. M., and Symonds, G. (1995). "Sediment transport near the break point associated with cross-shore gradients in vertical eddy diffusivity." *Coastal Engineering*, 26(3-4), 153-175.

Black, K. P., and Vincent, C. E. (2001). "High-resolution field measurements and numerical modelling of intra-wave sediment suspension on plane beds under shoaling waves." *Coastal Engineering*, 42(2), 173-197.

Boczar-Karakiewicz, B., Forbes, D. L., and Drapeau, G. (1995). "Nearshore Bar Development In Southern Gulf Of St-Lawrence." *Journal Of Waterway Port Coastal And Ocean Engineering-Asce*, 121(1), 49-60.

Bosboom, J., Aarninkhof, S., Reniers, A., Roelvink, J. A., Pechon, P., and Southgate, H. N. (1997). "UNIBEST-TC 2.0, Overview of model formulations." Report H2305, Delft Hydraulics, Delft, The Netherlands.

Bowen, A. J. (1980). "Simple models of nearshore sedimentation: Beach profiles and longshore bars, in the coastline of Canada." *Pap. Geol. Surv. Can.*, 80(10), 1-11.

Bruun, P. (1962). "Sea level rise as a cause of shore erosion." *Journal of the Waterways and Harbors Division* 1, 116-130.

Camenen, B., and Larson, M. (2005). "Phase-lag effects in sheet flow transport." *Coastal Engineering*, In Press, Corrected Proof.

Clarke, S., Dodd, N., and Damgaard, J. (2004). "Modeling flow in and above a porous beach." *Journal of Waterway Port Coastal and Ocean Engineering-Asce*, 130(5), 223-233.

Dally, W. R., and Dean, R. G. (1984). "Suspended Sediment Transport and Beach Profile Evolution." *Journal of Waterway Port Coastal and Ocean Engineering-Asce*, 110(1), 15-33.

Davies, A. G. (1995). "Effects Of Unsteadiness On The Suspended Sediment Flux In Co-Linear Wave-Current Flow." *Continental Shelf Research*, 15(8), 949-979.

Davies, A. G., and Li, Z. (1997). "Modelling sediment transport beneath regular symmetrical and asymmetrical waves above a plane bed." *Continental Shelf Research*, 17(5), 555-582.

Davies, A. G., Ribberink, J. S., Temperville, A., and Zyserman, J. A. (1997). "Comparisons between sediment transport models and observations made in wave and current flows above plane beds." *Coastal Engineering*, 31(1-4), 163-198.

Davies, A. G., and Thorne, P. D. (2005). "Modeling and measurement of sediment transport by waves in the vortex ripple regime." *Journal of Geophysical Research-Oceans*, 110(C5).

Davies, A. G., van Rijn, L. C., Damgaard, J. S., van de Graaff, J., and Ribberink, J. S. (2002). "Intercomparison of research and practical sand transport models." *Coastal Engineering*, 46(1), 1-23.

Davies, A. G., and Villaret, C. (1999). "Eulerian drift induced by progressive waves above rippled and very rough beds." *Journal Of Geophysical Research-Oceans*, 104(C1), 1465-1488.

Davies, A. G., and Villaret, C. (2002). "Prediction of sand transport rates by waves and currents in the coastal zone." *Continental Shelf Research*, 22(18-19), 2725-2737.

De Vriend, H. J., Capobianco, M., Chesher, T., Deswart, H. E., Latteux, B., and Stive, M. J. F. (1993a). "Approaches to long-term modeling of coastal morphology - a review." *Coastal Engineering*, 21(1-3), 225-269.

De Vriend, H. J., Zyserman, J., Nicholson, J., Roelvink, J. A., Pechon, P., and Southgate, H. N. (1993b). "Medium-Term 2dh Coastal Area Modeling." *Coastal Engineering*, 21(1-3), 193-224.

Dean, R. G. (1973). "Heuristic models of sand transport in teh surf zone." Proc. Conf. Eng. Dynamics in the Surf Zone, Sydney, 208-214.

Dean, R. G. (1977). "Equilibrium beach profiles: U.S. Atlantic and Gulf coasts." *Department of Civil Engineering, Ocean Engineering Report No. 12*, University of Delaware, , Newark, DE.

Dean, R. G., and Dalrymple, R. A. (1991). *Water Wave Mechanics for Engineers and Scientists*, World Scientific, Singapore.

Dean, R. G., and Dalrymple, R. A. (2002). *Coastal Processes with Engineering Applications*, Cambridge University Press, Cambridge.

Dean, R. G., Kriebel, D. L., and Walton, T. (2002). "Cross-Shore Sediment Transport Processes In: David King. (editor), Coastal Engineering Manual, Part 3 - Chapter 3." Engineer Manual 1110-2-1100, U.S. Army Corps of Engineers, Washington, DC.

Deigaard, R., Fredsoe, J., and Hedegaard, I. B. (1986). "Suspended Sediment In The Surf Zone." *Journal Of Waterway Port Coastal And Ocean Engineering-Asce*, 112(1), 115-128.

Deigaard, R., Fredsoe, J., and Hedegaard, I. B. (1987). "Suspended Sediment In The Surf Zone - Closure." *Journal Of Waterway Port Coastal And Ocean Engineering-Asce*, 113(5), 557-562.

Deigaard, R., Jakobsen, J. B., and Fredsoe, J. (1999). "Net sediment transport under wave groups and bound long waves." *Journal Of Geophysical Research-Oceans*, 104(C6), 13559-13575.

Dibajnia, M., Moriya, T., and Watanabe, A. (2001). "A representative wave model for estimation of nearshore local transport rate." Coastal Engineering Journal, 43(1), 1-38.

Doering, J. C., Elfrink, B., Hanes, D. M., and Ruessink, B. G. (2000). "Parameterization of velocity skewness under waves and its effect on cross-shore sediment transport." Proc. 27th International Conf. on Coastal Engineering, ASCE, Sydney, Australia, 1383-1396.

Dohmen-Janssen, C. M., and Hanes, D. M. (2002). "Sheet flow dynamics under monochromatic nonbreaking waves." Journal Of Geophysical Research-Oceans, 107(C10).

Dohmen-Janssen, C. M., and Hanes, D. M. (2005). "Sheet flow and suspended sediment due to wave groups in a large wave flume." *Continental Shelf Research*, 25(3), 333-347.

Dohmen-Janssen, C. M., Hassan, W. N., and Ribberink, J. S. (2001). "Mobile-bed effects in oscillatory sheet flow." *Journal Of Geophysical Research-Oceans*, 106(C11), 27103-27115.

Dohmen-Janssen, C. M., Kroekenstoel, D. F., Hassan, W. N., and Ribberink, J. S. (2002). "Phase lags in oscillatory sheet flow: experiments and bed load modelling." *Coastal Engineering*, 46(1), 61-87.

Dong, P., and Zhang, K. (2002). "Intense near bed sediment motions in waves and currents." *Coastal Engineering*, 45, 75-87.

Drei, E., Lamberti, A., and Svendsen, I. A. (2000). "Current analysis around a submerged breakwater." Proc. IVth Int. Conf. Hydrodyn., Yokohama, 693 -698.

Dulou, C., Belzons, M., and Rey, V. (2000). "Laboratory study of wave bottom interaction in the bar formation on an erodible sloping bed." *Journal of Geophysical Research*, 105(C8), 19745-62.

Dulou, C., Belzons, M., and Rey, V. (2002). "Bar formation under breaking wave conditions: A laboratory study." *Journal of Coastal Research*, 18(4), 802-809.

Elfrink, B., and Baldock, T. (2002). "Hydrodynamics and sediment transport in the swash zone: a review and perspectives." *Coastal Engineering*, 45(3-4), 149-167.

Elfrink, B., Hanes, D. M., and Ruessink, B. G. (2006). "Parameterization and simulation of near bed orbital velocities under irregular waves in shallow water."

Engelund, F., and Fredsoe, J. (1976). "Sediment Transport Model For Straight Alluvial Channels." *Nordic Hydrology*, 7(5), 293-306.

Foster, D., and Holman, R. (1994). "Correlation between sediment suspension events and shear instabilities in the bottom boundary layer of the surf zone." Proceedings Coastal Dynamics. ASCE., Barcelona.

Fredsoe, J. (1984). "Turbulent boundary layer in wave-current motion." *Journal Of Hydraulic Engineering-Asce*, 110(8), 1103–1120.

Fredsoe, J., Anderson, A. H., and Silberg, S. (1985). "Distribution of Suspended Sediment in Large Waves." *Journal Of Waterway Port Coastal And Ocean Engineering-Asce*, 111(6), 1041-1059.

Fredsoe, J., and Deigaard, R. (1992). *Mechanics of Coastal Sediment Transport*, World Scientific, Singapore.

Gallagher, E. L., Elgar, S., and Guza, R. T. (1998). "Observations of sand bar evolution on a natural beach." *Journal Of Geophysical Research-Oceans*, 103(C2), 3203-3215.

Grant, W. D., and Madsen, O. S. (1979). "Combined Wave And Current Interaction With A Rough Bottom." *Journal Of Geophysical Research-Oceans And Atmospheres*, 84(NC4), 1797-1808.

Grant, W. D., and Madsen, O. S. (1986). "The continental shelf bottom boundary layer." *Annual Review of Fluid Mechanics*, 18, 265-305.

Grasmeijer, B. T., and Kleinhans, M. G. (2004). "Observed and predicted bed forms and their effect on suspended sand concentrations." *Coastal Engineering*, 51(5-6), 351-371.

Haas, K. A., and Cambazoglu, M. K. (2006). "Video observations of longshore currents Myrtle Beach, South Carolina." ICCE 06, San Diego.

Haas, K. A., Demir, H., Work, P. A., Voulgaris, G., and Obley, S. (2004). "Myrtle Beach nearshore experiment Dec 10 to Dec 15 2003. Part 2: Morphological and remote imagery measurements." Georgia Institute of Technology Technical Report, Savannah.

Haas, K. A., and Hanes, D. M. (2004). "Process based modeling of total longshore sediment transport." *Journal Of Coastal Research*, 20(3), 853-861.

Haas, K. A., Svendsen, I. A., Haller, M., and Zhao, Q. (2003). "Quasi 3D modeling of rip current systems." *Journal of Geophysical Research*, 108(C7), 3217.

Hagatun, K., and Eidsvik, K. J. (1986). "Oscillating Turbulent Boundary-Layer With Suspended Sediments." *Journal Of Geophysical Research-Oceans*, 91(C11), 3045-3055.

Hanes, D. M., and Bowen, A. J. (1985). "A granular fluid model for steady-intense bed load transport." *Journal of Geophysical Research*, 90(C5), 9149-9158.

Hassan, W. N., and Ribberink, J. S. (2005). "Transport processes of uniform and mixed sands in oscillatory sheet flow." *Coastal Engineering*, 52(9), 745-770.

Henderson, S. M., Allen, J. S., and Newberger, P. A. (2004). "Nearshore sandbar migration predicted by an eddy-diffusive boundary layer model." *Journal Of Geophysical Research-Oceans*, 109(C6).

Hoefel, F., and Elgar, S. (2003). "Wave-induced sediment transport and sandbar migration." *Science*, 299(5614), 1885-1887.

Holman, R. A., and Sallenger, A. H. (1993). "SandBar Generation: A Discussion of the Duck Experiment Series." *Journal of Coastal Research*, SI(15), 76-92.

Holmedal, L. E., Myrhaug, D., and Eidsvik, K. J. (2004). "Sediment suspension under sheet flow conditions beneath random waves plus current." *Continental Shelf Research*, 24(17), 2065-2091.

Holmedal, L. E., Myrhaug, D., and Rue, H. (2003). "The sea bed boundary layer under random waves plus current." *Continental Shelf Research*, 23(7), 717-750.

Horikawa, K., Watanabe, A., and Katori, S. (1983). "Sediment transport under sheet flow conditions." ASCE, New York, NY, USA, Cape TownS Afr, 1335-1352.

Hsu, T. J., and Hanes, D. M. (2004). "Effects of wave shape on sheet flow sediment transport." *Journal Of Geophysical Research-Oceans*, 109(C5).

Hsu, T. J., Jenkins, J. T., and Liu, P. L. F. (2003). "On two-phase sediment transport: Dilute flow." *Journal Of Geophysical Research-Oceans*, 108(C3).

Hsu, T. W., and Ou, S. H. (1994). "Mean Sediment Concentration And Turbulent Boundary-Layer Of Wave-Induced Sheet Flow." *Journal Of Hydraulic Research*, 32(5), 675-687.

Isobe, M., and Horikawa, K. (1982). "Study on water particle velocities of shoaling and breaking waves." *Coastal Engineering in Japan* 25, 109-123.

Jenkins, J. T., and Hanes, D. M. (1998). "A sheared layer of colliding grains driven from above by a turbulent fluid." *Journal Of Fluid Mechanics*, 370, 29-52.

Johnson, D. (2002). "DIWASP, a directional wave spectra toolbox for MATLAB®: User Manual." Centre for Water Research, University of Western Australia.

Johnson, H. K., and Zyserman, J. A. (2002). "Controlling spatial oscillations in bed level update schemes." *Coastal Engineering*, 46(2), 109-126.

Kaczmarek, L. M. (1991). "Mathematical model for oscillatingsheet flow." Proc. Euromech 262 Colloquium on Sand Transport in Rivers, Estuaries and the Sea. A.A. Balkema., Rotterdam, pp. 197– 202.

Kaczmarek, L. M., Biegowski, J., and Ostrowski, R. (2004). "Modelling cross-shore intensive sand transport and changes of bed grain size distribution versus field data." *Coastal Engineering*, 51(5-6), 501-529.

Kaczmarek, L. M., and Ostrowski, R. (2002). "Modelling intensive near-bed sand transport under wave-current flow versus laboratory and field data." *Coastal Engineering*, 45(1), 1-18.

Kirby, J. T. (2001). "Publications Related to REFDIF Model Development and Applications" http://chinacat.coastal.udel.edu/programs/refdif/refdif_pubs.html. (Accessed March 5, 2007).

Kirby, J. T. (2006). "NearCom: Nearshore Community Model" http://chinacat.coastal.udel.edu/programs/nearcom (Accessed November 5, 2006).

Kirby, J. T., and Dalrymple, R. A. (1983). "A parabolic equation for the combined refraction diffraction of stokes waves by mildly varying topography." *Journal of Fluid Mechanics*, 136 543-566.

Kirby, J. T., Dalrymple, R. A., and Shi, F. (2004). "Refraction-Diffraction Model REF/DIF S Version 1.3 Documentation and User's Manual." *CACR-04-01*, University of Delaware, Newark.

Kobayashi, N., and Johnson, B. D. (2001). "Sand suspension, storage, advection, and settling in surf and swash zones." *Journal Of Geophysical Research-Oceans*, 106(C5), 9363-9376.

Komar, P., and Miller, M. (1975). "The initiation of oscillatory ripple marks and the development of plane-bed at high shear stresses under waves. ." *J. Sediment. Petrol.* , 45(3), 697–703.

Kraus, N. C., and Larson, M. (1988). "Beach profile change measured in the tank for large waves." Tech. Rpt. CERC-88-6 U.S. Army Coastal Engineering Research Center, Vicksburg.

Kriebel, D. L. (1982). "Beach and dune response to hurricanes," MCE Thesis, University of Delaware, Newark.

Kundu, P. K., and Cohen, I. M. (2002). *Fluid Mechanics*, Academic Press, San Diego.

Kuriyama, Y. (2002). "Medium-term bar behavior and associated sediment transport at Hasaki, Japan." *Journal Of Geophysical Research-Oceans*, 107(C9).

Lee, G. H., Dade, W. B., Friedrichs, C. T., and Vincent, C. E. (2004). "Examination of reference concentration under waves and currents on the inner shelf." *Journal of Geophysical Research-Oceans*, 109(C2).

Lee, G. H., Friedrichs, C. T., and Vincent, C. E. (2002). "Examination of diffusion versus advection dominated sediment suspension on the inner shelf under storm and swell conditions, Duck, North Carolina." *Journal Of Geophysical Research-Oceans*, 107(C7), 3084.

Lee, T. H., and Hanes, D. M. (1996). "Comparison of field observations of the vertical distribution of suspended sand and its prediction by models." *Journal Of Geophysical Research-Oceans*, 101(C2), 3561-3572.

Li, Z., and Davies, A. G. (2001). "Turbulence closure modelling of sediment transport beneath large waves." *Continental Shelf Research*, 21(3), 243-262.

Lippmann, T. C., Brookins, A. H., and Thornton, E. B. (1996). "Wave energy transformation on natural profiles." *Coastal Engineering*, 27(1-2), 1-20.

Long, W., Kirby, J. T., and Shao, Z. (2006). "Numerical schemes for bed level updating in sediment transport." *in press*.

Longuet-Higgins, M. S. (1953). "Mass transport in water waves." *Royal Society of Phil. Trans.*, 245A, 535-581.

Longuet-Higgins, M. S. (1956). "The mechanics of the boundary layer near the bottom in a progressive wave." ASCE Proc. 16th Int. Conf. Coastal Engineering, 184-193.

Madsen, O. S., and Grant, W. D. (1976). "Sediment transport in the coastal environment." Rep. 209, Ralph M. Parsons Lab., Mass. Inst. of Technol., Cambridge.

Malarkey, J., Davies, A. G., and Li, Z. (2003). "A simple model of unsteady sheet-flow sediment transport." *Coastal Engineering*, 48(3), 171-188.

Masselink, G. (2004). "Formation and evolution of multiple intertidal bars on macrotidal beaches: application of a morphodynamic model." *Coastal Engineering*, 51(8-9), 713-730.

McLean, S. R., Ribberink, J. S., Dohmen-Janssen, C. M., and Hassan, W. N. (2001). "Sand transport in oscillatory sheet flow with mean current." *Journal Of Waterway Port Coastal And Ocean Engineering-Asce*, 127(3), 141-151.

Meyer-Peter, E., and Muller, R. (1948). "Formulas for bed-Load Transport." International Association for Hydraulic Structures Research, Report on the Second Meeting, Stockholm, 39-64.

Nairn, R. B., and Southgate, H. N. (1993). "Deterministic Profile Modeling Of Nearshore Processes .2. Sediment Transport And Beach Profile Development." *Coastal Engineering*, 19(1-2), 57-96.

Nielsen, P. (1986). "Suspended sediment concentrations under waves." *Coastal Engineering*, 10, 23-31.

Nielsen, P. (1992). Coastal Bottom Boundary Layers and Sediment Transport, World Scientific, Singapore.

Nielsen, P., and Callaghan, D. P. (2003). "Shear stress and sediment transport calculations for sheet flow under waves." *Coastal Engineering*, 47(3), 347-354.

Nielsen, P., van der Wal, K., and Gillan, L. (2002). "Vertical fluxes of sediment in oscillatory sheet flow." *Coastal Engineering*, 45(1), 61-68.

O' Connor, B., Pan, S., Nicholson, J., MacDonald, N., and Huntley, D. A. (1998). "A 2D model of waves and undertow in the surf zone." Proc. 26th Coastal Engineering, ASCE, 286-296.

O'Donoghue, T., and Wright, S. (2004). "Flow tunnel measurements of velocities and sand flux in oscillatory sheet flow for well-sorted and graded sands." *Coastal Engineering*, 51(11-12), 1163-1184.

O'Hare, T. J., and Davies, A. G. (1990). "A laboratory study of sand bar evolution." *Journal of Coastal Research*, 6(3), 531-44.

Obley, S., Voulgaris, G., Haas, K. A., Demir, H., and Work, P. A. (2004). "Myrtle Beach nearshore experiment Dec. 10 to Dec. 15 2003. Part 1: Hydrodynamic measurements." University of South Carolina CPSD Technical report.

Ohnaka, S., and Watanabe, A. (1990). "Modeling of wave-current interaction and bed change." Proc. 22nd ICCE, Delft, 2443-2456.

Puleo, J. A., Mouraenko, O., and Hanes, D. M. (2004). "One-dimensional wave bottom boundary layer model comparison: Specific eddy viscosity and turbulence closure models." *Journal of Waterway Port Coastal and Ocean Engineering-Asce*, 130(6), 322-325.

Putrevu, U., and Svendsen, I. A. (1999). "Three-dimensional dispersion of momentum in wave-induced nearshore currents." *European Journal of Mechanics B-Fluids*, 18(3), 409-427.

Qin, W., and Svendsen, I. A. (2003). "Modeling nearshore processes." *CACR-03-04*, Center for Applied Coastal Research, Newark, Delaware.

Rakha, K. A., Deigaard, R., and Broker, I. (1997). "A phase-resolving cross shore sediment transport model for beach profile evolution." *Coastal Engineering*, 31(1-4), 231-261.

Ribberink, J. S. (1998). "Bed-load transport for steady flows and unsteady oscillatory flows." *Coastal Engineering*, 34(1-2), 59-82.

Ribberink, J. S., and Al-Salem, A. A. (1994). "Sediment Transport In Oscillatory Boundary-Layers In Cases Of Rippled Beds And Sheet Flow." *Journal Of Geophysical Research-Oceans*, 99(C6), 12707-12727.

Ribberink, J. S., and Al-Salem, A. A. (1995). "Sheet Flow And Suspension Of Sand In Oscillatory Boundary-Layers." *Coastal Engineering*, 25(3-4), 205-225.

Roelvink, J. A., and Broker, I. (1993). "Cross-shore profile models." *Coastal Engineering*, 21(1-3), 163.

Roelvink, J. A., and Reniers, A. J. H. M. (1995). "LIP 11D delta flume experiments " *Data Rep. H 2130.*, Delft Hydraulics, Delft.

Roelvink, J. A., and Stive, M. J. F. (1989). "Bar-Generating Cross-Shore Flow Mechanisms On A Beach." *Journal Of Geophysical Research-Oceans*, 94(C4), 4785-4800.

Rouse, H. (1937). "Modern conceptions of the mechanics of turbulence." *Trans. Am. Soc. Civ. Eng.*, , 102, 463- 543.

Ruessink, B. G., and Kroon, A. (1994). "The Behavior Of A Multiple Bar System In The Nearshore Zone Of Terschelling, The Netherlands - 1965-1993." *Marine Geology*, 121(3-4), 187-197.

Ruessink, B. G., and Terwindt, J. H. J. (2000). "The behaviour of nearshore bars on the time scale of years: a conceptual model." *Marine Geology*, 163(1-4), 289-302.

Russell, P. E., and Huntley, D. A. (1999). "A cross-shore transport "shape function"' for high energy beaches." *Journal Of Coastal Research*, 15(1), 198-205.

Sajjadi, S. G., and Waywell, M. N. (1997). "Application of roughness-dependent boundary conditions to turbulent oscillatory flows." *International Journal Of Heat And Fluid Flow*, 18(4), 368-375.

Sawamoto, M., and Yamashita, T. (1986). "Sediment transport rate due to wave action." *J. Hydros. Hydraul. Eng.*, 4, 1-15.

Schoonees, J. S., and Theron, A. K. (1995). "Evaluation Of 10 Cross-Shore Sediment Transport Morphological Models." *Coastal Engineering*, 25(1-2), 1-41.

Shand, R. D., Bailey, D. G., and Shepherd, M. J. (1999). "An inter-site comparison of net offshore bar migration characteristics and environmental conditions." *Journal Of Coastal Research*, 15(3), 750-765.

Sierra, J. P., Azuz, I., Rivero, F., Sanchez-Arcilla, A., and Rodriguez, A. (1997). "Morphodynamic modelling in the nearshore area." Proc. of Coastal 97, La Coruna, Spain, 433-442.

Sleath, J. F. A. (1984). *Sea Bed Mechanics*, Wiley Interscience, New York.

Sleath, J. F. A., and Wallbridge, S. (2002). "Pickup from rippled beds in oscillatory flow." *Journal Of Waterway Port Coastal And Ocean Engineering-Asce*, 128(6), 228-237.

Smith, J. D., and McLean, S. R. (1977). "Spatially averaged flow over a wavy surface." *Journal of Geophysical Research*, 82(12), 1735-1746.

Staub, C., Jonsson, I. G., and Svendsen, I. A. (1996). "Sediment suspension in oscillatory flow: Measurements of instantaneous concentration at high shear." *Coastal Engineering*, 27(1-2), 67-96.

Stive, M. J. F., and Battjes, J. A. "A model for offshore sediment transport." *Proceedings of the 19th. Coastal Engineering Conference*, Houston, TX, USA, 1420-1436.

Sturm, T. W. (2001). *Open Channel Hydraulics*, McGrawHill, Boston.

Sumer, B. M., Kozakiewicz, A., Fredsoe, J., and Deigaard, R. (1996). "Velocity and Concentration Profiles in Sheet-Flow Layer of Movable Bed." *Journal of Hydraulic Engineering*, 122(10), 549-558.

Sutherland, J., Walstra, D. J. R., Chesher, T. J., van Rijn, L. C., and Southgate, H. N. (2004). "Evaluation of coastal area modelling systems at an estuary mouth." *Coastal Engineering*, 51(2), 119-142.

Svendsen, I. A. (2006). *Introduction to Nearshore Hydrodynamics*, World Scientific, Singapore.

Svendsen, I. A., Haas, K. A., and Zhao, Q. (2002). "Quasi-3D Nearshore Circulation Model (SHORECIRC)." *CACR-02-01*, Center for Applied Coastal Research, Univ. of Delaware.

Svendsen, I. A., and Putrevu, U. (1994). "Nearshore Mixing and Dispersion." Proceedings of the Royal Society of London Series a-Mathematical Physical and Engineering Sciences, 445(1925), 561-576.

Thorne, P. D., Williams, J. J., and Davies, A. G. (2002). "Suspended sediments under waves measured in a large-scale flume facility." *Journal of Geophysical Research-Oceans*, 107(C8).

Thornton, E. B., and Guza, R. T. (1983). "Transformation Of Wave Height Distribution." *Journal Of Geophysical Research-Oceans And Atmospheres*, 88(NC10), 5925-5938.

Thornton, E. B., Humiston, R. T., and Birkemeier, W. (1996). "Bar/trough generation on a natural beach." *Journal Of Geophysical Research-Oceans*, 101(C5), 12097-12110.

Trowbridge, J., and Madsen, O. S. (1984a). "Turbulent Wave Boundary-Layers .1. Model Formulation And 1st-Order Solution." *Journal Of Geophysical Research-Oceans*, 89(NC5), 7989-7997.

Trowbridge, J., and Madsen, O. S. (1984b). "Turbulent Wave Boundary-Layers .2. 2nd-Order Theory And Mass-Transport." *Journal Of Geophysical Research-Oceans*, 89(NC5), 7999-8007.

Van Dongeren, A. R., Sancho, F. E., Svendsen, I. A., and Putrevu, U. (1994). "SHORECIRC: A quasi 3-D nearshore model." Proc., 24th Int. Conf. on Coast. Engrg., ASCE, 2741-2754.

Van Dongeren, A. R., Svendsen, I. A., and Sancho, F. E. (1995). "Application of the Q-3D SHORECIRC model to surfbeat." Coastal Dynamics'95 ASCE, Gdanaask, Poland, 233-244.

Van Dongeren, A. R., Svendsen, I. A., and Sancho, F. E. (1996). "Generation of infragravity waves." In Proc., 25th Int. Conf. on Coast. Engrg., ASCE, , 1335-1348.

Van Rijn, L. C. (1984). "Sediment Pick-Up Functions." *Journal Of Hydraulic Engineering-Asce*, 110(10), 1494-1502.

Van Rijn, L. C. (1986). "Applications Of Sediment Pick-Up Function." *Journal Of Hydraulic Engineering-Asce*, 112(9), 867-874.

Van Rijn, L. C. (1993). *Principles of Sediment Transport in Rivers, Estuaries and Coastal Seas*, Aqua Publications, Amsterdam, The Netherlands.

Van Rijn, L. C. (2000). "General view on sand transport by currents and waves; TRANSPOR2000 and CROSMOR2000 models." Report Z2899.20/2099.30.2824.30 Delft Hydraulics, Delft, The Netherlands.

Van Rijn, L. C., Walstra, D. J. R., Grasmeijer, B., Sutherland, J., Pan, S., and Sierra, J. P. (2003). "The predictability of cross-shore bed evolution of sandy beaches at the time scale of storms and seasons using process-based Profile models." *Coastal Engineering*, 47(3), 295-327.

Vincent, C. E., and Green, M. O. (1990). "Field-Measurements Of The Suspended Sand Concentration Profiles And Fluxes And Of The Resuspension Coefficient-Gamma-0 Over A Rippled Bed." *Journal Of Geophysical Research-Oceans*, 95(C7), 11591-11601.

Watanabe, A., Maruyama, K., Shimuzu, T., and Sakakaiyama, T. (1986). "Numerical prediction model of three dimensional beach deformation around a structure." *Coastal Engineering in Japan*, 29, 179-194.

Watanabe, A., Riho, Y., and Horikawa, Y. (1980). "Beach profile and on-offshore sediment transport." Proc. 17th ICCE Sydney, Australia, 1106-1121.

Wei, G., and Kirby, J. T. (1995). "A time dependent numerical code for extended Boussinesq equations." *Journal Of Waterway Port Coastal And Ocean Engineering-Asce*, 120, 251-261.

Wikramanayeke, P. N. (1993). "Velocity profiles and suspended sediment transport," PhD Dissertation, Mass. Inst. of Technology, Cambridge.

Wilson, K. C. (1987). "Analysis of bed load motion at high shear stress." *Journal of Hydraulic Engineering, ASCE*, 113(1), 97-103.

Wilson, K. C. (1989). "Mobile-bed friction at high shear stress." *Journal of Hydraulic Engineering*, 115(6), 825-830.

Work, P. A., and Wiederhold, C. (2006). "Nearshore Hydrodynamics and Beach Morphology Experiment, Myrtle Beach, SC, December 10-18, 2005." Georgia Institute of Technology Savannah, Savannah, GA.

Wright, L. D., and Short, A. D. (1984). "Morphodynamic variability of surf zones and beaches: a synthesis." *Marine geology*, 56(1-41-4), 93-118.

Yoo, J., Fritz, H., Haas, K., Work, P., and Barnes, C. (2005). "Wave property estimation using linear feature extraction from nearshore wave images." WAVES 05, Madrid, Spain, 11.

Zala Flores, N., and Sleath, J. F. A. (1998). "Mobile layer in oscillatory sheet flow." *Journal Of Geophysical Research-Oceans*, 103(c6), 12783-12794.

Zedler, E. A., and Street, R. L. (2006). "Sediment Transport over Ripples in Oscillatory Flow." *Journal of Hydraulic Engineering*, 132(2), 180-193.

Zyserman, J. A., and Fredsoe, J. (1994). "Data-Analysis Of Bed Concentration Of Suspended Sediment." *Journal Of Hydraulic Engineering-Asce*, 120(9), 1021-1042.